Doctoral thesis

Spectroscopic research of Λ hypernuclei up to medium-heavy mass region with the (e,e'K^+) reaction

(e,e'K^+)反応を用いた中重質量数領域に及ぶΛハイパー核分光研究

Toshiyuki Gogami

Department of Physics, Graduate School of Science,

Tohoku University

2014

Abstract

In 2009 (August-November), the E05-115 experiment was carried out at JLab to investigate Λ hypernuclei in the wide mass region up to $A = 52$ ($^{7}_{\Lambda}$He, $^{10}_{\Lambda}$Be, $^{12}_{\Lambda}$B and $^{52}_{\Lambda}$V) with the (e,e$'K^+$) reaction. This is the first attempt to investigate a medium heavy Λ hypernucleus with the (e,e$'K^+$) reaction. Experimentally, it is difficult to measure heavier Λ hypernuclei as background rates of particles which originate from electromagnetic processes are roughly in proportion to Z^2 (Z: target proton number) in the (e,e$'K^+$) experiment. To perform the experiment, many experimental techniques have been developed and introduced such as optimization of the electron spectrometer configuration (tilt method), clean kaon identification, particle tracking under high multiplicity environment, precise energy scale calibration and so on. In the present thesis, experimental results of the elementary process of p(e,e$'K^+)\Lambda$, Λ hypernuclei of $^{7}_{\Lambda}$He, $^{10}_{\Lambda}$Be, $^{12}_{\Lambda}$B and $^{52}_{\Lambda}$V are shown.

Elementary processes of the electroproduction of Λ and Σ^0, p(e,e$'K^+)\Lambda$, Σ^0 were used for the absolute energy scale calibration of our spectrometer systems. A careful Monte Carlo simulation shows that the binding energy can be obtained with a systematic error of 0.11 MeV with our energy scale calibration method. A study of the elementary process of Λ is important to understand Λ hypernuclei as it is essential for theoretical calculations of Λ hypernuclei. The differential cross section of the p(e,e$'K^+)\Lambda$ reaction at the small K^+ scattering angle ($\theta^{\rm CM}_{\gamma K} \simeq 15.5^\circ$), the small Q^2 ($\simeq 0.01$ [GeV/c]^2) and the total energy of $W = 1.92$ GeV, where no experimental data exists was obtained to be $235 \pm 13^{+28}_{-24}$ nb/sr.

The ground state ($1/2^+$) binding energy of $^{7}_{\Lambda}$He was already measured in JLab E01-011 (2005). In the present work, the binding energy of $1/2^+$ state was determined to be $B_\Lambda = 5.55 \pm 0.10 \pm 0.11$ MeV with five times more statistic and smaller systematic errors than those of the previous experiment. The ground state binding energy is important to test the phenomenologically introduced CSB (Charge Symmetry Breaking) ΛN interaction for $A = 7$, $T = 1$ hypernuclear systems. In addition, a peak which is interpreted as $3/2^+$ and $5/2^+$ states was measured to be $B_\Lambda = 3.65 \pm 0.20 \pm 0.11$ MeV with sufficient statistic for the first time.

Only three events of the ground state of $^{10}_{\Lambda}$Be had been observed in the emulsion experiments. The present experiment is the first spectroscopic measurement of $^{10}_{\Lambda}$Be, and the detailed structures have been successfully measured for the first time. About three times better energy resolution was achieved in the present experiment (0.78 MeV in FWHM) than that of the mirror Λ hypernucleus, $^{10}_{\Lambda}$B (2.2 MeV in FWHM) which was measured in the (π^+,K^+) experiment at KEK. The result of the ground state binding energy was obtained to be $B_\Lambda = 8.55 \pm 0.07 \pm 0.11$ MeV which serves also to discuss about the CSB effect in the ΛN interaction.

$^{12}_{\Lambda}$B has been measured with the world best energy resolution of 0.5 MeV (FWHM) among the reaction spectroscopy of Λ hypernuclei. The results of $^{12}_{\Lambda}$B are compared with the experimental results in the previous experiments to confirm the consistency. Furthermore, the obtained ground state binding energies of $^{12}_{\Lambda}$B ($B_\Lambda = 11.38 \pm 0.02 \pm 0.11$ MeV) and $^{52}_{\Lambda}$V ($B_\Lambda = 21.88 \pm 0.59 \pm 0.11$ MeV) indicate that the reported value of $^{12}_{\Lambda}$C which has been used as a reference of binding energy measurements for the (π^+,K^+) experiments would be shallower by ~ 0.5 MeV.

A pilot study for investigation in the medium-heavy mass region with the (e,e$'K^+$) experiment was performed by measuring $^{52}_{\Lambda}$V. The ground state binding energy of $^{52}_{\Lambda}$V has been measured, overcoming high multiplicity environment. The results are discussed with the experimental results of $^{51}_{\Lambda}$V measured at KEK. The present result is the first measurement of Λ's binding energy of the ground state without the emulsion reference in the medium-heavy mass region, which could be a substantial improvement in the information needed for understanding the single particle potential of Λ.

In the present experiment, Λ hypernuclear measurement with a small systematic error of $\sim$ 0.1 MeV by the (e,e$'K^+$) reaction has been established. Moreover, the present work opened a door to the heavier Λ hypernuclear measurement with the (e,e$'K^+$) reaction in the future.

Contents

Chapter 1

Introduction

1.1 Significance of Λ Hypernuclear Research

One of the ultimate question is "what is fundamental elements to make our world". Many scientists have been trying to answer the questions. Nowadays, six quarks and six leptons are considered to be elementary particles. An atoms consists of a nucleus and electrons. A normal nucleus surrounding us consists of nucleons (proton and neutron). A proton and a neutron are composed of *uud* and *udd* in quark level, respectively. Interacting force among nucleons (NN interaction) have been well studied by nucleon-nucleon (NN) scattering experiments and spectroscopy of normal nucleus.

A Λ is the lightest baryon which has a strangeness quark (*sud*). A Λ can be bound in deeply inside nucleus as the single embedded Λ is not subject to the Pauli exclusion principle from nucleons. It means that a Λ can be a probe to investigate deeply inside nucleus where is not easily studied by spectroscopy of normal nuclei. Additionally, the natural width of Λ hypernucleus is narrower as the life time is relatively longer (a few 100 ps) than that of normal nucleus. In the case of 1d-shell state of ^{208}Pb, for example, the spreading width is $\sim$5 MeV which is too wide to perform precise spectroscopic study. Therefore, precise nuclear structures can be investigated by Λ hypernuclear spectroscopy in principle.

One of the largest topics in nuclear physics is extending our understanding of the nuclear force describing the NN interaction to that of the baryon-baryon (BB) interaction. Investigating hyperon-nucleon (YN) and hyperon-hyperon (YY) are natural extensions as the first step for studying the BB interaction. However, YN (YY) scattering experiments are not practical so far as the lifetime of hyperons are too short to perform the scattering experiments (e.g. $\tau \sim$260 ps for Λ). Therefore, spectroscopic information of Λ hypernuclei is used to deduce YN (YY) information.

Assuming a Λ hypernuclear wave function can be decomposed into a Λ hyperon and a core nucleus, the Λ hypernuclear Hamiltonian ($H_{\rm HY}$) is described as the following [1]:

$$H_{\rm HY} = H_{\rm core} + t_\Lambda + \sum v_{\Lambda N}^{\rm effective} \tag{1.1}$$

where $H_{\rm core}$ is a Hamiltonian of a core nucleus, t_Λ is the kinetic energy of the Λ hypernucleus and $\sum v_{\Lambda N}^{\rm effective}$ is an effective ΛN potential. The effective ΛN potential is constructed by G-matrix calculation, which is started from the two-body interaction. To describe the elementary two-body interaction, one-boson-exchange models such as Nimegen [2][3] and Julich [4][5] interactions are extensively used. Analytically the effective potentials are widely given in the form of three-range Gaussian [6]:

$$V_{\Lambda N}(r) = \sum_i (a_i + b_i k_f + c_i k_f^2) \exp\Big(\frac{-r^2}{\beta_i^2}\Big). \tag{1.2}$$

Λ hypernuclear structures and reaction cross sections are calculated by using this potential and compared with experimental data.

In the case of p-shell Λ hypernuclei, the effective ΛN interaction might be expressed as the following [7]:

$$V_{\Lambda N}(r) = V_0(r) + V_\sigma(r) s_\Lambda s_N + V_\Lambda(r) l_{\Lambda N} s_\Lambda + V_N(r) l_{\Lambda N} s_N + V_T(r) S_{12} \tag{1.3}$$

where $S_{12} = 3(\sigma_\Lambda \hat{r})(\sigma_N \hat{r}) - \sigma_\Lambda \sigma_N$. The terms are potentials of central one, ΛN spin-spin interaction, Λ spin-orbit interaction, N spin-orbit interaction and tensor. Low-lying level energies of p-shell Λ hypernuclei are calculated with radial integrations of those five terms. The integrals denoted as $\overline{V}$, Δ, S_Λ,S_N and T are determined by experimental data of p-shell Λ hypernuclei and compared with theoretical predictions.

New forms and aspects of hadronic matter are expected to be investigated through a quantitative research of YN (YN) interaction. Particularly, detailed YN and YY interactions are essential to understand high-density matter such as inside of a neutron star where hyperons might be appeared energetically.

1.2 Λ hypernuclear measurements in the past

Many species of Λ hypernuclei were measured in the past experiments (Fig. 1.1 [10]) since a Λ particle had been discovered in 1953 [27]. There are four major stages of Λ hypernuclear measurements as follows:

1. Emulsion experiments with the (K^-,π^-) reaction at CERN[*1] and BNL[*2] (1960's),
2. Counter experiments with the (K^-,π^-) reaction at CERN and BNL (1970's - 1980's),
3. Counter experiments with the (π^+,K^+) reaction at BNL and KEK[*3] (1980's - 1990's),
4. Counter experiments with the (e,e′K^+) reaction at JLab[*4] (2000-).

The three Λ production reactions, (K^-,π^-), (π^+,K^+) and (e,e′K^+) reactions are shown above. These reactions will be explained in the next section before the past Λ hypernuclear experiments are described.

1.2.1 Λ production reactions

Three major three reactions, the (K^-,π^-), (π^+,K^+) and (e,e′K^+) are used to produce Λ hypernuclei. Schematic descriptions of those reactions are shown in Fig. 1.2. The simplest way to produce Λ is bringing a strange quark in an incident particle into a target nucleus. In the (K^-,π^-) reaction, a strange quark is brought by a K^- into the target nucleus. A down quark in the target neutron was exchanged for the strange quark in K^- beam as shown in Fig. 1.2. On the other hand, a strange and unti-strange quark pair is associatively generated in the (π^+,K^+) and (e,e′K^+) reactions.

Fig. 1.3 and Fig. 1.4 show the momentum transfers to a Λ by the (K^-,π^-), (π^+,K^+) and (e,e′K^+) reactions as a function of beam momentum with scatting angle of 0° and 10°, respectively. The momentum transfer is small in the case of (K^-,π^-) reaction (less than

[*1] European Organization for Nuclear Research, Geneve, Switzerland
[*2] Brookhaven National Laboratory, NY, US
[*3] High Energy Accelerator Organization, Ibaraki, Japan
[*4] Thomas Jefferson National Accelerator Facility, VA, US

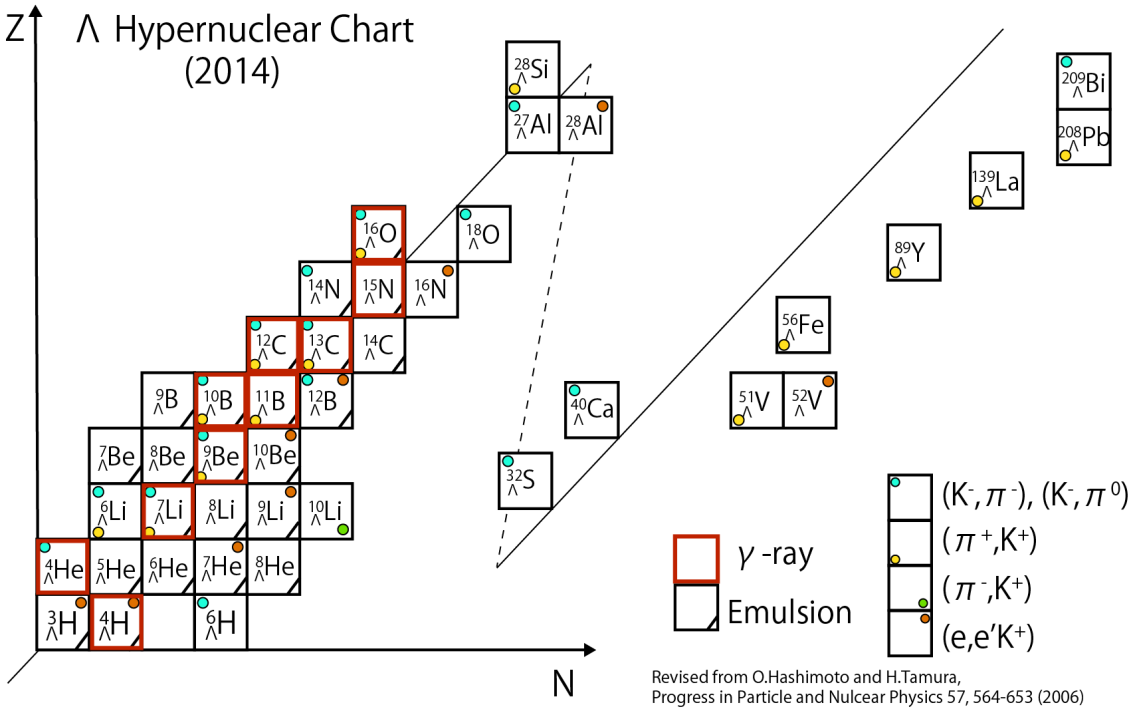

Figure 1.1: A hypernuclear chart.

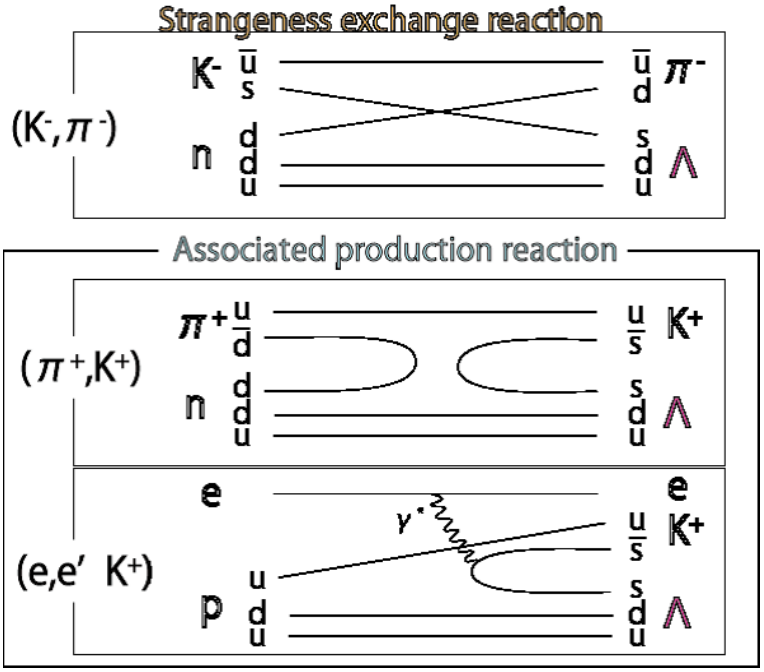

Figure 1.2: Schematic descriptions of Λ productions by the (K^-, π^-), (π^+, K^+) and (e,e′K^+) reactions.

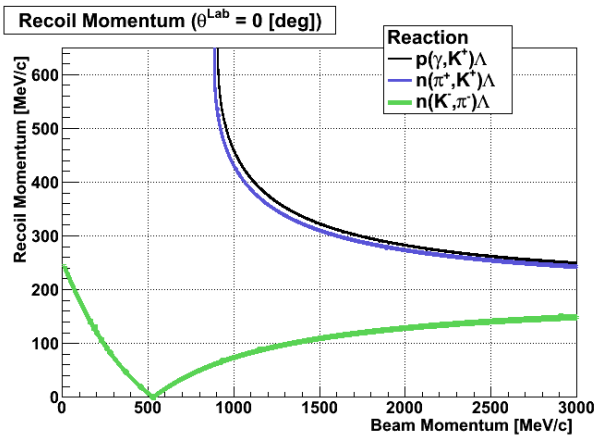

Figure 1.3: Momentum transfers to a Λ by the (K^-,π^-), (π^+,K^+) and (e,e$'K^+$) reactions as a function of beam momentum with scatting angle of 0°.

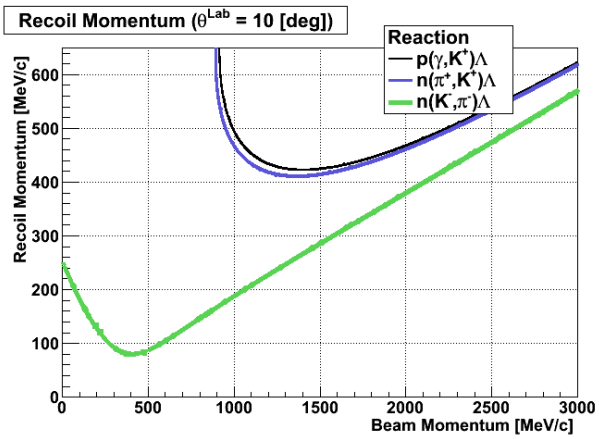

Figure 1.4: Momentum transfers to a Λ by the (K^-,π^-), (π^+,K^+) and (e,e$'K^+$) reactions as a function of beam momentum with scatting angle of 10°.

100 MeV/c at beam momentum of 1000 MeV/c and scattering angle of 0°). In addition, there is a "magic momentum" where the recoil momentum is zero. Thus, It preferentially populates substitutional states in which a nucleon is converted into a Λ in the same orbit without orbital angular transfer ($\Delta L = 0$). On the contrary, momentum transfers are larger (more than 400 MeV/c at beam momentum of 1000 MeV/c and scattering angle of 0°) in the cases of the (π^+,K^+) and (e,e$'K^+$) reactions. Therefore, high-spin hypernuclear states with a nucleon-hole having large angular momentum and a Λ having small angular momentum can be excited.

A neutron is converted into a Λ in the (K^-,π^-), (π^+,K^+) reactions. On the other hand, a proton converted into a Λ in the (e,e$'K^+$) reaction. Thus, mirror hypernuclei can be investigated. When the target is ^{12}C, for instance, $^{12}_{\Lambda}$B and $^{12}_{\Lambda}$C are generated in the (e,e$'K^+$) reaction and (K^-,π^-), (π^+,K^+) reactions, respectively. One of the largest advantages of the (e,e$'K^+$) experiment is an absolute energy scale calibration with Λ and Σ^0 by using a proton target (H nucleus). They are used for the energy scale calibration since their masses are well known [68]. In the (π^+,K^+) experiments, on the other hand, the binding energies were measured by using a reported binding energy of $^{12}_{\Lambda}$C in emulsion experiments as a reference.

In the (e,e$'K^+$) reaction, spin-flip hypernuclear states as well as spin-nonflip states sizably can be populated , which is a interesting characteristic, since the photon has spin 1 [8][9]. In contrast, the (K^-,π^-) and (π^+,K^+) reactions dominantly populate spin-nonflip states of hypernuclei since the spin-flip amplitudes in those reactions are small unless appropriate kinematic conditions are selected.

It is noted that hypernuclear formation cross sections is smaller in the (e,e$'K^+$) reaction than those of (K^-,π^-) and (π^+,K^+) by the order of two to four. This is the one of the reasons that (e,e$'K^+$) experiment was not able to be performed until 2000. Experimental difficulties of the (e,e$'K^+$) experiment including the small formation cross section are described in Sec. 2.2.

The main characteristics for the (K^-,π^-), (π^+,K^+) and (e,e$'K^+$) reactions are summarized in Table. 1.1.

1.2.2 Historical background

Λ hypernuclei with A$\leq$16 were measured by the emulsion technique in 1960's. Λ binding energies for the ground states were determined from their weak decay processes after Λ hypernuclear generation by the (K^-,π^-) reaction. The ground state measurements gave an important fact

Table 1.1: Main characteristics for the (K^-,π^-), (π^+,K^+) and (e,e′K^+) reactions.

Reaction	Conversion	Typical cross section [μb/sr]	Typical beam momentum [GeV/c]	Λ recoil momentum [MeV/c]	Λ spin (at forward angle)
In-flight (K^-,π^-)	$n \to \Lambda$	10^3	0.8	< 100	nonflip
Stopped (K^-,π^-)	$n \to \Lambda$	10^2	0.0	250	nonflip
(π^+,K^+)	$n \to \Lambda$	10^0	1.0	> 300	nonflip
(e,e′K^+)	$p \to \Lambda$	10^{-1}	1.5 (virtual photon)	> 300	flip/nonflip

that ΛN potential depth is 2/3 of NN one. In the emulsion experiments, however, excited states cannot be investigated except for a few cases.

In the early 1970's, counter experiment by the (K^-,π^-) reaction had been started at CERN and later at BNL. Spectroscopic studies of Λ hypernuclei including excited states became possible. In-flight (K^-,π^-) reaction experiments with almost recoilless conditions were performed and various Λ hypernuclei were measured [11][12][13][14][15][16] after the first counter experiment by the stopped (K^-,π^-) reaction experiment [17]. Particularly, the structures of p-shell Λ hypernuclei were studied and it was found that Λ's spin-orbit splittings are quite small compared with that of nucleon [16]. The (K^-,π^-) is the powerful tool to investigate especially p-shell Λ hypernuclei. However, it often suffered from the low statistic and limited energy resolution due to K^- beam intensity and quality.

Spectroscopic studies with the (π^+,K^+) reaction had been started in the middle of 1980's at BNL [18][19]. The (π^+,K^+) experiment was dramatically extended at KEK with Superconducting Kaon Spectrometer (SKS). High quality Λ hypernuclear spectra for many species of Λ hypernuclei were measured [20][21][22][23][24]. At the late stage, new experimental techniques have been significantly developed. One is γ-ray spectroscopy of Λ hypernuclei. It can measure the state spacing with an ultra-high resolution of a few keV (FWHM) by using a germanium detector [25], and it has proven the new quantitative information of YN interaction. The other is spectroscopy with the (e,e′K^+) reaction which will be described in the next section.

1.3 Spectroscopic experiments by the (e,e′K^+) reaction

Since 2000, Λ hypernuclear spectroscopic experiment with the (e,e′K^+) reaction have been performed at the experimental hall C and hall A in JLab. The (e,e′K^+) experiments can achieve a sub-MeV (FWHM) energy resolution , in contrast with a few MeV (FWHM) energy resolution in the (π^+,K^+) and (K^-,π^-) reactions, thanks to 1) a high quality primary electron beam and 2) a thinner target ($\sim$ 0.1 g/cm^2 in contrast to a few g/cm^2 in (K^-,π^-) and (π^+,K^+) experiments). The high intensity primary electron beam allows us to use such thinner target, and thus, the energy straggling of particles in the target are minimized. With (e,e′K^+) experiments, therefore, more detailed spectroscopic studies can be performed. So far, three (e,e′K^+) experiments in JLab hall C and one (e,e′K^+) experiment in JLab hall A have been performed, and described in this section.

1.3.1 JLab E89-009 experiment (hall C)

The first experiment with the (e,e′K^+) reaction was performed at JLab hall C in 2000 (JLab E89-009). Fig. 1.3.1 shows the experimental setup of the JLab E89-009 [28][29]. An electron of 1.8 GeV was incident on targets (20 mg/cm^2) located at the entrance of a splitter magnet (dipole magnet). A scattered electron of 0.3 GeV/c was measured by the split pole spectrometer (ENGE [30]), and a K^+ of 1.5 GeV/c was measured with the Short Orbit Spectrometer (SOS).

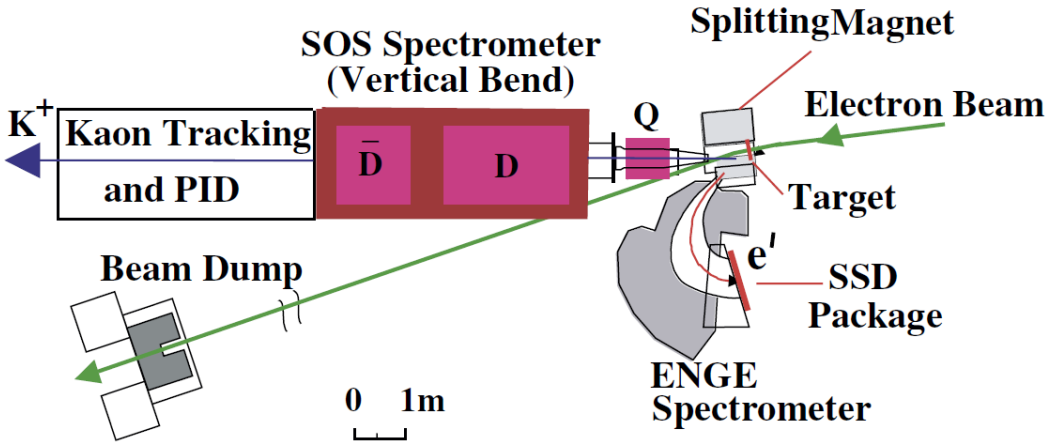

Figure 1.5: The experimental setup of JLab E89-009 [28]. An electron with 1.8 GeV was incident on targets located at the entrance of a splitter magnet. A scattered electron with 0.3 GeV/c was measured by the ENGE spectrometer [30], and a K^+ with 1.5 GeV/c was measured by the SOS spectrometer.

A spectrum of the ^{12}C(e,e′K^+)$^{12}_{\Lambda}$B is shown in the Figure 1.3.1 with the energy resolution of 0.9 MeV (FWHM) which was the highest energy resolution at that time in reaction spectroscopy of Λ hypernuclei. The JLab E89-009 experiment successfully has proved a feasibility of spectroscopic study of hypernuclei with the (e,e′K^+) reaction.

In the experiment, two issues to be overcome for the next generation experiment were arose as follows:

- Beam current needed to be suppressed due to huge amount of background electrons in the electron arm spectrometer.
- Missing mass resolution was limited due to the kaon spectrometer (SOS).

1.3.2 JLab E01-011 experiment (hall C)

In the JLab E89-009 experiment, there were huge amount of background particles originated from electromagnetic processes in the electron spectrometer. To suppress the background particles, and maximize a signal to noise ratio and an yield of Λ hypernucleus, tilt method was introduced for the electron spectrometer. Thanks to the tilt method, a rate in the electron spectrometer was suppressed down to 1/200 though a luminosity was increased by 200 times compared to the E01-011 experiment. A kaon spectrometer named High resolution Kaon Spectrometer (HKS, $\Delta p/p \sim 2.0 \times 10^{-4}$) was newly constructed and introduced to achieve the better energy resolution and to increase the yields. Fig. 1.3.2 shows the experimental setup of the E01-011 experiment. An electron beam of 1.8 GeV was sent to the target located at the entrance of the splitter magnet. A scattered electron of $\sim$ 0.3 GeV and a kaon of $\sim$ 1.2 GeV were

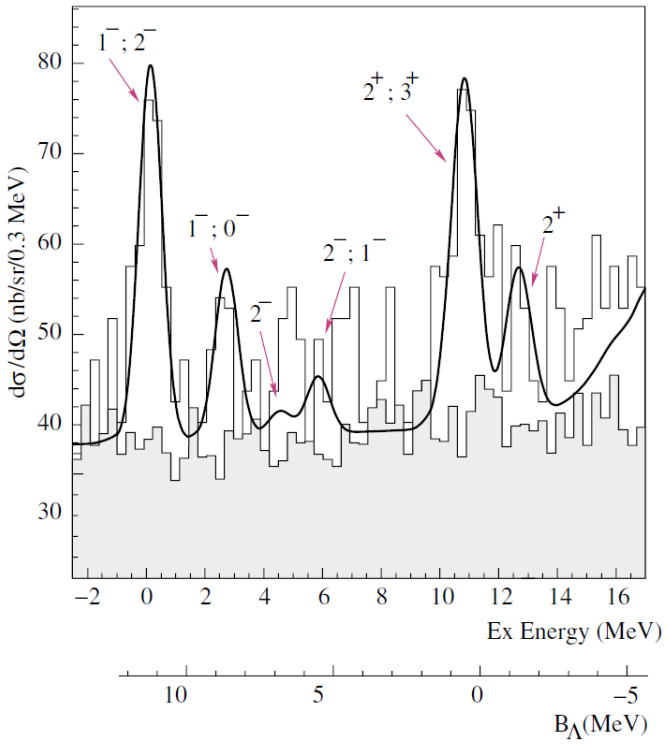

Figure 1.6: A spectrum of the ^{12}C(e,e′K^+)$^{12}_{\Lambda}$B with the energy resolution of 0.9 MeV (FWHM).

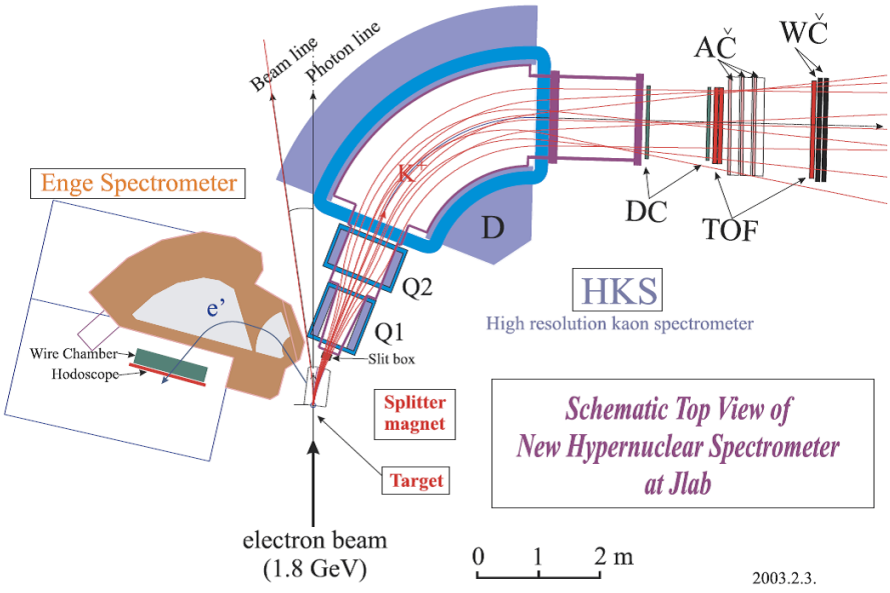

Figure 1.7: Experimental setup of JLab E01-011 in 2005 [32].

measured in ENGE [30] and HKS, respectively. In the experiment, spectroscopic measurements of Λ, Σ^0, ${}^{7}_{\Lambda}$He (Fig. 1.8), ${}^{12}_{\Lambda}$B (Fig. 1.9) and ${}^{28}_{\Lambda}$Al (Fig. 1.3.2) have been done.

Fig. 1.9 shows a missing mass spectrum of ^{12}C(e,e$'K^+$)${}^{12}_{\Lambda}$B with the energy resolution of 0.61 MeV (FWHM) for the ground state. The energy resolution was improved thanks to introduction of the new spectrometer, HKS compared to JLab E89-009 experiment. An important remark is that peak structures of core excited states (peak number 2 and 3) seen between peaks of s_Λ and p_Λ (peak number 1 and 4) were observed at the first time. The energy resolution improvement made discussions of Λ hypernuclear core configurations possible.

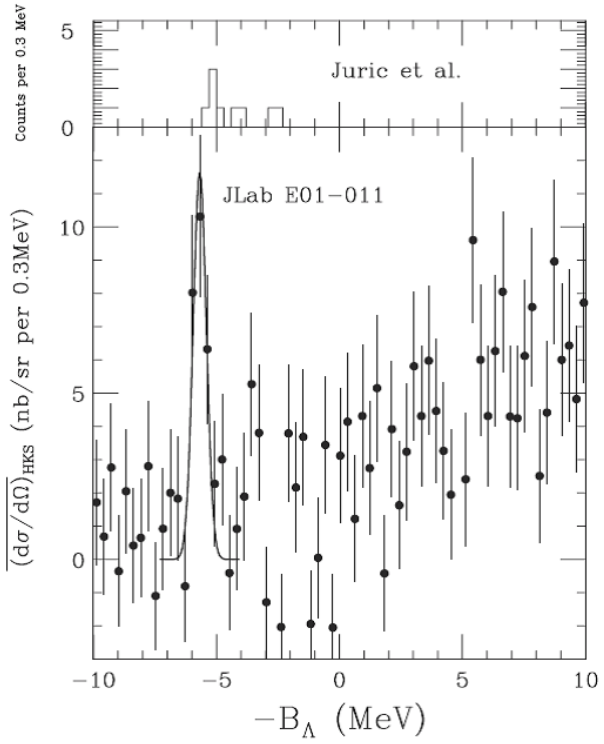

Figure 1.8: ${}^{7}_{\Lambda}$He in the E01-011 experiment (bottom) comparing with events of the emulsion measurement (top) [31].

Charge symmetry breaking (CSB) effect in the ΛN interaction is one of interesting topics. Recently, precise four-body cluster model calculations were performed by E. Hiyama *et al.* [33] to test the CSB effect in the $A = 7$, $T = 1$ iso-triplet hypernuclei, ${}^{7}_{\Lambda}$He($\alpha nn\Lambda$), ${}^{7}_{\Lambda}$Li*($\alpha pn\Lambda$) and ${}^{7}_{\Lambda}$Be($\alpha pp\Lambda$). A ground state binding energy of ${}^{7}_{\Lambda}$He could not be determined in the past emulsion experiment although those of ${}^{7}_{\Lambda}$Li* and ${}^{7}_{\Lambda}$Be were measured [34][36]. Therefore, binding energy measurement of ${}^{7}_{\Lambda}$He had been awaited to test the phenomenologically introduced ΛN CSB effect for those iso-triplet hypernuclei. Fig. 1.8 shows a missing mass spectrum of the ${}^{7}_{\Lambda}$He in the E01-011 experiment (bottom) comparing with events of the emulsion measurement (top) [31]. It is the first clear observation of the ${}^{7}_{\Lambda}$He ground state which determined the ground state binding energy to be $-B_\Lambda = 5.68 \pm 0.03$(statistic) $\pm$ 0.25(systematic) with the energy resolution of 0.63 MeV (FWHM).

The first *sd*-shell hypernucleus, ${}^{28}_{\Lambda}$Al was successfully measured with the (e,e$'K^+$) reaction, and it had opened a door to measurements of heavier hypernuclei with the (e,e$'K^+$) reaction. Two prominent peaks of s_Λ (peak number 1 in Fig.1.3.2) and p_Λ (peak number 2 in Fig.1.3.2) are discussed compared with the mirror hypernucleus, ${}^{28}_{\Lambda}$Si [10][22] and theoretical calculations [37] in Ref. [32]. The energy spacing between s_Λ and p_Λ of ${}^{28}_{\Lambda}$Al is larger than those of ${}^{28}_{\Lambda}$Si and also the predictions. It indicates that further systematic studies of Λ hypernuclei are necessary

experimentally and theoretically to improve the ΛN interaction.

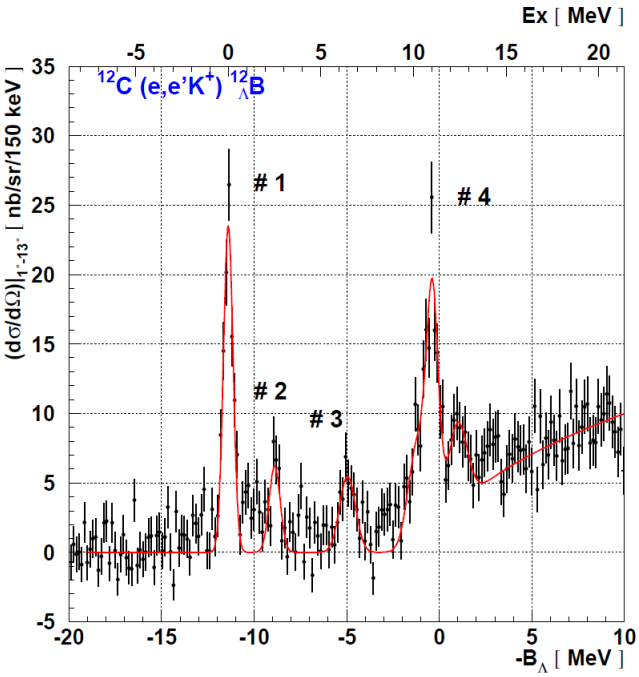

Figure 1.9: A binding energy spectrum of the ^{12}C(e,e′K^+)$^{12}_{\Lambda}$B with the energy resolution of 0.61 MeV (FWHM, for the first peak) [32].

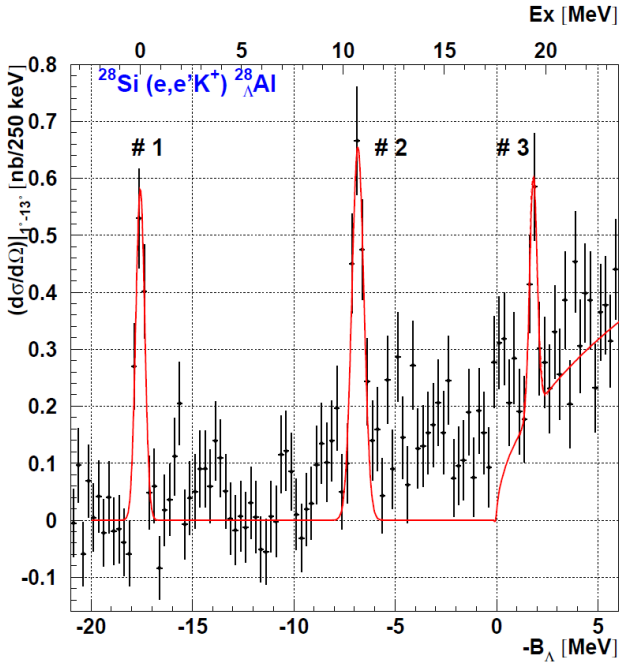

Figure 1.10: A binding energy spectrum of the ^{28}Si(e,e′K^+)$^{28}_{\Lambda}$Al with the energy resolution of 0.52 MeV (FWHM, for the first peak) [32].

1.3.3 JLab E94-107 experiment (hall A)

E94-107 experiment was performed at JLab hall A to measure $^{9}_{\Lambda}$Li [38], $^{12}_{\Lambda}$B [38][39] and $^{16}_{\Lambda}$N [40]. Two of High Resolution Spectrometers (HRS, $\Delta p/p$ ~1×10^{-4}) existed in JLab hall A were used for the momentum analyses of a scattered electron and a K^+. To maximize yields of Λ hypernuclei, both of a scattered electron and a K^+ need to be detected with their small scattering angles as shown in Sec. 2.3.4. In order to allow the measurement with smaller scattering angles than the HRS minimum angle (12.5°), a superconducting septum magnet was used for each HRS. An electron beam of E_e = 3.77 GeV was incident on the target, and a scattered electron of $p_{e'}$ = 1.56 GeV/c and a K^+ of p_K = 1.96 GeV/c was measured in each HRS.

An excitation spectrum of the $^{12}_{\Lambda}$B is shown in Fig. 1.11 [38]. The energy resolution of the first peak is 1.15±0.18 MeV (FWHM, for the first peak). Fig. 1.12 shows the $^{16}_{\Lambda}$N binding energy spectrum with the energy resolution of 1.71±0.70 MeV (FWHM, for the first peak) [40]. The Λ binding energy for the first peak was obtained to be $B_\Lambda = 13.76 \pm 0.16$ MeV.

Also in the experimental hall A, Λ hypernuclear measurement using (e,e′K^+) reaction had been established.

1.4 Purpose of the present research

1.4.1 Elementary processes of p(e,e′K^+)Λ,Σ^0

Λ and Σ^0 from a hydrogen nucleus are used for an absolute energy scale calibration. This calibration is the one of most important advantages of the (e,e′K^+) reaction experiment.

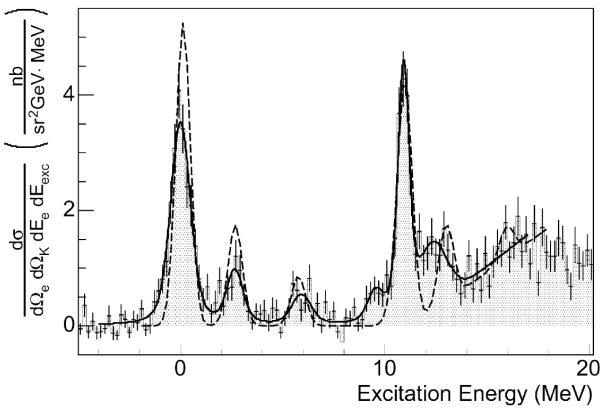

Figure 1.11: An excitation energy spectrum of the ^{12}C(e,e′K^+)$^{12}_{\Lambda}$B with the energy resolution of 1.15 MeV (FWHM, for the first peak) [38].

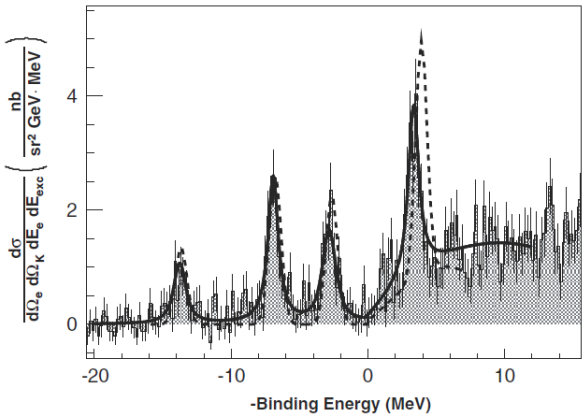

Figure 1.12: A binding energy spectrum of the ^{16}O(e,e′K^+)$^{16}_{\Lambda}$N with the energy resolution of 1.71 MeV (FWHM, for the first peak) [40].

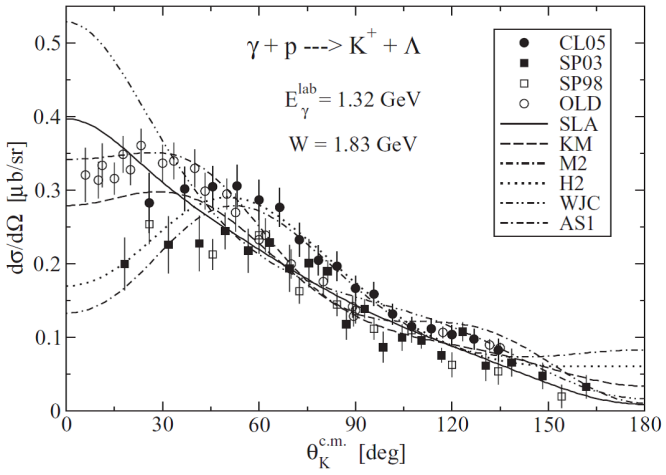

Figure 1.13: Differential cross sections as a function of K^+ scattering angle in the center of mass frame for data of CLAS [41], SAPHIR [42][43] and an older one [44][45] and some of theoretical calculations [46]. This figure was taken from [46].

The (e,e′K^+) reaction is described by a virtual photon-exchange, and the virtual photon can be almost treated as a real photon in our experimental setup as will be described in Sec.2.1. The information of the elementary amplitude is vital for the cross section calculation of the Λ hypernuclei. One of the examples showing situations of the study for the $p(\gamma,K^+)\Lambda$ reaction is shown in Fig. 1.13. It shows the differential cross sections as a function of K^+ scattering angle in the center of mass frame ($\theta_{\gamma K}^{\rm CM}$) for data of CLAS [41], SAPHIR [42][43] and an older one [44][45] and some of theoretical calculations [46]. The experimental data show lack of consistency at the small K^+ scattering angle ($\theta_{\gamma K}^{\rm CM}$ <40°) where the Λ hypernuclear spectroscopy is performed. Moreover, theoretical calculations behave differently particularly at the small K^+ scattering angle as well as the experimental results. To give constraints for the theoretical descriptions of the elementary process, data with the small K^+ scattering angle have been awaited. In the present work, the differential cross sections of $p(\gamma^*,K^+)\Lambda$ with the scattering angle of $\theta_{\gamma K}^{\rm CM} \leq 20°$ aimed to be obtained.

1.4.2 ^{7}Li(e,e′K^+)$^{7}_{\Lambda}$He

$^{7}_{\Lambda}$He is a good sample for a test of the charge symmetry breaking (CSB) effect in ΛN interaction in four-body cluster model calculations [33]. Originally, the discussion of the ΛN CSB effect had been started from $A = 4$, T =1/2 systems ($^{4}_{\Lambda}$H and $^{4}_{\Lambda}$He). Their binding energy differences for the ground state (0^+) and excited state (1^+) are 0.35 ± 0.06 MeV and 0.24 ± 0.06 MeV, respectively. The differences cannot be explained by only Coulomb effect [98][100][99]. Thus, the binding energy differences after the Coulomb effect are subtracted are attributed to the CSB effect in ΛN interaction [100].

The origin of the CSB effect in ΛN interaction are tried to be explained by taking into account Λ-Σ^0 mixing and $\Sigma^{\pm,0}$ mass differences [49]. However, it was not succeeded to reproduce the experimental results of $^{4}_{\Lambda}$He and $^{4}_{\Lambda}$H simultaneously up to now [50][51]. Therefore, the origin of the CSB effect in $^{4}_{\Lambda}$H and $^{4}_{\Lambda}$He is an open question.

A phenomenologically introduced CSB interaction of which potential was determined so as to reproduce $^{4}_{\Lambda}$H and $^{4}_{\Lambda}$He were applied to calculate $A = 7$, $T = 1/2$ hypernuclei, $^{7}_{\Lambda}$He, $^{7}_{\Lambda}$Li* [34] [25] and $^{7}_{\Lambda}$Be [34] as already explained in Sec. 1.3.2. $^{7}_{\Lambda}$He was spectroscopically measured in JLab E01-011. However, errors including the systematic errors was rather large (30 keV of statistical error, 250 keV of systematic error). Moreover, excited states ($3/2^+$,$5/2^+$) which are expected to be seen ∼ 1.8 MeV above the ground state in some theoretical predictions could not be observed due to low statistic. The excited states are bound states though corresponding states in a core nucleus, ^{6}He is an unbound state. It is interesting to see the phenomenon that the the unbound state becomes the bound states due to the presence of Λ in the nucleus. In the present work, both the ground state and the excited states aimed to be measured with smaller errors than that of JLab E01-011.

1.4.3 ^{10}B(e,e′K^+)$^{10}_{\Lambda}$Be

Only three events of $^{10}_{\Lambda}$Be were measured in emulsion experiments [34][35]. In the present work, the first spectroscopic measurement of $^{10}_{\Lambda}$Be is aimed.

The phenomenological ΛN CSB interaction in interaction can be tested in $A = 10$, $T = 1/2$ iso-doublet hypernuclei, $^{10}_{\Lambda}$Be and $^{10}_{\Lambda}$B. In the present work, the ground state (1^-, 2^-) binding energy is aimed to be measured with small systematic errors (∼100 keV).

In addition, the glue-like role of Λ is aimed to be confirmed by observing a phenomenon that a unbound state in the core nucleus (^{9}Be) becomes bound states in $^{10}_{\Lambda}$ due to the presence of Λ in the nucleus.

1.4.4 ^{12}C(e,e′K^+)$^{12}_{\Lambda}$B

Spectroscopic studies of $^{12}_{\Lambda}$B were performed in the past experiments. Thus, measurement of $^{12}_{\Lambda}$B can be used as the reference not only for the binding energy but also the cross section for each state. Moreover, it is useful to see progresses of the analyses particularly for the inverse transfer matrix optimization.

1.4.5 ^{52}Cr(e,e′K^+)$^{52}_{\Lambda}$V

This experiment is the first challenge to investigate a medium-heavy Λ hypernucleus with the (e,e′K^+) reaction. Experimentally, the measurement with heavier target is harder since the rates of background particles which originate from electromagnetic processes are roughly in proportion to Z^2 (Z: target proton number).

Λ hypernuclei with heavier mass numbers up to $A = 208$ have been measured by the (π^+,K^+) and (K^-,π^-) reaction spectroscopy with the energy resolution of a few MeV in FWHM. The major structures of those Λ hypernuclei were well studied [10]. As a next step, finer structures such as the spin-orbit (ls) splitting and core-configuration mixing states are tried to be measured with better energy resolution of sub-MeV in FWHM. In Ref. [124], the ls splitting and core-configuration mixing states in medium heavy mass region are discussed, and they are expected to be observed with the energy resolution of sub-MeV. This new information of finer structures of Λ hypernuclei in medium mass region where the γ-ray spectroscopy is hard to be performed so far leads us for further understanding of ΛN interaction.

Using systematic studies of Λ's binding energies in various hypernuclei, single particle potential of Λ has been investigated. It was found that a Wood-Saxon well with a depth (∼ 30 MeV) and a radius parameter (r_0) which decreases with A can fit the experimental single particle binding energies [52]. Fig. 1.14 shows the Λ's binding energies as a function of $A^{-2/3}$

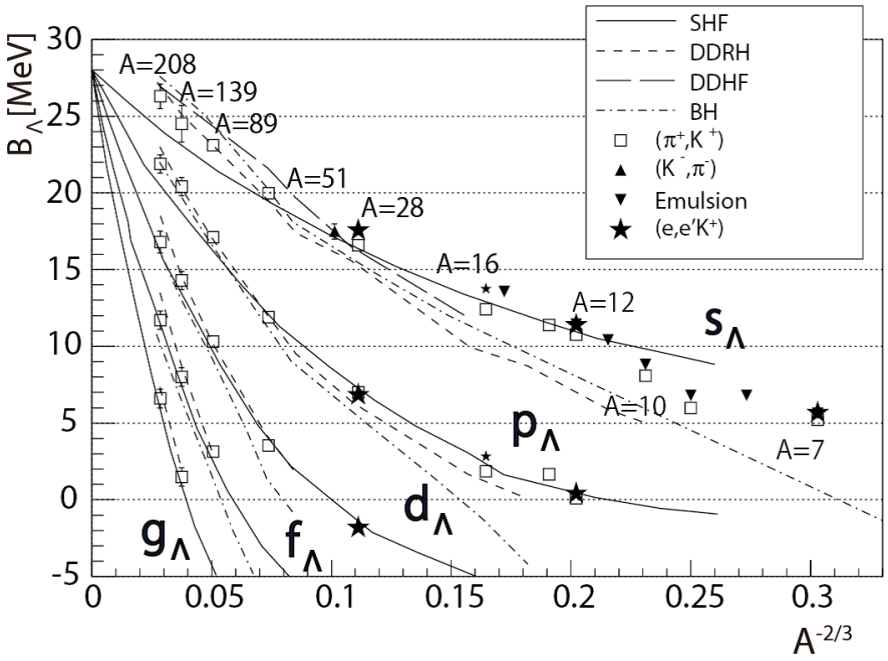

Figure 1.14: Λ's binding energies as a function of $A^{-2/3}$ for experimental data and theoretical predictions.

for experimental data and theoretical predictions (SHF [54], DDRH [55], DDHF [56], BH [57]). The experimental data were taken from Ref. [10][22][24] for the (π^+,K^+) experiments, Ref. [53]

for the (K^-,π^-) experiments, Ref. [34] for emulsion experiments and Ref. [28][29][32][31][38][40] for the (e,e$'K^+$) experiments. Many theoretical works have been performed to describe these experimental data of single particle energies. For example, D. J. Millener *et al.* fit the data up to $A = 89$ using density-dependent and non-local ΛN potential motivated by the spherical Skyrme Hartree-Fock calculations (indicated by SHF). Solid line in Fig. 1.14 is the solutions obtained for a Woods-Saxon well with a depth of 28 MeV and a radius parameter $r_0 = 1.128+0.439A^{-2/3}$. The density dependent relativistic hadron (indicated by DDRH) field theory was extended to hypernuclear system, and their calculations are shown as dashed line. So far, these theoretical calculations were obtained by fitting to data of the (K^-,π^-), (π^+,K^+) and emulsion experiments. More precise data measured by (e,e$'K^+$) experiments with the higher energy resolution could be useful for further understanding of the single particle potential of Λ.

In the present work, a feasibility of the measurement of a Λ hypernucleus with medium-heavy mass number ($A = 52$) is aimed to be confirmed. Moreover, new data points of the binding energies of medium-heavy Λ hypernucleus, ${}^{52}_{\Lambda}$V in addition to other lighter Λ hypernuclei measured in the present experiment are aimed to be provided for the discussion of the Λ's single particle potential.

Chapter 2

Experimental setup

In 2009 (August - November), E05-115 experiment was performed with the (e,e′K^+) reaction at JLab experimental hall C. The experiment was designed to measure Λ hypernuclei up to medium heavy mass region. For this purpose an electron spectrometer and a splitter magnet which dedicate for the measurement of Λ hypernuclei were newly constructed and used for the experiment. A kaon spectrometer, HKS which was constructed and used in the previous (e,e′K^+) experiment was also used in the experiment. Thus, spectrometer systems including the splitter magnet dedicate for the Λ hypernuclear measurement. In this section, kinematics of the (e,e′K^+) reaction and whole experimental setup of JLab E05-115 are described.

2.1 Kinematics of the (e,e′K^+) reaction

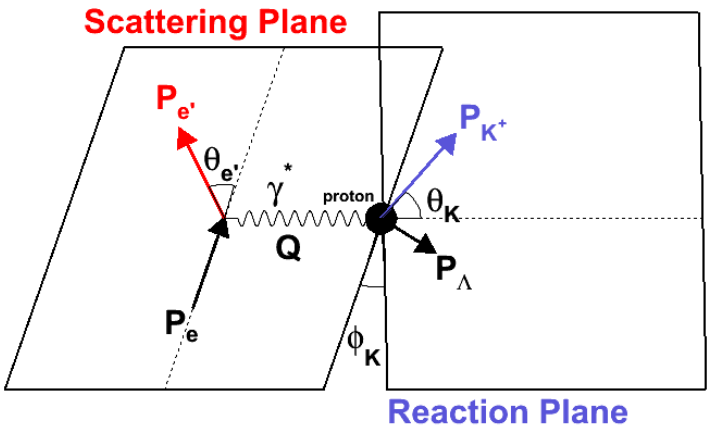

Figure 2.1: A schematic drawing of the (e,e′K^+) reaction.

The kinematics of the (e,e′K^+) reaction,

$$e(p_e) + p(p_p) \rightarrow e(p_{e'}) + \Lambda(p_\Lambda) + K^+(p_K) \tag{2.1}$$

is shown in Fig. 2.1. The variables in the parentheses in Eq. (2.1) denote four-momentum of each particle. The energy and momentum of the virtual photon are defined to be:

$$\omega = E_e - E_{e'} , \tag{2.2}$$

$$\vec{q} = \vec{p}_e - \vec{p}_{e'} . \tag{2.3}$$

The differential cross sections for the elementary electroproduction process is described by the following form [58][59]:

$$\frac{d^3\sigma}{dE_{e'}d\Omega_{e'}d\Omega_K} = \Gamma\Big(\frac{d\sigma_U}{d\Omega_K} + \epsilon_L\frac{d\sigma_L}{d\Omega_K} + \epsilon\frac{d\sigma_P}{d\Omega_K}\cos 2\Phi_K + \sqrt{2\epsilon_L(1+\epsilon)}\frac{d\sigma_I}{d\Omega_K}\cos\Phi_K\Big) \tag{2.4}$$

where σ_U, σ_L, σ_P and σ_I are the unpolarized transverse, longitudinal, polarized transverse and interference cross sections, respectively. Γ is the virtual photon flux represented by:

$$\Gamma = \frac{\alpha}{2\pi^2 Q^2}\frac{E_\gamma}{1-\epsilon}\frac{E_{e'}}{E_e}\,. \tag{2.5}$$

where $\alpha = e^2/4\pi = 1/137$ and $Q^2 = -q^2 > 0$. The virtual photon transverse polarization (ϵ), longitudinal polarization (ϵ_L) and the effective photon energy (E_γ) in Eq. 2.4 and Eq. 2.5 are defined as:

$$\epsilon = \Big(1 + \frac{2|\vec{q}|^2}{Q^2}\tan^2\frac{\theta_e}{2}\Big)^{-1}, \tag{2.6}$$

$$\epsilon_L = \frac{Q^2}{\omega^2}\epsilon, \tag{2.7}$$

$$E_\gamma = \omega + \frac{q^2}{2m_p}, \tag{2.8}$$

where θ_e is the electron scattering angle in the laboratory frame. For real photon case, only the unpolarized transverse term is nonvanishing since $Q^2 \to 0$. In our experimental setup, the virtual photon can be treated as almost real photon as Q^2 is quite small (Q^2 ~0.01 [GeV/c]^2).

2.2 Continuous Electron Beam Accelerator Facility in JLab

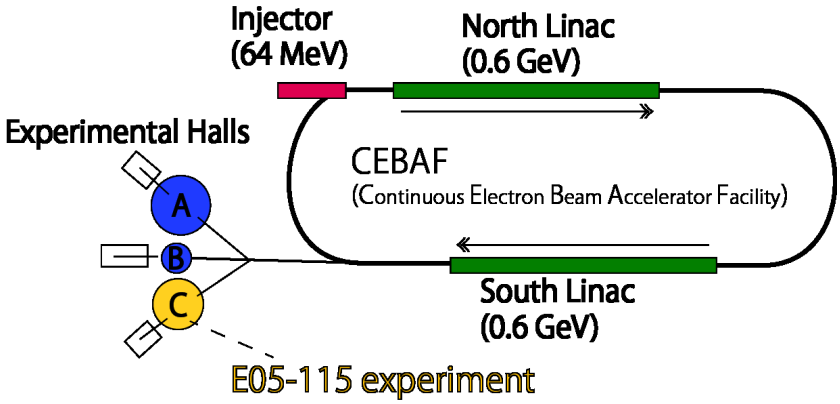

Figure 2.2: A schematic drawing of the CEBAF. An injected electron with 64 MeV is accelerated by the north and south linac which give an electron 0.6 GeV for each linac. An electron gains 6.0 GeV at maximum after 5 cycles of acceleration. The E05-115 experiment was performed at the experimental hall C.

Continuous Electron Beam Accelerator Facility (CEBAF) in JLab provides a high quality and high intensity primary electron beam which is an important tool to perform nuclear physics experiments which need high precision by using reactions with small cross sections.

Fig. 2.2 shows a schematic drawing of the CEBAF. Electrons are generated at an injector with 1497 MHz short bursts. Then, the electrons are divided into three bursts ($\frac{1497\ \mathrm{MHz}}{3} = 499$ MHz) by an RF chopper. The electrons are accelerated by two linacs which give the electrons 0.6 GeV for each linac. At maximum, 6 GeV electrons are provided to three experimental halls, Hall-A, B and C [60]. The main parameters of the CEBAF are listed in Table 2.1.

Table 2.1: The main parameters of the CEBAF.

Maximum beam energy	6 GeV
Maximum beam intensity	200 μA/Hall
Beam emittance	2 μm·mrad
Beam energy spread	$\leq 1 \times 10^{-4}$ (FWHM)
Beam bunch interval	2 ns (499 MHz)

The CEBAF is a unique facility to perform Λ hypernuclear spectroscopic experiments with the (e,e$'K^+$) reaction as it satisfies the following experimental requirements:

- **The maximum beam energy is above the energy threshold of Λ formation (the total energy of W $\sim$1.6 GeV).**

- **The beam energy spread is less than 1.0×10^{-4} [61][62] which corresponds to $\sim$200 keV contributions to a missing mass when 2.344 GeV electron beam is used.**
  This beam energy spread is comparable level to the momentum resolutions of the our spectrometers.

- **The beam spot size is small at target position (σ $\sim$100 μm).**
  Transfer matrices are used to derive K^+ and e' momentum vectors at a target from positions and angles at focal planes (reference planes) for each spectrometer. The beam spot size affects momentum resolutions of the spectrometers since the matrices are generated with an assumption that a strangeness production occurs at one-point. The beam spot size of σ $\sim$100μm is almost no effect on the momentum resolutions according to a Monte Carlo simulation as shown in Sec. 4.6.2.

- **The duty factor is high ($\sim$ 100%).**
  The (e,e$'K^+$) experiment is a coincidence experiment between a K^+ and a scattered electron. A signal to noise ratio (S/N) in coincidence experiments gets worse as a beam intensity is higher. Hence, in terms of S/N, it is important to keep a beam current low for the (e,e$'K^+$) experiment as long as an enough statistic of a hypernucleus is accumulated in a given beam time.

- **High intensity electron beam can be provided (a few μA to 50 μA).**
  The Λ hypernuclear production cross sections with the (e,e$'K^+$) reaction are much smaller than those of (K^-, π^-) and (π^+, K^+) reactions by the order of 2 to 4. This can be compensated by the high intensity beam of CEBAF.

  Furthermore, thinner targets ($\sim$0.1 g/cm^2) than those of hadron beam experiments (a few g/cm^2) can be used thanks to the high intensity beam. Enough Λ hypernuclear yields are expected even when such thinner target is used. The thinner target reduces effects on the mass resolution deterioration due to the energy straggling in the target.

2.3 Experimental setup

2.3.1 Overview

The (e,e′K^+) reaction is described by the one (virtual-)photon exchange model as described in Sec.2.1. To maximize yields of Λ hypernuclei and hyperons, $K^+\Lambda$ and $K^+\Sigma^0$ photo-production cross sections were considered. Fig. 2.3 and Fig. 2.4 show experimental results of $K^+\Lambda$ and $K^+\Sigma^0$ photo-production cross sections taken from Ref. [41]. There are enhancements for both $K^+\Lambda$ and $K^+\Sigma^0$ at the total energy, W ∼1.9 GeV which corresponds to photon energy, $\omega_{\max}$ ∼1.5 GeV. In this condition, the K^+ momentum, p_K ∼1.2 GeV. Furthermore, 2.344 GeV/c electron beam which was higher energy than that of E01-011 experiment was used to improve S/N (see Sec.2.3.6). Thus, a central momentum of a scattered electron spectrometer was chosen to be $p_{e'} \sim E_{e'} = 2.344 - \omega_{\max} = 0.844$ GeV/c.

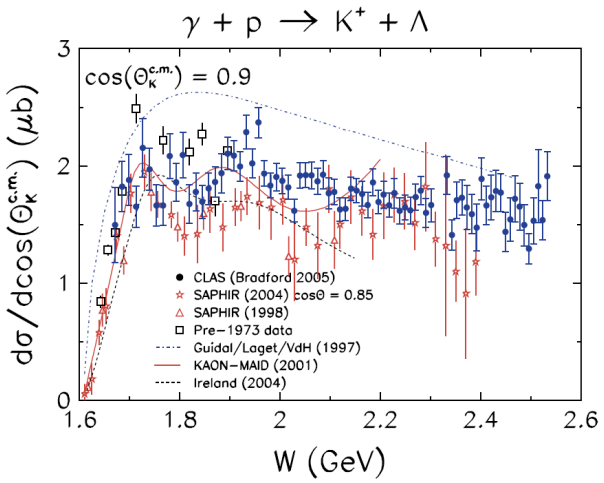

Figure 2.3: The differential cross section of $K^+\Lambda$ photo-production as a function of total energy (W) taken from Ref. [41].

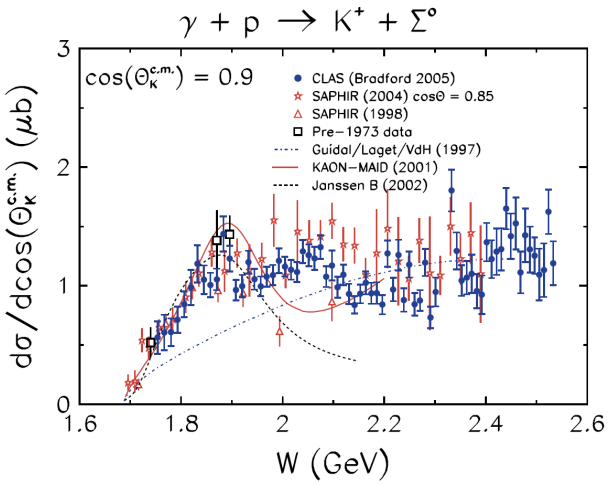

Figure 2.4: The differential cross section of $K^+\Sigma^0$ photo-production as a function of total energy (W) taken from Ref. [41].

Fig. 2.5 and Fig. 2.6 show a schematic drawing and a photograph of the experimental setup of the E05-115 experiment. It consists of a splitter magnet (SPL), a High resolution Kaon Spectrometer (HKS) and a High resolution Electron Spectrometer (HES). Each of HKS and HES consists of two quadrupole magnets and one dipole magnet (QQD configuration). An electron beam with the energy of 2.344 GeV is incident on a target located at the entrance of the splitter magnet. A K^+ and a scattered electron with the central momentum of 1.2 GeV and 0.844 GeV were separated into opposite directions with SPL, and measured in HKS and HES, respectively. HKS which was constructed and used in the E01-011 experiment for kaon measurement was also used in the E05-115 experiment. HES and SPL was newly constructed for the E05-115 experiment. The main experimental parameters are summarized in Table. 2.2.

In this section, experimental designs and specifications of the target system, SPL, HKS, HES and pre-chicane beam line which was also designed for the present experiment are described.

2.3.2 Pre-chicane beam line

Dumping directions of beams and Bremsstrahlung photons generated in a target toward their fixed dumps were determined by adopting the pre-chicane beam line in the experiment. Fig. 2.7 shows a schematic drawing of the E05-115 experimental setup including the pre-chicane beam

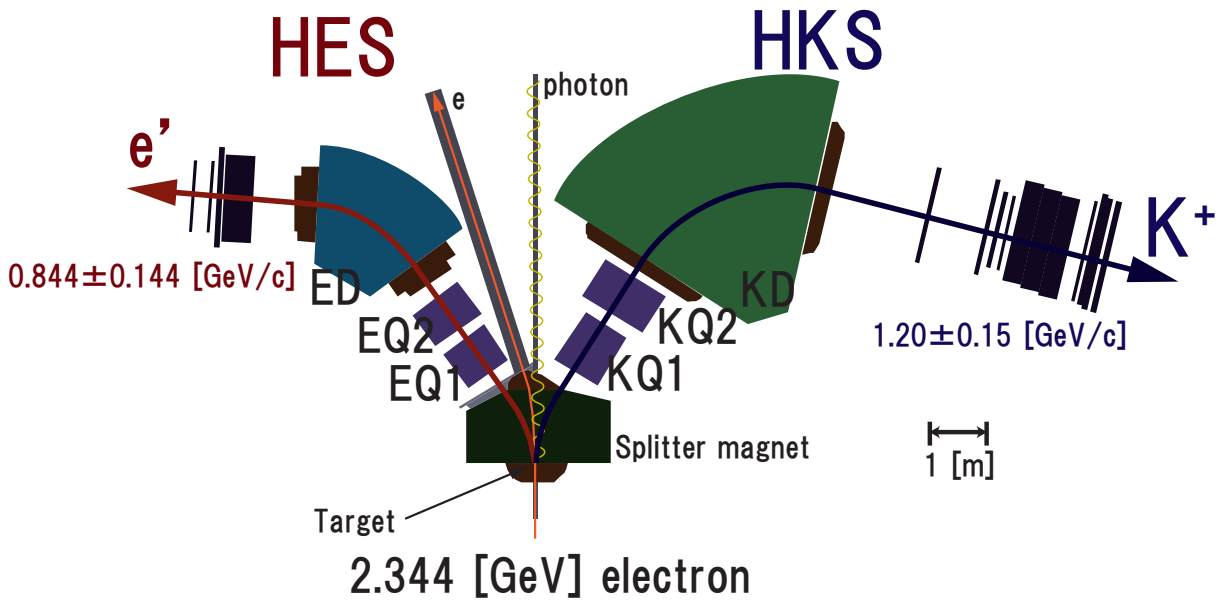

Figure 2.5: A schematic drawing of the JLab E05-115 experimental setup. It consists of SPL (splitter magnet), HKS and HES. An electron beam with the energy of 2.344 GeV was incident on the target located at the entrance of SPL. A K^+ and a scattered electron with the momenta of $\sim$1 GeV/c were measured in HKS and HES, respectively.

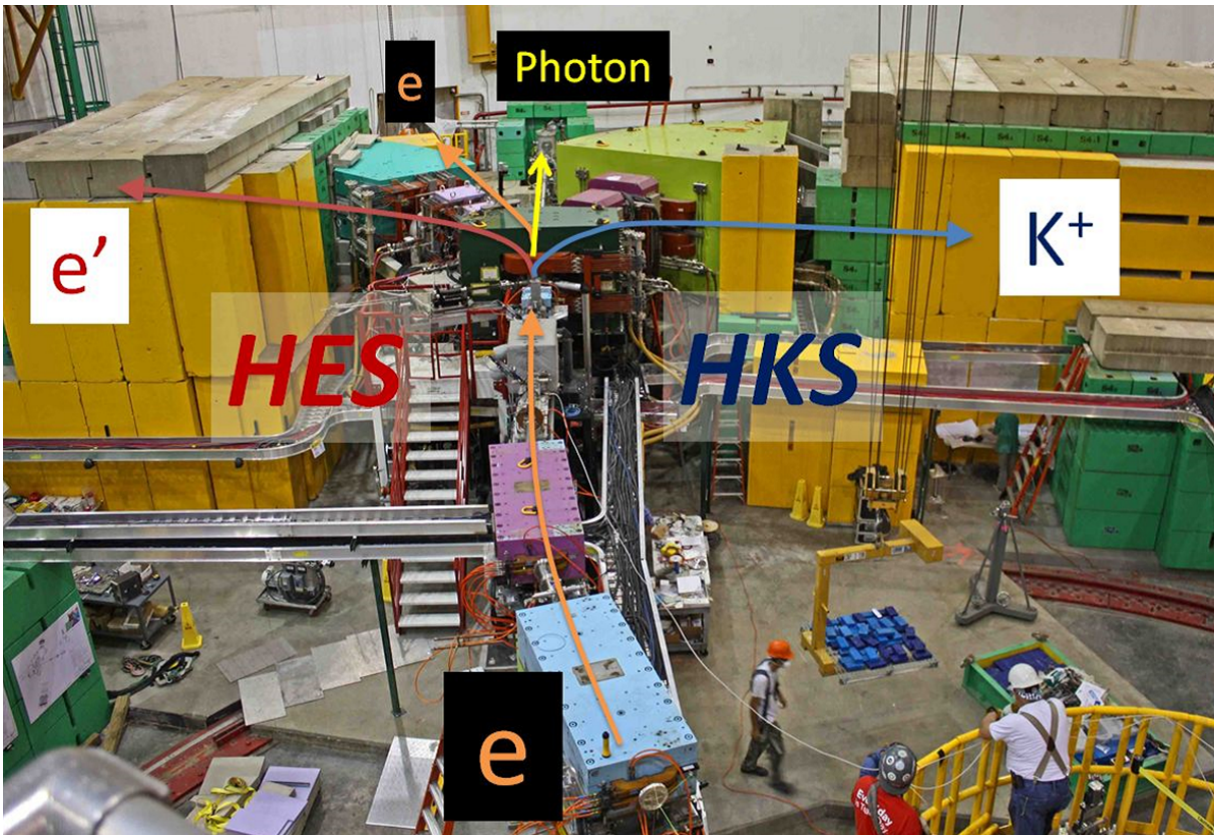

Figure 2.6: A photograph of the E05-115 experimental setup at JLab Hall C in 2009.

Table 2.2: Experimental conditions and parameters of JLab E05-115.

Beam (e)	
Energy	2.344 GeV
Energy spread	$< 1.0 \times 10^{-4}$
HKS (K^+)	
Configuration	QQD (horizontal bend)
Central momentum	1.2 GeV/c
Momentum acceptance	$\pm$12.5%
Momentum resolution ($\Delta p/p$)	2.0×10^{-4} (FWHM)
Solid angle	8.5 msr for the central momentum (Fig. 2.14)
Angular acceptance	(horizontal) -30 mrad to -230 mrad
	(vertical) -70 mrad to 70 mrad
Flight path length	10 m
HES (e')	
Configuration	QQD (horizontal bend)
Central momentum	0.844 GeV/c
Momentum acceptance	$\pm$ 17.5%
Momentum resolution ($\Delta p/p$)	2.0×10^{-4} (FWHM)
Solid angle	7.0 msr for the central momentum (Fig. 2.26)
Angular acceptance	(horizontal) -200 mrad to 200 mrad
	(vertical) 30 mrad to 90 mrad
Vertical tilt angle	6.5 deg

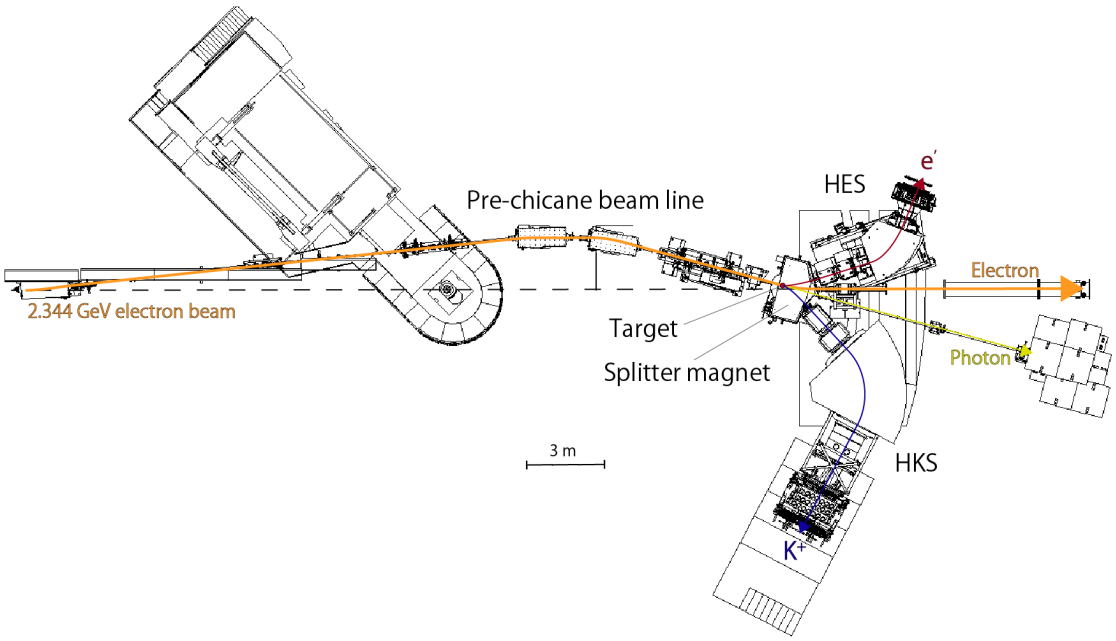

Figure 2.7: The experimental setup of E05-115 including the pre-chicane beam line. The pre-chicane beam line was designed and constructed for the E05-115 experiment instead of an original beam line of JLab Hall C.

line. In the E01-011 experiment, a "post"-chicane beam line was used. However, background particles in spectrometers could be increased since post-chicane magnets bent halo-particles generated in the target. To avoid a possibility the background particles contaminate spectrometers from the post-chicane beam line, the pre-chicane beam line was designed and constructed instead of an original beam line in the experimental hall C, taking into account the optical matching with our spectrometer systems.

2.3.3 Target

In the experiment, solid targets of ^{7}Li, ^{9}Be, ^{10}B, ^{12}C and ^{52}Cr were used for Λ hypernuclear production. In addition, polyethylene (CH_2) and water (H_2O) targets were used for an energy scale calibration by measuring Λ and Σ^0. The targets used in the experiment are listed in Table 2.3.

Table 2.3: List of targets used for the E05-115 experiment.

Target	Reaction	Thickness (x_t) [mg/cm^2]	Density [g/cm^3]	Purity [%]	Radiation length (X_0) [g/cm^2]	x_t/X_0
CH_2	p(e,e$'K^+$)Λ,Σ^0 ^{12}C(e,e$'K^+$)$^{12}_{\Lambda}$B	450.8	0.92	-	44.77	1.0×10^{-2}
H_2O	p(e,e$'K^+$)Λ,Σ^0 ^{16}O(e,e$'K^+$)$^{16}_{\Lambda}$N	500.0	1.00	-	36.08	1.4×10^{-2}
^{7}Li	^{7}Li(e,e$'K^+$)$^{7}_{\Lambda}$He	208.0	0.54	99.9	82.78	2.5×10^{-3}
^{9}Be	^{9}Be(e,e$'K^+$)$^{9}_{\Lambda}$Li	188.1	1.848	100.0	65.19	2.9×10^{-3}
^{10}B	^{10}B(e,e$'K^+$)$^{10}_{\Lambda}$Be	56.1	2.16	99.9	49.19	1.1×10^{-3}
^{12}C	^{12}C(e,e$'K^+$)$^{12}_{\Lambda}$B	87.5	1.75	98.89 (^{13}C:1.11)	42.70	2.0×10^{-3}
^{52}Cr	^{52}Cr(e,e$'K^+$)$^{52}_{\Lambda}$V	134.0 154.0	7.15	99.9	15.3	8.8×10^{-3}

The targets were put on a target holder which was attached on a target ladder as shown in Fig. 2.8 and Fig. 2.9. The target holder has several pockets to put the solid targets. Water was flowed along the edge of target ladder to cool down the solid targets, and also used as a target with 25 μm "HAVAR"[*1] foils (in back and front) at the end of target ladder.

The target holders were exchanged three times, and the three target sets are summarized in Table. 2.4. Radiation levels around the target were high for a while after the beam irradiation. In consideration of our health issue and given experimental time, once the target holder was set, the target position was remotely controlled from an experimental counting room.

Maximum beam current for each target was estimated [63] considering their melting points and heat conduction by using ANSYS[*2] which is a software with three-dimensional finite element method. In the calculation, target thickness was assumed to be 100 mg/cm^2. The expected maximum beam current are summarized in Table. 2.5

[*1] HAVAR is a non-magnetic cobalt-base alloy which exhibits high strength.
[*2] http://ansys.jp/

Table 2.4: Target sets used in the experiment.

Pocket number	Target set 1 (Holder 1)	Target set 2 (Holder 2)	Target set 3 (Holder 2)
1	BeO	BeO	BeO
2	^{52}Cr	^{52}Cr	^{52}Cr
3	^{10}B	CH_2	CH_2
4	^{11}B		
5	^{12}C		
6	^{7}Li	^{9}Be	^{12}C

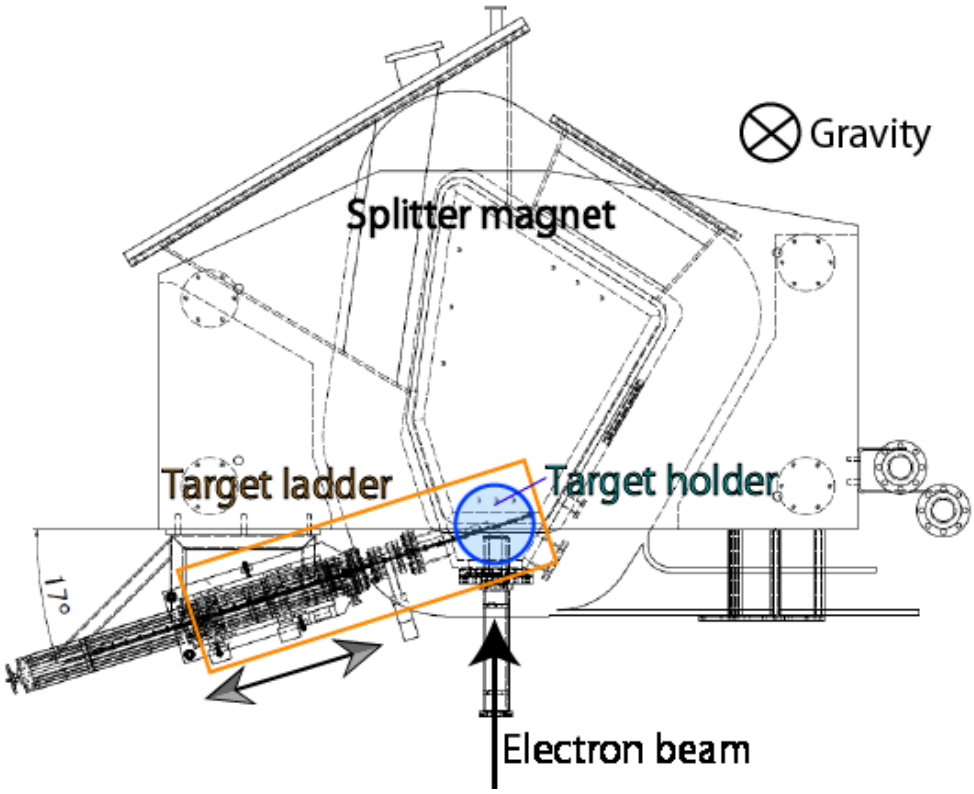

Figure 2.8: The target was set at the entrance of the splitter magnet.

Table 2.5: The expected maximum beam current for each target with 100 mg/cm^2 thickness [63]. The maximum beam current was estimated up to 50 μA.

Target	Melting point [64] [K]	Expected maximum temperature [K]	Beam current [μA]
^{7}Li	460	386	30
^{10}B	2200	970	50
^{12}C	3650	521	50
^{52}Cr	1890	988	50

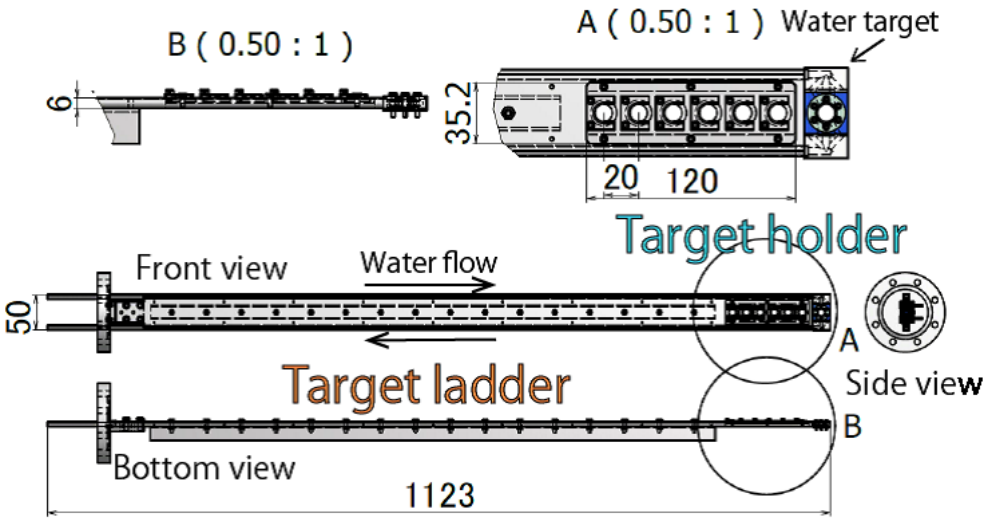

Figure 2.9: A schematic drawing of the target ladder. The target holder which has some pockets to hold targets was put on the ladder.

Table 2.6: Main parameters of SPL.

Pole gap height [mm]	190
Maximum magnetomotive force [A·turns]	214200
Number of turns	210
Conductor size	17 mm×17 mm (ϕ11 hole)
Maximum field [T]	1.74
Maximum current [A]	1020
Total magnet weight [ton]	31.7

2.3.4 Splitter magnet (SPL)

The splitter magnet (SPL) was newly constructed for the JLab E05-115 experiment to optimize an optical matching between HKS and newly constructed HES. A main role of the splitter magnet is to lead positive and negative charged particles toward opposite directions.

Fig. 2.10 shows the differential cross sections of ${}^{12}_{\Lambda}$B ground state as a function of K^+ scattering angle in the laboratory system by DWIA calculation [65]. On the other hand, virtual photon flux as a function of the e' scattering angle is shown in Fig. 2.11. Both Fig. 2.10 and Fig. 2.11 show forward peaks meaning that both a K^+ and an e' should be detected with their small scattering angles to maximize the yields of Λ hypernuclei. Therefore, SPL was introduced to measure both a K^+ and an e' with their small scattering angles avoiding physical interference between magnetic spectrometers.

Fig. 2.12 shows a drawing of SPL. Optical design for SPL had been done carefully since it has one entrance for an incident beam and four exits for an outgoing beam, a photon, a K^+ and an e^+.

2.3.5 High resolution Kaon Spectrometer (HKS)

HKS which consists of QQD magnets (Fig. 2.13) and some particle detectors was designed to achieve a momentum resolution of $\Delta p/p \simeq 2 \times 10^{-4}$ (FWHM) with a central momentum of 1.2 GeV/c. The main parameters of the HKS system are listed in Table. 2.2.

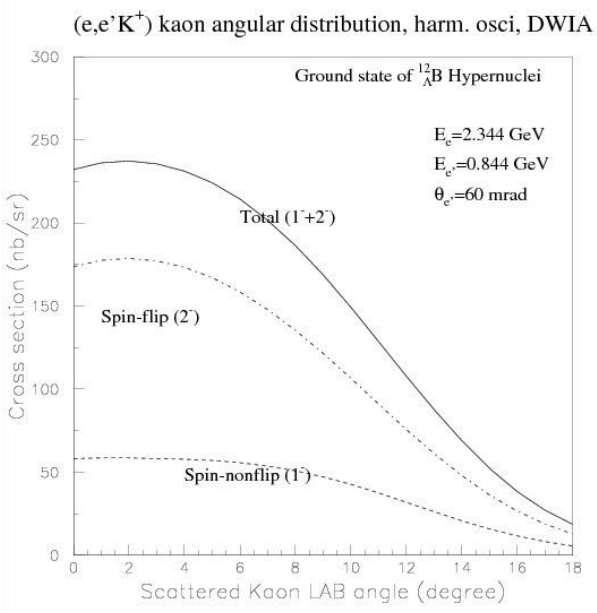

Figure 2.10: Theoretical calculation (DWIA) of the ${}^{12}_{\Lambda}$B ground state cross section as a function of K^+ scattering angle [65].

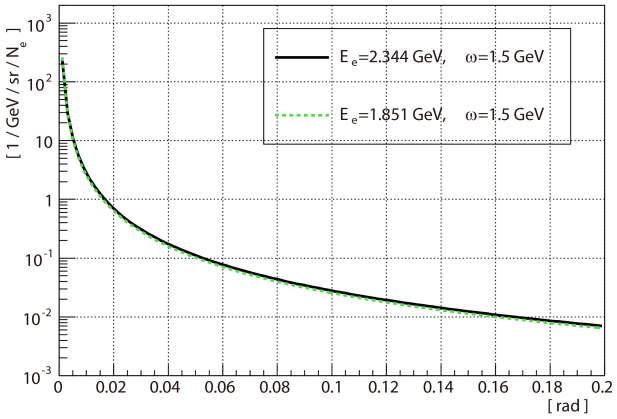

Figure 2.11: Calculation of the virtual photon flux as a function of e' scattering angle at $\omega = 1.5$ GeV and $E_e = 2.344$ GeV (solid line), 1.851 GeV (dashed line).

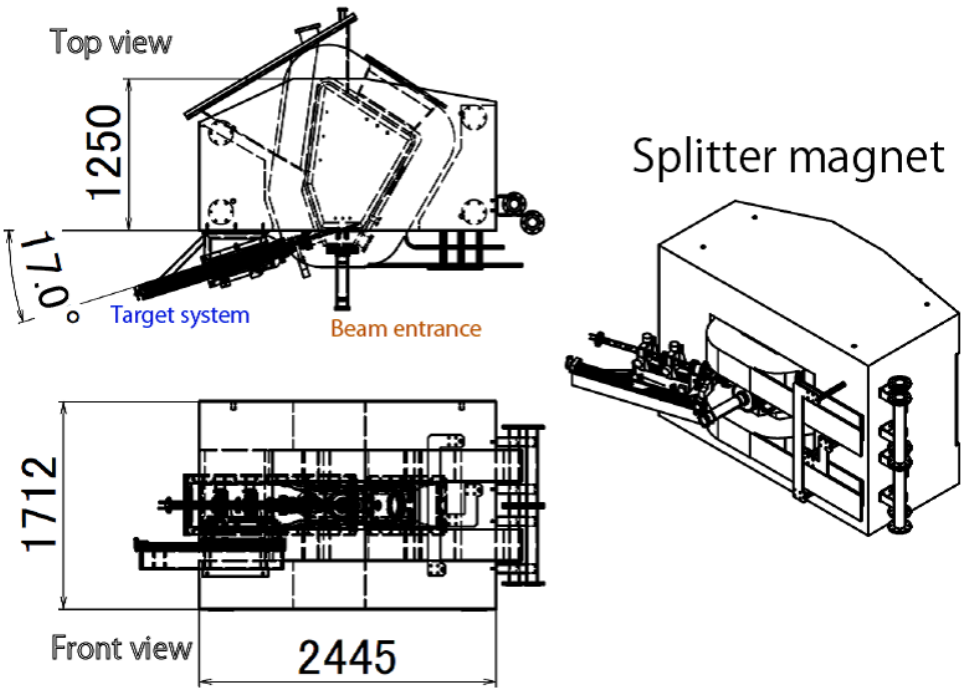

Figure 2.12: A schematic drawing of SPL. The unit is mm.

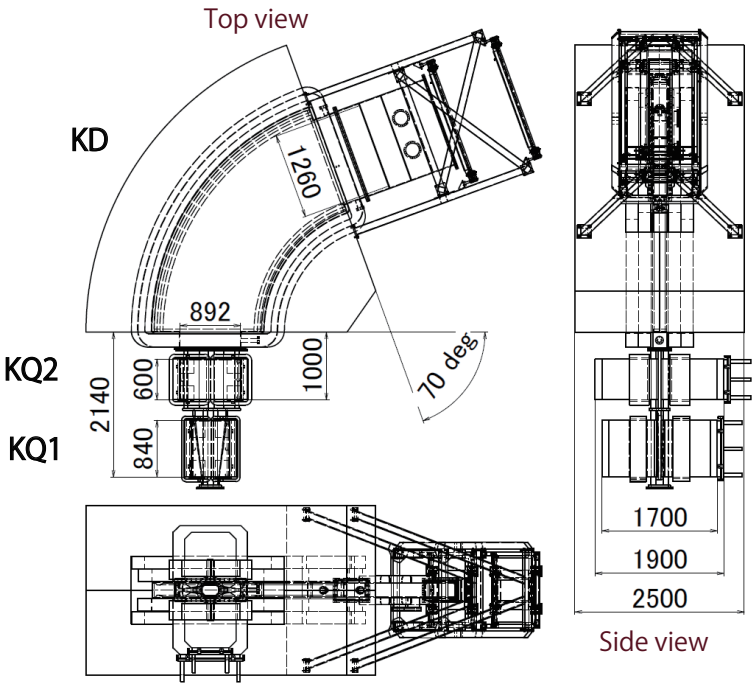

Figure 2.13: A schematic drawing of the HKS spectrometer. It consists of two quadrupole and one dipole magnets (KQ1, KQ2, KD). The unit is mm.

A clean K^+ identification (KID) is one of the key points to carry out the experiment since huge amount of π^+s and protons are included in HKS as background particles. Both on-line and off-line KID were done, and will be described in Sec. 4.3.2. Fig. 2.13 shows a schematic drawing of the HKS magnets (KQ1, KQ2, KD). The main parameters of these magnets are summarized in Table. 2.7.

An acceptance of HKS was estimated by a Monte Carlo simulation with Geant4. Fig. 2.14 shows the simulated results of a correlation between the K^+ momentum and scattering angle in the laboratory frame, and the solid angles as functions of the K^+ momentum and scattering angle. The HKS solid angle with the splitter magnet was 8.5 msr for the HKS central momentum.

HKS collimator and sieve slit

Fig. 2.15 shows a schematic drawing of the HKS collimator and sieve slit unit. It was made of an one inch thickness HEAVIMET which is tungsten alloy, and set just in front of KQ1. The collimator and sieve slit unit was movable. Its position was remotely controlled during the experiment.

The collimator was used for production data to avoid particles passing through around edge of KQ1 where magnetic field was not optimal as a spectrometer. On the other hand, the sieve slit was used for data for optics optimization of HKS in the off-line analysis as will be shown in Sec. 4.8.1.

Table 2.7: The main parameters of the HKS quadrupole magnets (KQ1, KQ2).

	KQ1	KQ2
Bore radius [mm]	120	145
Pole length [mm]	840	600
Maximum magnetomotive force [A·turns]	224000	144000
Number of turns	256	320
Conductor size	8×8 (ϕ6 hole)	13.5×11.5 (ϕ6.3 hole)
Coil winding	Double pancake	Solenoid
Maximum field gradient [T/m]	6.6	4.2
Maximum current [A]	875	450
Resistance [mΩ]	181 at 55°C	119 at 45°C
Cooling water flow rate [l/m]	49.6	17.3
Pressure Drop [MPa]	0.36	0.38
Number of coolant circuits	16	8
Total magnet weight [ton]	8.2	10.5

Table 2.8: The main parameters of the HKS dipole magnet (KD).

Pole gap height [mm]	200	
Pole length [mm]	1560	
Maximum magnetomotive force [A·turns]	291840	
Number of turns	256	
Conductor size [mm]	22×22 (ϕ12 hole)	
Maximum field [T]	1.53	
Maximum current [A]	1140	
Resistance [mΩ]	145 at 47.5°C	
	Gap side	Yoke side
Cooling water flow rate [l/m]	66.3	68.8
Pressure drop [MPa]	0.32	0.35
Number of coolant circuits	8	
Total magnet weight [ton]	210	

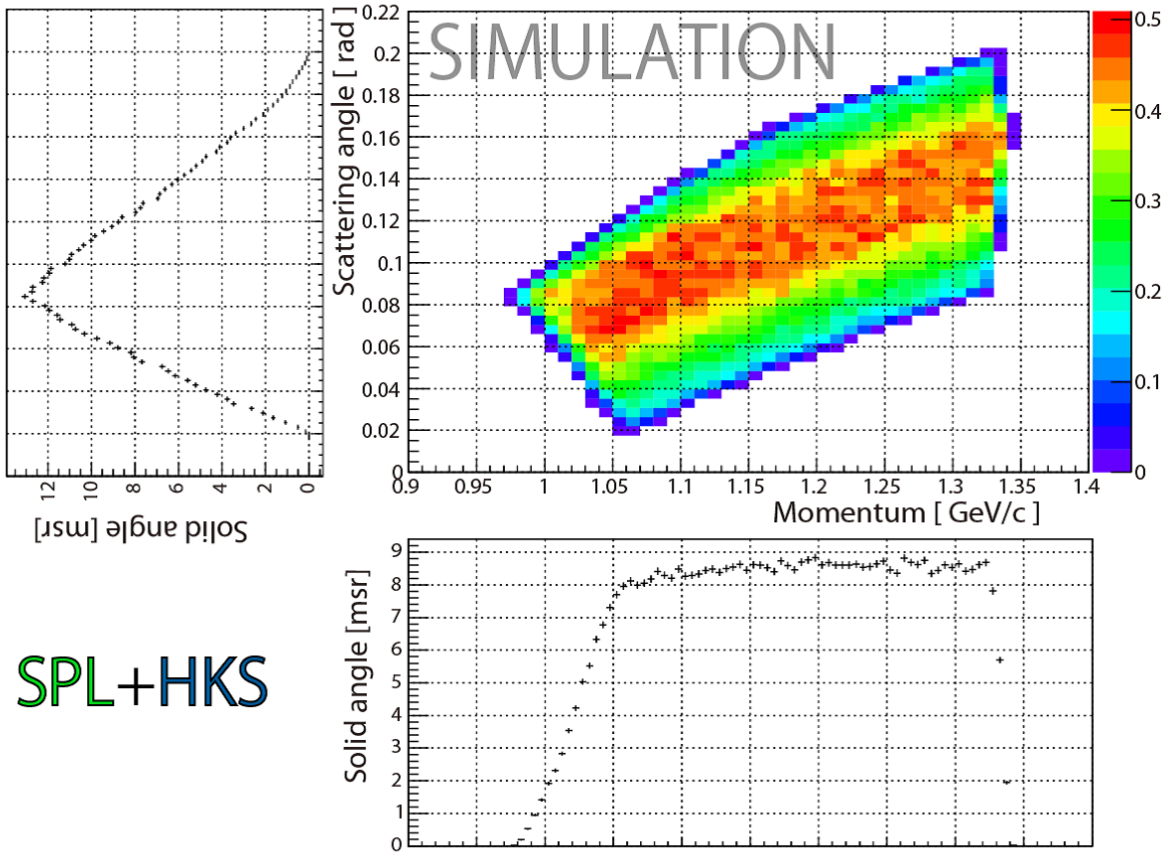

Figure 2.14: Simulation results of a correlation between the K^+ momentum and scattering angle in the laboratory frame, and the solid angles as functions of the K^+ momentum and scattering angle.

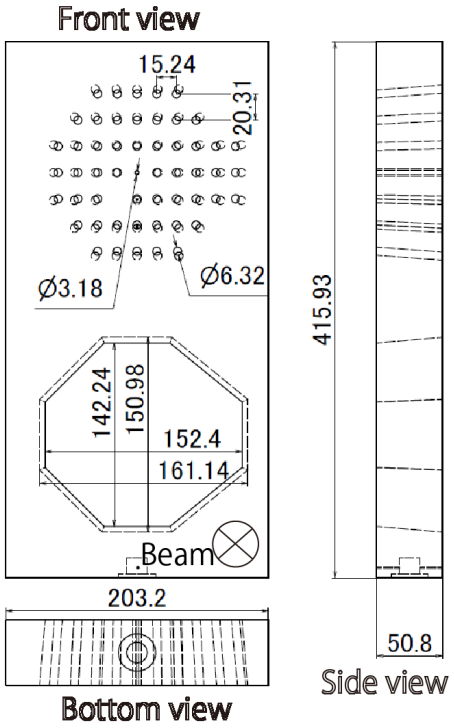

Figure 2.15: A schematic drawing of the HKS collimator and sieve slit unit. It was made of a one inch thickness HEAVIMET which is tungsten alloy, and set just in front of KQ1. The unit is mm.

2.3.6 High resolution Electron Spectrometer (HES)

HES which consists of QQD magnets (Fig. 2.16) and a detector package for high rate electrons was designed and constructed for the E05-115 experiment. HES was designed to achieve a momentum resolution of $\Delta p/p \simeq 2 \times 10^{-4}$ (FWHM) aiming to achieve 0.5 MeV missing mass resolution in FWHM. The main parameters of the HES magnets are listed in Table. 2.9 (quadrupoles) and Table. 2.10 (dipole).

It was expected that background particles originate from electromagnetic processes which are roughly in proportion to square of a target proton number, Z^2 increase in HES. Since it is the first attempt to measure a hypernucleus which have medium mass number with the (e,e$'K^+$) reaction, these background particles should be carefully considered in terms of yields and S/N of Λ hypernuclei particularly for the medium heavy Λ hypernucleus, ${}^{52}_{\Lambda}$V.

Table 2.9: The main parameters of the HES quadruple magnets (EQ1, EQ2).

	EQ1	EQ2
Bore radium [mm]	100	125
Pole length [mm]	600	500
Maximum magnetomotive force [A·turns]	144000	144000
Number of turns	180	180
Conductor size [mm]	9×9 (ϕ6 hole)	9×9 (ϕ6 hole)
Maximum field gradient [T/m]	7.8	5.0
Maximum current [A]	800	800
Total magnet weight [ton]	2.8	3.1

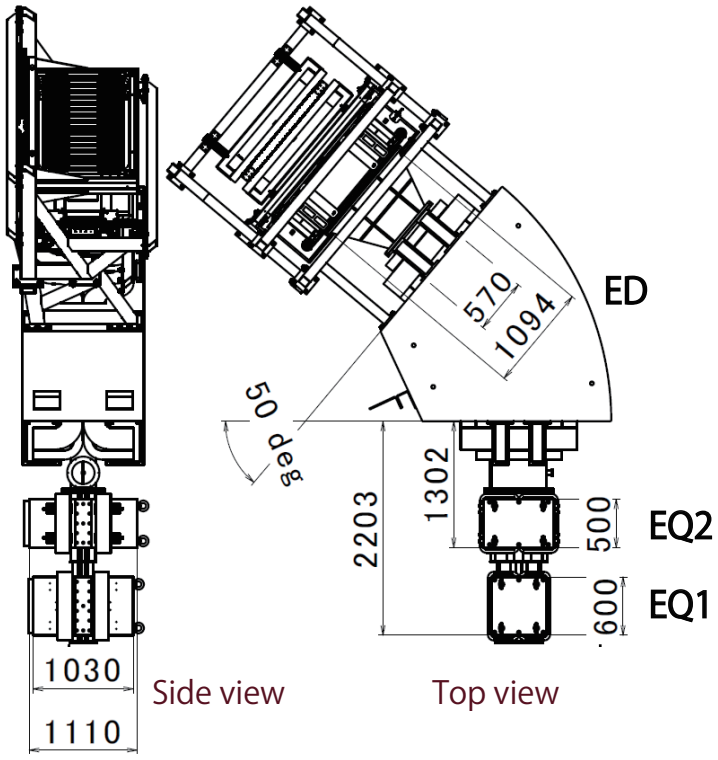

Figure 2.16: A schematic drawing of the HES magnets. It consists of two quadrupole and one dipole magnets (EQ1, EQ2, ED). The unit is mm.

Table 2.10: The main parameters of the HES dipole magnets (ED).

Pole gap height [mm]	194
Pole length [mm]	1560
Maximum magnetomotive force [A·turns]	289680
Number of turns	136
Conductor size [mm]	17×17 (ϕ11 hole)
Maximum field [T]	1.65
Maximum current [A]	1065
Total magnet weight [ton]	36.4

In this section, origins of background particles, treatments for the background particles (tilt method) and an acceptance estimation of HES with SPL are described.

Background electrons

There are two major background sources for the electron spectrometer. One is Bremsstrahlung and the another is Møller scattering.

- **Bremsstrahlung**
  Electrons which lose their energy in the target by the Bremsstrahlung process got into HES as background particles. The Bremsstrahlung electron rates are increased as the target proton number (Z) since its cross section is roughly in proportion to Z^2. It makes us difficult to perform an (e,e′K^+) experiment with medium or large mass number targets. The energy and angular distributions of Bremsstrahlung are represented by the following equation [66]:

$$\begin{aligned}
\frac{d^2\sigma_b}{d\Omega_k dk} &= \frac{2\alpha^3 E_e^2}{\pi k m_e^4}\Big(b_1(Z^2+Z)+b_2(X-2Z^2 f((\alpha Z)^2))\Big), \qquad (2.9)\\
b_1 &= \frac{2y-2}{(1+l)^2}+\frac{12l(1-y)}{(1+l)^4},\\
b_2 &= \frac{2-2y+y^2}{(1+l)^2}-\frac{4l(1-y)}{(1+l)^4},
\end{aligned}$$

  where k is the photon energy and,

$$\begin{aligned}
l &= \frac{\theta_k^2 E_e^2}{m_e^2}\ (\theta_{\mathbf{k}}:\text{photon angle}), \qquad (2.10)\\
y &= \frac{k}{E_e}<1, \qquad (2.11)\\
f(z) &= 1.202z-1.0369z^2+\frac{1.008z^3}{1+z}, \qquad (2.12)\\
X &= Z^2\Big[\ln\frac{a^2 m_e^2(1+l)^2}{a^2 t'_{min}+1}-1\Big]+Z\Big[\ln\frac{a'^2 m_e^2(1+l)^2}{a'^2 t'_{min}+1}-1\Big], \qquad (2.13)\\
a &= \frac{184.15(2.718)^{-1/2}Z^{-1/3}}{m_e}, \qquad (2.14)\\
a' &= \frac{1194(2.718)^{-1/2}Z^{-2/3}}{m_e}, \qquad (2.15)\\
t' &= \Big[\frac{k m_e^2(1+l)^2}{2E_e(E_e-k)}\Big]^2. \qquad (2.16)
\end{aligned}$$

  Fig.2.17 shows differential cross sections of Bremsstrahlung as a function of the electron scattering angle in the laboratory frame for ^{7}Li, ^{12}C and ^{52}Cr targets at $E_e = 2.344$ GeV and $p_{e'} = 0.844$ GeV/c. The cross section for ^{52}Cr target is larger than those for ^{12}C and ^{7}Li targets by factors of 14 and 50, respectively.

  In the E05-115 experiment, the beam energy of 2.344 GeV which was higher than that of the E01-011 experiment (E_e = 1.851 GeV) was used. A cross section comparison between E05-115 and E01-011 is shown in Fig. 2.18. The angular distribution become more forward with higher beam energy. In the HES angular acceptance ($\theta_{e'}$ = 0.035 to 0.200 rad), the cross section is suppressed by more than a factor of 10 comparing with the E01-011 experimental condition.

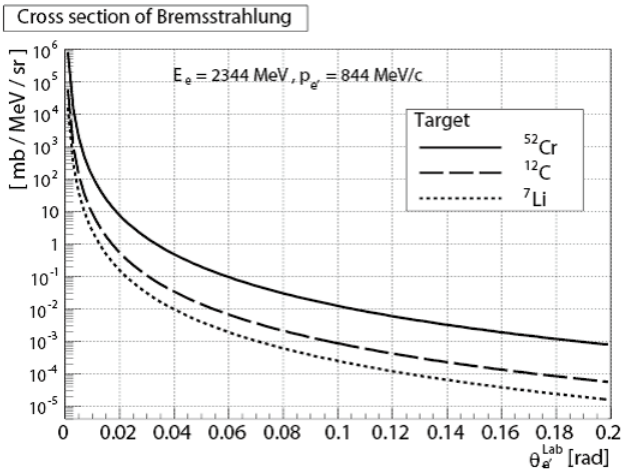

Figure 2.17: The differential cross sections of Bremsstrahlung as a function of the electron scattering angle for ^{7}Li, ^{12}C and ^{52}Cr targets at $E_e = 2.344$ GeV and $p_e = 0.844$ GeV/c.

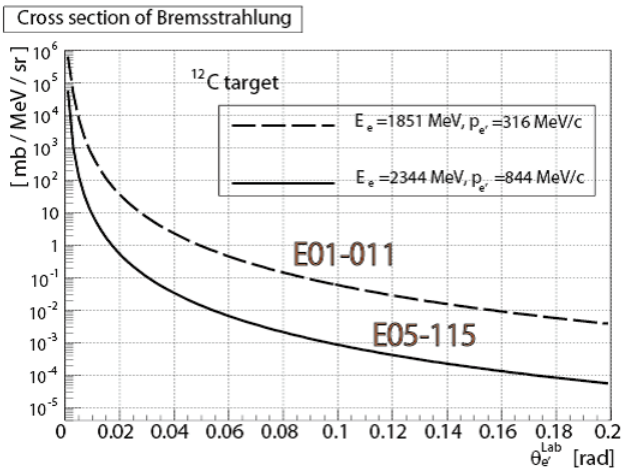

Figure 2.18: The differential cross sections of Bremsstrahlung as a function of the electron scattering angle for ^{12}C target for conditions of JLab E01-011 ($E_e = 1.851$ GeV, $p_e = 0.316$ GeV/c) and JLab E05-115 ($E_e = 2.344$ GeV, $p_e = 0.844$ GeV/c).

- **Møller scattering**
  Møller scattering, electron-electron scattering is another background source for HES. The differential cross section in the center-of-mass frame is written by the following equation [67]:

$$\left(\frac{d\sigma_m}{d\Omega}\right)_{CM} = \frac{\alpha^2(2E_{CM}^2 - m_e^2)^2}{4E_{CM}^2(E_{CM}^2 - m_e^2)^2}\left[\frac{4}{\sin^4\theta_{CM}} - \frac{3}{\sin^2\theta_{CM}} + \frac{(E_{CM}^2 - m_e^2)^2}{(2E_{CM}^2 - m_e^2)^2}\left(1 + \frac{4}{\sin^2\theta_{CM}}\right)\right]. \tag{2.17}$$

  Fig. 2.19 and Fig. 2.20 show the cross sections of Møller scattering as a function of the electron scattering angle in the laboratory frame ($\theta_{e'}^{\mathrm{Lab}}$) for experimental setups for E05-115 ($E_e = 2.344$ GeV) and E01-011($E_e = 1.851$ GeV). Once the scattering angle is fixed, the momentum of electron is determined since it is a two-body reaction. Colored region in the figures indicate momentum acceptance of electron spectrometers for JLab E05-115 and JLab E01-011.

Both electrons associated with virtual photon (Fig.4.43) and background electrons have forward peak distributions although its shapes are different. Thus, the angular acceptance of HES needed to be optimized to maximize the S/N and yields of Λ hypernuclei. This optimization is essential particularly for the measurement of a medium-heavy Λ hypernucleus.

Tilt method and setup optimization

To maximize the S/N and yields of Λ hypernuclei, the angular acceptance of HES was optimized by adopting a tilt method. HES was vertically tilted (tilt method) avoiding very small scattering angles where background electron rate is extremely high.

The tilt angle was optimized with a Monte Carlo simulation (Geant4). In the simulation, electron rate of each process was estimated as a function of the tilt angle (Fig. 2.21). A figure of merit (FoM) was defined to be:

$$\mathrm{FoM} = \frac{R_{\mathrm{VP}}}{\sqrt{R_{\mathrm{Brems}} + R_{\mathrm{Møller}}}} \tag{2.18}$$

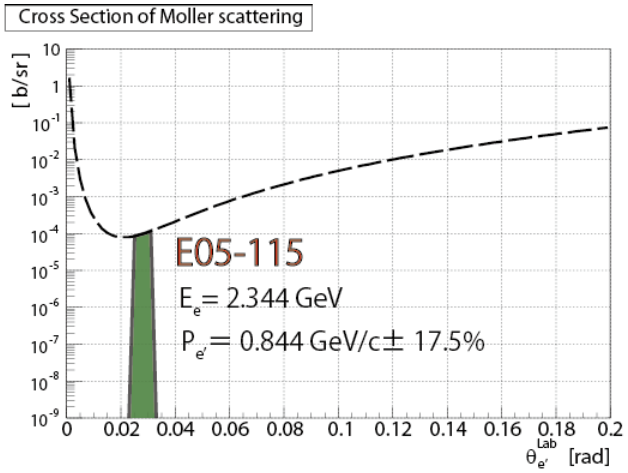

Figure 2.19: The differential cross section of Møller scattering as a function of electron scattering angle in the laboratory frame for the experimental setup of E05-115 (E_e = 2.344 GeV).

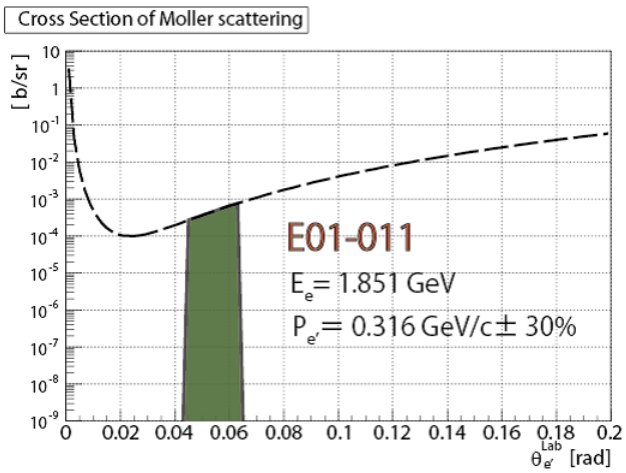

Figure 2.20: The differential cross section of Møller scattering as a function of electron scattering angle in the laboratory frame for the experimental setup of E01-011 (E_e = 1.851 GeV).

where $R_{\rm VP}$, $R_{\rm Brems}$ and $R_{\rm Møller}$ are rates of electrons associated with virtual photon, Bremsstrahlung and Møller scattering, respectively, in HES. The FoM is also shown in Fig. 2.21. The FoM becomes high with the tilt angle of $\geq$5.8 degrees. The yield of electrons associated with virtual photon is monotonically reduced as the tilt angle increases. Considering both S/N and yield, the tilt angle was chosen to be 6.5 degrees. A schematic drawing of HES with its tilt angle of 6.5 degrees (side view) is shown in Fig. 2.22.

The optimized angular acceptance of HES superimposing with angular distributions of scattered electrons associated with virtual photon, Bremsstrahlung and Møller scattering are shown in Fig. 2.23. The vertical axis unit is arbitrary.

Comparison with ENGE spectrometer

In the E05-115 experiment, beam energy was higher (E_e = 2.344 GeV) than that of the E01-011 experiment (E_e = 1.851 GeV). For those beam energies, the angular distributions of scattered electrons associated with virtual photon are similar as shown in Fig. 4.43. On the other hand, background electrons by Bremsstrahlung and Møller scattering become more forward distributions as a beam energy is increased. Thus, the S/N is improved even when the angular acceptance is exactly the same.

The HES angular acceptance could be set at more forward scattering angles than that of E01-011 experiment, thanks to the situation that the background electrons distribute at more forward scattering angles. Moreover, the HES angular acceptance is larger than that of ENGE which was used in the E01-011 experiment as the magnetic spectrometer for scattered electron. These facts increased the yields of electrons associated with virtual photons by $\sim$ 8 times comparing to that of the E01-011 experiment. Fig. 2.24 and Fig. 2.25 show Monte Carlo simulation results of $x'(=\frac{p_x}{p_z})$ vs. $y'(=\frac{p_y}{p_z})$ distributions of electrons associated with virtual photon, Bremsstrahlung and Møller scattering at the target for the E01-011 and E05-115 experimental conditions, respectively.

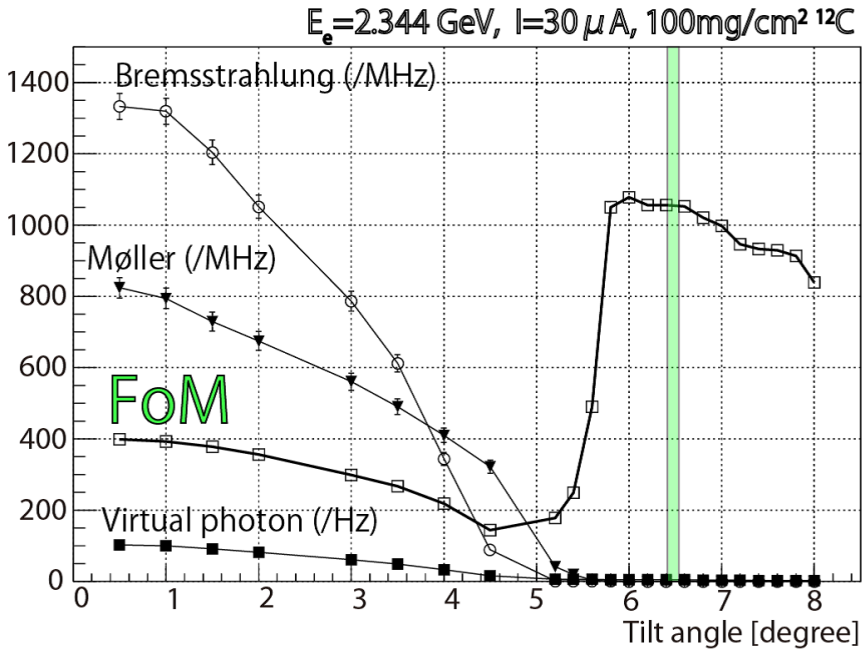

Figure 2.21: A Monte Carlo simulation results of rates of electrons associated with virtual photon, Bremsstrahlung and Møller scattering as a function of HES tilt angle. The figure of merit (FoM) which was defined by Eq. (2.18) is also plotted. Considering the FoM (S/N) and yield, the tilt angle was chosen to be 6.5 degrees.

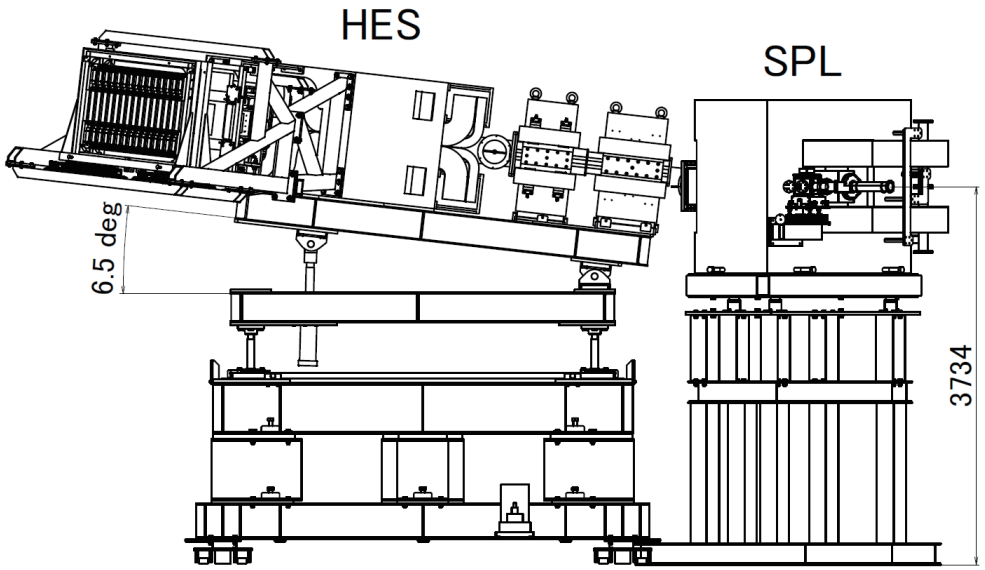

Figure 2.22: A schematic drawing of HES with its tilt angle of 6.5 degrees. The nuit is mm.

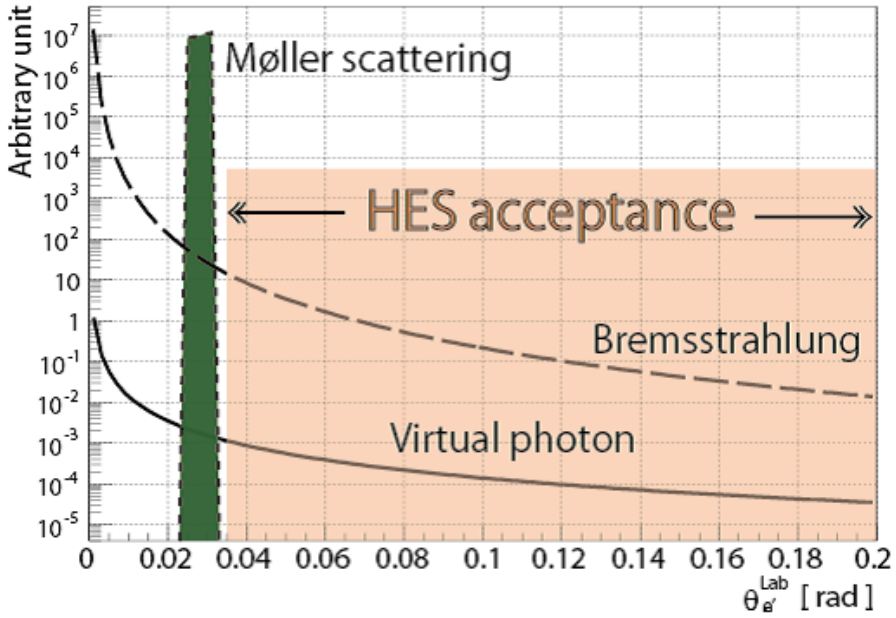

Figure 2.23: The optimized angular acceptance of HES superimposing with the angular distributions of electrons associated with the virtual photon, Bremsstrahlung and Møller scattering as a function of electron scattering angle in the laboratory frame. The vertical axis unit is arbitrary.

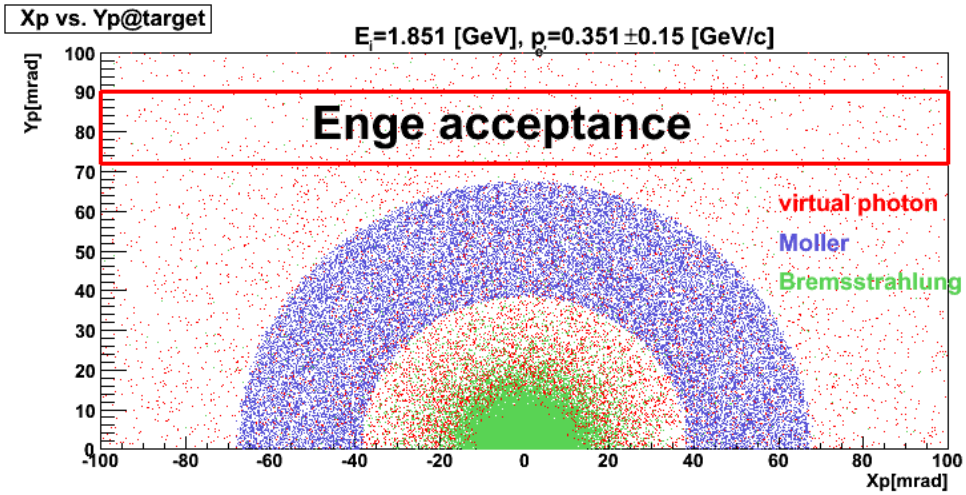

Figure 2.24: x' vs. y' distributions of electrons associated with virtual photon, Bremsstrahlung and Møller scattering at the target for the E01-011 experimental condition.

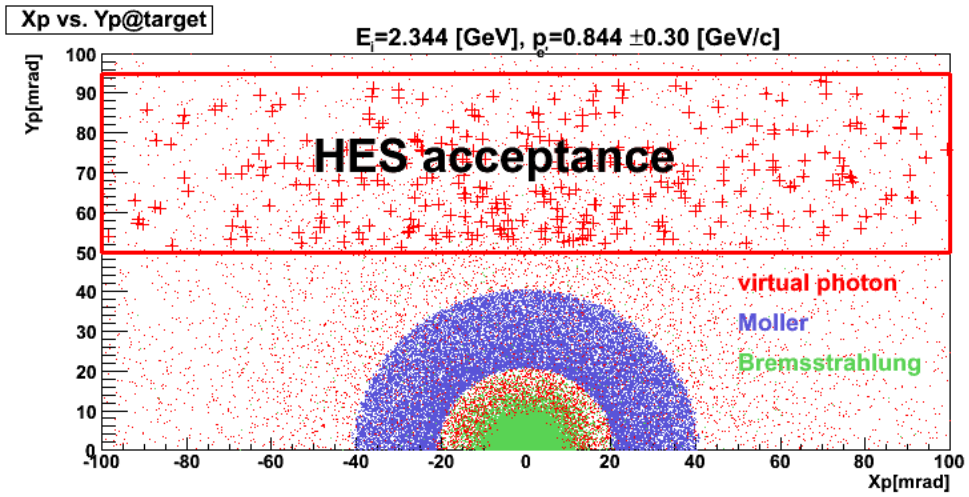

Figure 2.25: x' vs. y' distributions of electrons associated with virtual photon, Bremsstrahlung and Møller scattering at the target for the E05-115 experimental condition.

Acceptance

An acceptance of the HES spectrometer was estimated by a Monte Carlo simulation of Geant4. Fig. 2.26 shows the simulated results of a correlation between e' momentum and scattering angle in the laboratory frame, and the solid angles as functions of e$'$ momentum and scattering angle in the laboratory frame. The HES solid angle with the splitter magnet was 7.0 msr for the HES central momentum.

HES collimator and sieve slit

Fig. 2.27 shows a schematic drawing of the HES collimator and sieve slit unit. It was made of a two inch thickness HEAVIMET which is a tungsten alloy, and set just in front of EQ1. The collimator and sieve slit unit was movable. Its position was remotely controlled during the experiment.

The collimator was used for production data to avoid particles passing through around edge of KQ1 where magnetic field was not optimal as a spectrometer. On the other hand, the sieve slit was used for data for optics optimization of the HES in off-line analysis.

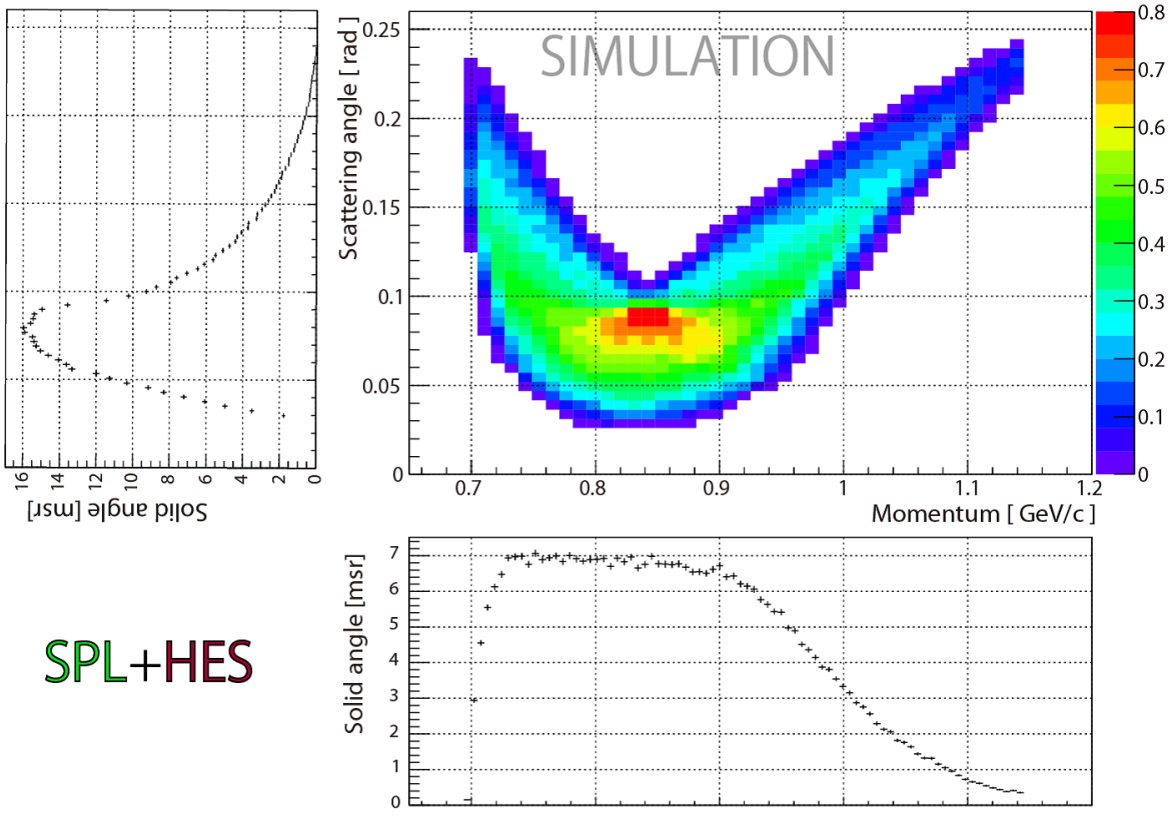

Figure 2.26: Simulation results of a correlation between e' momentum and scattering angle in the laboratory frame, and solid angles as functions of e' momentum and scattering angle in the laboratory frame.

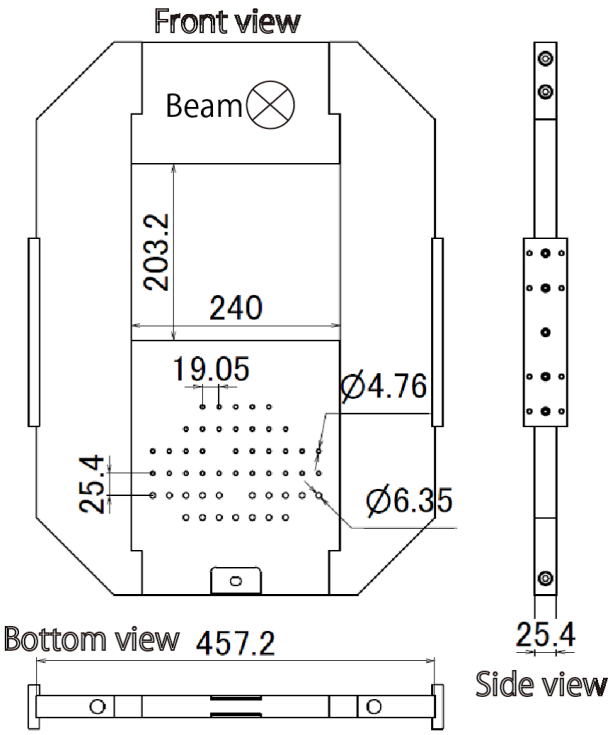

Figure 2.27: A schematic drawing of the HES collimator and sieve slit unit. It was made of a two inch thickness HEAVIMET which is tungsten alloy, and set just in front of EQ1. The unit is mm.

2.4 Momentum matching between HES and HKS

The HES and HKS momentum acceptance were optically designed to satisfy the following experimental requirements:

- Covering of interested Λ hypernuclei.
- Covering of Λ and Σ^0 simultaneously for the absolute energy scale calibration.

Fig. 2.28 show simulated results of momentum correlation between e' and K^+ in the HES-HKS system, showing that the requirements are satisfied.

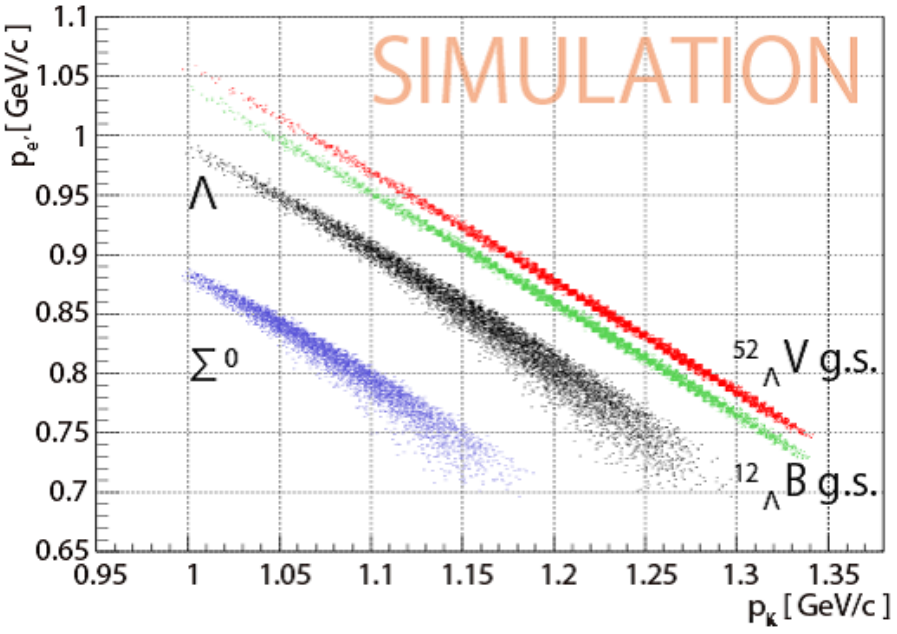

Figure 2.28: Simulated results of momentum correlations between scattered electrons and K^+s in the acceptance of HES and HKS. In the simulation, Λ, Σ^0, ${}^{12}_{\Lambda}$B (assumed binding energy of 11.37 MeV) and ${}^{52}_{\Lambda}$V (assumed binding energy of 20.0 MeV) were generated and plotted. Interested hypernuclei and hyperons (Λ, Σ^0) which are used for the absolute energy scale calibration are in the acceptance.

Chapter 3

Detectors and Data summary

3.1 HES side

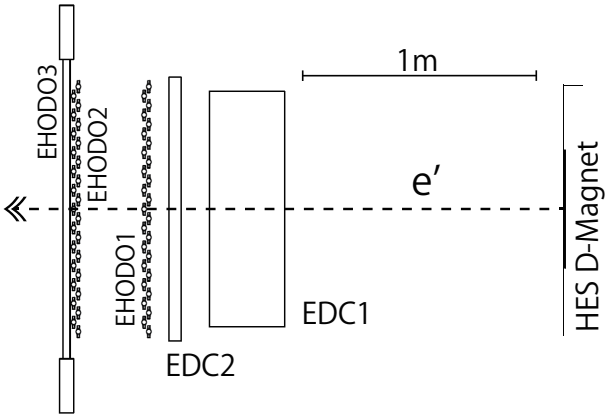

Figure 3.1: A schematic drawing of HES detectors. HES has two drift chambers (EDC1, EDC2) for particle tracking and three scintillation detectors (EHODO1, EHODO2, EHODO3) for TOF measurement.

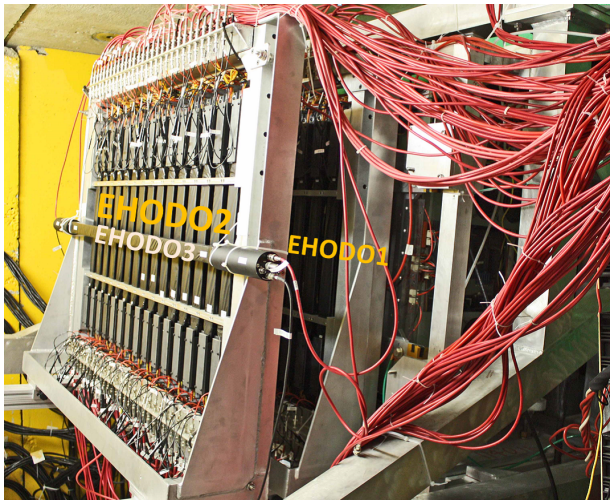

Figure 3.2: A photograph of HES detectors which was taken from the downstream of HES.

An HES detector package was designed to achieve a momentum resolution of $\Delta p/p \simeq 2.0 \times 10^{-4}$ (FWHM). The HES detector package consists of two drift chambers (EDC1, EDC2) for particle tracking and three scintillation detectors (EHODO1, EHODO2, EHODO3) for Time Of Flight (TOF) measurement. Fig. 3.1 shows a schematic drawing of HES detectors, and Fig. 3.2 is a photograph which was taken from the downstream of HES.

3.1.1 HES Drift Chambers (EDC1,2)

EDC1

EDC1 is a honeycomb cell structure drift chamber (Fig.3.3) which was also used in the E01-011 experiment for the electron arm tracking. The typical plane resolution and efficiency were 220 μm and 99 %, respectively in the JLab E01-011 experiment [32]. EDC1 had been stored in a container after the E01-011 experiment (2005) until a preparation of the E05-115 experiment (2009). It was found that hundreds of anode wires were broken. This is considered to be caused by a bad storage conditions, particularly the temperature conditions. Therefore, all of anode and cathode wires were replaced by new ones in 2008.

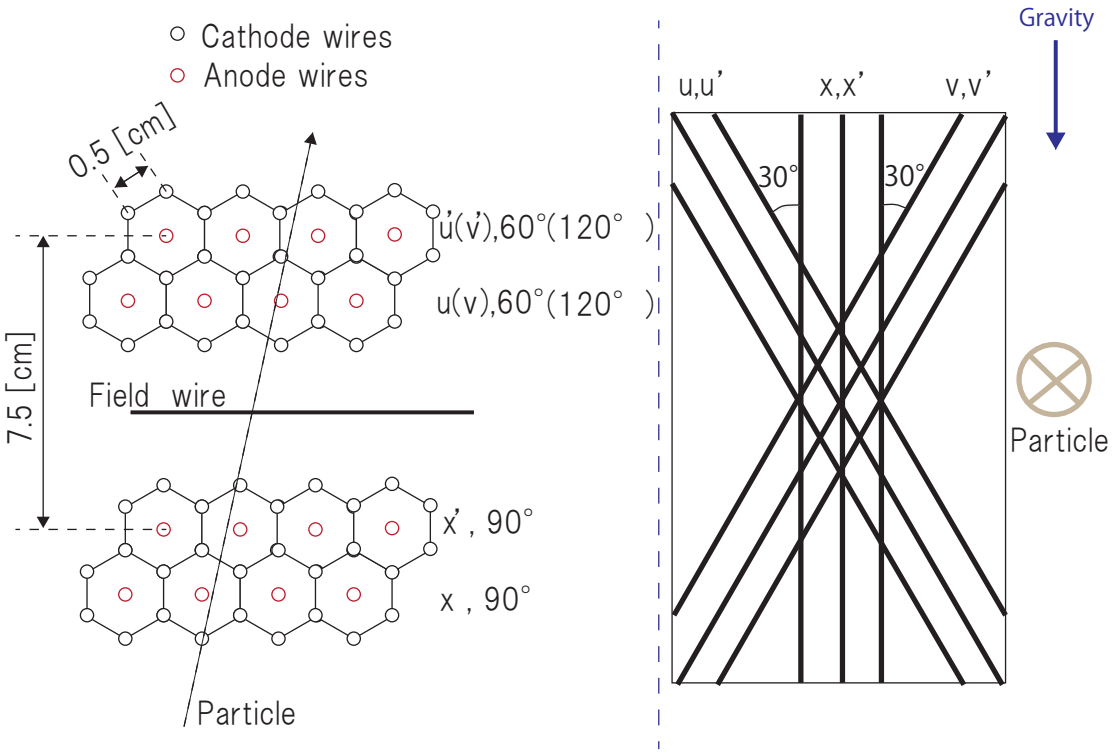

Figure 3.3: A schematic drawing of EDC1 wire configuration.

Fig. 3.3 shows a schematic drawing of wire configurations of EDC1. There were 10 layers (xx′uu′xx′vv′xx′). Wires of u and v layers had angles of +30° and -30° with respect to those of x layer. Wires of x′u′v′ layers were displaced by a half cell from xuv wires to solve left-right ambiguity for particle tracking. Gas of Ar+C_2H_6 (50:50) and amplifier discriminator of Nanometric N277L were used. Typical EDC1 parameters are given in Table. 3.1.

Table 3.1: The main EDC1 parameters.

Layer configuration	xx′uu′xx′vv′xx′ (10 layers)
Effective volume	$120^{H} \times 1000^{W} \times 300^{T}$ mm
Cell structure	Honeycomb
Cell size	5 mm
Window	Aluminized mylar (12.5 μm)
Anode wire	Gold-Plated tungsten ϕ20 μm
Cathode wire	Gold-Plated aluminum ϕ80 μm
Amplifier discriminator	Nanometric N277L
Gas	Ar + C_2H_6 (50:50)
Typical operation voltage	-2200 V

EDC2

EDC2 is an identical drift chamber with that of HKS (KDC1,2). The details are described in the Section 3.2.1.

3.1.2 HES Hodoscopes (EHODO1,2,3)

EHODO1,2

HES hodoscopes (EHODO1,2) were used for TOF measurement and the HES trigger. Fig. 3.4 shows a schematic drawing of EHODO1 (EHODO2). EHODO1 and EHODO2 are the same configuration. It has 29 segments for each layer. Each segment consists of two PMTs (H6612), two pieces of UVT acrylic light-guide and a scintillator (EJ-230). These were welded by ULTRA LIGHT-WELD 3094 produced by DYMAX corporation (DYMAX3094).

A required time resolution for EHODO was a few 100 ps (σ). A cosmic ray test showed that the time resolution was σ ~90 ps which satisfied the experimental requirement.

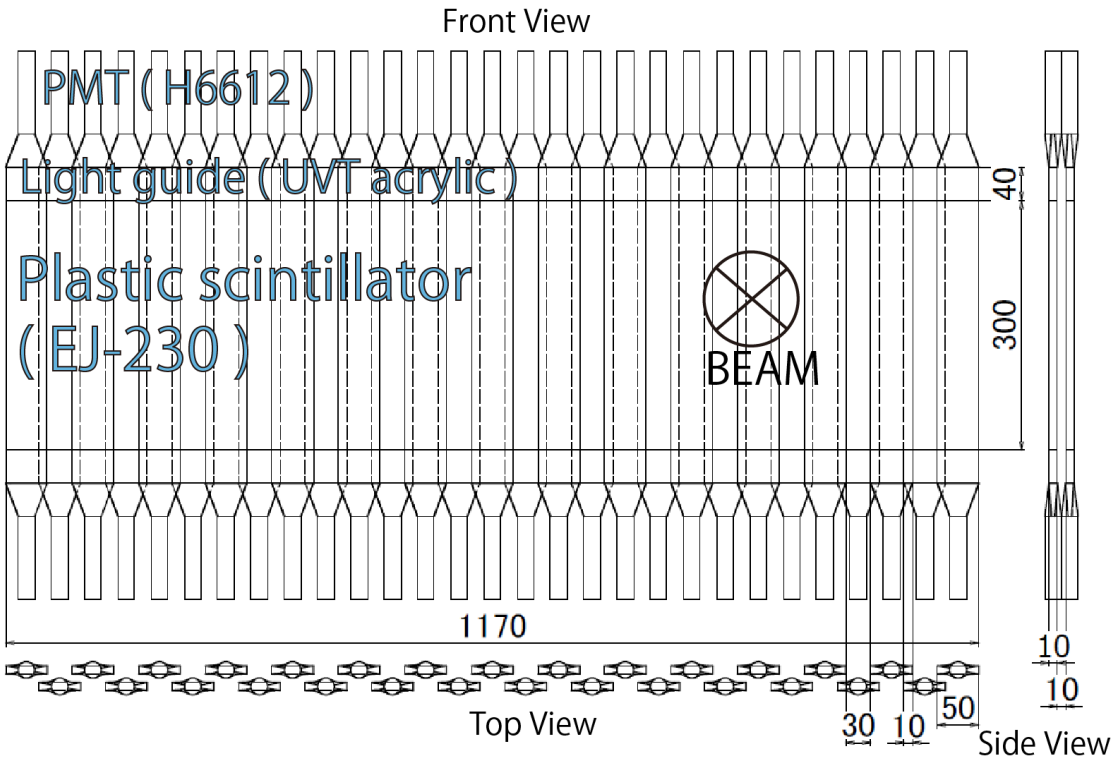

Figure 3.4: A schematic drawing of EHODO1 (EHODO2).

EHODO3

EHODO3 was used for time-zero adjustment of EHODO1,2. It was set just behind EHODO2. Fig. 3.5 is a drawing of EHODO3. It consist of two PMTs (H7195), two pieces of UVT acrylic light-guide and a scintillator (RP-408). These were welded by DYMAX3094.

The required time resolution was a few 100 ps (σ). The time resolution was σ ~100 ps in a cosmic-ray test, which satisfied the experimental requirement.

3.2 HKS side

An HKS detector package was designed to achieve the momentum resolution of $\Delta p/p \simeq 2.0 \times 10^{-4}$ (FWHM). The HKS detector package consists of two drift chambers (KDC1, KDC2) for particle tracking, four layers of scintillation detectors (KTOF1X, KTOF1Y, KTOF2X, KTOF2Y) for TOF measurement and aerogel and water Čerenkov detectors (AC1, AC2 , AC3,

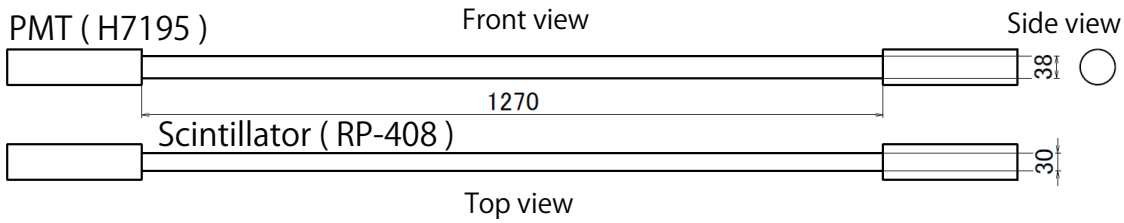

Figure 3.5: A drawing of EHODO3

WC1, WC2) for particle identification. Fig. 3.6 shows a schematic drawing of HKS detectors, and Fig. 3.7 is a photograph. The HKS detectors were used in JLab E01-011 experiment except for half segments of water Čerenkov detectors.

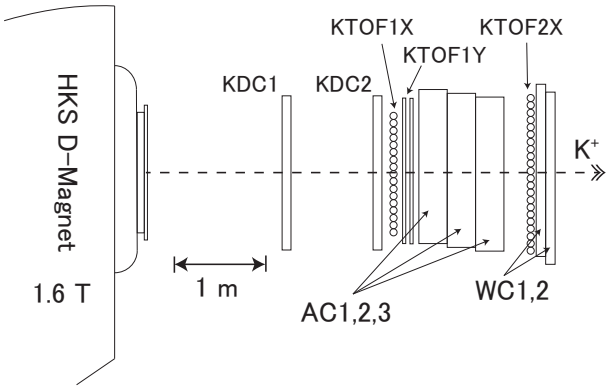

Figure 3.6: A schematic drawing of the HKS detectors. HKS has two drift chambers (KDC1, KDC2) for particle tracking, four layers of scintillation detectors (KTOF1X, KTOF1Y, KTOF2X, KTOF2Y) for TOF measurement and aerogel and water Čerenkov detectors (AC1, AC2 , AC3, WC1, WC2) for particle identification.

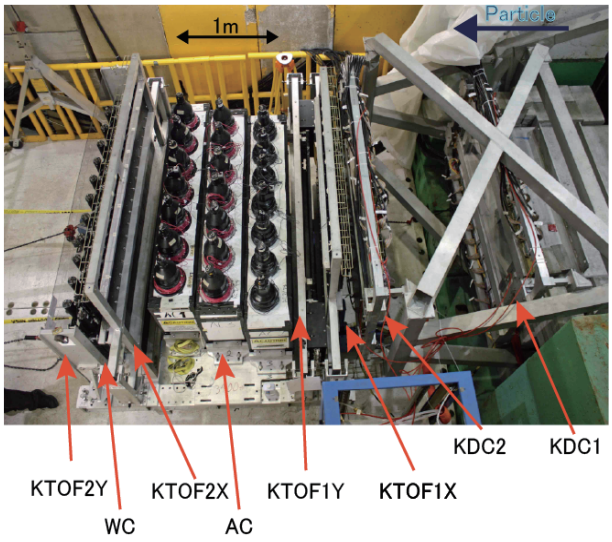

Figure 3.7: A photograph of the HKS detectors. A particle direction is from right to left in the figure, which is opposite direction of Fig. 3.6.

3.2.1 HKS Drift Chambers (KDC1,2)

KDC1 and KDC2 were planer drift chambers which were used in the JLab E01-011 experiment. The typical plane residual was $\sigma \sim 280$ μm. Fig. 3.8 shows a schematic drawing of KDC wire configuration. There are 6 layers (uu′xx′vv′).

3.2.2 HKS TOF Detectors (KTOF1X,2X,1Y,2Y)

KTOF1X

KTOF1X which was used in JLab E01-011 have 17 segments. Each segment consists of a scintillator (BC-408), two pieces of UVT acrylic light-guide and two PMTs (H1949). Fig. 3.9 shows a schematic drawing of KTOF1X.

Required time resolution was a few 100 ps (σ). The time resolution was σ ∼60 ps in a cosmic ray test, which was enough for the experimental requirement.

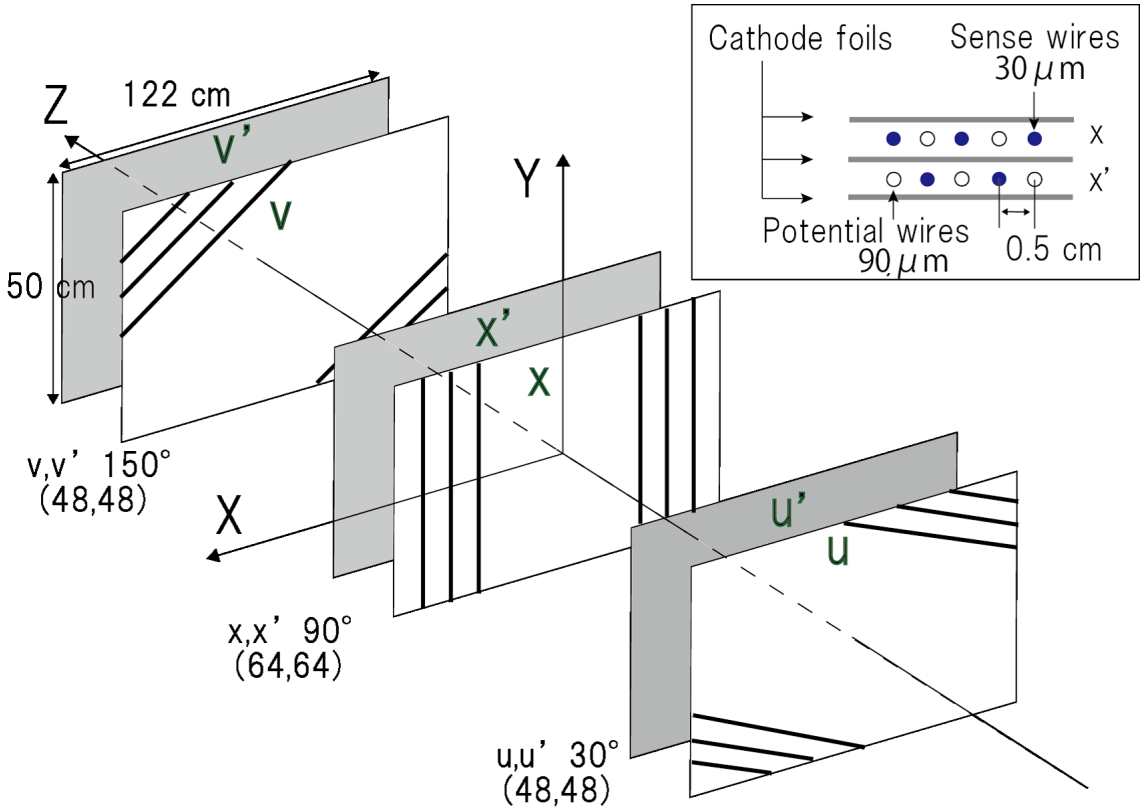

Figure 3.8: A schematic drawing of KDC wire configuration.

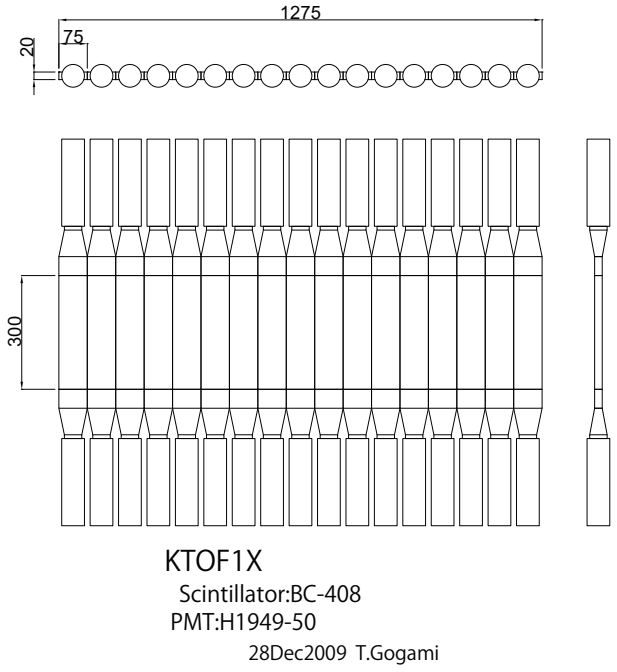

Figure 3.9: A drawing of KTOF1X. There were 17 segments. Each segment consists of a scintillator (BC-408), two pieces of UVT acrylic light-guide and two PMTs (H1949).

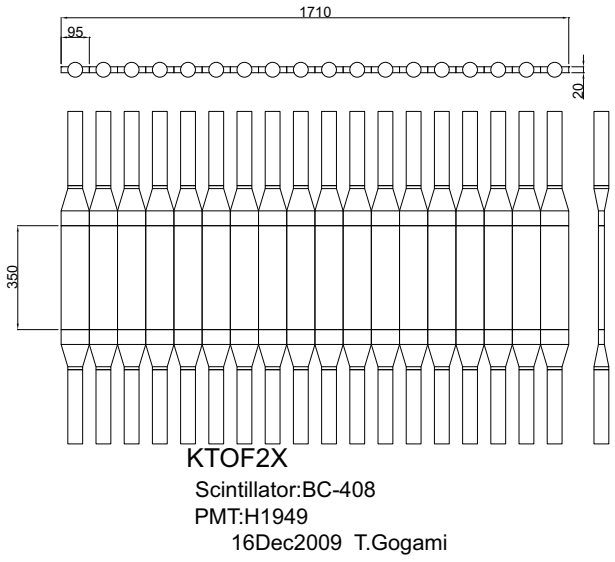

Figure 3.10: A schematic drawing of KTOF2X. There were 18 segments. Each segment consists of a scintillator (BC-408), two pieces of UVT acrylic light-guide and two PMTs (H1949).

KTOF2X

KTOF2X which was used in JLab E01-011 have 18 segments. Each segment consists of a scintillator (BC-408), two pieces of UVT acrylic light-guide and two PMTs (H1949). Fig. 3.10 shows a schematic drawing of KTOF2X.

Required time resolution was a few 100 ps (σ). The time resolution was σ ~60 ps in a cosmic-ray test, which was good enough for the experimental requirement.

KTOF1Y

KTOF1Y had 9 segments. Each segment consists of a scintillator (BC-408), two pieces of UVT acrylic light-guide and two PMTs (H1949). These were welded by DYMAX3094. Fig. 3.11 shows a schematic drawing of KTOF1Y.

KTOF1Y was used in JLab E01-011. However, there were small gaps between scintillators because of the frame design. To avoid event losses from those gaps, KTOF1Y was redesigned with staggered configuration. The design with staggered configuration was optimized by a Monte Carlo simulation with GEANT4.

Required time resolution was a few 100 ps (σ). The time resolution was σ ~70 ps in a cosmic-ray test, which was good enough for the experimental requirement.

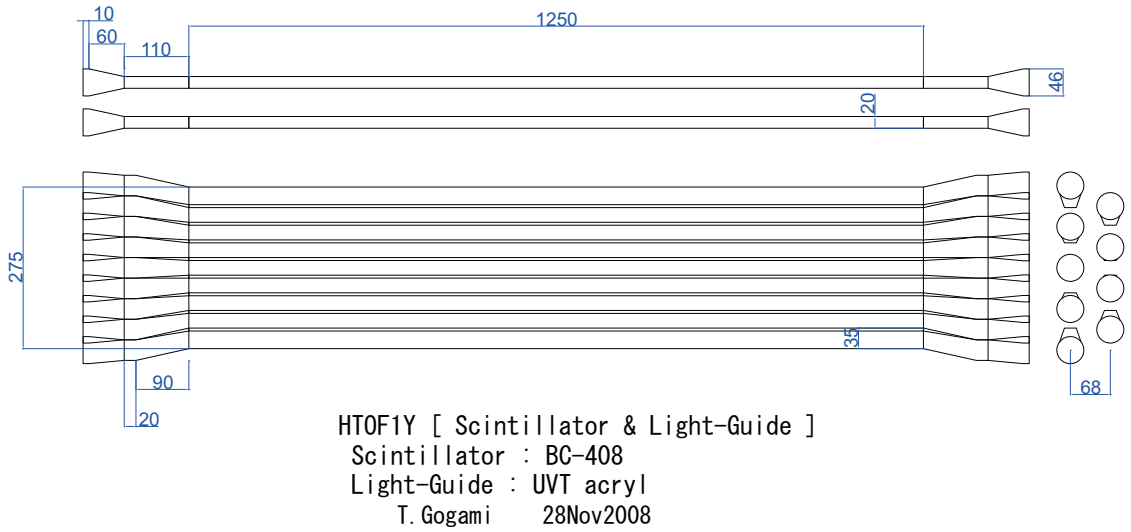

Figure 3.11: A schematic drawing of KTOF1Y.

KTOF2Y

KTOF2Y was used for time-zero adjustment of KTOF1X, KTOF1Y and KTOF2X. Fig. 3.12 shows a schematic drawing of KTOF2Y. It consists of a scintillator (RP-408), two pieces of UVT acrylic light-guide and two PMTs (H7195). These were welded by DYMAX3094.

Required time resolution was σ ~150 ps. The time resolution was σ ~110 ps in a cosmic ray test, which was good enough for the experimental requirement.

3.2.3 Čerenkov Detectors

Over the HKS momentum acceptance of 1.05 GeV/c to 1.35 GeV/c, the number of background particles were 30:1 for protons and 80:1 for π^+s relative to K^+s. Efficient K^+ identification in

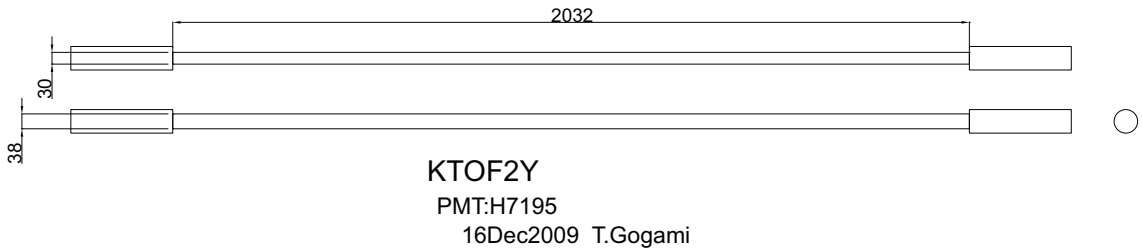

Figure 3.12: A schematic drawing of KTOF2Y.

on-line (hardware trigger level) and off-line plays an important role to maximize the yield and the signal to noise ratio (S/N) of Λ hypernuclei, in a limit of given beam time. Using silica aerogel and water, Čerenkov detector index of refraction values of 1.05 and 1.33 were chosen to reject π^+s and protons, respectively.

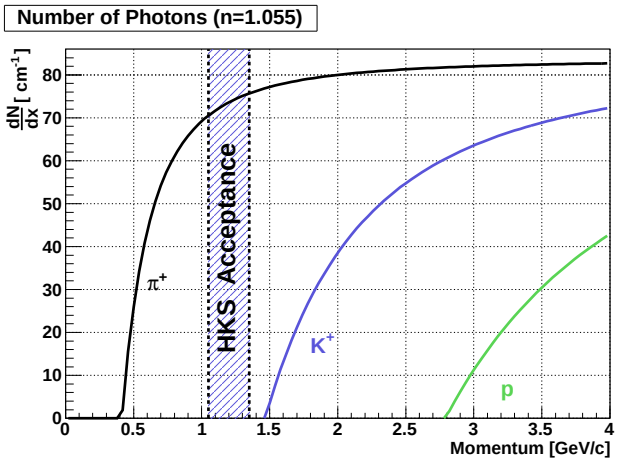

Figure 3.13: Čerenkov photon yield per centimeter in the medium of silica aerogel (n=1.05) as a function of momenta of π^+, K^+ and p. π^+ was distinguished from other particles in on-line and off-line.

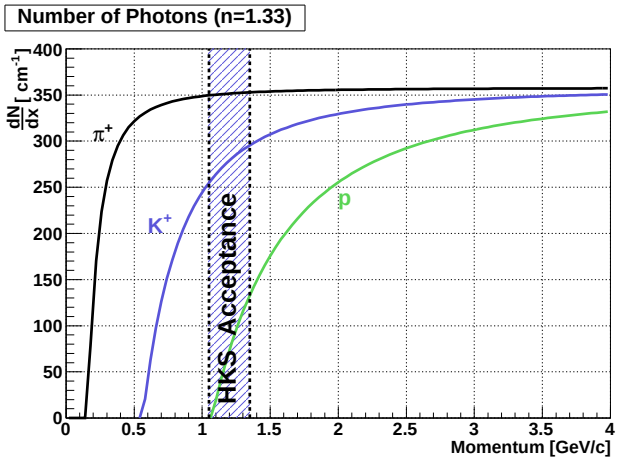

Figure 3.14: Čerenkov photon yield per centimeter in the medium of water (n =1.33) as a function of momenta of π^+, K^+ and p. p was distinguished from other particles by choosing a optimal threshold of the photon yield in on-line and off-line.

Fig. 3.13 and Fig. 3.14 show Čerenkov photon yields for the three particle species in the two radiator media calculated by [68]:

$$\frac{d^2N}{dxd\lambda} = \frac{2\pi\alpha z^2}{\lambda^2}\left(1 - \frac{1}{\beta^2 n^2(\lambda)}\right) \tag{3.1}$$

where

α : Fine structure constant
N : Number of photons
x : Path length [m]
λ : Wavelength of the Cerenkov light [m]
z : Charge of the particle
β : Velocity factor of the particle
$n(\lambda)$: Refraction index of the medium

In Fig. 3.13 and Fig. 3.14, the wavelength was integrated between 300 nm and 650 nm which correspond to typical sensitive wavelength of the PMT, and $n(\lambda)$ was fixed at 1.05 and 1.33 for aerogel and water, respectively. Only π^+ generates Čerenkov light in radiator medium of aerogel in the HKS momentum acceptance. On the other hand, all of three species generate Čerenkov light in radiator medium of water in the HKS acceptance. Therefore, p was distinguished from other particles by choosing a optimal threshold of the photon yield in on-line and off-line.

The HKS detectors were close to the dipole magnet since HKS was designed to measure a K^+ which has the short mean life time (1.2×10^{-8} seconds). A fringe field of 4 to 7 Gauss (G) was observed on PMTs which was put on HKS detectors. Magnetic field particularly parallel to PMT axis deteriorates PMT performances. A PMT (H7195) ADC peak value reduction by 60% was measured when the magnetic field of 5 G was yielded parallel to the PMT axis, in a test. PMT performance deterioration results in lower separation powers of background particles, which directly reduce yields of Λ hypernuclei within a given beam time. There were no shields against magnetic field for PMTs of Čerenkov detectors although PMTs of TOF detectors were shielded by μ-metal plates which were units of the detector frame. In addition, it is hard to shield magnetic field which is parallel to PMT axis efficiently, and huge amount of irons are needed. Therefore, bucking coils were implemented on PMTs of Čerenkov detectors to cancel magnetic field locally and actively. Details about test experiment, implementation and performance of the bucking coils were reported in Ref. [69][70].

Aerogel Čerenkov detectors (AC1,2,3)

Aerogel Čerenkov detectors (AC1, AC2, AC2) were used to distinguish π^+ from the other particles (p , K^+) in both on-line and off-line by using it as a veto. Fig. 3.15 shows a schematic drawing of the aerogel Čerenkov detectors. There are three layers which have 7 segments for each layer. One segment consists of structurally strengthened paper box, 40 pieces of hydrophobic silica aerogel tiles (SP-50 , Matsushita[*1] , the refraction index of 1.05) and two PMTs (XP4572B/D1, Photonis, photocathode of bialkali, dynode stages of 10, typical supply voltage of +2100 V, typical gain of 2.0×10^7), located on the top and bottom of the box without any windows.

Water Čerenkov Detectors (WC1,2)

Water Čerenkov detectors were used to distinguish p from the other particles (K^+,π^+) by choosing an optimal threshold of the number of photoelectrons.

Fig. 3.2.3 shows a schematic drawing of the water Čerenkov detectors. There were two layers with 12 segments for each layer. A detector segment consists of an acrylic box with its inside surface covered by a teflon sheet, and PMTs (H7195) on top and bottom of the box with UVT-glass windows. Deionized water (resistivity of 18 MΩ·cm, refraction index of 1.33) was used as the radiation medium.

Two types of boxes of water Čerenkov detectors were used in the experiment. The main differences between them were reflective materials and PMT choice. On the low momentum side (segment numbers from 1 to 6, BOX1), white acrylic as reflective material and H7195 PMTs were used. On the high momentum side where stricter particle identification is required (segment numbers from 7 to 12, BOX2) [71], teflon sheets as the reflective material and H7195UV PMTs which has UVT-glass window were used. H7195UV has higher efficiency to ultra violet light. In a cosmic ray tests, the average number of photoelectrons in BOX1 and BOX2 type segments were $\sim$50 and $\sim$100, respectively.

[*1] Currently produced by the Japan Fine Ceramics Center

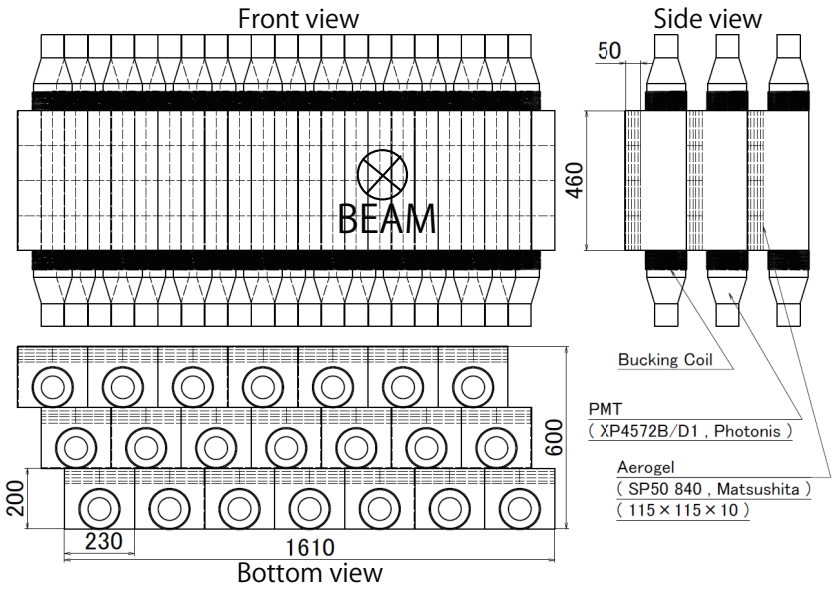

Figure 3.15: A schematic drawing of the aerogel Čerenkov detectors. There are three layers which have 7 segments for each segment.

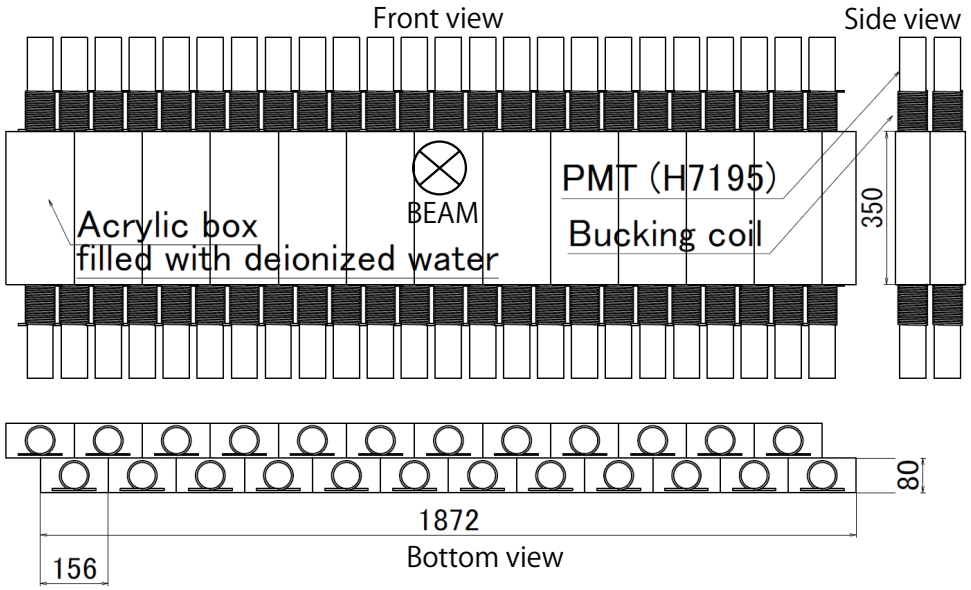

Figure 3.16: A schematic drawing of water Čerenkov detectors. There are two layers which have 12 segments for each layer.

3.3 Trigger systems

In the experiment, charged particle trigger ($CP_{trigger}$), HKS trigger ($HKS_{trigger}$), HES trigger ($HES_{trigger}$), coincidence trigger ($COIN_{trigger}$) and pedestal trigger ($PED_{trigger}$) were used (Fig. 3.17). Those trigger signals were controlled by Trigger Supervisor (TS) [72] which is a module to control multiple trigger input signals. Data with those triggers were pre-scaled by TS, and taken simultaneously as long as data acquisition (DAQ) efficiency had been kept high enough.

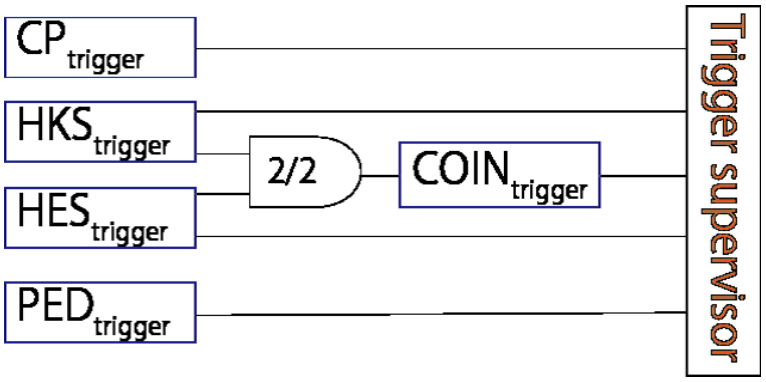

Figure 3.17: Main triggers used in the E05-115 experiment. Those trigger signals are controlled by Trigger Supervisor which is a module to control multiple trigger input signals.

$COIN_{trigger}$ is a main trigger for Λ hypernuclear data taking, which consists of the following logical condition:

$$COIN_{trigger} = HKS_{trigger} \otimes HES_{trigger} \ , \tag{3.2}$$

where $HKS_{trigger}$ and $HES_{trigger}$ will be explained in Sec. 3.3.2 and Sec. 3.3.3, respectively. $CP_{trigger}$ used for $HKS_{trigger}$ will be also described in Sec. 3.3.2. To take data of pedestals in ADC for run by run, first 1000 events were taken with a trigger generated by a clock generator ($PED_{trigger}$).

3.3.1 Tohoku Universal Logic module (TUL)

For electric circuits in the experiment, Tohoku Universal Logic module (TUL, TUL-8040) [76] which is a programmable logic module was developed and introduced to reduce NIM modules and cables. ALTERA[*2] APEX 20K series of Field Programmable Gate Array (FPGA) is mounted on the TUL. Major properties of the TUL is summarized in Table. 3.2.

3.3.2 HKS trigger

The HKS detectors are divided by 6 groups concerning HKS optics as shown in Fig. 3.18. Trigger was made for each group ($HKS^{i}_{trigger}$) and added logically (OR) to be the HKS trigger:

$$HKS_{trigger} = \sum_{i=1}^{6} HKS^{i}_{trigger}, \tag{3.3}$$

[*2] http://www.altera.com

Table 3.2: Major properties of the TUL.

FPGA	
Product	ALTERA APEX 20K (EP20K300E)
Maximum gate	72,800
Logic element	11,520
I/O	
Input	NIM: 16 ch
	ECL: 64 ch
	RotarySW: 4 bit
	DipSW: 16 bit
Output	NIM: 8 ch
	ECL: 32 ch
	LED: 4 bit
Internal clock	33 MHz

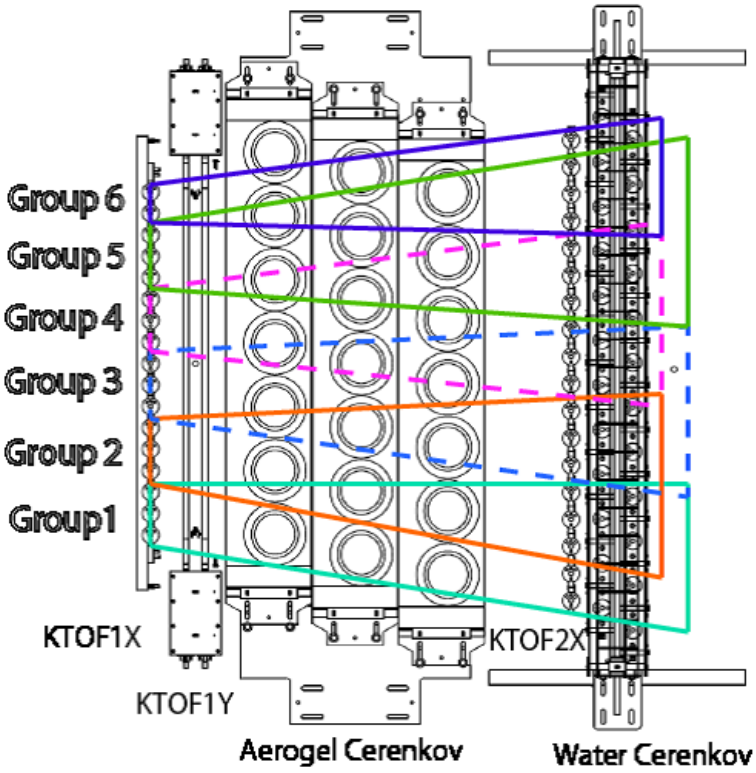

Figure 3.18: A schematic drawing of grouping in HKS.

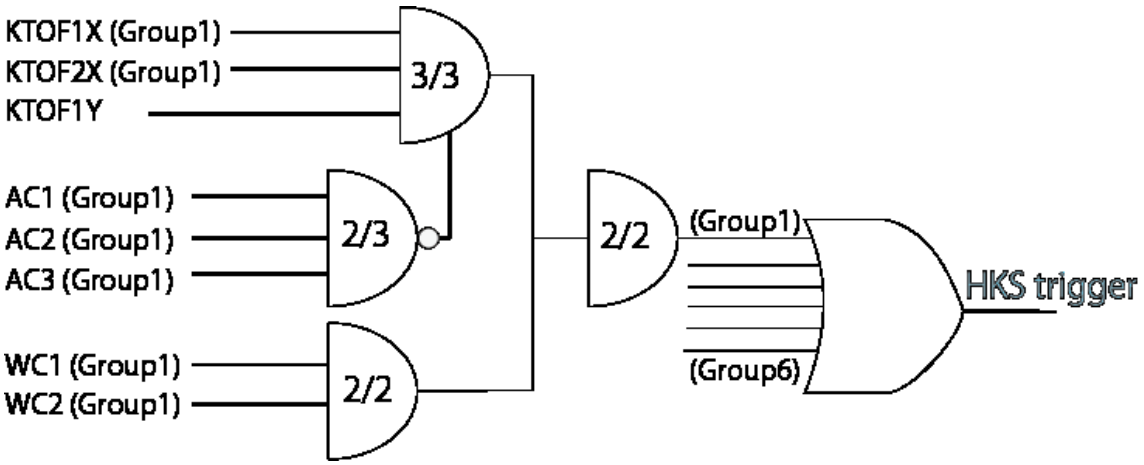

Figure 3.19: The HKS trigger logic.

where i is a group number (grouping trigger). The grouping trigger was adopted to suppress particles which are not on the HKS optics. The HKS trigger of i^{th} group consists of the following logical condition:

$$\mathrm{HKS}^{i}_{\mathrm{trigger}} = \mathrm{CP}^{i}_{\mathrm{trigger}} \otimes K^{i}_{\mathrm{trigger}} \tag{3.4}$$

where

$$\mathrm{CP}^{i}_{\mathrm{trigger}} = \mathrm{KTOF1X}^{i} \otimes \mathrm{KTOF1Y} \otimes \mathrm{KTOF2X}^{i}, \tag{3.5}$$

$$K^{i}_{\mathrm{trigger}} = \overline{\mathrm{AC}^{i}} \otimes \mathrm{WC}^{i}. \tag{3.6}$$

$\mathrm{CP}^{i}_{\mathrm{trigger}}$ ($\mathrm{CP}_{\mathrm{trigger}} \equiv \sum_{i=1}^{6} \mathrm{CP}^{i}_{\mathrm{trigger}}$) in Eq.(3.5) is a charged particle trigger which consists of the coincidence of three layers of TOF detectors ($\mathrm{KTOF1X}^{i}$, KTOF1Y and $\mathrm{KTOF2X}^{i}$). In Eq. (3.6), AC^{i} represents $(\mathrm{AC1} \otimes \mathrm{AC2})^{i} \oplus (\mathrm{AC2} \otimes \mathrm{AC3})^{i} \oplus (\mathrm{AC3} \otimes \mathrm{AC1})^{i}$, and WC^{i} represent $(\mathrm{WC1} \otimes \mathrm{WC2})^{i}$. The overline on AC^{i} means that the AC^{i} was used as veto to suppress π^{+}. The typical HKS trigger ($\mathrm{HKS}_{\mathrm{trigger}}$) rate was $\sim$2 kHz with a beam current of 2 μA on the polyethylene target (CH_2 , material thickness of 450 mg/cm^2).

3.3.3 HES trigger

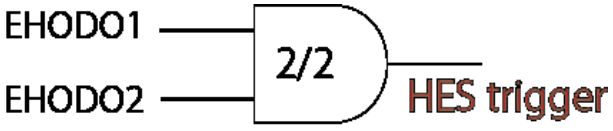

Figure 3.20: The HES trigger logic.

The HES trigger was made by the following logical condition:

$$\mathrm{HES}_{\mathrm{trigger}} = \mathrm{EHODO1} \otimes \mathrm{EHODO2}, \tag{3.7}$$

where

$$\text{EHODO1} = \sum_{j=1}^{29} \text{EHODO1}^j, \tag{3.8}$$

$$\text{EHODO2} = \sum_{j=1}^{29} \text{EHODO2}^j. \tag{3.9}$$

(j : segment number)

The typical HES trigger ($\text{HES}_{\text{trigger}}$) rate was ∼1200 kHz with a beam current of 2 μA on the polyethylene target (CH_2 , material thickness of 450 mg/cm^2).

3.3.4 Rate summary

Typical detector rates in HES and HKS are summarized in Table. 3.3 and Table.3.4, respectively. The trigger rates are summarized in Table. 3.5.

Table 3.3: Typical detector rates in HKS, which was obtained from TDC information in the off-line analysis.

Target	Target thickness	Beam current	Rate [MHz]				
	[mg/cm^2]	[μA]	KDC1	KDC2	KTOF1X	KTOF1Y	KTOF2X
CH_2	450.8	2.0	8.4	4.0	5.1	5.1	2.3
H_2O	500.0	2.8	29	15	32	32	11
^{7}Li	208.0	35	19	9.3	14	14	6.0
^{9}Be	188.1	40	23	11	19	19	7.9
^{10}B	56.1	40	8.2	3.9	4.9	4.9	2.3
^{12}C	87.5	10	5.7	2.7	3.6	3.5	1.7
		35	19	9.5	15	16	6.5
^{52}Cr	134.0	8.0	30	15	35	33	12

Table 3.4: Typical detector rates in HES, which was obtained from TDC information in the off-line analysis.

Target	Target thickness	Beam current	Rate [MHz]			
	[mg/cm^2]	[μA]	EDC1	EDC2	EHODO1	EHODO2
CH_2	450.8	2.0	3.0	3.4	2.8	2.9
H_2O	500.0	2.8	5.3	6.0	5.5	5.6
^{7}Li	208.0	35	9.4	11	9.8	9.7
^{9}Be	188.1	40	12	15	13	12
^{10}B	56.1	40	5.0	5.9	5.1	5.1
^{12}C	112.5	10	1.9	2.3	2.1	2.1
		35	12	13	13	13
^{52}Cr	134.0	8.0	6.7	7.8	7.3	7.3

Table 3.5: Typical trigger rates in the JLab E05-115 experiment.

Target	Target thickness	Beam current	Rate [kHz]			
	[mg/cm^2]	[μA]	$CP_{trigger}$	$HKS_{trigger}$	$HES_{trigger}$	$COIN_{trigger}$
CH_2	450.8	2.0	220	1.8	1200	0.10
H_2O	500.0	2.8	1100	20	1500	1.50
^{7}Li	208.0	35	540	7.3	2200	0.96
^{9}Be	188.1	40	710	1.0	2500	1.50
^{10}B	56.1	40	190	2.0	1600	0.17
^{12}C	112.5	10	160	1.3	1500	0.97
		35	630	7.9	2300	1.30
^{52}Cr	134.0	8.0	980	11	2500	1.80

3.3.5 Data acquisition

Data were taken and written on disks by the CEBAF On-line Data Acquisition (CODA) system which had been used at JLab since 1995 [73][74]. Main components of CODA are the readout controller (ROC), the event builder (EB) and the event recorder (ER). Additionally TS and the event transfer (ET) which is a replacement for older shared-memory data distribution system (DD) [75] were implemented. Data fragments are transferred from ROCs to EB by using standard network protocols. Then, the data fragments are sorted and built as complete events by the EB and submitted to ET in sequence. The ET sends the processed events to ER where they are buffered and written to disk or tape.

During the experiment, DAQ rate was controlled to be $\leq$2 kHz where its efficiency $\geq$90%.

3.3.6 Data summary

Data are summarized in Table. 3.6. Data set numbers defined in the table will be referred below here.

Table 3.6: Data summary of the E05-115 experiment.

Data set	Target	Thickness	Beam current [μA]		Total charge	Run time
		[mg/cm^2]	Nominal	Average	[C]	[hours]
1	CH_2	450.8	2.0	1.990	0.281	39.24
2	H_2O	500.0	2.5	2.681	0.204	21.13
3	^{7}Li	184.0	35	32.01	4.839	41.98
4	^{9}Be	188.1	40	38.28	5.332	38.69
5	^{10}B	56.10	40	38.71	6.253	44.88
6	^{12}C	112.5	10	8.07	0.142	4.9
7			20	19.41	1.076	15.4
8			35	32.90	4.659	39.3
9	^{52}Cr	134.0	7.5	7.66	0.825	29.9
10		154.0	7.5	7.61	5.525	201.4

Chapter 4

Analysis

In this section, data analyses to obtain a Λ binding energy and a formation cross section of Λ hypernucleus will be described.

4.1 Analysis overview

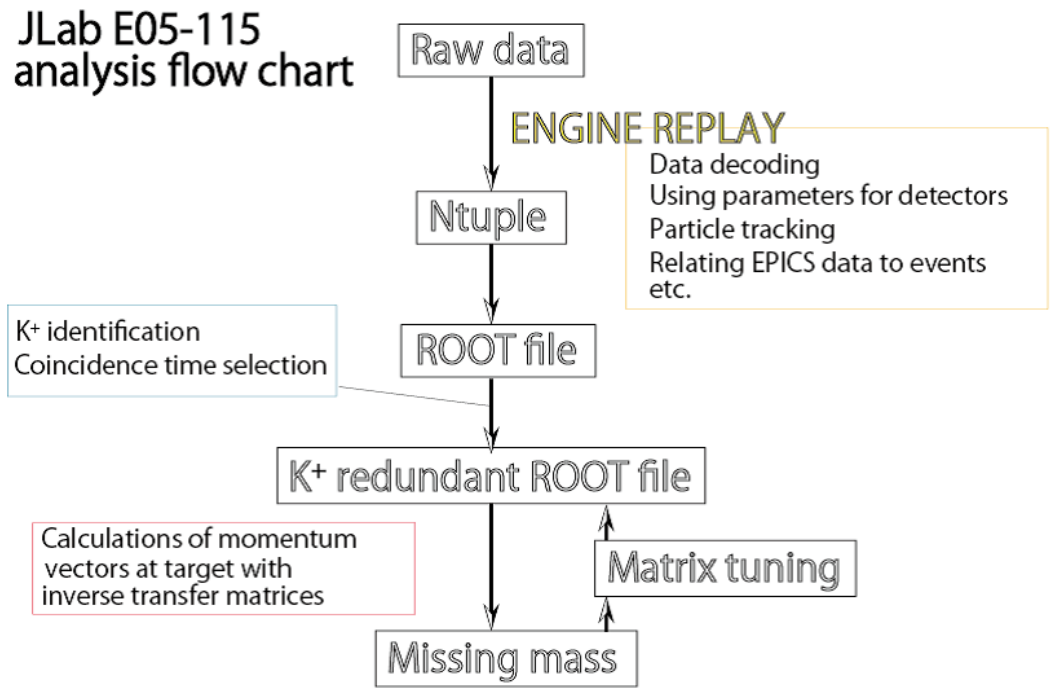

Figure 4.1: A flow chart of E05-115 data analysis.

An analysis flow chart of E05-115 is shown in Fig. 4.1. Firstly, raw data taken by CODA system (Sec. 3.3.5) were decoded and analyzed by "ENGINE REPLAY" which was a conventional analyzer in JLab Hall-C, written in FORTRAN. Major roles of ENGINE REPLAY are the following:

- Decoding row data of TDC and ADC,
- Particle tracking by using drift chambers and scintillation detectors,

- Associating hit detector information (Čerenkov detectors etc.) with extracted tracks,
- Converting TDC and ADC information into physical quantities such as times in the scintillation detectors and number of photo-electrons in the Čerenkov detectors,
- Relating data from EPICS[*1] such as beam current, target position, collimator position, raster information, magnetic fields of magnets and so on to the events. The EPICS information was read every two seconds.

The data were filled in files with FORTRAN format (Ntuple[*2]) in the process of ENGINE REPLAY. To analyze data with C++ base code in further processes, the Ntuple was converted to a ROOT file[*3]. Then, a K^+ identification (Sec. 4.3.2) and an $e'K^+$ coincidence time selection (Sec. 4.5) were applied to reduce the file size. The reduced ROOT files (K^+ redundant ROOT files) were then used for a missing mass reconstruction with the inverse transfer matrices (Sec. 4.7) which were optimized in a later process by using the Λ, Σ^0 and ${}^{12}_{\Lambda}$B ground state events (Sec. 4.8). Finally, Λ's binding energies and formation cross sections of Λ hypernuclei were obtained from missing mass spectra with the optimized inverse transfer matrices.

4.2 HES Analysis

In HES, particle tracking was performed by using two drift chambers (EDC1, EDC2). Then, positions and angles of particles at the HES reference plane were obtained. A typical tracking residual for a plane of the drift chamber is $\sigma \sim$250 μm. Position and angular resolutions at the reference plane are summarized in Table. 4.1.

Table 4.1: Typical position and angular resolution at the reference plane in HES (CH_2 target) [77].

δx [μm]	$\delta x'$ [mrad]	δy [μm]	$\delta y'$ [mrad]
97	0.8	120	1.5

After the tracking procedure, a time when a particle passed at the reference plane was calculated by using time (TDC) information of two layers of scintillation detectors (EHODO1, EHODO2) to derive a coincidence time (Sec. 4.5). Typical TOF resolution between EHODO1 and EHODO2 was $\sigma \sim$ 350 ps (Fig. 4.2) which was good enough to separate different bunches (2 ns separation) in a coincidence time.

Fig. 4.3 shows hit patterns of EHODO1 and EHODO2, and a hit segment correlation between them. Events in bins of half integer indicate that both neighbored segments have hits. The particle distribution is not flat as shown in the figure. Therefore, counting rate particularly for center part of the detectors needed to be carefully monitored and controlled by changing the collimator position, depending on targets.

Almost all particles in HES were considered to be electrons originating from Bremsstrahlung as shown in Sec. 2.3.6. A ratio of number of electrons associated with strangeness production to those of Bremsstralung was 10^{-3} to 10^{-4} in the HES acceptance according to the counting rate in real data (Table. 3.5), which is consistent with the calculation (Sec. 2.3.6). Fig. 4.4 shows normalized rates in HES as a function of target's proton number squared, Z^2, for a calculation

[*1] Experimental Physics and Industrial Control System
[*2] http://wwwsad.web.cern.ch/wwwasd/paw/reference_manual/NTUPLE.html
[*3] http://root.cern.ch/

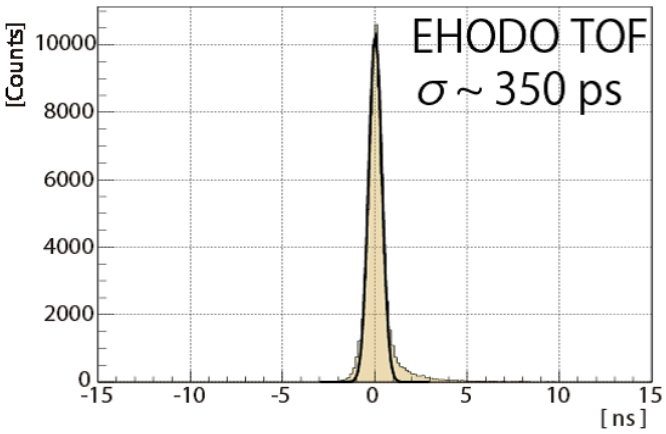

Figure 4.2: A TOF distribution measured with two layers of EHODO. The TOF resolution was $\sigma \sim 350$ ps.

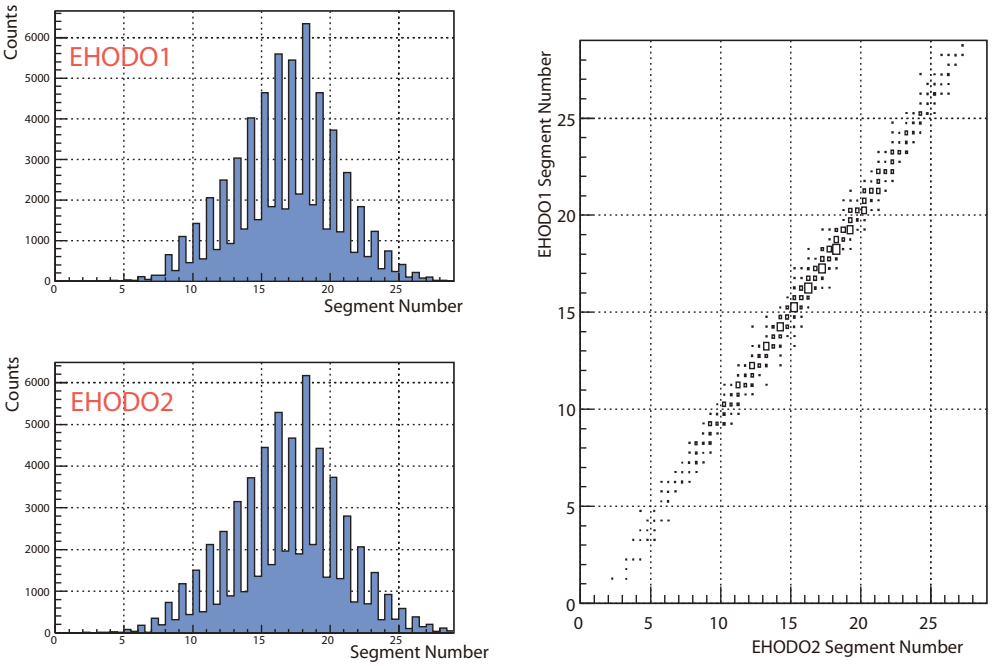

Figure 4.3: Hit patterns of EHODO1 and EHODO2, and hit segment correlation between them. Events in bins of half integer indicate that both neighbored segments have hits.

and a real data. The calculation was done by using Eq. (2.9) for each target, and normalized the rate of ^{12}C to be unity. The data point for each target was obtained by normalizing the counting rate by the target thickness and the beam current, and the normalized the rate of ^{12}C to be unity as well as the calculation. The target dependence of HES rate is consistent with the calculation.

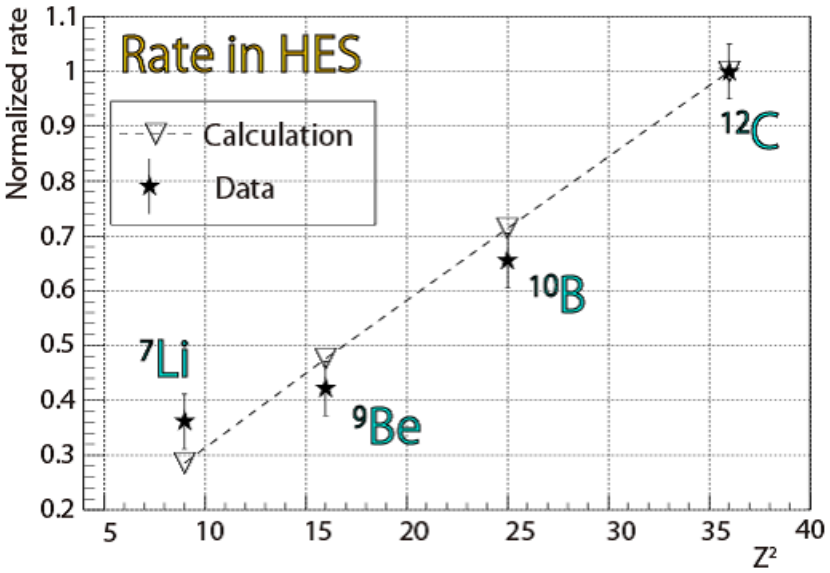

Figure 4.4: Normalized rates in HES as a function of target proton number squared, Z^2 for a calculation and a real data.

4.3 HKS Analysis

In HKS, a K^+ identification with aerogel and water Čerenkov detectors was done to suppress background particles of π^+ and p in addition to the particle tracking.

4.3.1 Particle tracking

Particle tracking was done by using two drift chambers (KDC1, KDC2). Then, positions and angles of particles at the HKS reference plane were obtained. A typical tracking residual for a plane of the drift chamber is σ ~150 μm. Position and angular resolutions at the reference plane are summarized in Table. 4.2.

Table 4.2: Typical position and angular resolution at the reference plane in HKS (CH_2 target) [77].

δx [μm]	$\delta x'$ [mrad]	δy [μm]	$\delta y'$ [mrad]
100	0.2	160	0.3

After the tracking procedure, a time when a particle passed at the reference plane was calculated by using time (TDC) information of the scintillation detectors (KTOF1X, KTOF2Y, KTOF2X) to derive a coincidence time.

4.3.2 K^+ identification

Table 4.3: Sensitivity for each particles in water (n=1.33) and aerogel (n=1.05) Čerenkov detectors. See also Fig. 3.13 and Fig. 3.14.

	π^+	K^+	proton
Water Čerenkov	◯	◯	△
Aerogel Čerenkov	◯	×	×

Both on-line and off-line K^+ identifications (KID) were essential for the experiment since huge amount of background particles contaminate in HKS. Main background particles are protons, π^+s, electrons and positrons. Counting rates of those particles in HKS were obtained in off-line analyses and summarized in Table. 4.4 [69]. Proton and π^+ rejections with Čerenkov and mass squared information are described in this section. Electron and positron background events in HKS will be explained in Sec.4.4.

Table 4.4: Counting rates of K^+, π^+, p and e^-, e^+ in HKS, obtained in off-line analyses [69]. The errors are statistical and systematic errors which originate from the fitting procedures.

Target	Thickness	Beam	Rate			
	[mg/cm^2]	[μA]	K^+ [Hz]	π^+ [kHz]	p [kHz]	e^-,e^+ [kHz]
CH_2	450.8	2.0	73.2±0.1±3.4	6.3±0.1±0.03	6.6±0.1±0.03	14.7±0.1±0.1
^{7}Li	208.0	31.6	299±1±13	25.0±0.4±0.2	34.1±0.4±0.2	24.7±0.4±0.1
^{9}Be	188.0	37.9	248±1±12	21.4±1.0±0.1	29.1±1.1±0.2	27.3±1.1±0.2
^{10}B	56.1	38.2	135±0.1±6	11.1±0.1±0.6	14.1±0.1±0.1	13.8±0.1±0.1
^{12}C	87.5	19.3	110±0.4±5	9.0±0.2±0.4	10.9±0.2±0.1	14.3±0.2±0.1
		37.9	171±1±8	15.1±1.1±0.1	18.4±1.3±0.1	27.9±1.6±0.1
^{52}Cr	134.0	7.3	34.5±0.8±3.7	4.2±0.5±0.3	3.1±0.4±0.2	24.0±1.1±1.9

In on-line (at hardware trigger level), KID was done with the water (refractive index of 1.33) and aerogel (refractive index of 1.05) Čerenkov detectors (see Sec. 3.2.3). Table. 4.3 summarizes sensitivities of water and aerogel Čerenkov detectors for π^+, K^+ and proton in the HKS momentum acceptance (see also Fig. 3.13 and Fig. 3.14). The water Čerenkov detector was sensitive to all of three particles. However, proton could be separated from π^+ and K^+, and suppressed by setting a threshold of the adequate number of photoelectrons. The aerogel Čerenkov detector was sensitive just only for π^+. Therefore, π^+ was rejected by using the aerogel Čerenkov detector as a veto. Avoiding over-cut of K^+, discriminator thresholds for water and aerogel Čerenkov detectors were not set to be strict. Consequently, some portion of π^+s and protons remained in data, and were rejected in off-line analysis.

In off-line, KID was done with tighter selection with Čerenkov and mass squared (m^2) information which is calculated by the following equation:

$$m^2 = p^2\Big(\frac{1}{\beta^2} - 1\Big) \tag{4.1}$$

where β and p are velocity factor obtained by TOF measurement and momentum which was reconstructed by the inverse transfer matrix (see Sec. 4.7).

Top figure of Fig. 4.5 shows correlation between mass square and number of photoelectrons of aerogel (sum of 3 layers) and bottom one is x-projection of the top figure. π^+s can be separated by aerogel Čerenkov detectors as you can see in the figure. In the same way, top of Fig. 4.6

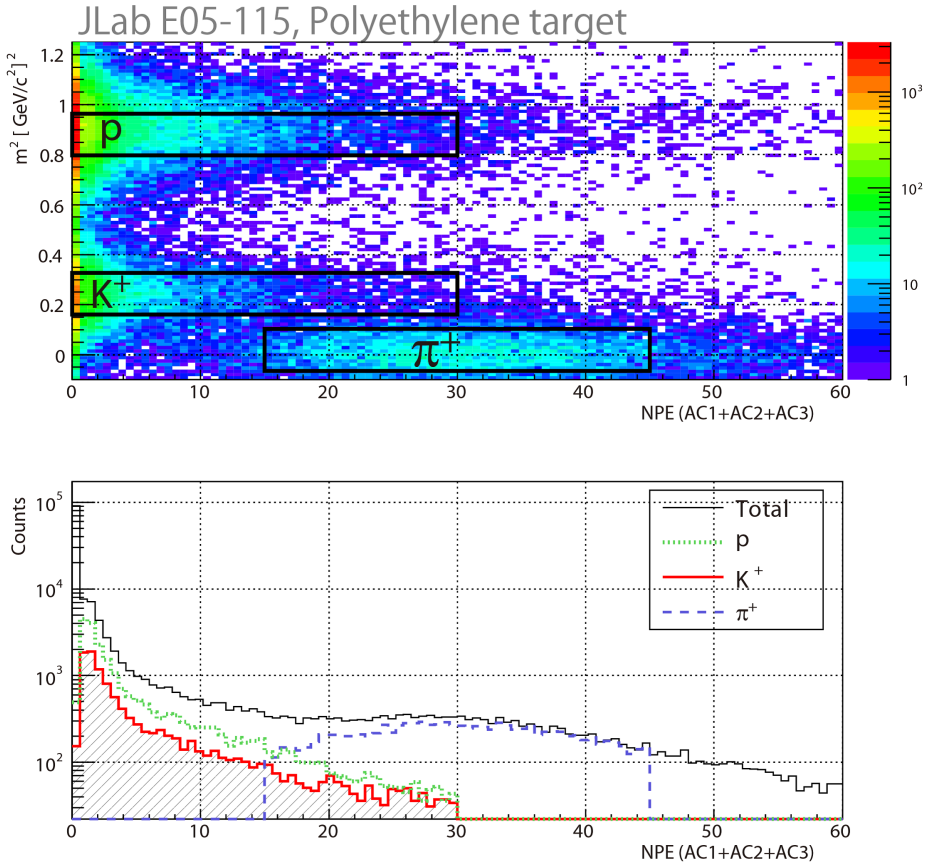

Figure 4.5: (Top) mass squared vs. summed number of photoelectrons of the three layers of aerogel Čerenkov detectors, (bottom) x-projection of the top figure.

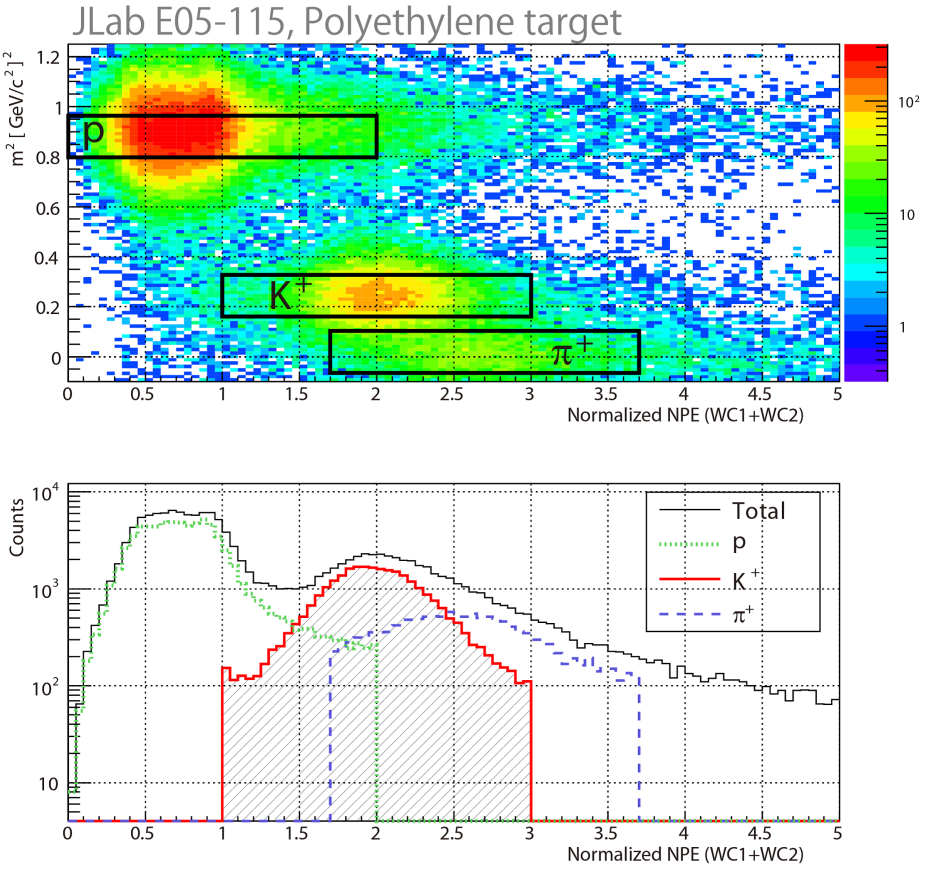

Figure 4.6: (Top) mass squared vs. summed normalized number of photoelectrons of the two layers of water Čerenkov detectors, (bottom) x-projection of the top figure.

shows correlation between mass squared and normalized number of photoelectrons in the water Čerenkov detector and the bottom one is x-projection of the top figure. Since two different types of boxes were used for the water Čerenkov detector (See Sec.3.2.3), particle separation powers are different between these two. Therefore, normalized number of photoelectrons was introduced to adjust K^+ peak to be unity.

It is noted that long tail can be seen in both Fig.4.5 (aerogel) and Fig.4.6 (water) especially in p cluster. This is considered to be caused by scintillation light generated in the box materials and the reflection materials (teflon) inside the boxes.

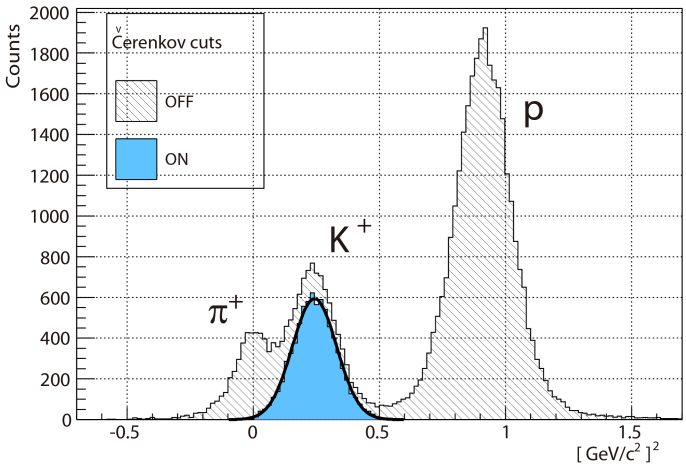

Figure 4.7: Mass squared distribution with and without Čerenkov cuts on the number of photoelectrons.

4.4 e^-, e^+ background

In HKS, particles which were not on the HKS optics were included in data. The background events were already recognized during the experiment. However, it seemed to be difficult to shield them physically since they passed through inside an vacuum extension according to on-line analysis. Additionally, shields potentially generate more backgrounds. Hence, data taking were done with those background particles which could be rejected in off-line analysis. In this section, the background source and its effects on the data quality are described.

4.4.1 Background source

Distribution of x vs. x' ($\equiv \frac{p_x}{p_z}$) in the real data is shown in Fig. 4.8. There are two clusters in the figure. Events in a black box are particles which were on the HKS optics. On the other hand, events in a red box were particles which were not on the HKS optics. Fig. 4.9 shows the visualized particle tracks in the HKS detectors from its top and side view. The visualized tracks indicated a location of the background source. It indicates the background particles had come into the HKS detector package from a region of NMR port and side of vacuum extension which were made of stainless steel (SUS304).

A background contamination rate ($R_{\rm BG}$) is defined as the following equation:

$$R_{\rm BG} = \frac{N_{\rm B}}{N_{\rm A} + N_{\rm B}} \tag{4.2}$$

where N_A and N_B are the numbers of events being on the HKS optics and that being not on the HKS optics. R_{BG} for each target is summarized in Table. 4.5. R_{BG} is 11% for the small proton number target, ^{7}Li. On the other hand, R_{BG} is 58% for the large proton number target, ^{52}Cr.

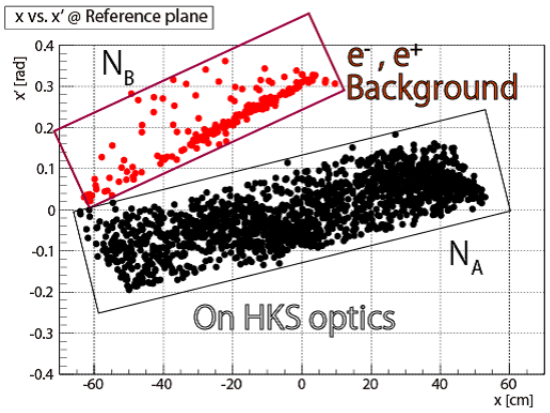

Figure 4.8: Distribution of x vs. x′ at the HKS reference plane (real data). Boxes indicate e,e$^+$ background events (red) and events which were on the HKS optics (black). See also Fig. 4.9.

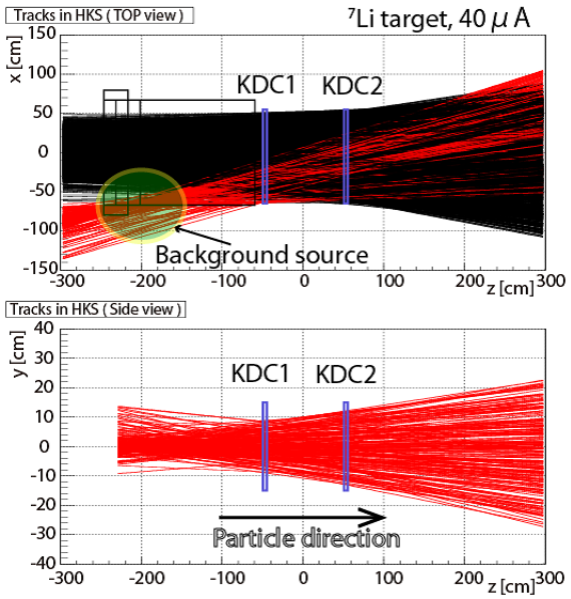

Figure 4.9: Top and side views of tracks in HKS (real data). Tracks indicated by black and red color are particles which are on the HKS optics and those which are not on the HKS optics, respectively.

Table 4.5: The e and e^+ background contamination rate (R_{BG}) in the HKS drift chamber for each target. More than half events are e and e^+ background particles for ^{52}Cr target.

Target	Thickness [mg/cm^2]	Length in radiation length	R_{BG} [%]
CH_2	450.8	1.0×10^{-2}	20
H_2O	500.0	1.4×10^{-2}	44
^{7}Li	208.0	2.5×10^{-3}	11
^{9}Be	188.1	2.9×10^{-3}	14
^{10}B	56.1	1.4×10^{-3}	10
^{12}C	87.5	2.0×10^{-3}	19
^{52}Cr	134.0	8.8×10^{-3}	58

Fig. 4.10 shows a normalized background counting rate in the HKS drift chamber (KDC1) as a function of target proton number, Z. The points could be fitted by the second order polynomial functions. The background particles are considered to originate from electro-magnetic processes since the background rate is in proportion as Z^2.

A Monte Carlo simulation was done to confirm the origin of the background, and it turns out that the background origin could be positrons generated in target. In the simulation, positrons with lower momentum (p_K = 0.86-1.00 GeV/c) and more forward scattering angle (θ_K = 0-2 mrad) relative to the HKS acceptance were generated, and visualized tracks are shown

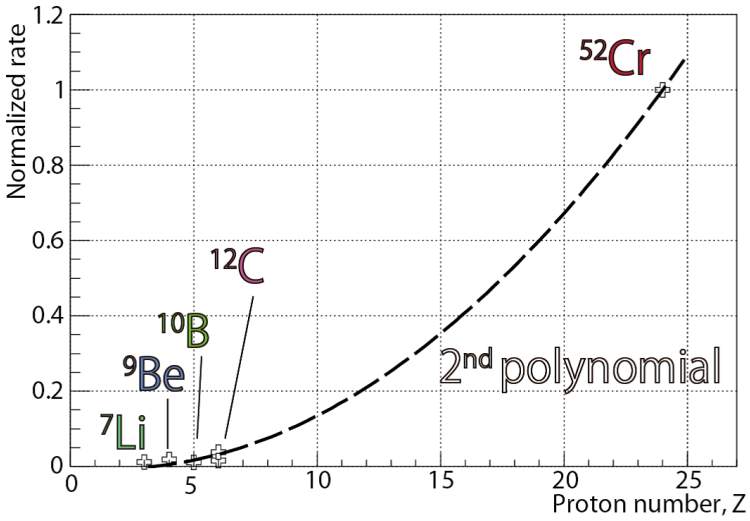

Figure 4.10: Normalized e, e^+ background counting rate as a function of target proton number, Z. The data was fitted by a 2^{nd} order polynomial function.

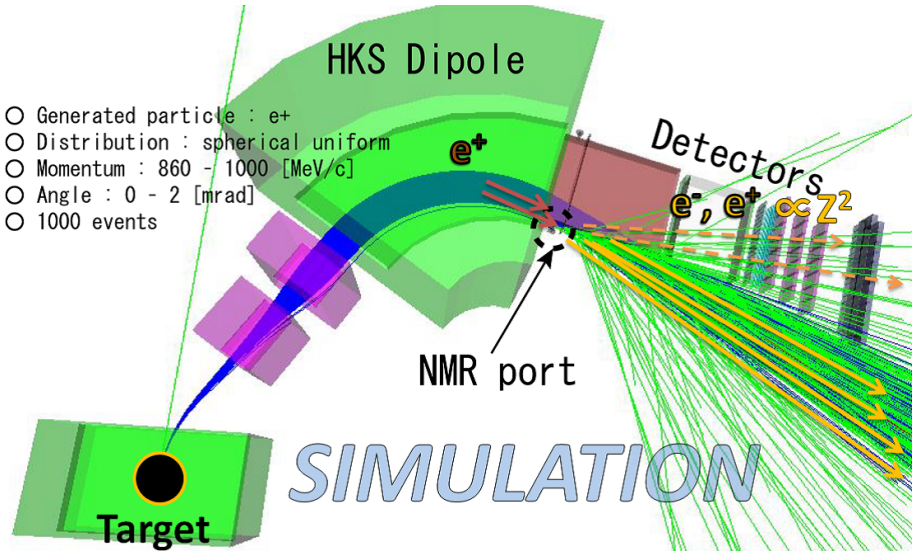

Figure 4.11: Visualized particle tracks in a Monte Carlo simulation for HKS. Positrons with lower momentum (p_K = 0.86-1.00 GeV/c) and more forward scattering angle (θ_K = 0-2 mrad) relative to the HKS acceptance were generated at the target position.

in Fig. 4.11. Those generated positrons hit the NMR port and/or side of vacuum extension made of stainless steel (SUS304), then secondary particles such as positrons and electrons were generated by pair-production process. Small portion of the secondary particles got into HKS detector package although almost all of the secondary particles go toward outside of HKS. However, rate of the small portion of secondary particles detected in HKS was no longer low since high intensity electron beam (10^{13}-10^{14} Hz) was used for the experiment. In fact, those background particles caused a high rate and a high multiplicity for the HKS detectors. Data quality particularly for ^{52}Cr target was affected by the backgrounds as described in the next section.

4.4.2 Effects

The background contamination cased high rate and high multiplicity particularly for larger Z targets. The detector multiplicities were proportional to the counting rates. Fig. 4.12 and Fig. 4.13 show multiplicities of a scintillation detector (KTOF1X) and a layer of a drift chamber (KDC1) for the polyethylene and ^{52}Cr targets, respectively. The multiplicities of KTOF1X and KDC1 for the ^{52}Cr target were higher (KTOF1X:∼6, KDC1:∼4) than those for the polyethylene target (KTOF1X:∼3, KDC1:∼2).

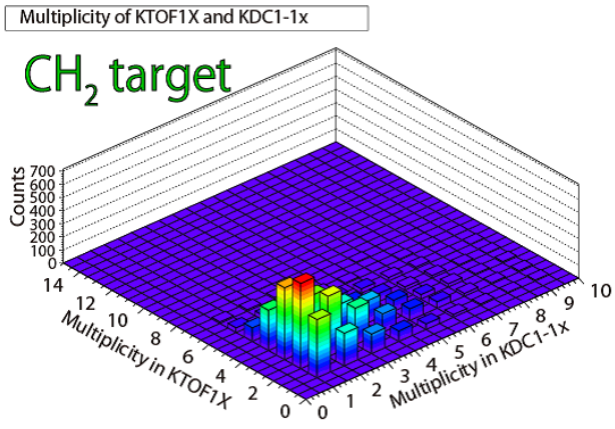

Figure 4.12: Multiplicities in KTOF1X and a layer of KDC1 for the polyethylene target.

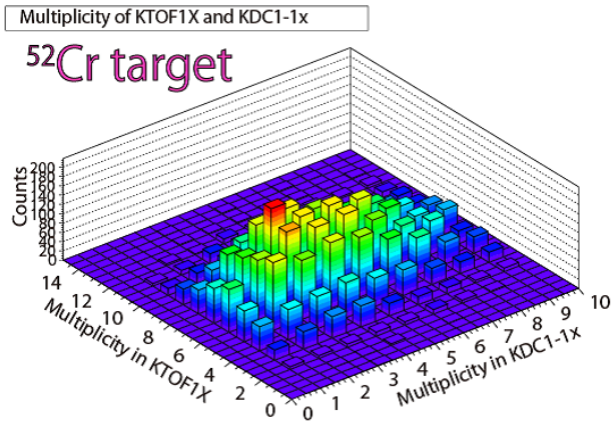

Figure 4.13: Multiplicities in KTOF1X and a layer of KDC1 for the ^{52}Cr target.

The high multiplicity deteriorate detector performance and particle tracking quality. Fig. 4.14 shows an event display of hit wires of KDC1,2 and an extracted track for the polyethylene target. Extracting particle tracks were relatively easier as the multiplicities in KDC1,2 were low for the polyethylene target. In the case of ^{52}Cr target, however, particle tracking was not easy since the multiplicities in KDC1,2 were high as shown in Fig. 4.15.

This tracking difficulty affect a quality of position determination which is directly effect on a missing mass resolution. Tracking residuals in a typical layer of KDC1 are shown in Fig. 4.16 for the polyethylene and ^{52}Cr targets. The tracking residual for the ^{52}Cr target was σ ∼300 μm although that for the polyethylene target was σ ∼150 μm. Furthermore, the distribution has a long tail. Fig. 4.17 shows a typical plane efficiencies of KDC1 as a function of counting rate in KDC1. The efficiencies get lower as the rates become higher.

As described above, the e and e^+ backgrounds which were not on the HKS optics caused not only deterioration of tracking quality but also particle detection efficiencies particularly for higher Z, ^{52}Cr target.

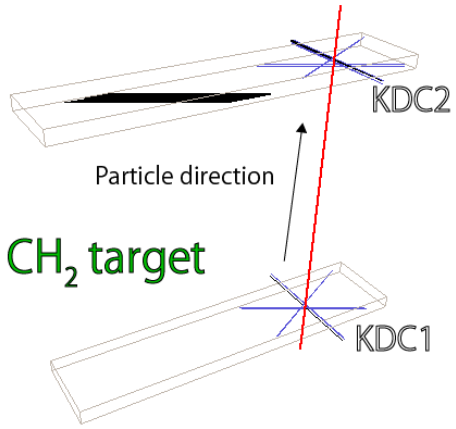

Figure 4.14: An event display of KDC1 and KDC2 for a typical event of data of the polyethylene target. Hit wires in KDC1 and KDC2 and an extracted track are shown.

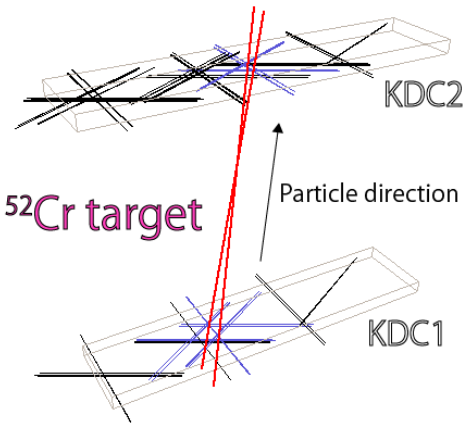

Figure 4.15: An event display of KDC1 and KDC2 for a typical event of data of ^{52}Cr target. Hit wires in KDC1 and KDC2 and an extracted track are shown.

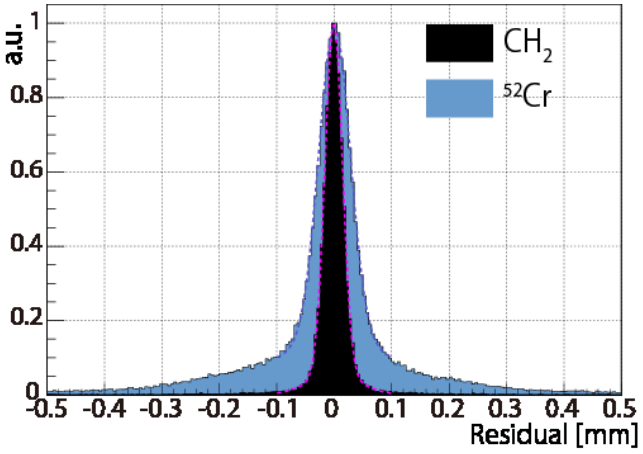

Figure 4.16: Tracking residuals for the polyethylene and ^{52}Cr target data. The residual for the ^{52}Cr target was σ ~300 μm although that for the polyethylene target was σ ~150 μm.

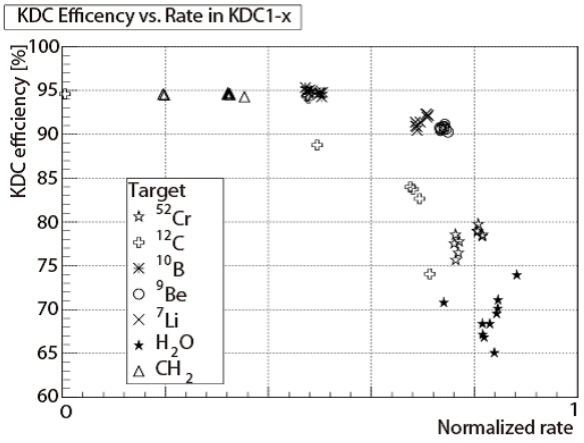

Figure 4.17: A plane efficiency of KDC1 as a function of normalized counting rate. The efficiency get lower as the rate is higher.

4.5 Coincidence between HES and HKS

To select coincident events between K^+s and electrons which were associated with the strangeness production, coincidence times were used. The coincidence time ($\mathrm{T_{COIN}}$) was defined as the following:

$$\mathrm{T_{COIN}} = \mathrm{T_{HKS}} - \mathrm{T_{HES}} \tag{4.3}$$

where $\mathrm{T_{HKS}}$ and $\mathrm{T_{HES}}$ are times of particles at the target, which were measured in HKS and HES, respectively. $\mathrm{T_{HKS}}$ and $\mathrm{T_{HES}}$ were calculated by the following:

$$\mathrm{T_{HKS,HES}} = \mathrm{T^{RD}_{HKS,HES}} - \frac{L^{\mathrm{recon}}_{\mathrm{HKS,HES}}}{(\beta^{\mathrm{recon}}_{\mathrm{HKS,HES}} c)} \tag{4.4}$$

where $\mathrm{T^{RD}_{HKS,HES}}$, $L^{\mathrm{recon}}_{\mathrm{HKS,HES}}$ and $(\beta^{\mathrm{recon}}_{\mathrm{HKS,HES}} c)$ are times at reference detectors, path lengths from the reference detectors to the target, and velocities of particles measured in HKS and HES, respectively. The path length, $L^{\mathrm{recon}}_{\mathrm{HKS,HES}}$ were reconstructed with inverse transfer matrices as described in Sec.4.7. $\beta^{\mathrm{recon}}_{\mathrm{HKS,HES}}$ were calculated by the following equation:

$$\begin{aligned} \beta^{\mathrm{recon}}_{\mathrm{HKS,HES}} &= \frac{p}{E} && (4.5) \\ &= \frac{p}{\sqrt{p^2 + m^2_{K^+}}}\,, && (4.6) \end{aligned}$$

where m_{K^+} is mass of K^+ taken from Ref. [68] and p is a particle momentum reconstructed with inverse transfer matrices (Sec.4.7).

Fig. 4.18 shows a correlation between coincidence time and mass squared. In the figure, clusters of $e'\pi^+$, $e'K^+$ and $e'p$ coincidences are clearly observed. Fig. 4.19 shows the coincidence time distribution after the K^+ selection was done with the Čerenkov and mass squared information. The peaks with 2 ns time separation correspond to the CEBAF beam structure as described in Sec. 2.2. A true $e'K^+$ coincidence peak sits on the zero with a resolution of $\sigma \sim 270$ ps, and others originate from accidental coincidence. In the analysis, events of $|\mathrm{T_{COIN}}|<1.0$ ns were chosen as true $e'K^+$ coincident events.

4.6 Missing Mass

Momenta of a K^+ and a scattered electron at the reference planes were measured with the spectrometers. This information was converted to momentum vectors at the target by using inverse transfer matrices of HES and HKS spectrometers. Then, a missing mass (M_{HYP}) was calculated by using the following equation:

$$\begin{aligned} M_{\mathrm{HYP}} &= \left[E^2_{\mathrm{HYP}} - \vec{p}^{\,2}_{\mathrm{HYP}}\right]^{\frac{1}{2}} && (4.7) \\ &= \left[(E_e + M_{\mathrm{target}} - E_K - E_{e'})^2 - (\vec{p}_e - \vec{p}_K - \vec{p}_{e'})^2\right]^{\frac{1}{2}} && (4.8) \\ &= \Big[(E_e + M_{\mathrm{target}} - E_K - E_{e'})^2 - (p_e^2 + p_K^2 + p_{e'}^2 \\ &\qquad -2p_e p_K \cos\theta_{eK} - 2p_e p_{e'} \cos\theta_{ee'} + 2p_{e'} p_K \cos\theta_{e'K})\Big]^{\frac{1}{2}} && (4.9) \end{aligned}$$

where E, $\vec{p}$ and M_{target} are the energy and momentum vectors of each particle, and the mass of the target nucleus. θ_{eK^+}, $\theta_{ee'}$ and $\theta_{e'K^+}$ are the angles of the particles. The beam momentum

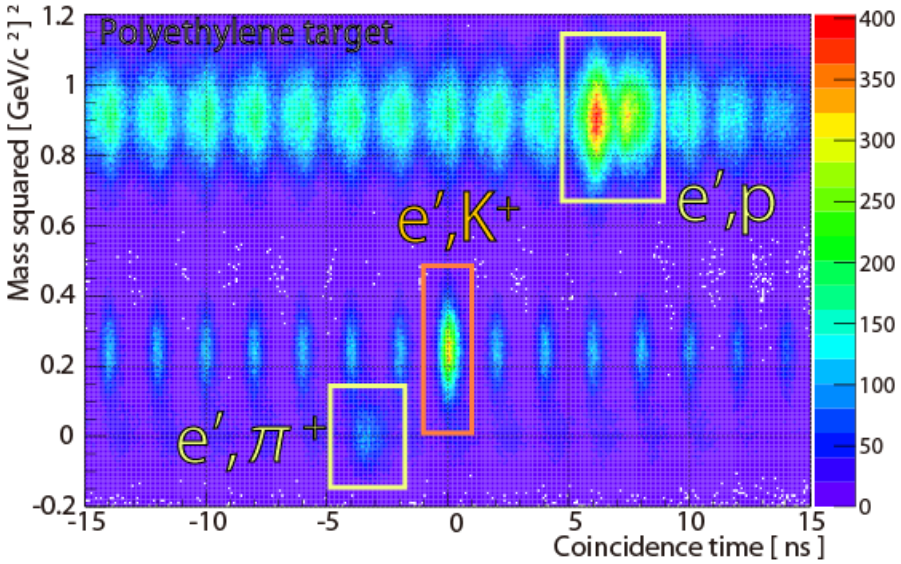

Figure 4.18: Coincidence time vs. mass squared distribution from a typical polyethylene data. Clusters of $e'\pi^+$, $e'K^+$ and $e'p$ coincidences are seen.

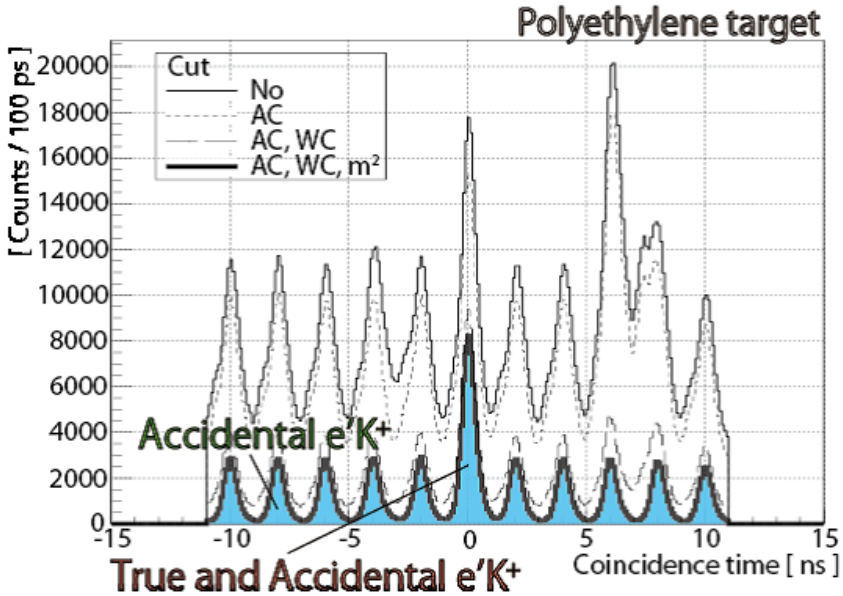

Figure 4.19: The coincidence time distributions with different cut conditions. Cut conditions of water Čerenkov, aerogel Čerenkov and mass squared were applied for this plot. The coincidence time resolution was σ ∼270 ps.

vector ($\vec{p}_e$) were precisely determined and measured in the accelerator (Table. 2.1). The beam energy, $E_e = \sqrt{m_e^2 + \vec{p}_e^{\,2}}$ was derived with $\vec{p}_e$ since m_e is well. Therefore, only momentum vectors of a K^+ ($\vec{p}_{K^+}$) and a scattered electron ($\vec{p}_{e'}$) were necessary to deduce a missing mass in the experiment.

Initial transfer matrices of the spectrometers were derived by a full modeled Monte Carlo simulation with Geant4. In the simulation, magnetic field maps of spectrometers were necessary. The magnetic field maps of spectrometers were calculated with Opera3D (TOSCA) which is a magnetic field calculation software using three dimensional finite element method. However, the initial transfer matrices were not perfect due to arithmetic limitation of TOSCA and geometrical imperfections of the models implemented in the TOSCA calculation and Geant4 simulation. Thus, the initial transfer matrices needed to be optimized as will be explained in Sec.4.8.

4.6.1 Energy loss correction

Momenta of a scattered electron and a K^+ are measured in the spectrometers after their energy are lost in the target. On the other hand, an incident beam lost its energy in the target before the reaction occurs. Therefore, the following corrections were applied for the missing mass calculation:

$$E_{e'} = E_{e'} + \delta E_{e'}, \tag{4.10}$$
$$E_{K^+} = E_K + \delta E_K, \tag{4.11}$$
$$E_e = E_e - \delta E_e \tag{4.12}$$

where $\delta E_{e'}$, δE_K and δE_e are energy loss correction values. These correction values were estimated by a Monte Carlo simulation with Geant4.

Fig. 4.20 shows an energy loss distribution of scattered electrons in the simulation. In this simulation, particles were generated at the center of target, and particles accepted in HES were stored in data. The energies of e, e' and K^+ are straggle in the target as shown in Fig. 4.20 when the particle generation points were fixed at the center of tilted target (Sec.2.3.3). In reality, however, strangeness production points were uncertain along the incident beam axis in the target. Fig. 4.21 shows simulated energy loss distributions when the generation points were randomly moved along the incident beam axis in the tilted target (Sec.2.3.3). These energy loss distributions of e, e' and K^+ such as Fig. 4.21 affect a shape and a width of missing mass. In fact, the distribution of energy loss are main origins of an asymmetric shape and a long tail of a reconstructed missing mass. Energy loss correction values were determined in the simulation with fixed particle generation at the center of tilted target. A most probable value of each particle obtained by fitting to the distribution with a Landau function was chosen to be the energy loss correction value (Fig. 4.20). The obtained correction values are summarized in the Table. 4.6. The fitting errors were less than a few keV for all targets. It is noted that the energy losses of incident electrons and K^+s (scattered electrons) have negative correlations as shown in Fig. 4.22. On the other hand, the energy losses of scattered electrons and K^+s have positive correlations as shown in Fig. 4.23.

Fig. 4.24 shows a simulation result of missing mass distribution after the energy loss correction was applied. The simulation was done with a 87.5 mg/cm^2 ^{12}C target assuming $^{12}_{\Lambda}$B with its binding energy of 11.37 MeV. The horizontal axis of the figure is $M_{\rm HYP} - M_{\rm core} - M_\Lambda + 11.37$ MeV

[*4] The thickness of the ^{7}Li target with respect to the incident beam was calculated to be 295 mg/cm^2 according to the actual measurement of the weight, area and thickness of the target just before mounting the target on the target holder. Originally, the thickness of the prepared ^{7}Li target was 208 mg/cm^2. The target is considered to be nitrided from the surface (Li_3N) during storing. Therefore, the cross section was calculated with 208 mg/cm^2 ^{7}Li, and the energy loss correction values were evaluated with 295 mg/cm^2 ^{7}Li (Li_3N).

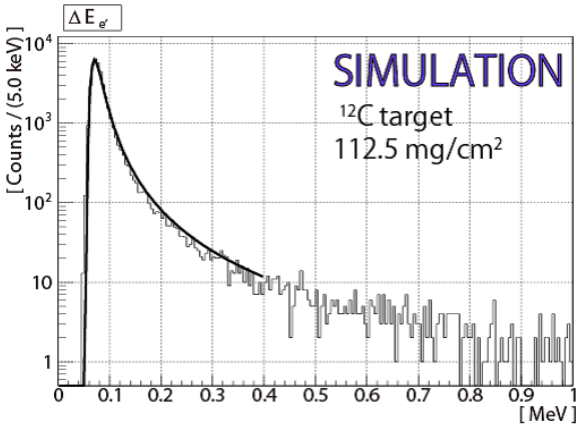

Figure 4.20: A typical energy loss distribution of scattered electrons in the simulation. The particles were generated at the center of tilted target, and stored in data when they were accepted in the spectrometer.

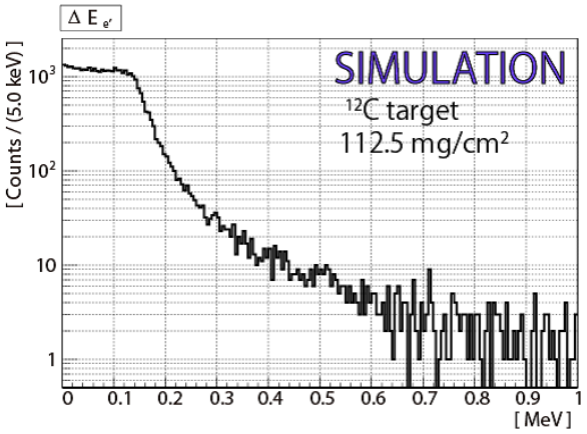

Figure 4.21: A typical energy loss distribution of scattered electrons in the simulation. The particles were generated along the incident beam axis in the tilted target, and stored in data when they were accepted in the spectrometer.

Table 4.6: Energy loss correction values obtained by a Monte Carlo simulation.

Target	Thickness [mg/cm^2]	δE_e [keV]	$\delta E_{e'}$ [keV]	δE_K [keV]
CH_2	450	374	374	465
^{7}Li	208	127	127	158
	295[*4]	184	184	228
Li_3N	295	188	188	236
^{9}Be	188	111	111	140
^{10}B	56	34	34	43
^{12}C	87	55	55	68
^{52}Cr	134	74	74	86
	154	86	86	99

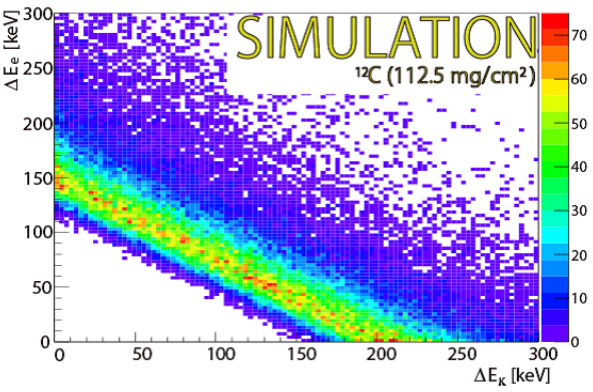

Figure 4.22: An energy loss correlation between incident electrons and K^+s.

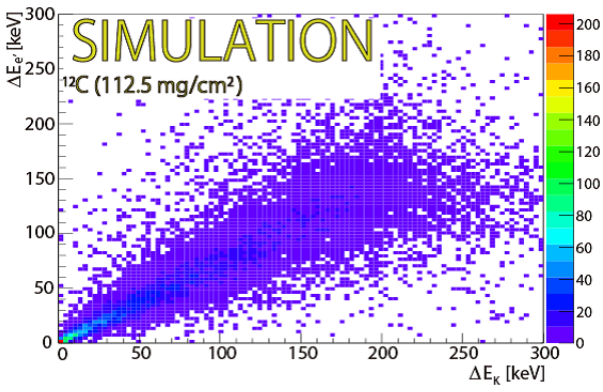

Figure 4.23: An energy loss correlation between scattered electrons and K^+s.

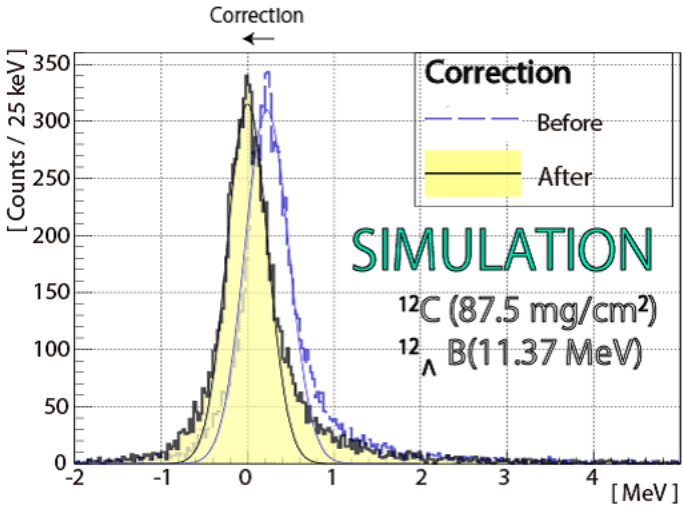

Figure 4.24: A simulation result of missing mass distribution before and after the energy loss corrections. The simulation was done with a 87.5 mg/cm^2 ^{12}C target assuming $^{12}_{\Lambda}$B with its binding energy of 11.37 MeV.

where $M_{\rm core}$ and M_{Λ} are masses of a core nucleus (^{11}B in this case) and a Λ. Thus, the peak should be located at 0 if the energy loss corrections work. Fitting results by a single Gaussian function with the range from -400 keV to $+400$ keV showed that the mean value of the Gaussian function was within a 30 keV, which means the energy loss corrections described here work well.

4.6.2 Achievable mass resolution

A missing mass resolution is mainly affected by the following sources:

1. Intrinsic mass resolution.
2. Production point displacement from an assumed origin of the matrices.
3. Mass offset due to the energy loss in target.

In this section, contributions of those sources to the missing resolution will be explained.

Intrinsic mass resolution

An intrinsic mass resolution is determined not only by momentum and angular resolutions of magnetic spectrometers, but also the beam quality such as beam energy spread and emittance. The beam quality was guaranteed by CEBAF as described Sec. 2.2. In the estimation of intrinsic mass resolution, typical beam energy spread value of $\Delta E/E = 3.0 \times 10^{-5}$ was used. In addition, the beam angle and size (emittance) were assumed to be zero in the simulation since the emittance of CEBAF is negligible small (~ 2.0 μm·mrad, Table. 2.1). Momentum and angular resolutions of spectrometers were evaluated with a Monte Carlo simulation (Table. 4.7) by using the position and angular resolutions at the reference planes shown in Sec. 4.2 and Sec. 4.3.1.

The derivative of $M^2_{\rm HYP}$ is

$$\frac{dM^2_{\rm HYP}}{dM_{\rm HYP}} = 2M_{\rm HYP}. \tag{4.13}$$

Table 4.7: Momentum and angular resolutions of spectrometers obtained in a simulation by using the realistic position and angular resolutions at the reference planes.

$\Delta p/p$	e'	4.2×10^{-4}
	K^+	2.0×10^{-4}
$\Delta\theta$ [mrad] (RMS)	e'	4.0
	K^+	0.4

Table 4.8: Contribution of each term of a missing mass formula (Eq. (4.8)) to the intrinsic mass resolutions for our experimental setup. Momentum and angular resolutions at the reference planes, which were used for these estimations are summarized in Table. 4.7.

Terms		Mass resolution [keV/c^2] (FWHM)					
		Λ	${}^{7}_{\Lambda}$He	${}^{9}_{\Lambda}$Li	${}^{10}_{\Lambda}$Be	${}^{12}_{\Lambda}$B	${}^{52}_{\Lambda}$V
Beam	$\frac{1}{2M_{\rm HYP}}\left(\frac{\partial E^2_{\rm HYP}}{\partial p_e}\right)\Delta p_e$	70	70	70	70	70	70
	$\frac{1}{2M_{\rm HYP}}\left(\frac{\partial p^2_{\rm HYP}}{\partial p_e}\right)\Delta p_e$	20	3	2	2	2	0.4
K^+ momentum	$\frac{1}{2M_{\rm HYP}}\left(\frac{\partial E^2_{\rm HYP}}{\partial p_K}\right)\Delta p_K$	220	220	220	220	220	220
	$\frac{1}{2M_{\rm HYP}}\left(\frac{\partial p^2_{\rm HYP}}{\partial p_K}\right)\Delta p_K$	70	10	8	7	6	1
e' momentum	$\frac{1}{2M_{\rm HYP}}\left(\frac{\partial E^2_{\rm HYP}}{\partial p_{e'}}\right)\Delta p_{e'}$	370	360	360	360	360	360
	$\frac{1}{2M_{\rm HYP}}\left(\frac{\partial p^2_{\rm HYP}}{\partial p_{e'}}\right)\Delta p_{e'}$	100	15	12	10	9	2
Angles	$\frac{1}{2M_{\rm HYP}}\left(\frac{\partial p^2_{\rm HYP}}{\partial \theta_{eK}}\right)\Delta\theta_{eK}$	100	20	16	14	10	3
	$\frac{1}{2M_{\rm HYP}}\left(\frac{\partial p^2_{\rm HYP}}{\partial \theta_{ee'}}\right)\Delta\theta_{ee'}$	520	90	70	60	50	12
	$\frac{1}{2M_{\rm HYP}}\left(\frac{\partial p^2_{\rm HYP}}{\partial \theta_{e'K}}\right)\Delta\theta_{e'K}$	460	90	70	60	50	12
Total		830	440	440	440	430	430

Therefore,

$$dM_{\rm HYP} = \frac{1}{2M_{\rm HYP}} dM^2_{\rm HYP}. \tag{4.14}$$

A contribution from each term in Eq. (4.8) to $dM_{\rm HYP}$ which corresponds to an intrinsic mass resolution was calculated for each target, and is summarized in Table. 4.8. Results indicated by "Total" in the list were obtained by summing all terms quadratically. It is noted that, to be exact, those terms cannot be simply summed up quadratically since each term is not independent.

Effects which were not included in this estimation such as energy straggling in a target, beam raster, production point displacements from the origin of inverse transfer matrices, and mass offset due to energy loss in the target will be described later.

Production point displacement from the assumed origin of matrices

In the experiment, inverse transfer matrices (will be explained in Sec. 4.7) which derive momentum vectors of particles at target were used to reconstruct a missing mass. The inverse transfer matrices were generated with an assumption that a reaction occurs at a point. In the actual situation, however, the production points were uncertain in a finite volume in target. In

addition, beam raster was adopted for the polyethylene and ^{7}Li target to avoid that the targets are melted by the heat. Fig. 4.25 and Fig. 4.26 show the raster patterns for the polyethylene and ^{7}Li targets in the real data. The raster patterns were obtained by analyzing counting rate in the spectrometer systems and applied power voltages which were used for dipole magnets for the raster. It is noted that a counting rate around $0.05 < y < 0.05$ cm for the polyethylene target is low since a crack was made by heat. An yield reduction due to the heat problem will be discussed in Sec. 4.10.2. The displacements of the production points from the assumed origin of matrices could affect the missing mass resolution.

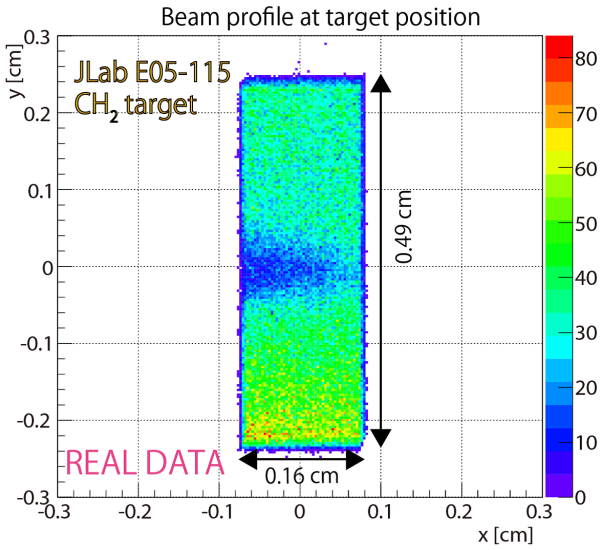

Figure 4.25: Beam profile at the polyethylene target in the real data. Beam raster in the area of $0.16^{x} \times 0.46^{y}$ cm^2 were adopted for the target.

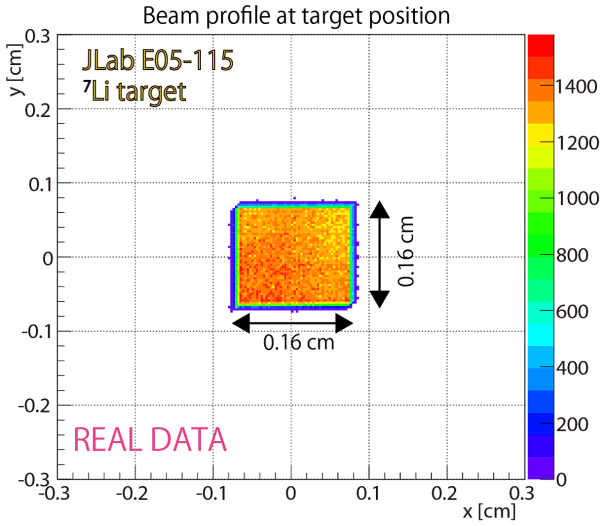

Figure 4.26: Beam profile at the ^{7}Li target in the real data. Beam raster in the area of $0.16^{x} \times 0.16^{y}$ cm^2 were adopted for the target.

z-dependence It was found that there was a strong correlation between a displacement of production point in z-direction (along to the incident beam) and a missing mass in a Monte Carlo simulation. Fig. 4.27 and Fig. 4.28 show the missing mass vs. production point displacement in z-direction for Λ and ${}^{7}_{\Lambda}$He (assumed binding energy of 5.5 MeV). In the simulation, targets were not put and particles (e, e' and K^{+}) were randomly generated in the range of actual target thickness (only z-direction) (Sec. 2.3.3). The mass difference ($\Delta M_{\rm offset}^{{\rm Matrix}(z)}$) for Λ between $z = -0.25$ cm and 0.25 cm was 0.73 MeV/c^2. Similarly, the mass difference for the ${}^{7}_{\Lambda}$He between $z = -0.195$ cm and 0.195 cm was 0.68 MeV/c^2. This effect is smaller for thinner target such as ^{12}C ($\leq$0.10 MeV/c^2). The mass difference for each target is summarized in Table. 4.9.

x and y-dependence Beam rasters in the area of $0.16^{x} \times 0.46^{y}$ cm^2 and that of $0.16^{x} \times 0.16^{y}$ cm^2 were adopted for the polyethylene and the lithium target which have relatively lower melting points than the others (Fig. 4.26 and Fig. 4.26). Therefore, there are effects on the missing masses by the displacements from the matrix origin in x- and y-directions for those targets. To see the effects of x and y dependencies of a missing mass, particles were randomly generated in xy plane within the area of the target, but the target material was not set to avoid the effects of the energy loss. Fig. 4.29 and Fig. 4.31 show correlations between Λ missing mass and the displacements in x- and y-directions, respectively. In the case of displacement in

Table 4.9: Calculated missing mass offset ($\Delta M_{\rm offset}^{{\rm Matrix}(z)}$) due to production point displacement in z-direction from the matrix origin.

Target	Target thickness		Hypernucleus (Hyperon)	Assumed binding energy [MeV]	$\Delta M_{\rm offset}^{{\rm Matrix}(z)}$ [MeV/c^2]
	[mg/cm^2]	[mm]			
CH_2	450.8	5.0	Λ	-	0.73
^{7}Li	208.0	3.9	$^{7}_{\Lambda}$He	-5.5	0.68
^{9}Be	188.1	1.1	$^{9}_{\Lambda}$Li	-8.7	0.18
^{10}B	56.1	0.3	$^{10}_{\Lambda}$Be	-8.7	0.04
^{12}C	87.5	0.5	$^{12}_{\Lambda}$B	-11.37	0.09
^{52}Cr	134.0	0.2	$^{52}_{\Lambda}$V	-20.0	0.03
	154.0	0.2	$^{52}_{\Lambda}$V	-20.0	0.04

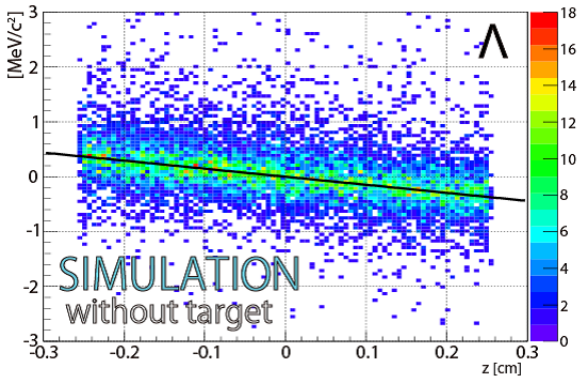

Figure 4.27: Missing mass vs. production point displacement in z-direction for Λ. The mass difference between $z = -0.25$ cm and 0.25 cm was 0.73 MeV/c^2.

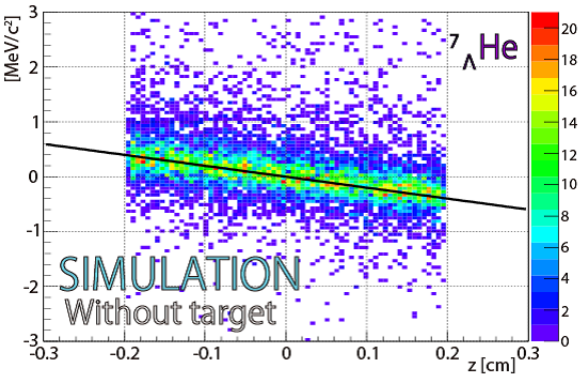

Figure 4.28: Missing mass vs. production point displacement in z-direction for $^{7}_{\Lambda}$He. The mass difference between $z = -0.195$ cm and 0.195 cm was 0.68 MeV/c^2.

x-direction, there is a linear dependence although the mass difference between raster edges is ≤ 100 keV. For displacement in y-direction, there is a quadratic dependence. The quadratic dependence in y-direction makes an asymmetric tail in missing mass if it is not corrected. A simulation with the polyethylene target was also done, and results are shown in Fig. 4.30 and Fig. 4.32. The displacement in x-direction has z information since the target is tilted as shown in Sec. 2.3.3. The effect of z information compensates the x dependence of a missing mass (Fig. 4.30).

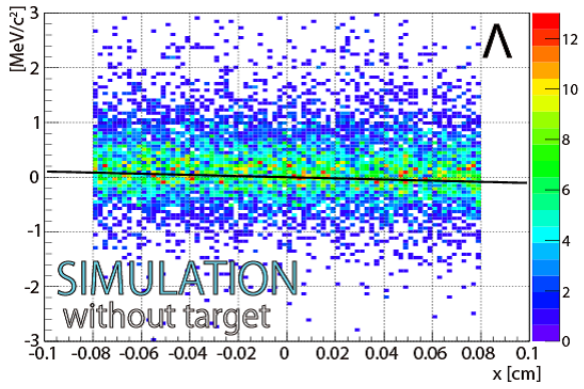

Figure 4.29: Correlation between a Λ missing mass and a x-displacement of particle generation point from the matrix origin. In this simulation, the target was not set to avoid the effects of the energy loss.

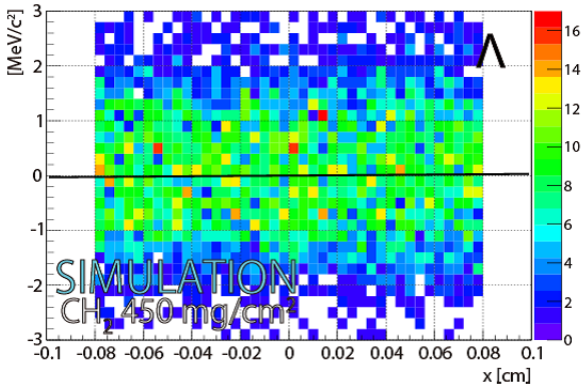

Figure 4.30: Correlation between a Λ missing mass and a x-displacement of particle generation point from the matrix origin. In the simulation, particles were randomly generated in the tilted polyethylene target.

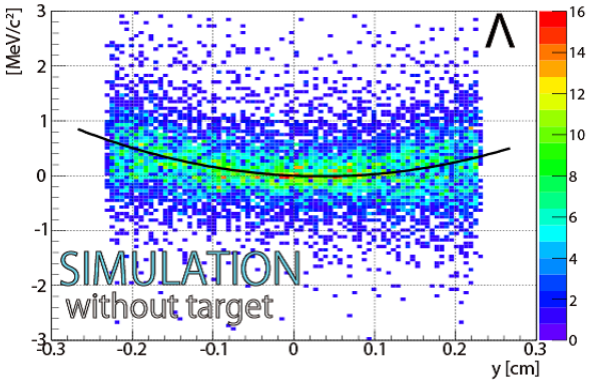

Figure 4.31: Correlation between a Λ missing mass and a y-displacement of particle generation point from the matrix origin. In this simulation, the target was not set to avoid the effects of the energy loss.

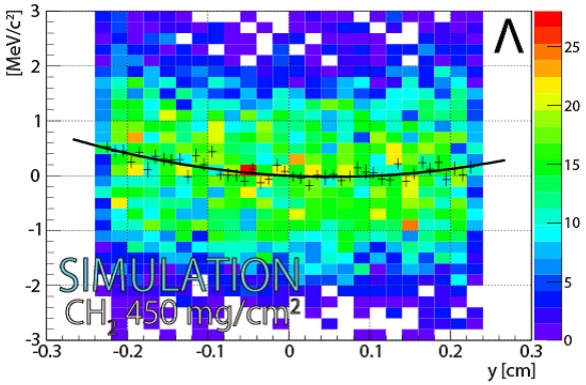

Figure 4.32: Correlation between a Λ missing mass and a y-displacement of particle generation point from the matrix origin. In the simulation, particles were randomly generated in the tilted polyethylene target.

Mass offset due to energy loss in target

Most probable energy loss for each particle is different for different production point in z-direction in target. For example, there is no energy loss for an incident beam, but there are $\sim 2 \times \delta E_{e',K}$ most probable energy losses for a scattering electron and a kaon when the

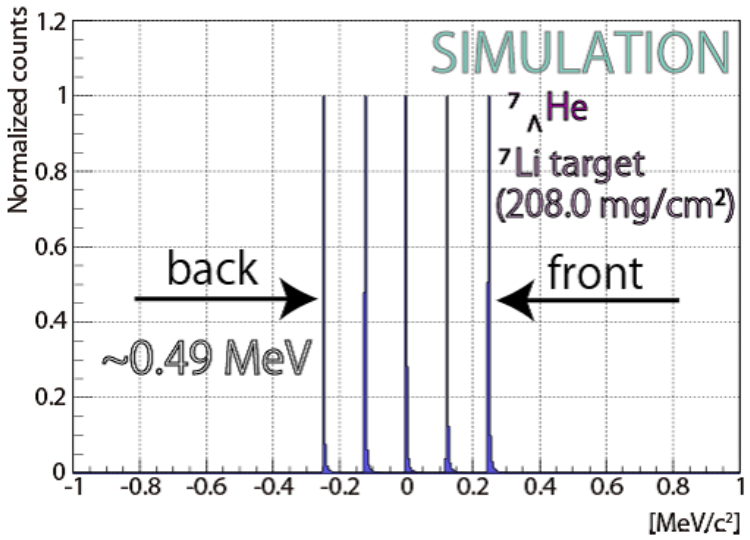

Figure 4.33: The reconstructed missing masses of $^{7}_{\Lambda}$He assuming the production points are at front edge, back edge, center, between front-and-center and between back-and-center of the target. The mass difference between front and back edge of the target was 0.49 MeV in this case.

Table 4.10: Missing mass offset ($\Delta M_{\rm offset}^{\rm EnergyLoss}$) due to most probable energy loss differences between front and back edges of each target.

Target	Target thickness [mg/cm^2]	Hypernucleus (Hyperon)	Assumed binding energy [MeV]	Mass offset ($\Delta M_{\rm offset}^{\rm EnergyLoss}$)[MeV/c^2]
CH_2	450.8	Λ	-	0.68
^{7}Li	208.0	$^{7}_{\Lambda}$He	-5.5	0.49
^{9}Be	188.1	$^{9}_{\Lambda}$Li	-8.5	0.27
^{10}B	56.1	$^{10}_{\Lambda}$Be	-8.7	0.08
^{12}C	87.5	$^{12}_{\Lambda}$B	-11.37	0.17
^{52}Cr	134.0	$^{52}_{\Lambda}$V	-20.0	0.17

production point is at the front edge of target. On the other hand, $\sim 2 \times \delta E_e$ energy loss for the incident beam, but there is no energy losses for the scattering electron and the kaon when the production point is at the end edge of target. Fig. 4.33 shows the reconstructed missing masses of $^{7}_{\Lambda}$He assuming the production points are at front edge, back edge, center, between front-and-center and between back-and-center. The mass difference between front and back edge ($\Delta M_{\rm offset}^{\rm EnergyLoss}$) is 0.49 MeV in this case. $\Delta M_{\rm offset}^{\rm EnergyLoss}$ for each target is summarized in Table. 4.10.

The mass offset due to energy loss differences depending on production point makes an almost linear z-dependence of missing mass. Fig. 4.34 and Fig. 4.35 show correlations between a missing mass and a production point displacement in z-direction for Λ and $^{7}_{\Lambda}$He. In the simulation, the particles were randomly generated in the tilted target (CH_2, ^{7}Li). Thus, those z-dependence were contributed by both effects of production point displacement in z-direction from the matrix origin and energy losses in the targets.

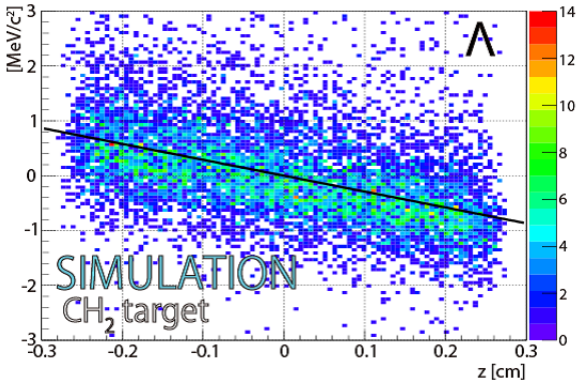

Figure 4.34: A z-dependence of missing mass for Λ. The z-dependence was contributed by both effects of production point displacement in z-direction from the matrix origin and energy losses in the targets.

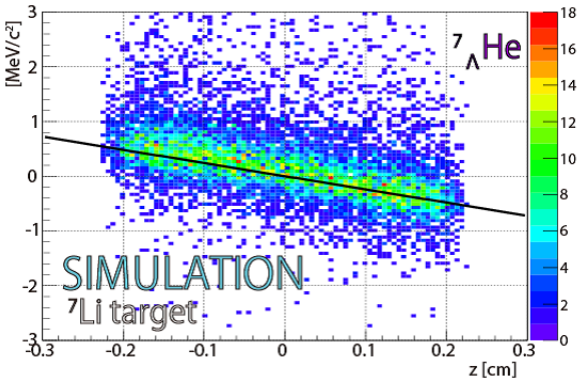

Figure 4.35: A z-dependence of missing mass for ${}^{7}_{\Lambda}$He. The z-dependence was contributed by both effects of production point displacement in z-direction from the matrix origin and energy losses in the targets.

Table 4.11: Fitting results of Fig. 4.36.

Target	Target thickness [mg/cm^2]	Hypernucleus (hyperon)	Assumed binding energy [MeV]	Fitting width (FWHM) [MeV/c^2]
CH_2	450.8	Λ	-	2.07 $\pm$ 0.35
^{7}Li	208.0	${}^{7}_{\Lambda}$He	-5.5	1.36 $\pm$ 0.08
^{9}Be	188.1	${}^{9}_{\Lambda}$Li	-8.5	0.74 $\pm$ 0.01
^{10}B	56.1	${}^{10}_{\Lambda}$Be	-8.7	0.59 $\pm$ 0.01
^{12}C	87.5	${}^{12}_{\Lambda}$B	-11.37	0.62 $\pm$ 0.01
^{52}Cr	134.0	${}^{52}_{\Lambda}$V	-20.0	0.65 $\pm$ 0.10

Total missing mass resolution

Total missing mass resolution cannot be simply estimated by a hand calculation as many sources contribute the resolution intricately. Some part of those sources are not independent each other. To estimated realistic missing mass resolution, a full modeled Monte Carlo simulation was performed. In the simulation, the intrinsic mass resolution (spectrometer resolutions determined by realistic detector resolutions), effect of production point displacement from the matrix origin in x, y, z coordinates, mass offset due to energy loss differences depending on the production point, energy straggling in the target were included. Fig. 4.36 shows a simulation result of missing mass for each Λ hypernucleus (hyperon). Peak widths obtained by fitting with a single Gaussian function in the range of peak center $\pm$ 500 keV are shown in the figure and also summarized in Table. 4.11 although their response functions are not simple single Gaussian.

Quantitative estimations of achievable energy resolutions were studied by a detailed Monte Carlo simulation as described in Sec. 4.11.1 (blind analysis). A result of the blind analysis can be a reference of the achievable resolution for each hypernucleus or hyperon. A typical result of the bind analysis for each target is summarized in Table. 4.12 with other contributions which were described in this section.

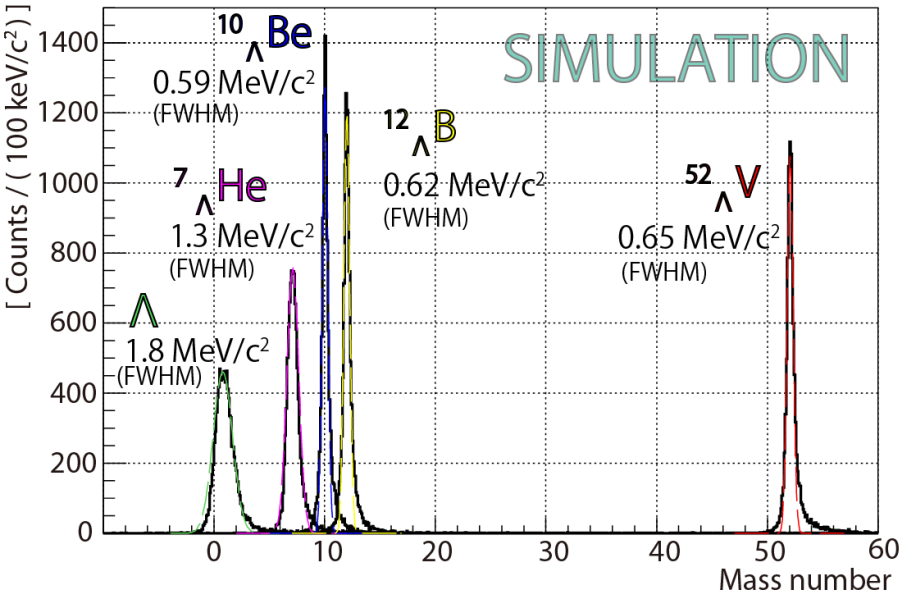

Figure 4.36: Simulated missing mass for each hypernucleus. Peak widths obtained by fitting with a single Gaussian function in the range of peak center ± 500 keV are shown.

Table 4.12: Summary of the missing mass resolution for each Λ hypernucleus or hyperon in the simulation.

Target		CH_2	^{7}Li	^{9}Be	^{10}B	^{12}C	^{52}Cr
[mg/cm^2]		450.8	208.0	188.1	56.1	87.5	134.0
[mm]		5.0	3.9	1.1	0.3	0.5	0.2
Hypernucleus (Hyperon)		Λ	$^{7}_{\Lambda}$He	$^{9}_{\Lambda}$Li	$^{10}_{\Lambda}$Be	$^{12}_{\Lambda}$B	$^{52}_{\Lambda}$V
Intrinsic resolution [MeV/c^2]	beam momentum	0.07	0.07	0.07	0.07	0.07	0.07
	K^+ momentum	0.23	0.22	0.22	0.22	0.22	0.22
	e' momentum	0.38	0.37	0.37	0.37	0.37	0.37
	Angle	0.70	0.13	0.10	0.09	0.07	0.02
	Total	0.83	0.44	0.44	0.44	0.43	0.43
$\Delta M_{\rm offset}^{\rm Matrix(z)}$ [MeV/c^2]		0.73	0.68	0.18	0.04	0.09	0.03
$\Delta M_{\rm offset}^{\rm EnergyLoss}$ [MeV/c^2]		0.68	0.49	0.27	0.08	0.17	0.17
FWHM with initial matrices [MeV/c^2]		1.8	1.3	0.74	0.59	0.62	0.65
FWHM with typical tuned matrices [MeV/c^2]		1.6	1.3	0.80	0.60	0.50	0.75

4.6.3 Missing mass response function

The response function of the missing mass is not a simple Gaussian. It is asymmetric and has a long tail with particularly initial inverse transfer matrices (Fig. 4.24). The inverse transfer matrices were optimized in the real analysis as will be shown in Sec. 4.8. Therefore, the response function should be evaluated with optimized inverse transfer matrices to reproduce the real analysis.

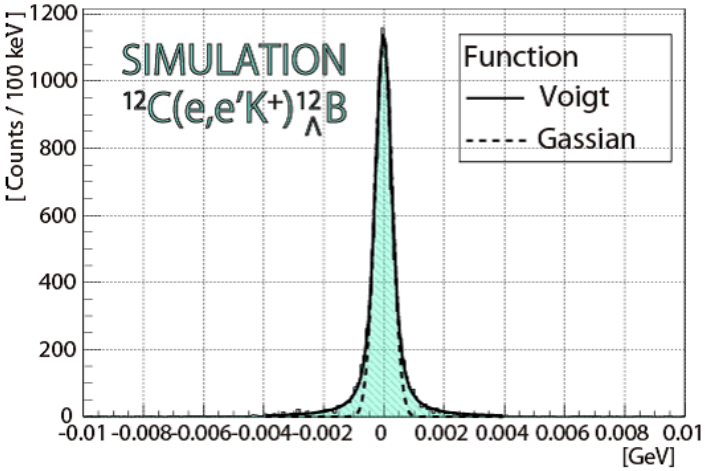

Figure 4.37: A simulated missing mass of $^{12}_{\Lambda}$B (assumed binding energy is 11.37 MeV) with optimized inverse transfer matrices obtained by using blind analysis technique. The missing mass was fitted by a single Gaussian function and a Voigt function. The Voigt function can fit the tail of the histogram where the single Gaussian function cannot.

Fig. 4.37 shows a simulated missing mass of $^{12}_{\Lambda}$B (assumed binding energy of 11.37 MeV) with optimized inverse transfer matrices obtained by using blind analysis technique (Sec. 4.11.1). It was fitted by a single Gaussian function and a Voigt function which is a convolution of Gaussian and Lorenzian functions. The Voigt function is defined as the following:

$$F_{\mathrm{Voigt}}(x) = \int_{-\infty}^{+\infty} G(x';\sigma)L(x-x';\gamma)dx' \tag{4.15}$$

$$\tag{4.16}$$

where

$$G(x) = \frac{1}{\sqrt{2\pi}\sigma}\exp\Big(\frac{x^2}{2\sigma^2}\Big), \tag{4.17}$$

$$L(x) = \frac{1}{2\pi}\frac{\gamma}{(x^2+\gamma^2/4)}. \tag{4.18}$$

The Voigt function can fit the tail where the single Gaussian function cannot. In the present study, therefore, the Voigt function was used for the fitting to a missing mass to obtain both of the binding energy and the cross section.

4.7 Transfer matrix descriptions

The first order transfer matrix (M_0) which relates quantities at the target (indicated by a subscript T) into those at the reference plane (indicated by a subscript RP) is described as:

$$\begin{pmatrix} x_{\rm RP} \\ x'_{\rm RP} \\ y_{\rm RP} \\ y'_{\rm RP} \\ p \end{pmatrix} = M_0 \begin{pmatrix} x_{\rm T} \\ x'_{\rm T} \\ y_{\rm T} \\ y'_{\rm T} \\ p \end{pmatrix} \tag{4.19}$$

where p, x, y , $x'\left(\equiv \frac{p_x}{p_z}\right)$ and $y'\left(\equiv \frac{p_y}{p_z}\right)$ are momentum (p), positions (x,y) and angles (x',y') of a particle. In order to analyze data, quantities at the reference plane which were measured by tracking devices of the spectrometers needed to be converted into those at the target. Therefore, an inverse transfer matrix (M_0^{-1}) which satisfies the following equation is necessary:

$$\begin{pmatrix} x_{\rm T} \\ x'_{\rm T} \\ y_{\rm T} \\ y'_{\rm T} \\ p \end{pmatrix} = M_0^{-1} \begin{pmatrix} x_{\rm RP} \\ x'_{\rm RP} \\ y_{\rm RP} \\ y'_{\rm RP} \\ p \end{pmatrix}. \tag{4.20}$$

This is a basic idea how the momentum vector at the target is obtained to reconstruct a missing mass. In the actual situation of the SPL-HES-HKS system, higher order matrix was necessary to describe its optics with an accuracy of $\Delta p/p \simeq 10^{-4}$. In our case, a matrix represented as the following equation was used,

$$\begin{pmatrix} x_{\rm RP} \\ x'_{\rm RP} \\ y_{\rm RP} \\ y'_{\rm RP} \\ p \end{pmatrix} = M^{\rm T2R} \begin{pmatrix} x_{\rm T} \\ x'_{\rm T} \\ y_{\rm T} \\ y'_{\rm T} \\ p \\ x_{\rm T}^2 \\ x_{\rm T}x'_{\rm T} \\ \vdots \end{pmatrix}, \tag{4.21}$$

$$\begin{pmatrix} x_{\rm T} \\ x'_{\rm T} \\ y_{\rm T} \\ y'_{\rm T} \\ p \end{pmatrix} = M^{\rm R2T} \begin{pmatrix} x_{\rm RP} \\ x'_{\rm RP} \\ y_{\rm RP} \\ y'_{\rm RP} \\ x_{\rm RP}^2 \\ x_{\rm RP}x'_{\rm RP} \\ \vdots \end{pmatrix}. \tag{4.22}$$

There is no momentum term (p) on the right-hand side in Eq. (4.22) since it cannot be directly measured in the experiment. Thus, $M^{\rm R2T}$ and $M^{\rm T2R}$ are no more exact inverse matrices each other. Furthermore, $x_{\rm T}$, $y_{\rm T}$ are assumed to be zero as the electron beam size is quite small (See Sec. 2.2). The variables, $x'_{\rm T}$, $y'_{\rm T}$ and p in Eq. (4.22) are written by the $n^{\rm th}$ order polynomial

Table 4.13: The number of terms of each of Eq. (4.23), (4.24) and (4.25) for the n^{th} order polynomial description.

Order (n)	1	2	3	4	5	6	7	8
Number of terms	5	15	35	70	126	210	330	495

functions as following,

$$x'_{\text{T}} = \sum_{a+b+c+d=0}^{n} C_x(a,b,c,d)(x_{\text{RP}})^a(x'_{\text{RP}})^b(y_{\text{RP}})^c(y'_{\text{RP}})^d, \tag{4.23}$$

$$y'_{\text{T}} = \sum_{a+b+c+d=0}^{n} C_y(a,b,c,d)(x_{\text{RP}})^a(x'_{\text{RP}})^b(y_{\text{RP}})^c(y'_{\text{RP}})^d, \tag{4.24}$$

$$p = \sum_{a+b+c+d=0}^{n} C_p(a,b,c,d)(x_{\text{RP}})^a(x'_{\text{RP}})^b(y_{\text{RP}})^c(y'_{\text{RP}})^d \tag{4.25}$$

where $C_{x,y,p}(a,b,c,d)$ are components of M^{R2T}.

The number of terms of each of Eq. (4.23), (4.24) and (4.25) for the n^{th} order polynomial descriptions are summarized in Table. 4.13. According to an optics simulation, function with n=6 are needed at minimum for optical descriptions of the spectrometers with the order of $\Delta p/p \simeq 10^{-4}$.

The inverse transfer matrices were obtained in the full-modeled Monte Carlo simulations. Magnetic field maps which were calculated by Opera3D (TOSCA) for each magnet were used in the simulation. Models of SPL+HKS and SPL+HES were separately prepared, taking into account the realistic geometrical information. Then, particles were generated at the target point uniformly into the each spectrometer acceptance, and inverse transfer matrices (M^{R2T}) were obtained by using a fitting algorithm. These inverse transfer matrices were not perfect for the real spectrometer systems because of imperfections of the simulation models. An achievable momentum resolution ($\Delta p/p$) is 10^{-2} to 10^{-3} accuracy at this point. Therefore, the inverse transfer matrices need to be optimized to achieve $\Delta p/p \sim 10^{-4}$ accuracy. In the optimization process, a required computation power gets larger as larger n is used. For instance, 1260 terms (210×3 for HES, 210×3 for HKS) have to be optimized in the case of n=6. Concerning both momentum resolution and computation cost, n=6 was chosen for the present analyses. The inverse transfer matrix optimization will be described in the next section.

4.8 Transfer matrix optimization

The energy scale calibration was done by optimizing the inverse transfer matrices of spectrometers. Masses of Λ and Σ^0 which were taken with the polyethylene and water targets were used for the inverse transfer matrix optimization since their masses are well known [68]. Additionally, ${}^{12}_{\Lambda}$B ground state events were also used for the optimization.

4.8.1 Sieve slit pattern matching

Before the inverse transfer matrix optimization, a sieve slit (Sec. 2.3.5 and Sec. 2.3.6) pattern matching was done for each spectrometer to make the initial inverse transfer matrix as close as the real one. The purposes of this procedure are the following:

- Reducing risks that linearity of the inverse transfer matrices are distorted in the inverse transfer matrix optimization.

- Making the convergence speed faster in the inverse transfer matrix optimization.

The particle distributions at the sieve slits were obtained by using transfer matrices (M^{T2S}) which convert momentum vectors at target into positions at sieve slits for e' and K^+. The matrix, M^{T2S} for each spectrometer was calculated in Monte Carlo simulations. In the simulation, matrices which can reproduce the hole patterns of sieve slits were sought by modifying a magnetic field maps calculated by TOSCA for each magnet. Fig. 4.38 shows particle distributions at the sieve slits in HKS and HES after the field modifications [77].

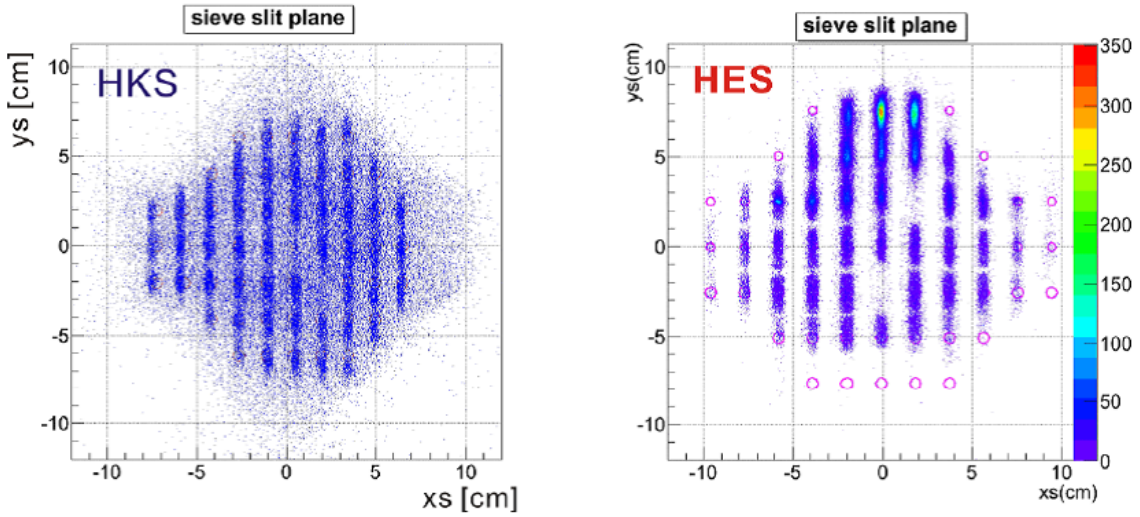

Figure 4.38: Particle distributions at the sieve slits in HKS (Sec. 2.3.5) and HES (Sec. 2.3.6) after the field modifications [77]. The hole patterns of sieve slits were designed to be antisymmetric to avoid a false recognition of the coordinates systems of obtained particle distributions.

4.8.2 Inverse transfer matrix optimization

The inverse transfer matrix optimization was proceeded as the following (see also Fig. 4.39):

1. **Event selection for tuning**
   Events for tuning process are selected by a cut of missing mass (e.g. $\mid$ Missing mass $\mid < 1\sigma$) which was reconstructed by initial inverse transfer matrices for the first loop.

2. **Missing mass reconstruction**
   Variables of positions and angles at reference planes are converted into momentum vectors at the target with inverse transfer matrices, and a missing mass is reconstructed.

3. **Inverse transfer matrix optimization**
   Find optimal M^{R2T} in Eq. (4.22) ($C_{x,y,p}(a,b,c,d)$ in Eq. (4.23), Eq. (4.24) and Eq. (4.25))

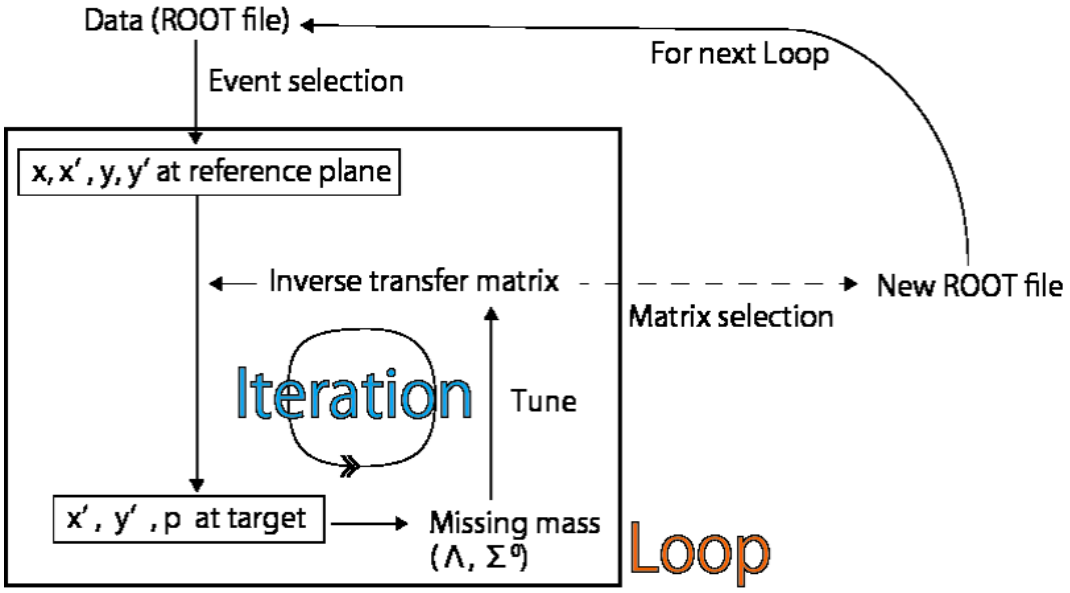

Figure 4.39: A flow chart of the inverse transfer matrix optimization.

to minimized χ^2 which was defined to be:

$$\chi^2 = \frac{1}{3}w_\Lambda\chi^2(\Lambda) + \frac{1}{3}w_{\Sigma^0}\chi^2(\Sigma^0) + \frac{1}{3}w_{\rm H}\chi^2({}^{12}_{\Lambda}\mathrm{B\ g.s.}), \tag{4.26}$$

$$\chi^2(\Lambda) = \frac{1}{N_\Lambda}\sum_{i=0}^{N_\Lambda}\left(\frac{M^i_\Lambda - M_\Lambda}{\sigma_\Lambda}\right)^2, \tag{4.27}$$

$$\chi^2(\Sigma^0) = \frac{1}{N_{\Sigma^0}}\sum_{j=1}^{N_{\Sigma^0}}\left(\frac{M^j_{\Sigma^0} - M_{\Sigma^0}}{\sigma_{\Sigma^0}}\right)^2, \tag{4.28}$$

$$\chi^2({}^{12}_{\Lambda}\mathrm{B\ g.s.}) = \frac{1}{N_{\rm H}}\sum_{k=0}^{N_{\rm H}}\left(\frac{M^k_{\rm H} - M_{\rm H}}{\sigma_{\rm H}}\right)^2, \tag{4.29}$$

where $M^{i,j}_{\Lambda,\Sigma^0,\mathrm{H}}$ are reconstructed masses, M_{Λ,Σ^0} are well known masses taken from Ref. [68], $M_{\rm H}$ is a mean value obtained by a single Gaussian fitting to the ground state of ${}^{12}_{\Lambda}$B and $\sigma_{\Lambda,\Sigma^0,\mathrm{H}}$ are the standard deviations. $N_{\Lambda,\Sigma^0,\mathrm{H}}$ and $w_{\Lambda,\Sigma^0,\mathrm{H}}$ are the number of events and weights for each peak.

The momentum components (Eq. (4.25)) and the angular components (Eq. (4.23) and Eq. (4.24)) of the inverse transfer matrices were alternatively optimized in the optimization process. Ratios of the weights of $w_\Lambda : w_{\Sigma^0} : w_{\rm H} = 1 : 1 : 2$ were used for the optimization for the momentum components. The weight of the ${}^{12}_{\Lambda}$B g.s. was set to be larger than those of hyperon to reduce the relatively larger contributions of the angular term of hyperons to the missing mass (Table. 4.12). On the other hand, ratios of the weights of $w_\Lambda : w_{\Sigma^0} : w_{\rm H} = 1 : 1 : 0$ were used for the optimization for the angular components. The weight of ${}^{12}_{\Lambda}$B g.s. was set to be zero ($w_{\rm H}$ =0) for the angular component optimization since the angular contributions of ${}^{12}_{\Lambda}$B to the missing mass is smaller relative to Λ ($\sim$1/10) as shown in Table. 4.12.

4. **Iteration**
Iterate process of 2 and 3 for certain times (indicated by "Iteration" in Fig. 4.39). Process from 2 to 4 is indicated by "Loop".

5. **Matrix selection**
   Once a Loop is done, matrices which will be used for next Loop are selected with some conditions (peak positions of a Λ and a Σ^0, peak widths of a hypernucleus and so on).

6. **Next Loop**
   New ROOT files[*5] are generated by using the selected matrices, and used for next Loop.

7. **Repeat**
   Repeat the processes from 1 to 6.

4.9 Mixed event analysis

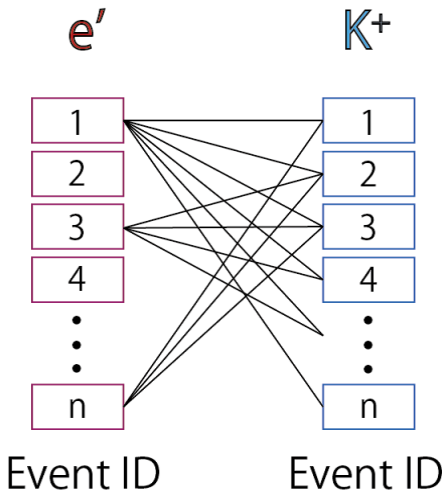

Figure 4.40: Events in the accidental $e'K^+$ coincidence bunches in Fig. 4.19 were randomly combined to obtain the accidental background distribution of the missing mass in the mixed event analysis.

Distributions of the $e'K^+$ accidental background events which are included in the missing mass spectra, were obtained by the coincidence time selection. A left histogram of Fig. 4.41 shows a missing mass spectrum from the polyethylene target when six bunches of accidental coincidence peaks in Fig. 4.19 were selected. A right histogram of Fig. 4.41 shows a missing mass spectrum when K^+s and scattered electrons which are in the accidental coincidence bunches in Fig. 4.19 were randomly combined 300 times in off-line analysis (Fig. 4.40, mixed event analysis). It is note that the combinations can be made more in principle. The accidental background distribution for each hypernucleus (hyperon) spectrum was obtained by the mixed event analysis. This analysis makes the effects of the statistical errors from the accidental background negligible small when the accidental background distributions were subtracted from the original spectrum.

[*5] http://root.cern.ch/

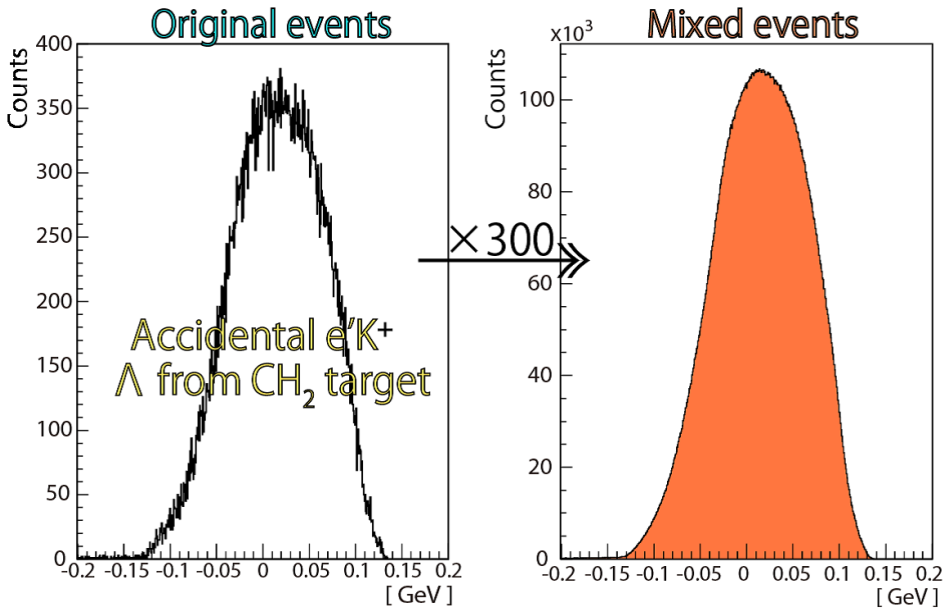

Figure 4.41: (Left figure) Missing mass distribution when the accidental $e'K^+$ coincidence events were selected. Six bunches of the accidental $e'K^+$ coincidence events in Fig. 4.19 were selected in this case. (Right figure) A missing mass distribution of the accidental background events obtained by the mixed event analysis. The right figure is the case of 300 times more statistic than the left figure.

4.10 Cross section derivation

The differential cross section of the (γ^*,K^+) reaction, used in the present study is defined to be:

$$\overline{\left(\frac{d\sigma}{d\Omega_K}\right)}\Big|_{1^\circ-13^\circ} = \frac{\int_{\rm HKS} d\Omega_K (\frac{d\sigma}{d\Omega_K})}{\int_{\rm HKS} d\Omega_K} \tag{4.30}$$

$$= \frac{1}{N_T}\frac{1}{N_{\gamma^*}}\frac{1}{\epsilon^{\rm common}}\sum_{i=0}^{N_{\rm HYP}}\frac{1}{\epsilon_i^{\rm HKS}\epsilon_i^{\rm HES}\Delta\Omega_{\rm HKS}} \tag{4.31}$$

where N_T is the number of nuclei in the target, N_{γ^*} is the number of virtual photons, $\epsilon^{\rm common,HKS,HES}$ are the efficiencies and $\Delta\Omega_{\rm HKS}$ is the HKS solid angle estimated by a Monte Carlo simulation. The differential cross section is an averaged value over the HKS acceptance ($1^\circ < \theta_K^{\rm lab} < 13^\circ$). The number of nuclei (N_T) is derived by the following equation:

$$N_T = \frac{x_t}{A}N_A \tag{4.32}$$

where x_t is the target thickness in mg·cm^{-2} shown in Table. 2.3 and N_A is the Avogadro's constant. N_T for each target with the dimension of cm^{-2} is summarized in Table 4.14.

The number of virtual photons (N_{γ^*}) and the efficiencies ($\epsilon^{\rm common,HKS,HES}$) will be described in Sec. 4.10.1 and Sec. 4.10.2.

4.10.1 Number of virtual photon

The number of virtual photons was derived by a Monte Carlo simulation. In the simulation, electrons associated with virtual photon (Eq. 2.5) were generated at the target point, and

Table 4.14: Number of nuclei (N_T) for each target.

Nucleus	Target Thickness [mg/cm^2]	N_T [cm^{-2}]
H in CH_2	450.8	38.71×10^{21}
H in H_2O	500.0	33.46×10^{21}
^{7}Li	208.0	17.89×10^{21}
^{9}Be	188.1	12.59×10^{21}
^{10}B	56.1	3.38×10^{21}
^{12}C	87.5	4.39×10^{21}
^{52}Cr	134.0	1.55×10^{21}
	154.0	1.78×10^{21}

accepted electrons in the full-modeled HES were used to obtain the number of virtual photons. Positions of the HES collimator (Sec. 2.3.6) needed to be considered since they were changed during the experiments to control the HES counting rate. There were two sets of positions. One was the position accepting particles above -4.7 cm from the mid-plane of the collimator, the other was that above -7.7 cm.

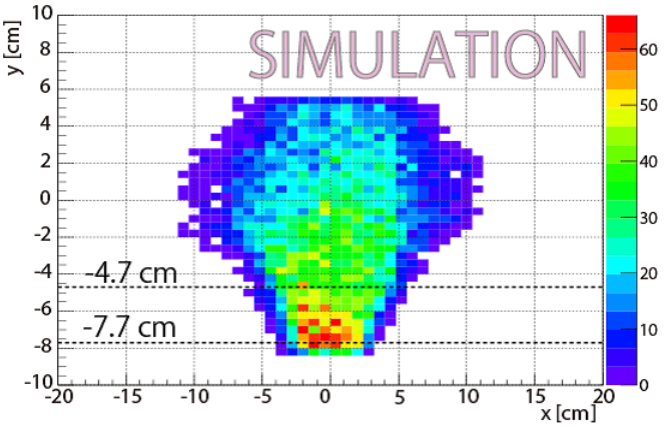

Figure 4.42: An x and y distribution at HES collimator position in a Monte Carlo simulation.

Fig. 4.42 shows an x vs. y distribution at the collimator position in the Monte Carlo simulation. The number of virtual photons were estimated with selections of $y \geq -4.7$ cm and $y \geq -7.7$ cm, respectively. A distribution of the virtual photon flux Γ which was defined in Eq. (2.5) as a function of scattered electron momentum with the cut of $y \geq -7.7$ cm is shown in Fig. 4.43. The integrated virtual photon flux ([/electron]) was obtained by integrating it over the HES acceptance. The integrated virtual photon fluxes for the different collimator positions and momentum selections are summarized in Table. 4.15. The variation of virtual photon flux when the collimator position was moved by 1 mm (the actual accuracy of the collimator was less than 1 mm) was less than 2% for each condition. Thus, the systematic error is considered to be 2% for the integrated virtual photon flux in the present study. Finally, the number of virtual photons (N_{γ^*}) for each target was obtained by multiplying the integrated virtual photon flux by the number of incident electrons.

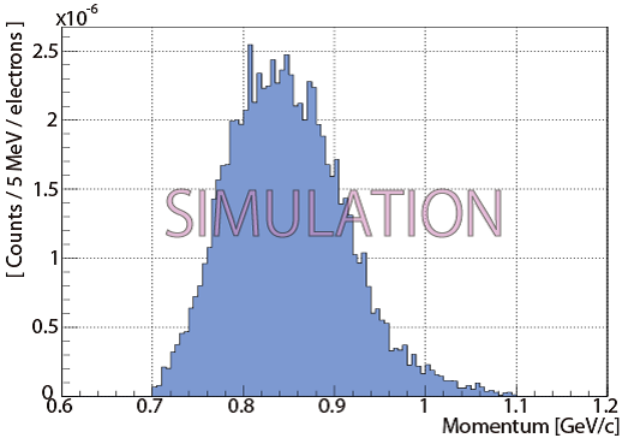

Figure 4.43: A virtual photon flux distribution as a function of scattered electron momentum.

Table 4.15: The virtual photon fluxes for different collimator positions and momentum selections. The systematic errors are 2%.

Collimator position [cm]	e' momentum selection [GeV/c]	Virtual photon flux [/electron]
-4.7	All	$(5.94\pm0.06)\times10^{-5}$
-7.7		$(7.78\pm0.07)\times10^{-5}$
-4.7	0.80-0.90	$(2.81\pm0.04)\times10^{-5}$
-7.7		$(4.33\pm0.05)\times10^{-5}$
-4.7	0.80-0.98	$(4.19\pm0.05)\times10^{-5}$
-7.7		$(5.67\pm0.06)\times10^{-5}$

4.10.2 Efficiencies and correction factors

In this section, efficiencies and correction factors to obtain the differential cross section such as the HKS solid angle, trigger efficiency, tracking efficiency, off-line K^+ selection efficiency etc. are described.

HKS solid angle

The HKS solid angle was evaluated by the Monte Carlo simulation as it was shown in Fig. 2.14. The solid angle which depends on a particle momentum. For the cross section calculation, therefore, the HKS solid angle was evaluated event by event depending on particle momentum. The systematic error for the HKS solid angle evaluation is estimated to be 2% considering acceptance edge discrepancy at the reference plane between the real data and the simulation (effects of $< 1\%$), and the collimator position precision (effects of $< 1\%$).

HKS trigger efficiency

Detection efficiency for K^+ at the hardware trigger level was evaluated by comparing data of the HKS trigger (Eq. 3.4) and the CP trigger (Eq. 3.5). Figure 4.44 shows mass squared distributions of data of the CP trigger (left figure) and the HKS trigger (right figure) , which were calculated by Eq. (4.1). In order to derive the K^+ trigger efficiency from these two histograms, a pre-scaling factor (Sec. 3.3) should be considered.

For the data of the polyethylene target with 2.0 μA beam, the K^+ trigger detection efficiency was 92% with π^+ and p rejection powers of 5.4×10^{-3} and 1.2×10^{-1}, respectively. The K^+ trigger efficiency for each data set is listed in Table. 4.16.

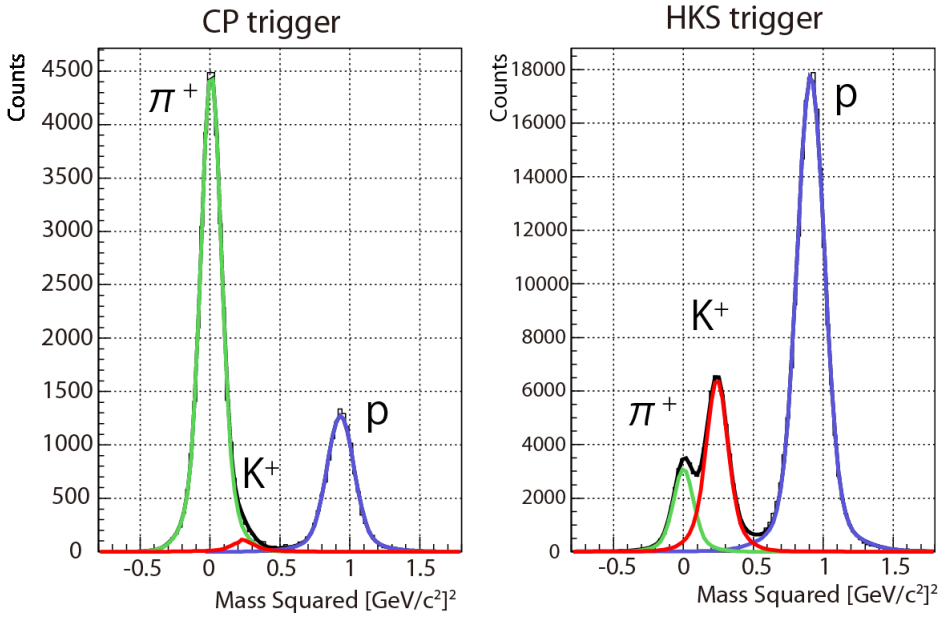

Figure 4.44: Mass squared distributions from the data of the polyethylene target with the CP trigger (left) and the HKS trigger (right). The pre-scaling factor ratio of the CP trigger to the HKS trigger was 1 : 125 for this data.

HES trigger efficiency

There were inefficient segments of EHODO1 (segment number of 13 and 17, Fig. 4.3) due to a problem of discriminator module. Number of lost events was estimated by comparing hit counts between inefficient segments and its neighboring segments, assuming the hit pattern distribution is smooth and efficiencies for the other segments are 100%. Efficiencies of those segments are described by the following equation:

$$\epsilon_i = n_i \times \left(\frac{n_{i-1} + n_{i+1}}{2} \right)^{-1} \tag{4.33}$$

where ϵ_i is the efficiency of the i^{th} segment (i=13, 17), and n_{i-1}, n_i and n_{i+1} are the hit counts of segment number of $i-1$, i and $i+1$, respectively. Then, the HES trigger efficiency was estimated to be $\epsilon_{13} \times \epsilon_{17}$. The HES trigger efficiencies were summarized in Table.4.16.

Table 4.16: The HKS and HES trigger efficiency for each data set.

Data set	HKS trigger efficiency [%]	HES trigger efficiency [%]
1	92.3 ± 1.8	97.7 ± 1.7
2	-	87.3 ± 1.4
3	90.9 ± 13.7	95.9 ± 3.7
4	93.1 ± 6.4	95.3 ± 4.4
5	94.1 ± 1.2	97.8 ± 1.6
6, 7	91.4 ± 3.1	98.2 ± 1.2
8	85.4 ± 6.1	77.2 ± 2.5
9	-	97.3 ± 1.9
10	-	94.7 ± 5.0

Tracking efficiency

The HKS and HES tracking efficiencies were estimated from layer efficiencies of the drift chambers (KDC1, KDC2, EDC1, EDC2).

In the HKS, tracking was done with two drift chambers (KDC1, KDC2). Each of the chambers has six layers (uu'xx'vv') as described in Sec. 3.2.1. In the tracking procedure, five layer hits out of six layers were required for each drift chamber to extract particle tracks. Once the layer efficiencies were estimated, the tracking efficiency ($\epsilon^{\rm HKS}_{\rm tracking}$) was calculated as the following equation,

$$\epsilon^{\rm HKS}_{\rm tracking} = P_{66} \times P_{65} \times P_{55} \tag{4.34}$$

$$\tag{4.35}$$

where

$$P_{66} = \prod_{i=1}^{12} \epsilon^{\text{layer}}(i) \tag{4.36}$$

$$P_{65} = \sum_{i=1}^{12} \sum_{j=1(j\neq i)}^{12} \epsilon^{\text{layer}}(j) \times \left(1 - \epsilon^{\text{layer}}(i)\right) \tag{4.37}$$

$$P_{55} = P_{55}^{1} \times P_{55}^{2} \tag{4.38}$$

$$P_{55}^{1} = \sum_{i=1}^{6} \sum_{j=1(j\neq i)}^{6} \epsilon^{\text{layer}}(j) \times \left(1 - \epsilon^{\text{layer}}(i)\right) \tag{4.39}$$

$$P_{55}^{2} = \sum_{i=7}^{12} \sum_{j=7(j\neq i)}^{12} \epsilon^{\text{layer}}(j) \times \left(1 - \epsilon^{\text{layer}}(i)\right) \tag{4.40}$$

$$\tag{4.41}$$

$\epsilon^{\text{layer}}(i)$ is the i^{th} layer efficiency. $i = 1$ to 6 are the layer numbers of KDC1 and $i = 7$ to 12 are for those of KDC2. The P_{66}, P_{65} and P_{55} correspond to the following conditions,

- P_{66}
  The probability that the all layers of drift chambers have hits for tracking.
- P_{65}
  The probability that there is one layer which do not have any hits for tracking.
- P_{55}
  The probability that there is one layer which do not have any hits for tracking, in each drift chamber.

In the HES, the EDC1 was used for particle tracking. There are ten layers in the EDC1 as already described in Sec. 3.1.1. Eight hit layers out of ten layers are required for the HES tracking. The HES tracking efficiency was estimated by a similar way to that of HKS.

The HKS and HES tacking efficiency for each data set is summarized in Table. 4.17.

Table 4.17: The HKS and HES tracking efficiencies for each data set.

Data set	HKS tracking efficiency [%]	HES tracking efficiency [%]
1	99.9 ± 0.8	92.9 ± 1.7
2	96.1 ± 0.2	90.3 ± 2.1
3	99.6 ± 2.1	82.8 ± 3.3
4	99.5 ± 0.5	90.9 ± 1.8
5	99.9 ± 0.9	94.2 ± 1.7
6,7	98.8 ± 0.2	91.3 ± 1.8
8	99.0 ± 0.5	77.2 ± 2.5
9,10	97.5 ± 0.3	87.5 ± 1.9

Off-line K^+ selection efficiency

Off-line selections were applied to separate K^+ events from background events by using the information of mass squared and Čerenkov detectors. The off-line cut efficiencies are discussed in this section.

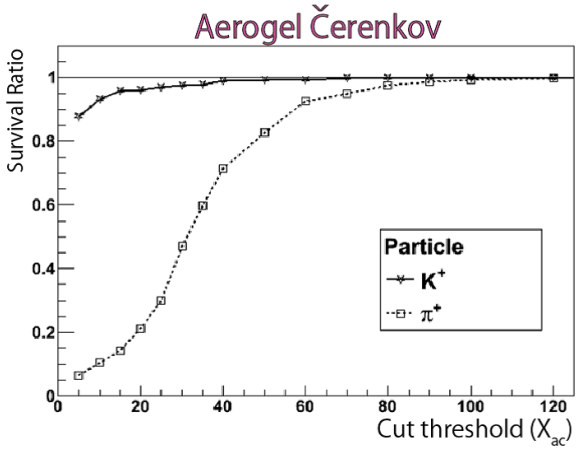

Figure 4.45: K^+ and π^+ survival ratios as a function of the cut threshold, X_{ac}. A typical CH_2 data was chosen for this plot.

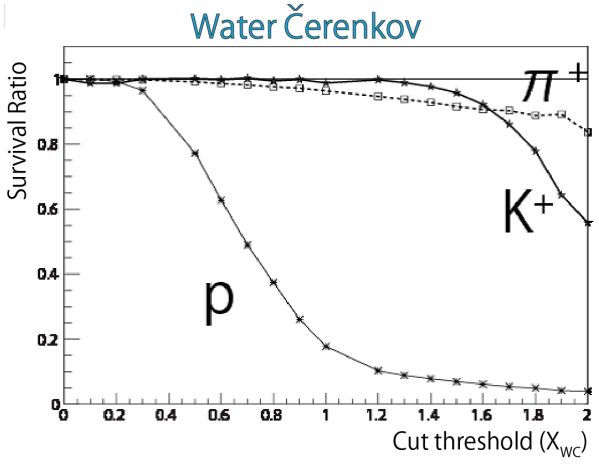

Figure 4.46: K^+ and p survival ratios as a function of the cut threshold, X_{wc}. A typical CH_2 data was chosen for this plot.

π^+ rejection with the aerogel Čerenkov detector

π^+s are rejected with cuts of number of photoelectrons in the aerogel Čerenkov detector. In the analysis, summed number of photoelectrons of the three layers of aerogel Čerenkov detectors (Fig. 4.5) were used for this purpose. K^+ and π^+ survival ratios were estimated by comparing number of events for each particle between before and after the cut. The estimation of the number of events was done in the mass squared distribution by fitting for each particles as shown in Fig. 4.44.

Events which are below a cut threshold, X_{ac} were remained as a K^+ candidate data. It means that events satisfying the following condition were remained:

$$N_{AC1} + N_{AC2} + N_{AC3} < X_{ac} \tag{4.42}$$

where N_{AC1}, N_{AC2}, N_{AC3} are the number of photoelectrons in each layer of aerogel Čerenkov detector. The survival ratios depend on the cut threshold, X_{ac}. The K^+ and π^+ survival ratios as a function of X_{ac} are shown in Fig. 4.45. The K^+ and π^+ survival ratios of the data set 1 (CH_2 target) were 96.4±0.5% and 21.5 ± 0.4%, respectively when $X_{ac} = 20$ was chosen. The survival ratios at $X_{ac} = 20$ are listed in Table. 4.18.

Table 4.18: K^+ and π^+ survival ratios after the aerogel Čerenkov cuts ($X_{ac} = 20$) are applied in the off-line analysis.

Data set	K^+ survival ratio [%]	π^+ survival ratio [%]
1	96.4 ± 0.5	25.1 ± 0.4
2	69.2 ± 1.2	19.2 ± 0.5
3	88.6 ± 0.8	18.7 ± 0.4
4	82.9 ± 0.8	10.0 ± 0.3
5	96.9 ± 0.4	23.4 ± 0.5
6,7	98.9 ± 0.5	30.0 ± 1.3
8	90.2 ± 1.4	16.2 ± 0.8
9,10	63.3 ± 0.5	8.0 ± 0.1

Proton rejection with the water Čerenkov detector

Protons were rejected with a cut of the number of photoelectrons of water Čerenkov detectors (Fig. 4.6) . The K^+ and proton survival ratios after the water Čerenkov cut were estimated with a similar way as that with the aerogel Čerenkov detectors. In the water Čerenkov case, events that satisfied the following condition are remained as a K^+ candidate data:

$$\mathrm{N_{WC1}} + \mathrm{N_{WC2}} > \mathrm{X_{wc}} \tag{4.43}$$

where $\mathrm{N_{WC1}}$ and $\mathrm{N_{WC2}}$ are the number of photoelectrons in each layer of water Čerenkov detector, and $\mathrm{X_{wc}}$ is a cut threshold. Fig. 4.46 shows the K^+ and proton survival ratios as a function of $\mathrm{X_{wc}}$ from a typical CH_2 data. The K^+ and proton survival ratios of the data set 1 (CH_2 target) were 94.9 ± 0.2 % and 18.8 ±0.1 %, respectively at $\mathrm{X_{wc}} = 1$. The survival ratio at $\mathrm{X_{wc}} = 1$ for each data set is summarized in Table. 4.19.

Table 4.19: K^+ and p survival ratios after the water Čerenkov cuts ($\mathrm{X_{wc}} = 1$) are applied in the off-line analysis.

Data set	K^+ survival ratio [%]	p survival ratio [%]
1	94.9 ± 0.2	18.8 ± 0.1
2	97.6 ± 0.9	12.7 ± 0.3
3	95.2 ± 0.3	20.4 ± 0.4
4	95.7 ± 0.4	21.0 ± 0.5
5	96.7 ± 0.2	17.4 ± 0.1
6,7	96.0 ± 0.5	20.1 ± 0.2
8	94.6 ± 0.6	18.0 ± 0.5
9,10	96.2 ± 0.6	34.5 ± 0.1

Mass squared cut

A mass squared information (Fig. 4.7) was also used to select K^+ events. The mass squared cut was efficient for the proton rejection although its resolution was not enough for the π^+ rejection.

In the analysis, the following condition was applied as a mass squared K^+ selection:

$$\mid m^2_{\mathrm{Measured}} - m^2_{K^+} \mid < 0.3\ . \tag{4.44}$$

m^2_{Measured} is a measured mass squared that was calculated by the Eq. (4.1), and the $m^2_{K^+}$ (=[0.493 GeV/c^2]^2) is a mass squared of the PDG value [68]. The K^+ survival ratio for each data set are summarized in Table. 4.20.

K^+ decay factor

The mean lifetime of K^+ is 1.2×10^{-8} seconds ($c\tau$=3.7 m). Some portion of K^+s decay in flight before they reach the end of HKS detectors. The main decay modes are $K^+ \to \mu^+\nu_\mu$ (63%) and $K^+ \to \pi^+\pi^0$ (23%).

A survival ratio of K^+ in HKS from the decay was estimated by a Monte Carlo simulation with Geant4 as a K^+ decay factor (f_{decay}). The decay factor, f_{decay} was derived by comparing the number of events when decay processes were included and those when they were not included. The following conditions were required in order to reproduce both the on-line and off-line K^+ selections of the experiment:

Table 4.20: The mass squared resolutions (for K^+ peak) and the K^+ survival ratio for each data set.

Data set	σ [GeV/c^2]^2	K^+ survival ratio [%]
1	$(8.8 \pm 0.03)\times10^{-2}$	99.9 ± 0.01
2	$(15.1 \pm 0.13)\times10^{-2}$	95.3 ± 0.05
3	$(11.1 \pm 0.06)\times10^{-2}$	99.3 ± 0.02
4	$(11.6 \pm 0.06)\times10^{-2}$	99.0 ± 0.02
5	$(9.2 \pm 0.02)\times10^{-2}$	99.9 ± 0.01
6,7	$(8.6 \pm 0.03)\times10^{-2}$	99.9 ± 0.01
8	$(10.6 \pm 0.10)\times10^{-2}$	99.5 ± 0.04
9	$(15.2 \pm 0.22)\times10^{-2}$	95.2 ± 0.09
10	$(16.5 \pm 0.22)\times10^{-2}$	93.1 ± 0.14

1. A K^+ is not decayed until it pass through the two tracking drift chambers (KDC1, KDC2).
2. The number of photo-electrons in the water Čerenkov detector are above a off-line cut threshold (Figure 4.47).
3. The number of photo-electrons in the aerogel Čerenkov detector are below a off-line cut threshold (Figure 4.47).

Fig. 4.47 shows the simulation results of the number of photo-electrons in the water (left figures) and aerogel (right figures) Čerenkov detectors for p, K^+ and π^+ when decay processes were included (lower figures) and they were not included (upper figures). Same number of events were generated for p, K^+ and π^+. Decayed particles generate larger number of photo-electrons than those of K^+ because once a K^+ decayed into lighter particles, the velocity factor, β became larger. The simulation results of the $f_{\rm decay}$ as a function of K^+ momentum with statistical errors is shown in Figure 4.48. The $f_{\rm decay}$ was $0.24 \sim 0.33$ over the HKS acceptance, depending on the K^+ momentum. The simulation results was fitted by the 9$^{\rm th}$ order polynomial function which was used for estimation of the cross sections. The K^+ decay factor, $f_{\rm decay}$ was $29.4 \pm 0.8\%$ for the K^+ momentum of 1.2 GeV/c.

K^+ absorption factor

Some K^+s are absorbed in the materials, and cannot be detected. This effect was taken into account as a K^+ absorption factor ($f_{\rm abs}$). The $f_{\rm abs}$ was estimated by comparing the number of events when inelastic processes are included and those when they are not included in a Geant4 Monte Carlo simulation. The simulation shows that $f_{\rm abs} = 93.31 \pm 0.07\%$ of which target dependence was negligible small.

Yield reduction of Λ from CH_2 target

The melting point of polyethylene is around at 100°C. It is too low for the small emittance and high intensity beam of JLab to be incident on the polyethylene target without being punched through. To prevent the polyethylene target from being punched through, beam raster with an area of 1.6^x mm $\times$ 4.9^y mm was adopted (Fig. 4.25). However, the rastered beam still generated enough amount of heat to carbonize the target. The carbonization was observed as a reduction of yields of Λ events, which corresponds to a reduction of hydrogen in the polyethylene target, even during the beam time. The target position was moved every certain beam irradiation time in order to take data of Λ and Σ^0 efficiently. Figure 4.49 is a photograph of the polyethylene

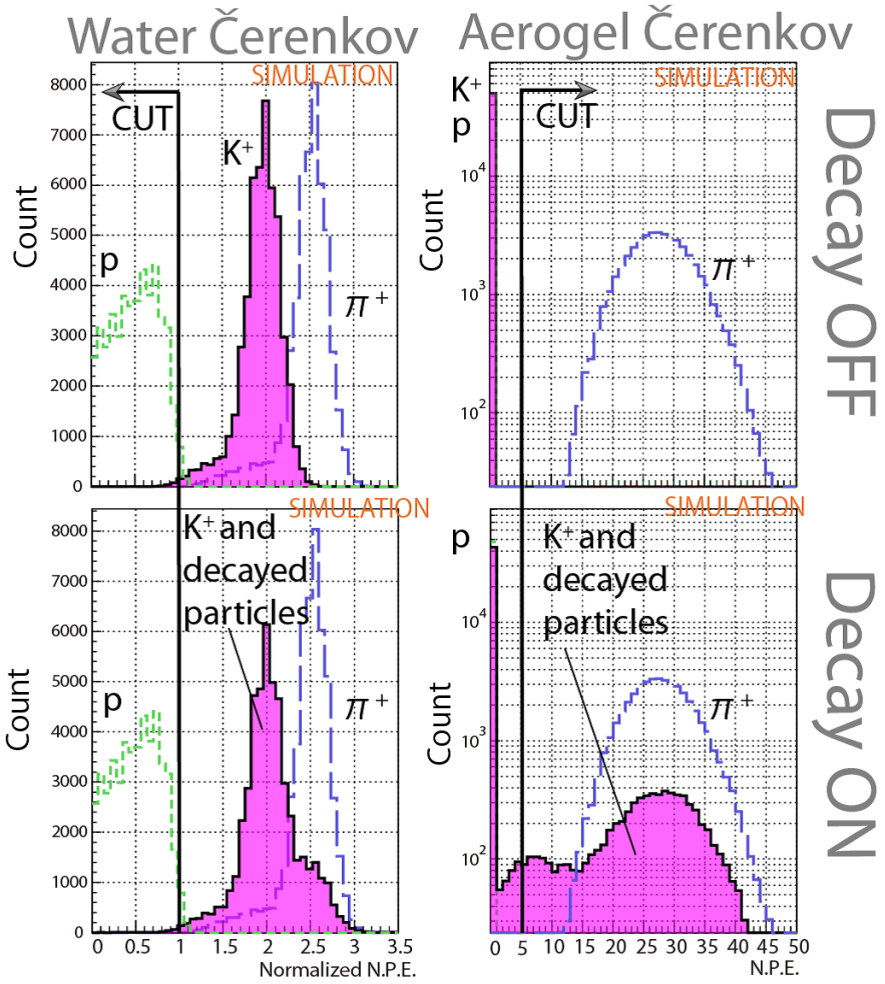

Figure 4.47: Simulation results of the number of photo-electrons in the water (left figures) and aerogel (right figures) Čerenkov detectors for p, K^+ and π^+ when decay processes were included (lower figures) and they were not included (upper figures)

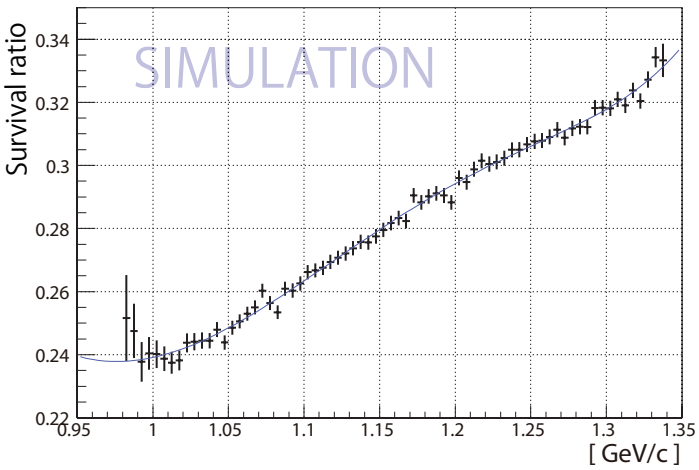

Figure 4.48: Simulation results of the survival ratio of K^+ in HKS from the decay (f_{decay}) as a function of K^+ momentum.

target before and after the electron beam was irradiated. Traces of rastered beam spots are seen in the photograph.

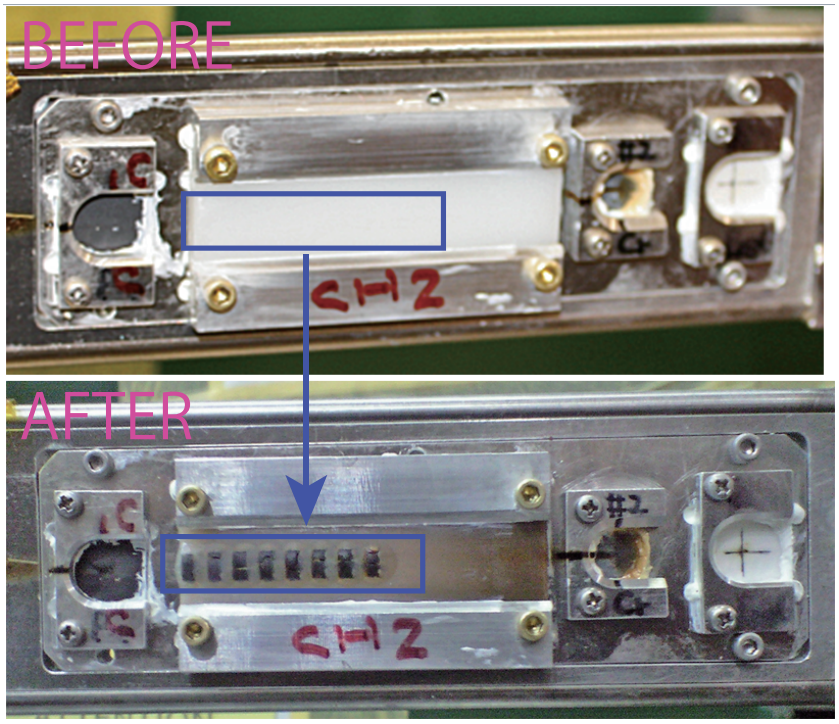

Figure 4.49: A photograph of the CH_2 target before and after the electron beam was irradiated with raster size of 1.6^x mm $\times$ 4.9^y mm.

Reduction rates of a Λ from a hydrogen nucleus, a quasi-free Λ from a ^{12}C nucleus and an accidental coincidence event between a K^+ and a scattered electron were estimated. Figure 4.50 shows normalized number of those events as a function of beam charge (time). The number of Λ events from hydrogen nuclei at 3000 μC beam irradiation was $82.4 \pm 6.4\%$ relative to those with no beam irradiation.

Fitting to missing mass spectrum

To obtain the cross section of each peak of Λ hypernucleus, the number of event was derived by fitting. On the other hand, the cross sections of Λ and Σ^0 hyperons were obtained by counting their events after the known background events were subtracted as will be shown in Sec. 5.1.

The counting efficiency by fitting to a spectrum depends on how good the assumed response function (Sec. 4.6.3) is fitted to the missing mass which is reconstructed by the optimized inverse transfer matrices. The counting efficiency by fitting for each peak was evaluated by using blind analyses (Sec. 4.11.1). In the blind analyses, realistic dummy data were generated taking into account detector resolution, spectrometer acceptance, energy straggling in the target and so on, and were optimized by using the same method as that for real data. A typical result is shown in Table. 4.21. In the table, the following items are listed:

1. **Ratio of the number of events which are in the range of peak center $\pm$10 MeV relative to generated events**
   Some portion of events are distributed outside of interested region due to a tail component of energy loss in the target (Fig. 4.21). Here, the event ratio which are in the range of peak center $\pm$ 10 MeV relative to the number of generated events is used to see the event loss due to the tail component of energy loss in the target as a reference.

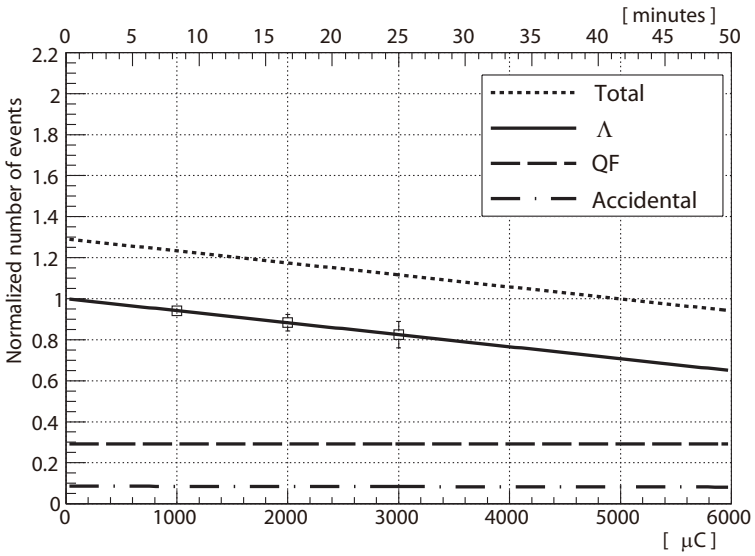

Figure 4.50: Normalized number of Λ events from hydrogen nuclei, quasi-free Λ from ^{12}C nuclei and accidental coincidence events, as a function of beam charge which is in proportional to time.

2. **Counting efficiency by fitting to the missing mass spectrum when the area of the function was integrated over mean value ±10 MeV**
   If the fitting is perfect, the counting efficiency is consistent with the ratio which described in the previous item.

3. **Counting efficiency by fitting to the missing mass spectrum when the area of the function was integrated over mean value ±∞**
   If the fitting is perfect, the counting efficiency is 1.0.

Results after the inverse transfer matrix depend on the initial inverse transfer matrices as shown in Sec. 4.11.1. Above test was done for several time with different initial transfer matrices. Finally, it was found that event miscount by fitting to the missing mass is less than ±5% for each Λ hypernucleus. Thus, the systematic errors for the counting events by fitting to the missing mass is estimated to be ±5% (This value is not used for hyperons, but hypernuclei). The number of events for Λ and Σ^0 were evaluated by just integrating the missing mass spectrum after the well understood background distributions were subtracted as will be shown in Sec. 5.1. It was found that the loss of the number of events due to event counting by integrating the missing mass spectrum is less than 7% for Λ and Σ^0. Therefore, the systematic errors for the counting events for Λ and Σ^0 are estimated to be +7%.

4.11 Systematic Errors

In this section, systematic errors of binding energy, excitation energy and differential cross sections which were obtained in the analyses are described.

4.11.1 Binding energy and excitation energy

Systematic errors of the binding energy and excitation energy are mainly originate from inverse transfer matrices which are optimized in our energy scale calibration method (Sec. 4.8.2). Target

Table 4.21: A typical counting efficiency by a peak fitting for each Λ hypernucleus (hyperon) in the simulation.

Hypernucleus (Hyperon)	Generated number of events	Event ratio (peak±10 MeV)	Fitting result (mean±10 MeV)	Fitting result (mean±∞)
${}^{7}_{\Lambda}$He	10000	0.989±0.014	0.983±0.014	0.994 ± 0.014
${}^{9}_{\Lambda}$Li	10000	0.988±0.014	0.983±0.014	0.994 ± 0.014
${}^{10}_{\Lambda}$Be	10000	0.994±0.014	0.997±0.014	1.009 ± 0.014
${}^{12}_{\Lambda}$B	10000	0.990±0.014	0.993±0.014	1.005 ± 0.014
${}^{52}_{\Lambda}$V	10000	0.958±0.014	0.959±0.014	0.976 ± 0.014
Λ	10000	0.967±0.014	0.962±0.014	0.975 ± 0.014
Σ^0	8000	0.980±0.016	0.941±0.015	0.947 ± 0.015

thickness uncertainty affects only binding energy since its basic effects are making a uniform shift in a missing mass spectrum. In this section, systematic errors for binding energy and excitation energy due to those origins will be described.

Origin from inverse transfer matrices

In the real world, the initial inverse transfer matrices are imperfect as described in Sec. 4.6. The imperfections of inverse transfer matrices cause shift and broadening of a missing mass spectrum. The matrix optimization was done to make the inverse transfer matrices be closer to the perfect optical description of the spectrometer systems, thus the shift and broadening were minimized. Systematic errors originate from the matrix optimization process carefully needed to be estimated since the matrix optimization dominantly determine accuracy of binding energy and excitation energy of Λ hypernucleus.

To evaluate the systematic errors originate from the inverse transfer matrices, dummy data and distorted inverse transfer matrices were prepared and calibrated with the exactly same method as that for real data. The analysis for the dummy data were proceeded as the following (see also Fig. 4.51),

1. **Dummy data generation**
   Dummy data of Λ, Σ^0 and anything which covers interested kinematic regions (e.g. ${}^{12}_{\Lambda}$B) were generated. Effects of realistic detector resolution, spectrometer acceptance, beam energy spread ($\Delta E_e/E_e$), beam raster, energy straggling in target, production point displacement from the matrix origin etc. were taken into account when the dummy data were generated. The number of events, S/N and shape of background of the dummy data were adjusted to be same as those for real data of Λ, Σ^0 and ${}^{12}_{\Lambda}$B ground state which were used for the inverse transfer matrix optimization. Fig. 4.52 shows a missing mass of ${}^{12}_{\Lambda}$B with the initial transfer matrices.

2. **Distorted inverse transfer matrix generation**
   The inverse transfer matrices were almost perfect in the simulation. Therefore, the transfer matrices were distorted to reproduce real situations such as shift and broadening in missing mass spectrum. Distorted inverse transfer matrices were generated by inputting displaced and deteriorated information at the reference planes (RP) when they were calculated in the simulation (Sec. 4.7). The displacement of particle positions at RP were up to a few centimeter in both x and y directions. The position and angular information RP were deteriorated by Gaussian distribution with a sigma of up to a few centimeter

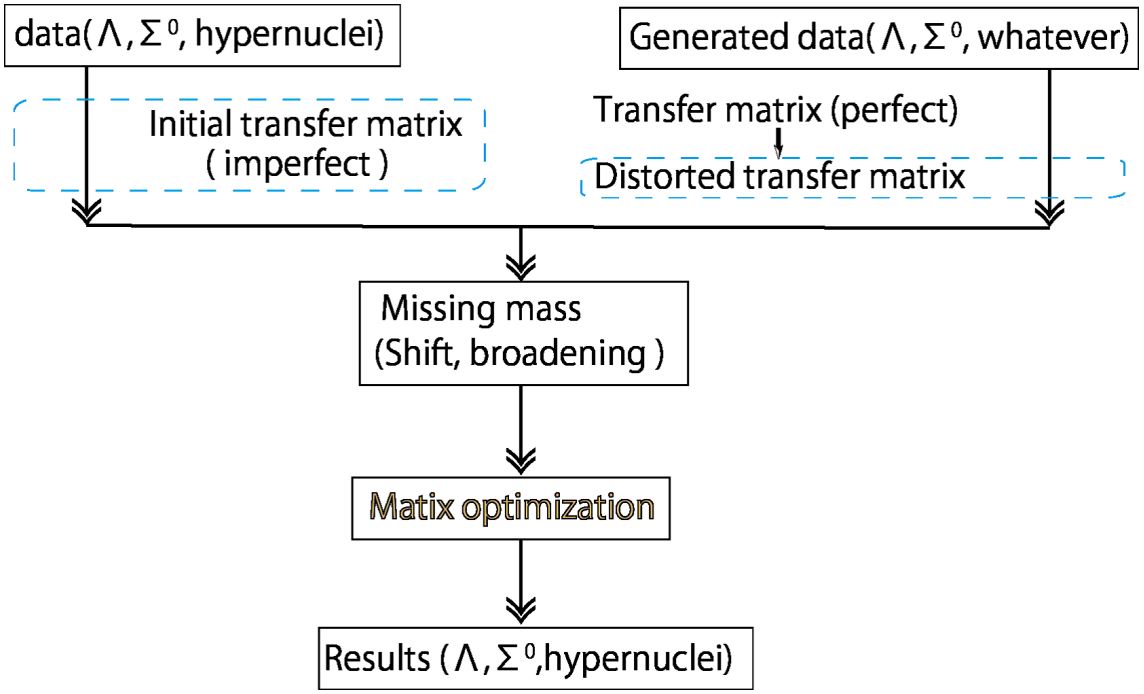

Figure 4.51: A flow chart of energy scale calibration process for real data and dummy data. Systematic errors of binding energy and excitation energy of Λ hypernucleus after the calibration was evaluated by using dummy data.

and a few mrad, respectively. Some of distortion patterns were applied when the distorted matrices were generated. Once distorted matrices were obtained, missing masses were reconstructed with them. Those missing masses reconstructed with distorted inverse transfer matrices were used for the further process. Fig. 4.53 shows a missing mass of $^{12}_{\Lambda}$B with distorted inverse transfer matrices.

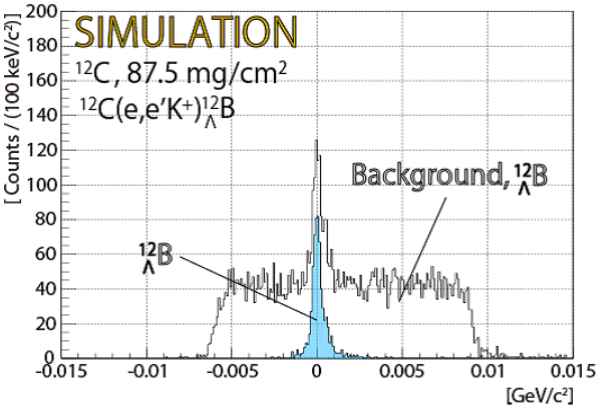

Figure 4.52: A missing mass spectrum of $^{12}_{\Lambda}$B with initial inverse transfer matrices.

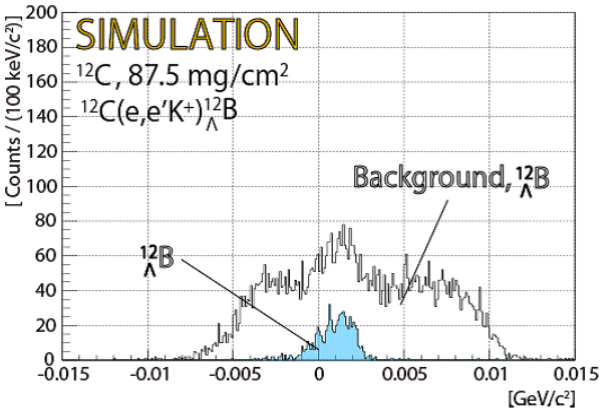

Figure 4.53: A missing mass spectrum of $^{12}_{\Lambda}$B with one of distorted inverse transfer matrices.

3. **Matrix optimization**
   The distorted inverse transfer matrices were optimized by using the exactly same code as that for real data. Fig. 4.54 shows a missing mass spectrum of $^{12}_{\Lambda}$B with the optimized inverse transfer matrices.

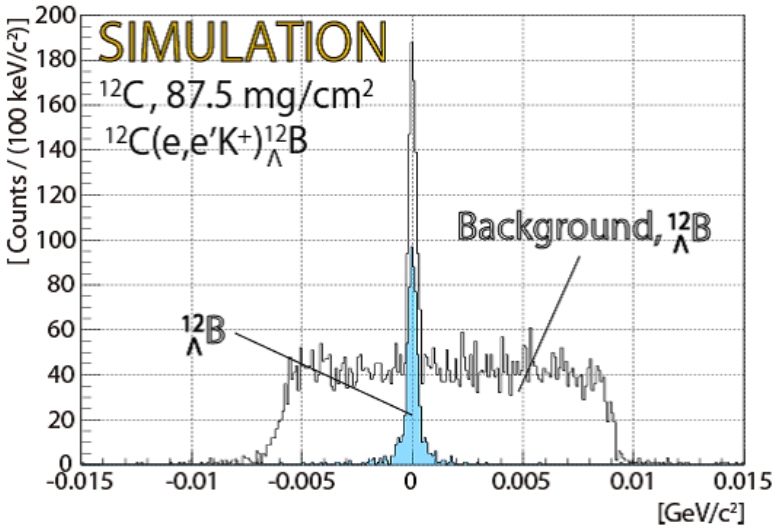

Figure 4.54: A missing mass spectrum of $^{12}_{\Lambda}$B with optimized inverse transfer matrices.

4. **Comparing tuned results to generated data**
   Results of the binding energies which were reconstructed by optimized inverse transfer matrices were compared to assumed binding energies.

The assumed binding energies which are compared with the optimization results are hidden from a person who performs the optimization to avoid an analysis bias. Thus, it is called blind analysis. A typical result will be shown below.

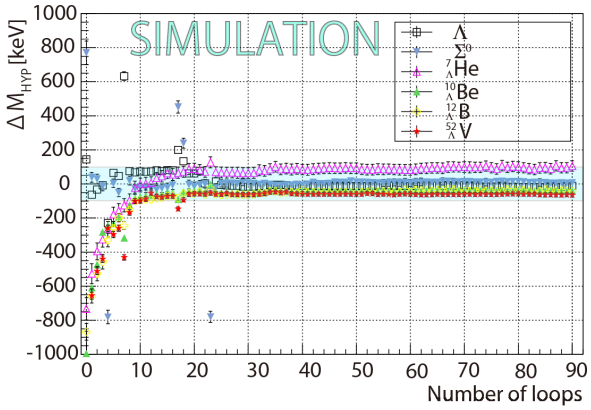

Figure 4.55: One of the results of blind analyses. The binding energy differences from assumed ones are plotted for every loop (five iterations for a loop).

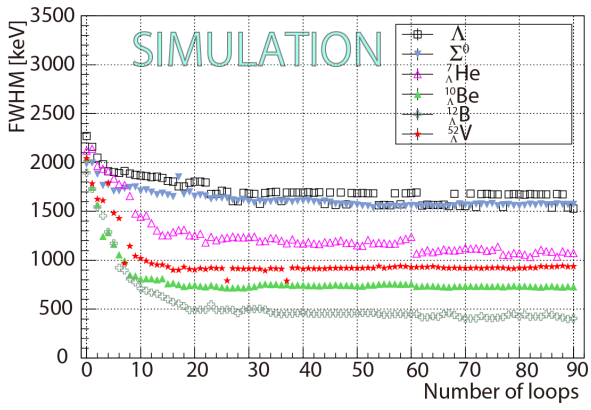

Figure 4.56: One of the results of blind analyses. The binding energy differences from assumed ones are plotted for every loop (five iterations for a loop).

Imitation data of Λ, Σ^0, $^{7}_{\Lambda}$He (assumed ground state binding energy, $-B_{\Lambda}^{\mathrm{g.s.}} = -5.5$ MeV), $^{9}_{\Lambda}$Li ($-B_{\Lambda}^{\mathrm{g.s.}} = -8.5$ MeV), $^{10}_{\Lambda}$Be ($-B_{\Lambda}^{\mathrm{g.s.}} = -8.7$ MeV), $^{12}_{\Lambda}$B ($-B_{\Lambda}^{\mathrm{g.s.}} = -11.37$ MeV), and $^{52}_{\Lambda}$V ($-B_{\Lambda}^{\mathrm{g.s.}} = -20.0$ MeV) with background events around their ground states were generated and those missing masses were reconstructed with the distorted matrices as an input for the inverse transfer matrix optimization. The distorted matrices were optimized by using Λ, Σ^0 and $^{12}_{\Lambda}$B in the same way as that for real data (Sec. 4.8.2). Fig. 4.55 and Fig. 4.56 show typical results

of blind analyses. Peak widths (FWHM) and binding energy differences from the assumed ones ($\Delta B_{\rm HYP}$) which were obtained by fitting to the missing mass spectra with Voigt functions were plotted for every loop (five iterations a loop) in the figures. The inverse transfer matrix optimization was terminated when the following conditions were satisfied,

- The fitting mean values of Λ and Σ^0 are close to their well knows values (PDG values $\pm$ a few 10 keV).
- Variations of the fitting mean values and FWHM become flat as shown in Fig. 4.55 and Fig. 4.56.

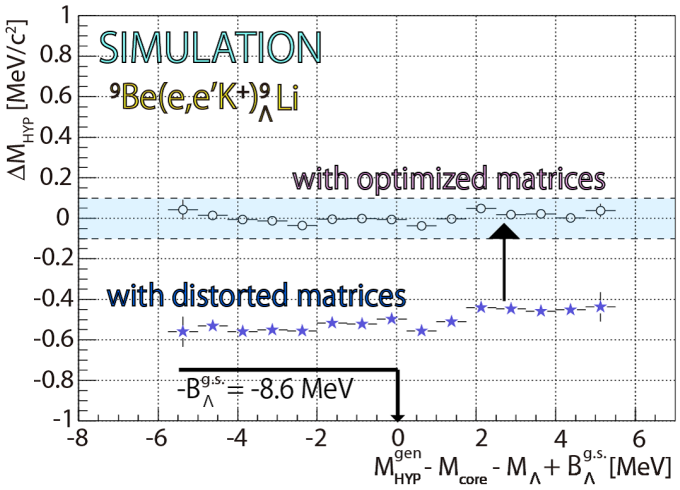

Figure 4.57: Missing mass difference from assumed one ($\Delta M_{\rm HYP}$) as a function of generated missing mass ($M^{\rm gen}_{\rm HYP} - M_{\rm core} - M_\Lambda + B^{\rm g.s.}_\Lambda$, meaning that $M^{\rm gen}_{\rm HYP} - M_{\rm core} - M_\Lambda + B^{\rm g.s.}_\Lambda = 0$ corresponds to the assumed ground state) before and after the inverse transfer matrix optimization.

Fig. 4.57 shows $\Delta M_{\rm HYP}$ as a function of generated missing mass ($M^{\rm gen}_{\rm HYP} - M_{\rm core} - M_\Lambda + B^{\rm g.s.}_\Lambda$, meaning that $M^{\rm gen}_{\rm HYP} - M_{\rm core} - M_\Lambda + B^{\rm g.s.}_\Lambda = 0$ corresponds to the assumed ground state) before and after the inverse transfer matrix optimization, for the ^{9}Be(e,e'K^+)$^9_\Lambda$Li. The data points with their statistical errors are distributed around generated values ($\Delta M_{\rm HYP} = 0$) after the inverse transfer matrix optimization.

A Y-axis projection of the data points after the inverse transfer matrix optimization (Fig. 4.57) is shown in Fig. 4.58. The distribution contributed by a statistical error of each data point ($\sigma_{\rm stat}$) and a differential non-linearity in the interested region due to the inverse transfer matrices ($\sigma_{\rm mat}$). Assuming that $\sigma_{\rm stat}$ and $\sigma_{\rm mat}$ are independent each other, the standard deviation of the histogram (σ) is considered to be:

$$\sigma = \sqrt{\sigma^2_{\rm stat} + \sigma^2_{\rm mat}} \tag{4.45}$$

where a mean value of statistical errors of data points was used as $\sigma_{\rm stat}$. Then, the differential non-linearity of interested region is calculated as the following:

$$\sigma_{\rm mat} = \sqrt{\sigma^2 - \sigma^2_{\rm stat}}\ . \tag{4.46}$$

One of the results of $\Delta B_{\rm HYP}$ and $\sigma_{\rm mat}$ for each hypernucleus (hyperon) is show in Table. 4.22.

The above tests were done with several distorted initial transfer matrices since the results depend on how the matrices were distorted. Finally, it was found that $\Delta B_{\rm HYP}$ and $\sigma_{\rm mat}$ are less

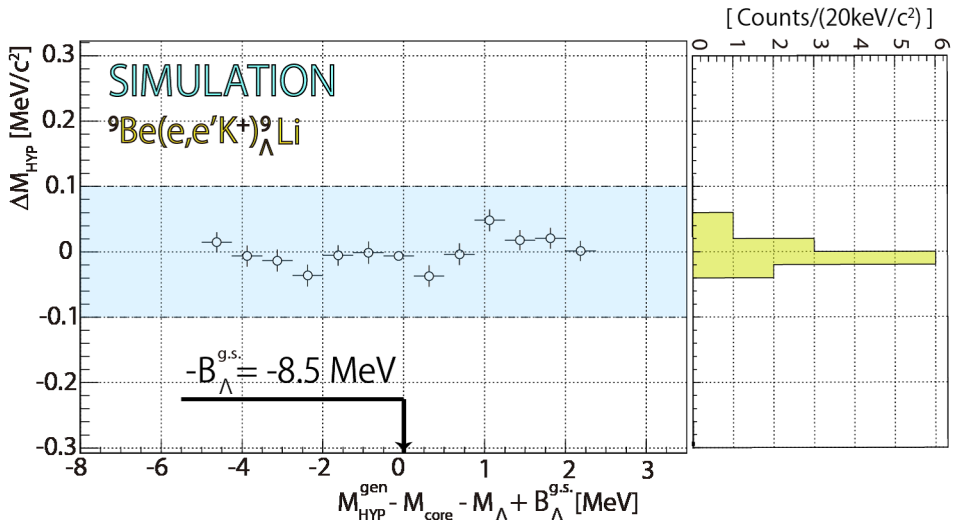

Figure 4.58: A projection of the data points on Y-axis after the inverse transfer matrix optimization in Fig. 4.57.

Table 4.22: A typical result of blind analyses showing the binding energy difference between fitting results and assumed ones ($\Delta B_{\rm HYP}$), and the differential non-linearity of each interested binding energy region due to inverse transfer matrices ($\sigma_{\rm mat}$).

Target (mg/cm^2)	Hypernucleus (Hyperon)	$\Delta B_{\rm HYP}$ [keV]	$\sigma_{\rm mat}$ [keV]
CH_2 (450.8)	Λ	-4.2 ± 11.0	21.2
	Σ^0	-15.3 ± 13.0	44.3
^{7}Li (208.0)	$^{7}_{\Lambda}$He	$+44.0 \pm 6.8$	23.0
^{9}Be (188.1)	$^{9}_{\Lambda}$Li	-25.4 ± 5.0	17.5
^{10}B (56.1)	$^{10}_{\Lambda}$Be	$+48.8 \pm 3.3$	19.9
^{12}C (87.5)	$^{12}_{\Lambda}$B	$+12.7 \pm 5.8$	15.6
^{52}Cr(134.0)	$^{52}_{\Lambda}$V	$+65.3 \pm 4.2$	5.2

than 80 keV and 50 keV, respectively after the inverse transfer matrix optimization. Therefore, the systematic error for binding energy due to inverse transfer matrices is considered to be $\sqrt{80^2 + 50^2} = 94$ keV. On the other hand, the systematic errors for excitation energy due to inverse transfer matrices is simply considered to be 50 keV ($\sigma_{\rm mat}$) as the obtained binding energy of ground state is subtracted from the results for the excitation energy calculation.

Target thickness uncertainty

The target thickness uncertainties are estimated to be 5% due to measurement accuracy. They correspond to ∼50 keV and a few 10 keV for Λ (Σ^0) and hypernuclei, respectively. The uncertainties of Λ and Σ^0 affect masses of hypernuclei since they were used for the inverse transfer matrix optimization as references. The target thickness uncertainty affects binding energy. On the other hand, the excitation energy in the interested range of a few 10 MeV for each Λ hypernucleus is not affected much since a basic behavior of the target thickness discrepancy is making a uniform shift of reconstructed missing mass.

Total systematic error for the excitation energy and binding energy

The total systematic errors for excitation energy and binding energy were respectively evaluated to be 50 keV and 110 keV for each Λ hypernucleus in the present study, considering possible discrepancy in the energy scale calibration process and the target thickness uncertainty.

4.11.2 Cross section

The cross section systematic errors which originate from uncertainties of efficiencies, correction factors and target thicknesses etc. The systematic errors for each target are summarized in Table. 4.23.

Table 4.23: Summary of cross section systematic errors.

	Cross section systematic error [%]						Remarks
Target	CH_2	^{7}Li	^{9}Be	^{10}B	^{12}C	^{52}Cr	
Hypernucleus (Hyperon)	Λ,Σ^0	$^{7}_{\Lambda}$He	$^{9}_{\Lambda}$Li	$^{10}_{\Lambda}$Be	$^{12}_{\Lambda}$B	$^{52}_{\Lambda}$V	
Virtual photon flux	±3.0						Sec. 4.10.1
HKS acceptance	±2.0						Sec. 4.10.2
Event counting	+7	±5.0					Sec. 4.10.2
H escape	±6.4	-					Sec. 4.10.2
Efficiencies, Correction factors	±4.4	±14.7	±7.3	±4.2	±9.6	-	Sec. 4.10.2
Target thickness	±5.0						
Total	+12,-10	±17	±10	±9	±12	-	

Chapter 5

Results and Discussion

At first, results of elementary processes of electroproduction of strangeness, p(e,e′K^+)Λ,Σ^0 which were used for the energy scale calibration will be shown. Subsequently, results of ^{12}C(e,e′K^+)$^{12}_{\Lambda}$B, ^{7}Li(e,e′K^+)$^{7}_{\Lambda}$He, ^{10}B(e,e′K^+)$^{10}_{\Lambda}$Be and ^{52}Cr(e,e′K^+)$^{52}_{\Lambda}$V will be shown and discussed.

5.1 Elementary production

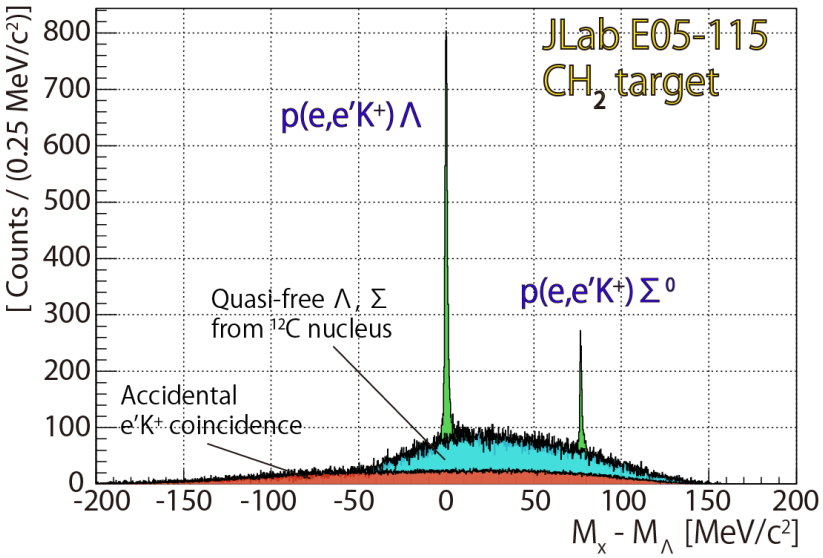

Figure 5.1: A missing mass spectrum of Λ and Σ^0 from the polyethylene target. Peaks of Λ and Σ^0 with the energy resolutions of $\sim$1.5 MeV (FWHM) are seen on widely distributed background events. The background events originate from 1) an accidental coincidence between K^+ and a scattered electron and 2) a quasi-free Λ from a ^{12}C nucleus in the polyethylene target.

p(e,e′K^+)Λ,Σ^0 were measured for the energy scale calibration and for studies of elementary processes of electroproduction of strangeness. Fig. 5.1 shows a missing mass spectrum of Λ and Σ^0 from the polyethylene target. The energy resolutions and mean value differences from the PDG values obtained by fitting are summarized in Table. 5.1. After the energy scale calibration with Λ and Σ^0, differences of mean values of Λ and Σ^0 from the PDG values are $+0.02 \pm 0.01$ MeV and -0.08 ± 0.03 MeV, respectively. The obtained widths of $\sim$1.5 MeV/c^2 (FWHM) are consistent with the estimations by the full-modeled Monte Carlo simulation as

Table 5.1: Mean value differences from PDG values and peak widths for Λ and Σ^0 after the energy scale calibration.

		Λ	Σ^0
Fitting with a Voigt function	$M_{\Lambda,\Sigma^0} - M_{\rm PDG}$ [MeV]	$+0.02 \pm 0.01$	-0.08 ± 0.03
	FWHM [MeV]	1.5	1.4
Number of events		5991±135	1696±103

shown in Sec. 4.6.2. Peaks of Λ and Σ^0 are seen with the energy resolution of ∼1.5 MeV (FWHM) on widely distributed background events. The background events originate from 1) an accidental coincidence between a K^+ and a scattered electron and 2) a quasi-free Λ from a ^{12}C nucleus in the polyethylene target. The background distribution from the latter source was deduced from from the independent data of the ^{12}C target. Fig. 5.2 shows a missing mass spectrum after the background distribution was subtracted. The number of events of Λ and Σ^0 were obtained by integrating histograms over each peak region without any fitting procedure.

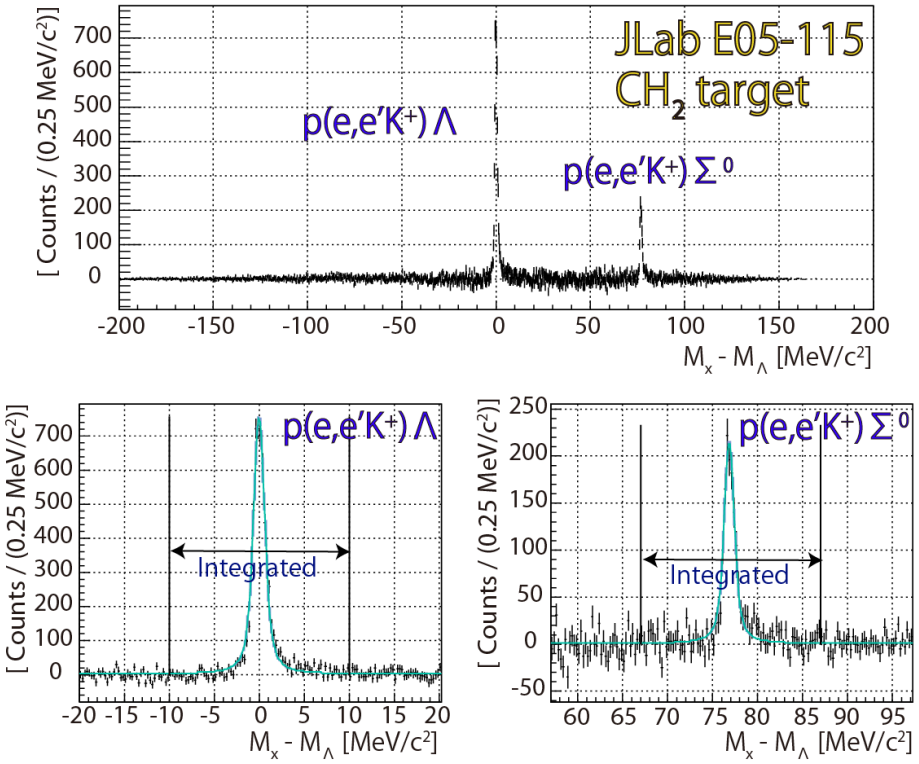

Figure 5.2: A missing mass spectrum of Λ and Σ^0 after the background distribution was subtracted.

The (e,e′K^+) experiments were performed at JLab and MAMI [78][79][80], and the differential cross sections of $K^+\Lambda$ and $K^+\Sigma^0$ productions were reported from some of them though the kinematics are different from each other. Fig. 5.3 shows the W and Q^2 coverage regions for those experiments. In the present experiment (JLab E05-115), data were taken at around $W = 1.92$ GeV and $Q^2 = 0.01$ [GeV/c]^2. The kinematic parameters are summarized in Table. 5.2.

Electroproduction results of $K^+\Lambda$ and $K^+\Sigma^0$ in our experiment can be compared with photoproduction data since covered Q^2 is quite small ($Q^2 = 0.01$ [GeV/c]^2). In this section,

Table 5.2: Typical kinematic parameters of experiments using the (e,e′K^+) reaction at JLab and MAMI.

Kinematic parameters	JLab					MAMI
	E05-115 (Hall C)	E01-011 (Hall C)	E89-009 (Hall C)	E91-016 (Hall C)	E94-107 (Hall A)	
E_e [GeV]	2.344	1.85	1.86	3.25	4.92/3.78/3.66	1.508
ω [GeV]	1.5	1.5	1.5	1.68	3.12/2.2/2.2	1.1
Q^2 [GeV/c]^2	0.01	0.004	∼0	0.35	0.07	0.05
W [GeV]	1.92	1.92	1.92	1.91	2.2	1.7
ϵ	0.63	0.34	∼1	0.83	0.68	0.4-0.5
$p_{e'}^{\rm lab}$ [GeV/c]	0.844	0.32	0.28	1.57	1.8/1.57/1.44	0.4
$\theta_{e'}^{\rm lab}$ [deg]	6.0	4.5	0.0	14.9	6.0	15.0
$p_K^{\rm lab}$ [GeV/c]	1.2	1.2	1.2	1.29	1.96	0.5
$\theta_K^{\rm lab}$ [deg]	7.0	7.0	7.0	13.4	6.0	32.0

results of electroproduction cross section of $K^+\Lambda$ will be shown comparing with photoproduction results of SAPHIR [42][43] and CLAS [41].

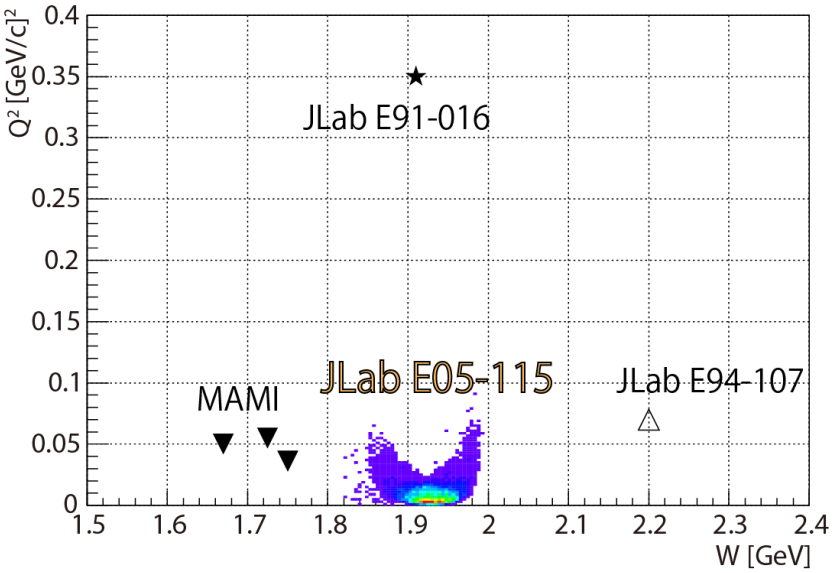

Figure 5.3: W and Q^2 coverage region for the p(e,e′K^+)Λ, Σ^0 measurement at JLab and MAMI experiments.

5.1.1 Angular dependence

The angular acceptance of HKS was divided by two regions to see angular dependence of the cross section. The cut conditions of $0.000 < \theta_K^{\rm lab} < 0.090$ rad and $0.090 < \theta_K^{\rm lab} < 0.025$ rad were applied, which correspond to $\theta_{\gamma K}^{\rm CM} = 0.270$ rad and $\theta_{\gamma K}^{\rm CM} = 0.351$ rad. The angular cut conditions were applied in the laboratory frame since the HKS solid angle which depends on particle momentum was evaluated in a single arm Monte Carlo simulation (SPL+HKS) and considered event by event for the cross section derivation. The total energy in the CM frame,

W was chosen to be $1.922 < W < 1.947$ GeV by choosing a momentum of scattering electron to be compared with the same W region of SAPHIR.

Table 5.3: The differential cross section of $K^+\Lambda$ and $K^+\Sigma^0$ for $\theta^{\rm CM}_{\gamma K} = 0.197, 0.351$ rad. The cross section with whole angular acceptance ($\theta^{\rm lab}_{eK}$ =0.000-0.250 rad corresponding to $\theta^{\rm CM}_{\gamma K} = 0.270$) is also shown as data point 3. ($1.922 < W < 1.947$ GeV, $Q^2 = 0.007$ [GeV/c]^2, ϵ =0.63)

Data point	Cut condition	$\theta^{\rm CM}_{\gamma K}$	Number of events		$\overline{\left(\frac{d\sigma}{d\Omega_K}\right)}$ [nb/sr]	
	$\theta^{\rm lab}_{eK}$ [rad]	[rad] ([deg])	Λ	Σ^0	Λ	Σ^0
1	0.000-0.090	0.197 (11.3)	201±21	188±45	$347\pm38^{+42}_{-35}$	$146\pm36^{+18}_{-15}$
2	0.090-0.250	0.351 (20.1)	420±29	31±21	$210\pm14^{+25}_{-21}$	$63\pm29^{+8}_{-6}$
3 (1, 2)	0.000-0.250	0.270 (15.5)	623±36	199±51	$235\pm13^{+28}_{-24}$	$97\pm24^{+12}_{-10}$

The results (Table. 5.3) superimposing with photoproduction data of SAPHIR and CLAS, and two theoretical predictions are shown in Fig. 5.4. The boxes in the figure indicate errors with systematic errors. The theoretical calculations are Kaon-Maid (KMAID) [82] and Saclay-Lyon A (SLA) [81] which are isobaric models. Major differences of these two models are the choice of particular resonances in the intermediate state and treatment of hadron structures in the strong vertices. Hadrons are treated as a point-like particle in SLA whereas hadronic form factors are included in the hadronic vertices in KMAID. Thus, the cross sections at small $\theta^{\rm CM}_{\gamma K^+}$ in KMAID are suppressed as shown in the figure. The present results show the cross section is larger at the smaller $\theta^{\rm CM}_{\gamma K}$ indicating a similar tendency to SLA. Three data points of JLab E91-016 [83] were also plotted though Q^2(= 0.35 [GeV/c]^2) is rather larger. The data show forward peak for the cross section as well. JLab E94-107 reported a data at $\theta^{\rm CM}_{\gamma K} = 6.0$ degree, $W = 2.2$ GeV and $Q^2 = 0.07$ [GeV/c]^2 [84]. W of JLab E94-107 experiment is larger than that of our experimental data. Assuming a measured W dependence reported in Ref. [41] (CLAS), the data point of JLab E94-107 should be shifted up by 25% ($d\sigma/d\Omega$ >630 nb/sr) to be compared with our experimental results. The result indicates steep angular dependence in smaller $\theta^{\rm CM}_{\gamma K}$ region, which cannot be explained theoretically so far. There might be a complex Q^2 dependence in small Q^2 region (Q^2 <0.5 [GeV/c]^2), that is related to longitudinal term contributions to the cross sections. Systematic studies with different Q^2 and other kinematics particularly at forward K^+ scattering angle are needed to understand further.

5.1.2 Q^2 dependence

Q^2 regions were selected by applying cuts of scattering angle of scattered electrons with respect to incident beam in the laboratory frame ($\theta_{ee'}$). The results of $K^+\Lambda$ and $K^+\Sigma^0$ at $Q^2 = 0.003$, 0.007 and 0.013 [GeV/c]^2 are shown in Table. 5.4. The differential cross sections as a function of Q^2 is shown in Fig. 5.5 superimposing with data of photoproduction (SAPHIR [42][43], $Q^2 = 0$ [GeV/c]^2) in $1.922 < W < 1.947$ GeV. The boxes on the data points indicate errors with systematic errors. The results shows that there is no Q^2 dependence for $Q^2 < 0.013$ [GeV/c]^2 in the error bars.

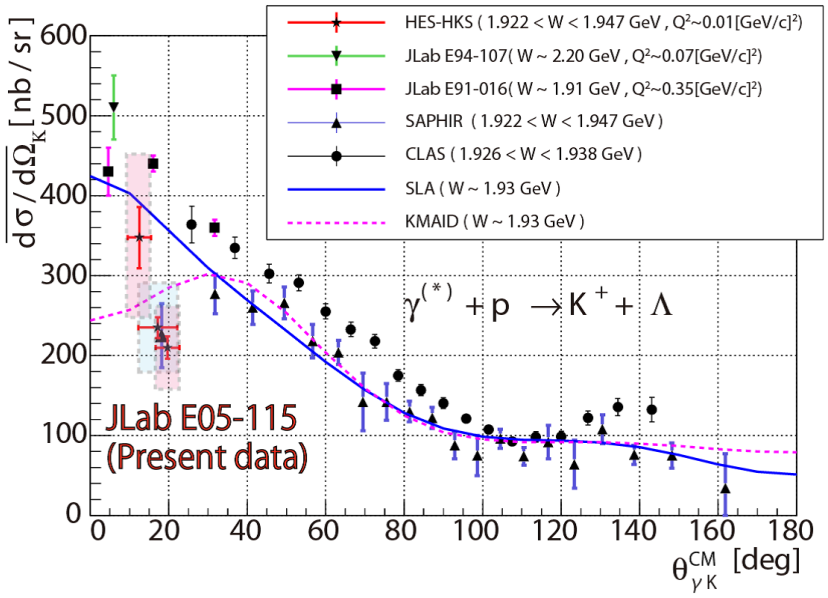

Figure 5.4: Results of the differential cross section of $K^+\Lambda$ production superimposing with other electroproduction data (JLab E91-016 [83], JLab E94-107 [84]), photoproduction data of SAPHIR [42][43] and CLAS [41], and two theoretical calculations (SLA [81], KMAID [82]).

Table 5.4: The differential cross sections of $K^+\Lambda$ and $K^+\Sigma^0$ at Q^2 = 0.003, 0.007 and 0.013 [GeV/c]^2. ($1.922 < W < 1.947$ GeV, $\theta^{\rm CM}_{\gamma K} = 0.28$ rad, ϵ =0.63)

Data point	Cut condition $\theta^{\rm lab}_{ee'}$ [rad]	Q^2 [GeV/c]^2	Number of events		$\overline{\left(\frac{d\sigma}{d\Omega_K}\right)}$ [nb/sr]	
			Λ	Σ^0	Λ	Σ^0
1	0.030-0.050	0.003	204±20	49±20	$198\pm29^{+24}_{-20}$	$66\pm36^{+8}_{-7}$
2	0.050-0.070	0.007	164±18	43±26	$183\pm21^{+22}_{-18}$	$61\pm36^{+7}_{-6}$
3	0.070-0.100	0.013	171±19	64±25	$190\pm21^{+23}_{-19}$	$98\pm35^{+12}_{-10}$

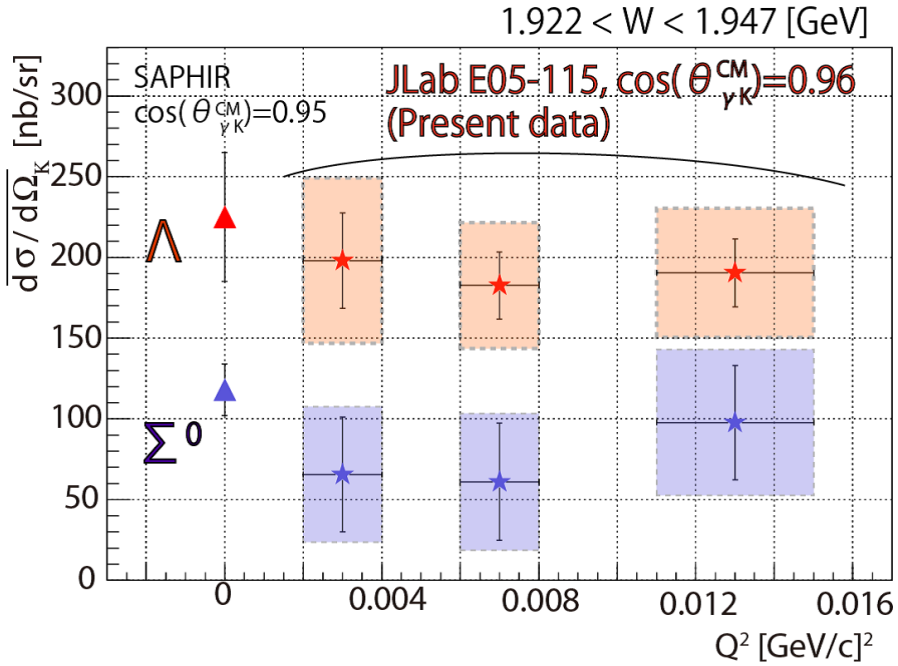

Figure 5.5: The differential cross sections for $K^+\Lambda$ and $K^+\Sigma^0$ electroproductions as a function of Q^2 superimposing with photoproduction data (SAPHIR [42][43], $Q^2 = 0$ [GeV/c]^2) in $1.922 < W < 1.947$ GeV. The distributions are flat for $Q^2 < 0.013$ [GeV/c]^2 in the error bars.

5.2 ^{12}C(e,e′K^+)$^{12}_{\Lambda}$B

$^{12}_{\Lambda}$B has been already measured in the previous (e,e′K^+) experiments. Thus, experimental results of this hypernucleus can be used for a consistency confirmation with the previous experiments. In this section, experimental results of $^{12}_{\Lambda}$B will be shown, and those of prominent peaks ($[1^-, 2^-]$ and $[2^+, 3^+]$) will be compared with the previous experimental results.

5.2.1 Results

Fig.5.6 shows a binding energy spectrum of ^{12}C(e,e′K^+)$^{12}_{\Lambda}$B. A distribution of the accidental background events shown in the figure was obtained by the mixed event analysis (Sec. 4.9) to make contributions of its statistical errors negligible small when the accidental coincidence events are subtracted from the original histogram. The ordinate axis in the figure was converted to the differential cross section for the ^{12}C(γ^*,K^+)$^{12}_{\Lambda}$B reaction by using Eq. (4.31), and the results is shown in Fig. 5.7.

Peak fitting

Fitting to the binding energy spectrum was performed as the following:

- **Accidental coincidence background event subtraction (① in Fig. 5.8)**
  The accidental coincidence background distribution which was obtained by the mixed event analysis (Sec. 4.9) was subtracted from the original binding energy spectrum.

- **Estimation of quasi-free Λ background distribution (① in Fig. 5.8)**
  A quasi-free Λ background distribution was obtained by fitting to the missing mass spectrum in the region of $+5 < -B_\Lambda < +20$ MeV by the third order polynomial function (Solid

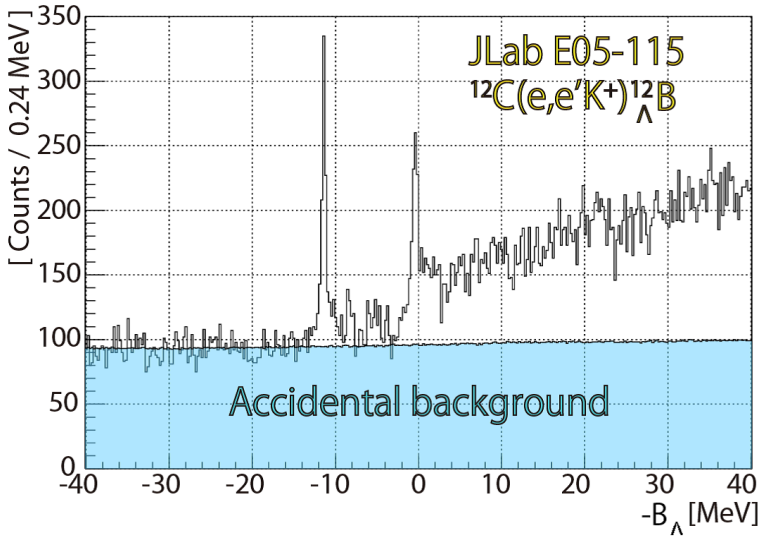

Figure 5.6: A binding energy spectrum for the ^{12}C(e,e'K^+)$^{12}_{\Lambda}$B. A distribution of the accidental background events shown in the figure was obtained by the mixed event analysis (Sec. 4.9).

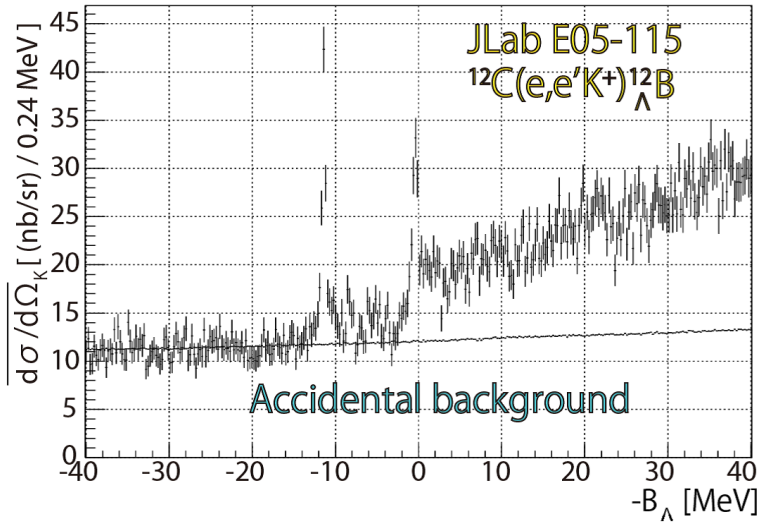

Figure 5.7: A binding energy spectrum for the ^{12}C(e,e'K^+)$^{12}_{\Lambda}$B. The ordinate axis is the differential cross section for the (γ^*,K^+) reaction which was defined in Eq. (4.31).

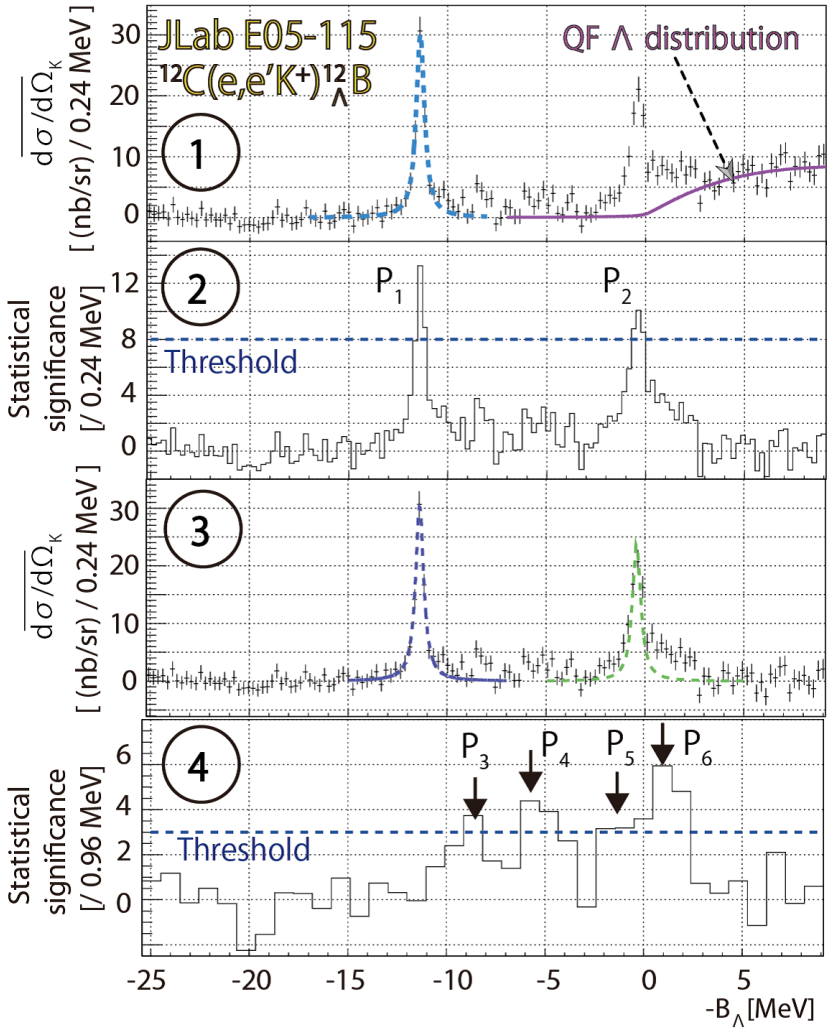

Figure 5.8: ①; A quasi-free Λ distribution was estimated by fitting with a third order polynomial function. The third order polynomial function was convoluted by a Voigt function of which parameters were determined by fitting to the first peak (dashed line) to take into account the energy resolution. ②; The quasi-free Λ distribution was subtracted, and the ordinate axis was converted to the statistical significance($= \frac{S}{\sqrt{S+N}}$). Peaks which are above a threshold ($\geq 8\sigma$ [/0.24 MeV]) were chosen as peak candidates for the final fitting ($P_{1,2}$). ③; $P_{1,2}$ were fitted with Voigt functions with the same width. The width was determined by fitting to P_1. ④; After the fitting functions of $P_{1,2}$ were subtracted, the ordinate axis was converted to the statistical significance. Peaks which are above a threshold ($\geq 3\sigma$ [/0.96 MeV]) were chosen as peak candidates for the final fitting ($P_{3,4,5,6}$).

line in ①). A contribution of the missing mass resolution to the quasi-free background distribution (polynomial function) was taken into account by convoluting a Voigt function of which parameters was determined by fitting to the first prominent peak (dashed line in ①, FWHM = 0.5 MeV).

- **Significant peak selection 1 (② in Fig. 5.8)**
  After the quasi-free background distribution was subtracted, the ordinate axis was converted to the statistical significance ($= \frac{S}{\sqrt{S+N}}$) (②). Peaks of P_1 and P_2, which are above a threshold of the peak significance ($\geq 8\sigma$ [/0.24 MeV]) were identified as peak candidates for the final fitting.

- **Prominent peak subtraction (③ in Fig. 5.8)**
  The peaks which were identified as peak candidates for fitting in ② were fitted by Voigt functions with a same width. The width was determined by fitting to P_1. The distributions of the two peak candidates were subtracted, and the ordinate axis was converted to the peak significance, which will be used in the next procedure (④).

- **Significant peak selection 2 (④ in Fig. 5.8)**
  Peaks of $P_{3,4,5,6}$ which are above a threshold of the statistical significance ($\geq 3\sigma$ [/0.96 MeV]) were identified as peak candidates for the final fitting.

- **Fitting to the selected peaks**
  At first, P_1 was fitted with a Voigt function to obtain a width which will be used for further process. Obtained width was 0.5 MeV (FWHM) that is considered to be an our experimental energy resolution for $^{12}_{\Lambda}$B. Then, $P_{1,2,3,4}$ were fitted with four Voigt functions with the same width. Events which remained after the four Voigt functions and the qasi-free Λ distribution were subtracted ($P_{5,6}$), were distributed widely rather than the energy resolution. Therefore, some states which cannot be separated by the experimental energy resolution are considered to be contained in $P_{5,6}$. Thus, in the present study, widths of Voigt functions for $P_{5,6}$ were not fixed at 0.5 MeV (FWHM). Finally, the third order polynomial function which was convoluted by a Voigt function of which parameters were determined by fitting to the P_1 for quasi-free Λ events, four Voigt functions with FWHM = 0.5 MeV for $P_{1,2,3,4}$, and two Voigt functions for $P_{5,6}$ were used for the final fitting. The obtained peak widths for $P_{5,6}$ were 1.1 MeV and 2.0 MeV, respectively. The reduced χ^2 of the fitting was 1.12. The fitting results are shown in Fig. 5.9.

Obtained binding energy, excitation energy and differential cross section for peak number 1 to 4 are summarized in Table. 5.5. State assignments for these peaks will be explained in Sec. 5.2.2. The peak assignments for the peak number 5 and 6 which have the differential cross sections of about 10 nb/sr and 50 nb/sr were not performed in the present study since it is hard to distinguish the states contained in those peaks by the experimental energy resolution.

5.2.2 Discussion

Comparison with past experiments

The binding energy of $^{12}_{\Lambda}$B was measured by both the emulsion [34] and the (e,e'K^+) experiments [28][29][32]. Therefore, results of the binding energy and the cross section can be compared with each other to check the consistencies. The results of present study and those measured in the past experiments are summarized in Table. 5.6.

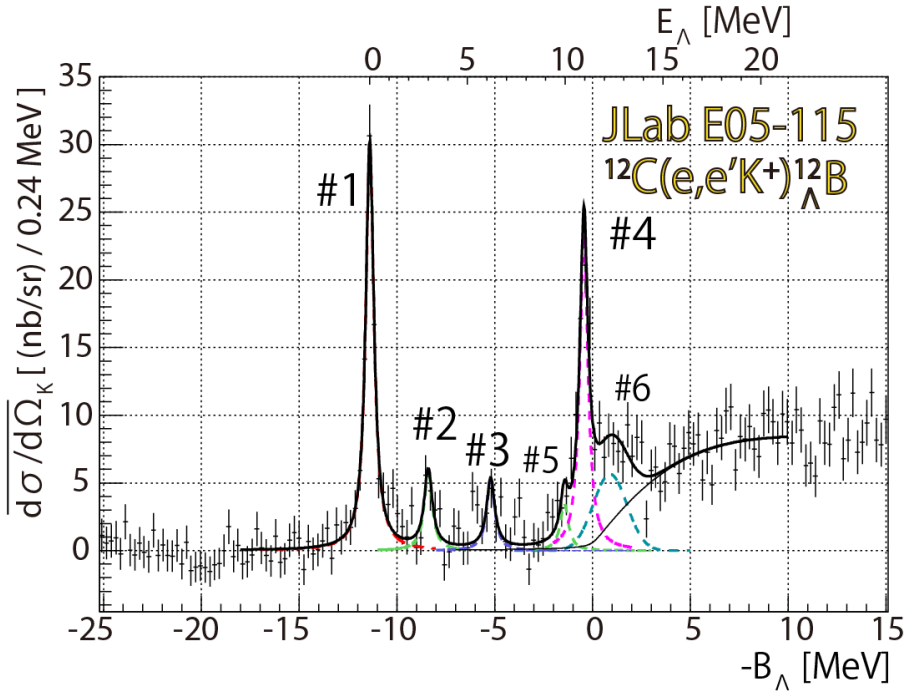

Figure 5.9: A binding energy spectrum after the accidental background events were subtracted. The spectrum was fitted with Voigt functions for peaks and a third order polynomial function for a quasi-free Λ events. The width of the Voigt functions for peak number 1, 2, 3 and 4 is 0.50 MeV in FWHM. The width of 0.5 MeV in FWHM was determined by fitting to the first peak (peak number 1).

Table 5.5: Fitting results of binding energy, excitation energy and differential cross section for each peak of ^{12}C(e,e′K^+)$^{12}_{\Lambda}$B.

Peak number	State ^{11}B$[J_C; E_\Lambda] \otimes j^\Lambda$	Number of events	$-B_\Lambda$ [MeV] (E_Λ)	$\overline{\left(\frac{d\sigma}{d\Omega_K}\right)}\Big\vert_{1^\circ-13^\circ}$ [nb/sr]
1	1^-, 2^- $[3/2^-;$ g.s.$] \otimes s^\Lambda_{1/2}$	774±15	-11.38±0.02±0.11 (0.0)	97.5±1.9±11.7
2	1^-, 0^- $[1/2^-;$ 2.12$] \otimes s^\Lambda_{1/2}$	149±3	-8.39±0.06±0.11 (2.99±0.06±0.05)	18.8±0.4±2.2
3	2^-, 1^- $[3/2^-;$ 5.02$] \otimes s^\Lambda_{1/2}$	133±3	-5.20±0.09±0.11 (6.18±0.09±0.05)	16.8±0.4±2.0
4	2^+, 3^+ $[3/2^-;$ g.s.$] \otimes p^\Lambda_{1/2}$ $[3/2^-;$ g.s.$] \otimes p^\Lambda_{3/2}$	598±12	-0.44±0.03±0.11 (10.95±0.03±0.05)	75.3±1.5±9.0

Obtained binding energies of the peak number 1 (1^-, 2^-) and the peak number 2 (2^+, 3^+) are:

$$\begin{aligned} -B_\Lambda(1^-, 2^-) &= -11.38 \pm 0.02(\text{stat.}) \pm 0.11(\text{sys.}) \text{ MeV}, \\ -B_\Lambda(2^+, 3^+) &= -0.44 \pm 0.03(\text{stat.}) \pm 0.11(\text{sys.}) \text{ MeV}, \end{aligned}$$

respectively. These results are consistent with past experiments within the errors. The obtained differential cross sections for the peak number 1 and 2 were $97.7 \pm 1.9 \pm 11.7$ nb/sr and $75.3 \pm 1.5 \pm 9.0$ nb/sr, respectively. In order to compare these results to the other experimental results of JLab E89-009[28][29] and JLab E01-011 [32], the K^+ scattering angle with respect to the virtual photon should be taken into account. The mean value of the K^+ scattering angle ($\theta_{\gamma K}$) with respect to the virtual photon are $\theta_{\gamma K} = 6.8$, 5.8 and 0 degrees for E05-115, E01-011 and E89-009 experiments, respectively. In the theoretical calculations in the DWIA framework by T.Motoba [86], ratios of the differential cross sections of E05-115 (present work) to those of E01-011 and E89-009 are:

$$\begin{aligned} & (\text{E05}-115) : (\text{E01}-011) : (\text{E89}-009) \\ = \; & 1 : 1.33 : 1.60 \quad \text{for } s_\Lambda, \\ & 1 : 1.10 : 1.35 \quad \text{for } p_\Lambda, \end{aligned}$$

respectively. On the other hand, the ratios of the differential cross sections for the experimental results are:

$$\begin{aligned} & (\text{E05}-115) : (\text{E01}-011) : (\text{E89}-009) \\ = \; & 1 : 1.03 \pm 0.06^{+0.58}_{-0.39} : 1.43 \pm 0.18^{+0.40}_{-0.32} \quad \text{for } s_\Lambda, \\ & 1 : 1.25 \pm 0.06^{+0.70}_{-0.55} : (N/A) \quad \text{for } p_\Lambda, \end{aligned}$$

respectively. Assuming the theoretical calculation, the differential cross sections of JLab E05-115 (present work) are consistent with the past experiments within the errors.

Table 5.6: Comparison of experimental results of the binding energy, excitation energy and the differential cross sections of $^{12}_{\Lambda}$B for s_Λ (1^-, 2^-) and p_Λ (2^+, 3^+).

Experiment ($\theta_{\gamma K}$ [deg])	$-B_\Lambda$ [MeV] (E_Λ [MeV])		$\overline{\left(\frac{d\sigma}{d\Omega_K}\right)}\Big\|_{1^\circ-13^\circ}$ [nb/sr] (Prediction [86])	
	s_Λ (1^-, 2^-)	p_Λ (2^+, 3^+)	s_Λ (1^-, 2^-)	p_Λ (2^+, 3^+)
JLab E05-115 (6.8)	-11.38±0.02±0.11 (0.0)	-0.44±0.03±0.11 (10.95±0.03±0.05)	97.7±1.9±11.7 (75)	75.3±1.5±9.0 (65)
JLab E01-011 [32] (5.8)	-11.40±0.02±0.14 (0.0)	-0.35±0.01±0.13 (11.05±0.01±0.19)	$101.0 \pm 4.2^{+38}_{-31}$ (85)	94.0±4.0±35.0 (72)
JLab E89-009 [28][29] (0.0)	-11.52±0.35 (0.0)	-0.49±0.16 (11.03±error)	140.0±17±18 (120)	- (88)
Emulsion [34]	-11.37±0.06 (0.0)	- (-)	- (-)	- (-)

Both the binding energies and the differential cross sections of the present experiment (JLab E05-115) for s_Λ and p_Λ are confirmed to be consistent with those of the previous experiments within the errors. It has proven that our new spectrometer systems, SPL(new)+HES(new)+HKS which were dedicated to the Λ hypernuclear measurement worked as well as what we designed.

Comparison with a mirror hypernucleus, $^{12}_{\Lambda}$C

A structure of $^{12}_{\Lambda}$B can be compared with a mirror Λ hypernucleus, $^{12}_{\Lambda}$C. Spectroscopically $^{12}_{\Lambda}$C has been measured in (K^-,π^-) and (π^+,K^+) experiments. In the (K^-,π^-) and (π^+,K^+) experiments, the ground state binding energy of $^{12}_{\Lambda}$C was adjusted to be the results of emulsion experiments [87]. It should be emphasized that the absolute energy scale is calibrated by using masses of Λ and Σ^0 in the (e,e′K^+) reaction experiment. The ground state binding energies of $^{12}_{\Lambda}$B (present data) and $^{12}_{\Lambda}$C are different by $0.62 \pm 0.19 \pm 0.11$ MeV (see also Table. 5.13 in Sec. 5.5.2), which cannot be theoretically explained yet. The binding energy difference between $^{12}_{\Lambda}$B and $^{12}_{\Lambda}$C will be discussed with experimental results of $^{52}_{\Lambda}$V in Sec. 5.5.2.

Fig. 5.10 shows spectra of $^{12}_{\Lambda}$C [24] measured at KEK (top) and $^{12}_{\Lambda}$B measured in the present experiment (bottom). Global structures are similar with each other (Fig. 5.11). The energy resolutions for the spectra of $^{12}_{\Lambda}$C and $^{12}_{\Lambda}$B are 1.45 MeV and 0.50 MeV in FWHM, respectively. The energy resolution of the present study is almost three times better than that of the (π^+, K^+) experiment, and it is the world best energy resolution in reaction spectroscopic experiments of Λ hypernuclei.

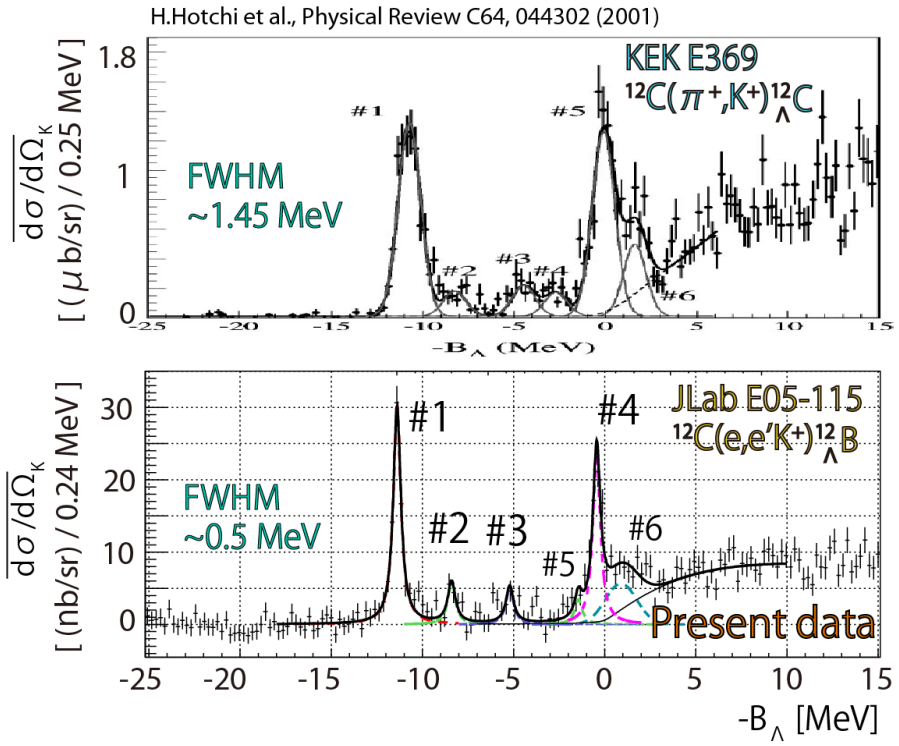

Figure 5.10: Binding energy spectra of $^{12}_{\Lambda}$C measured by the (π^+,K^+) reaction at KEK [24] and $^{12}_{\Lambda}$B measured in the present experiment. The FWHMs for the spectra of $^{12}_{\Lambda}$C and $^{12}_{\Lambda}$B are 1.45 MeV and 0.5 MeV, respectively.

Comparison with theoretical calculations

Fig. 5.11 shows the binding energy of the experimental results and theoretical calculations for $^{12}_{\Lambda}$B and $^{12}_{\Lambda}$C. State assignments for the obtained peaks shown in Table. 5.5 were based on the shell model calculation by T. Motoba [86]. The peak number 1 and 4 which are prominent peaks are interpreted to be 1^-, 2^- states ($[3/2^-;\text{g.s.}]\otimes s^{\Lambda}_{1/2}$) and 2^+, 3^+ states ($[3/2^-;\text{g.s.}]\otimes p^{\Lambda}_{1/2}, p^{\Lambda}_{3/2}$). These states were already measured in the past (e,e′K^+) experiments, and the results were

compared in Table. 5.6. The peak number 2 and 3 are considered to be states which a Λ sitting in *s*-orbit couples with the excited states of ^{11}B nucleus. Structures of these core excited were also measured and reported in the previous (e,e′K^+) experiments [32][38][39]. The peak number 7, 8 and 9 are states which a Λ sitting in *p*-orbit couples with the excited states of ^{11}B, which could not be separately measured by the experimental resolution.

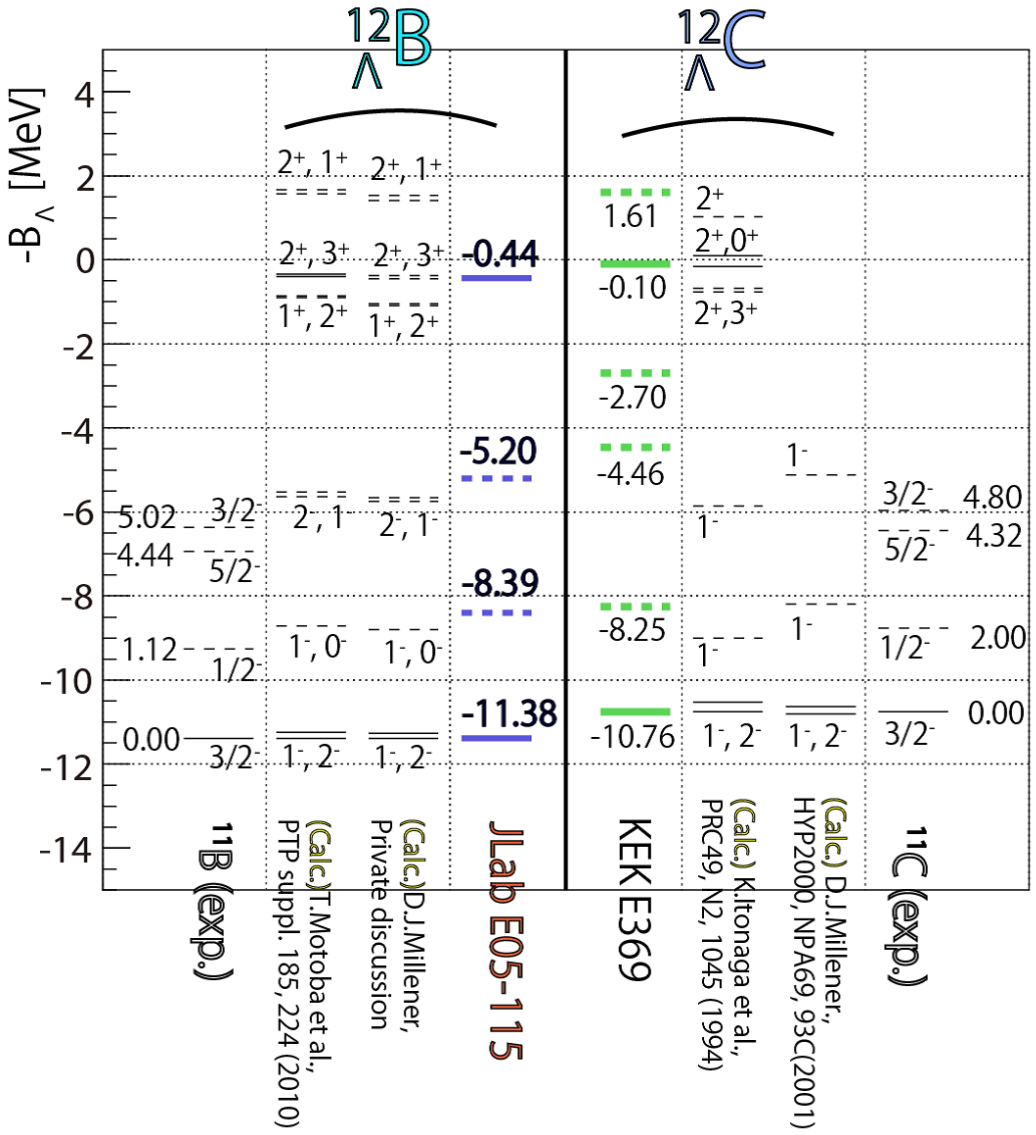

Figure 5.11: Binding energies of the experimental results and theoretical calculations for $^{12}_{\Lambda}$B and $^{12}_{\Lambda}$C. The ground state binding energies of the theoretical calculations were adjusted to be those of experimental results for $^{12}_{\Lambda}$B and $^{12}_{\Lambda}$C.

5.3 ^{7}Li(e,e′K^{+})$^{7}_{\Lambda}$He

The binding energy of $^{7}_{\Lambda}$He ground state ($1/2^{+}$) was measured in the previous (e,e′K^{+}) experiment (JLab E01-011). In the present experiment (JLab E05-115), data with five times higher statistic were taken for this hypernucleus than that of JLab E01-011. In this section, results of the ground state binding energy with smaller error will be shown with discussion of charge symmetry breaking effect in ΛN interaction. Moreover, results of the excited states ($3/2^{+}$, $5/2^{+}$) which cannot be separated by the experimental energy resolution will be shown and discussed for the first time.

5.3.1 Results

A binding energy spectrum of the $^{7}_{\Lambda}$He is shown in Fig.5.12. The ordinate axis was converted into the differential cross section for the (γ^{*},K^{+}) reaction by using Eq. (4.31), and the result is shown in Fig. 5.13.

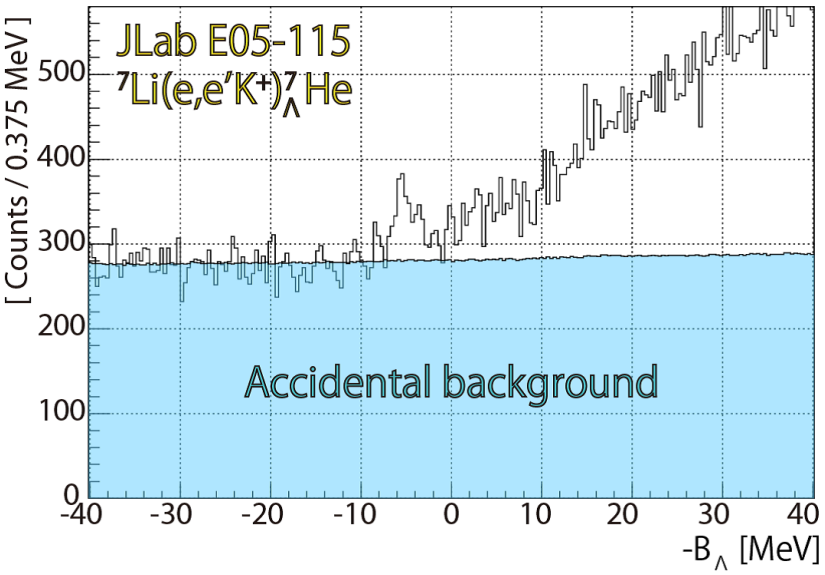

Figure 5.12: A binding energy spectrum of ^{7}Li(e,e′K^{+})$^{7}_{\Lambda}$He.

Peak fitting

A peak fitting to obtain the binding energy and differential cross section was performed as the following:

- **Significant peak search**
  The accidental coincidence background distributions which was obtained by the mixed event analysis (Sec. 4.9) was subtracted from the original binding energy spectrum,and the ordinate axis was converted to the statistical significance ($= \frac{S}{\sqrt{S+N}}$) (Fig. 5.14). The statistical significance is shown for different binning of 0.375 MeV/bin and 0.780 MeV/bin. Peaks ($P_{1,2}$) which are above a threshold ($\geq 4\sigma$ for 0.780 MeV/bin) were chosen as peak candidates for the final fitting.

- **Fitting to the spectrum**
  A fitting with two Voigt functions was performed for $P_{1,2}$ after the accidental background

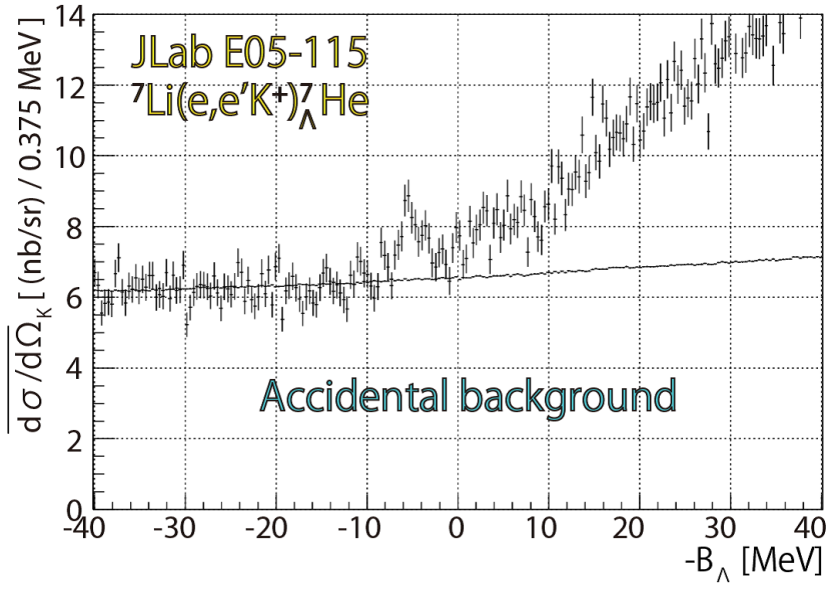

Figure 5.13: The binding energy spectrum of ^{7}Li(e,e'K^{+})$^{7}_{\Lambda}$He. The vertical axis is the differential cross section for the (γ^{*},K^{+}) reaction.

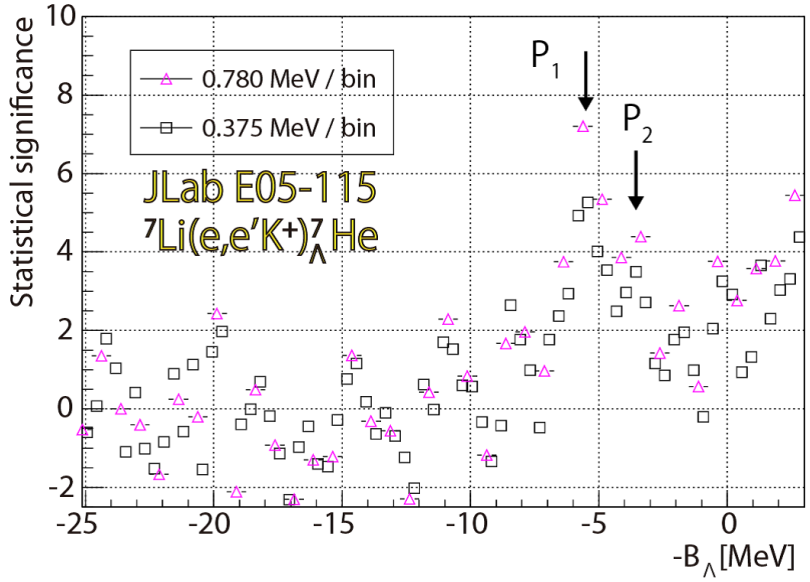

Figure 5.14: Statistical significance for the ^{7}Li(e,e'K^{+})$^{7}_{\Lambda}$He. Peaks ($P_{1,2}$) which are above a threshold ($\geq 4\sigma$ for 0.780 MeV/bin) were chosen as peak candidates for the final fitting.

events were subtracted from the original spectrum, assuming that widths of the two peaks are the same. Obtained width was 1.3 MeV in FWHM which is consistent with the estimation by the full-modeled Mote Carlo simulation (Sec. 4.6.2). The fitting result with $\chi^2/\mathrm{NDF} = 0.96$ is shown in Fig. 5.15.

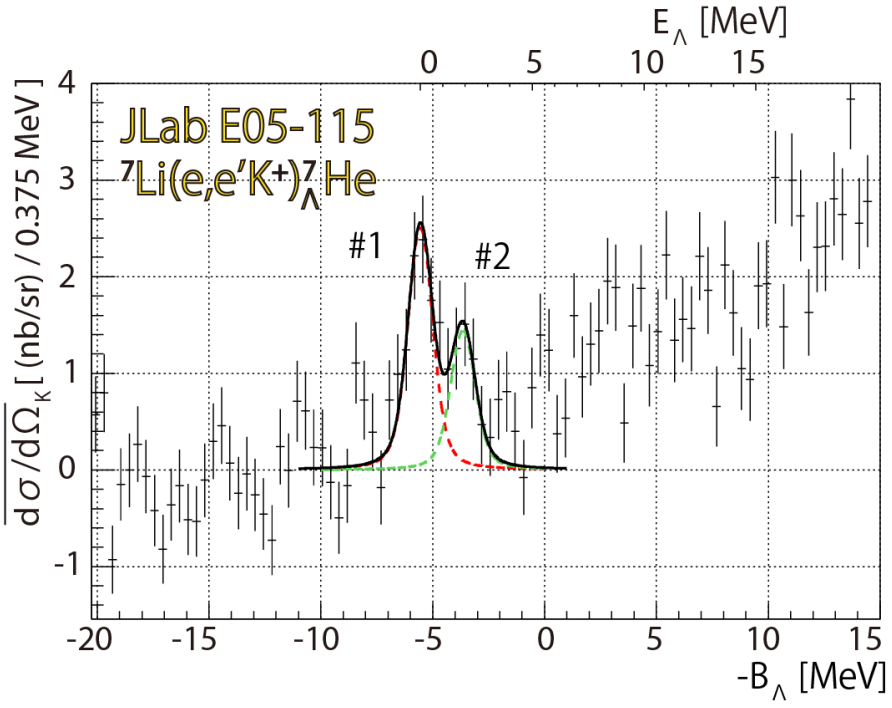

Figure 5.15: A binding energy and excitation energy spectrum for the ^{7}Li(e,e'K^+)$^7_\Lambda$He. The spectrum was fitted by two Voigt functions with the same width. The obtained width was 1.3 MeV in FWHM.

A state assignment for $^7_\Lambda$He was done by using a four-body cluster model calculation [33] and shell model calculations [58][88]. Peak number 1 is interpreted to be $1/2^+$ (^{6}He$[J_C; E_x] \otimes j^\Lambda = [0^+;$ g.s.$] \otimes s^\Lambda_{1/2}$) state. The second peak (peak number 2) is interpreted to be $3/2^+$, $5/2^+$ ($[2^+;\ 1.80] \otimes s^\Lambda_{1/2}$) states. Details about the state assignment will be explained in Sec. 5.3.2. Obtained binding energy, excitation energy and differential cross section for each peak are summarized in Table. 5.7.

Table 5.7: Obtained binding energy, excitation energy and he differential cross section averaged over the HKS acceptance for ^{7}Li(e,e'K^+)$^7_\Lambda$He.

Peak number	State ^{6}He$[J_C; E_x] \otimes j^\Lambda$	Number of events	$-B_\Lambda$ [MeV] (E_Λ)	$\left(\overline{\frac{d\sigma}{d\Omega_K}}\right)\Big\vert_{1^\circ-13^\circ}$ [nb/sr]
1	$1/2^+$ $[0^+;$ g.s.$] \otimes s^\Lambda_{1/2}$	413±38	-5.55±0.10±0.11 (0.0)	10.7±1.0±1.8
2	$3/2^+$, $5/2^+$ $[2^+;\ 1.80] \otimes s^\Lambda_{1/2}$	239±22	-3.65±0.20±0.11 (1.90±0.22±0.05)	6.2±0.6±1.1

5.3.2 Discussion

Comparison with experimental results of the previous experiment

In the past, the binding energy of $^{7}_{\Lambda}$He tried to be measured by emulsion experiment [34] and JLab E01-011 experiment using the (e,e$'K^{+}$) reaction [31]. In the emulsion experiment, the binding energy of the ground state ($1/2^{+}$) could not be determined since the results show a cluster with a broad tail. The origin of the broad tail was hypothesized to be from the decay from isomeric states of $^{7}_{\Lambda}$He although it was not experimentally confirmed [89][90][90]. The first determination of the ground state binding energy was successfully done in the JLab E01-011 experiment. The binding energy was $-B_{\Lambda} = -5.68 \pm 0.03(\text{stat.}) \pm 0.25(\text{sys.})$ MeV with the differential cross section of $(\overline{\frac{d\sigma}{d\Omega}}) = 26 \pm 5.1(\text{stat.}) \pm 9.0(\text{sys.})$ nb/sr. In JLab E05-115 (present study), data with four times larger statistic than that of JLab E01-011 was taken. A statistical significance, $(S/\sqrt{S+N})$ in the range of $-7.0 < -B_{\Lambda} < 4.0$ MeV was 7.5σ in the present study while that of JLab E01-011 was 5.5σ. Table. 5.8 shows experimental results of ground state of $^{7}_{\Lambda}$He of the present data and JLab E01-011. The results in the present study (Table. 5.7) are in good agreement with those of JLab E01-011. On the other hand, the excited states ($3/2^{+}$, $5/2^{+}$) were not discussed in JLab E01-011 as the statistic was not sufficient though there is an enhancement in the expected energy region. Therefore, the present study is the first measurement of the excited states with sufficient statistic.

Table 5.8: A comparison of the experimental results of JLab E05-115 (present study) and E01-011 for $^{7}_{\Lambda}$He ground state ($1/2^{+}$).

Experiment ($\theta_{\gamma K}$ [deg])	Ground state ($1/2^{+}$)		
	Peak significance $S/\sqrt{S+N}$	$-B_{\Lambda}$ [MeV]	$\left(\overline{\frac{d\sigma}{d\Omega_K}}\right)\Big\vert_{1^\circ-13^\circ}$ [nb/sr]
JLab E05-115 (6.8)	7.5	-5.55±0.10±0.11	10.7±1.0±1.7
JLab E01-011 (5.8)	5.5	-5.68±0.03±0.25	26.0±5.1±9.9

Differential cross section comparison with theoretical prediction

Fig. 5.16 shows excitation energy spectrum of the fitting result of the JLab E05-115 (present study) and a shell model calculation by O. Richter *et al.* [88]. The theoretical calculation was performed for the kinematic conditions at $E_{\gamma} = 1.2$ GeV and $\theta_{\gamma K} = 10.0^{\circ}$ while those for the present experiment was at $E_{\gamma} = 1.5$ GeV and $\theta_{\gamma K} = 5.8^{\circ}$. In the figure, the theoretical prediction was shown by Voigt functions with the experimental energy resolution of 1.3 MeV in FWHM. Not only the experimental results of differential cross section, but also those of excitation energy are similar with the theoretical predictions.

Ratios of the differential cross section of the ground state ($1/2^{+}$) to the excited states ($3/2^{+}$, $5/2^{+}$) for the experimental result and the theoretical prediction are:

$$0.61 \pm 0.08 \quad (\text{JLab E05} - 115) \text{ and}$$
$$0.63 \quad (\text{theoretical prediction}),$$

respectively. These are consistent, and the fact is the one of demonstrations that the second peak (peak number 2 in Fig. 5.15) corresponds to $3/2^{+}, 5/2^{+}$ states.

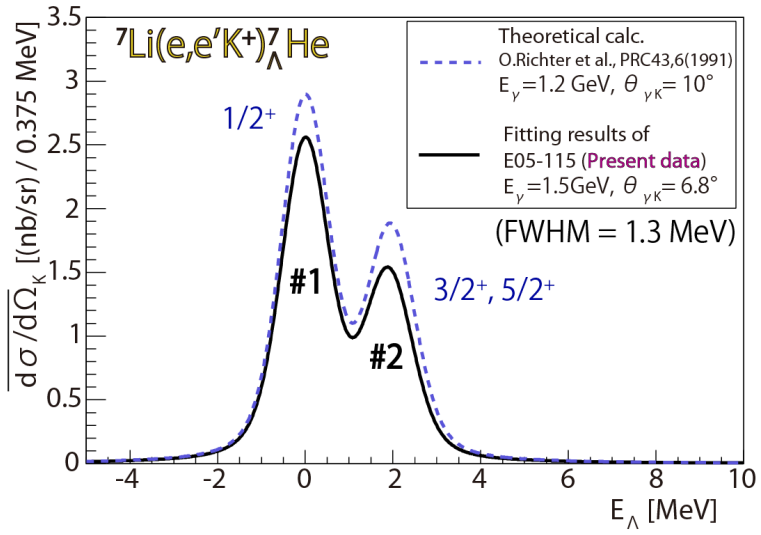

Figure 5.16: Excitation energy spectrum of the fitting result of the JLab E05-115 (present study, Fig. 5.15) and a shell model calculation by O. Richter *et al.* [88]. The theoretical calculation is shown by Voigt functions with the experimental energy resolution (FWHM = 1.3 MeV).

Glue-like role of Λ

A neutron halo nucleus, ^{6}He ($\alpha+n+n$) [92][93][94] is a core nucleus of $^{7}_{\Lambda}$He ($\alpha+n+n+\Lambda$). For ^{6}He nucleus, 0^+ and 2^+ are the ground state and the excited state, respectively. Experimental energy levels taken from Ref. [96] are summarized in Table. 5.9. The first excited state (2^+)[95] is a resonant state with $\Gamma = 133 \pm 20$ keV although the ground state (0^+) is a bound state.

Table 5.9: Energy levels of ^{6}He taken from Ref. [96].

Excitation energy E_X [MeV]	$J^\pi;T$	$\tau_{1/2}$ or Γ	Decay
g.s.	$0^+;1$	$\tau_{1/2} = 806.7 \pm 1.5$ msec	β^-
1.797±0.025	$2^+;1$	$\Gamma = 113 \pm 20$ keV	n,α
(13.6±0.5)		broad	
(15.5±0.4)		broad	γ
(23.2±0.7)		broad	γ

One of the interesting objects to see is changing of the energy level structure when a Λ is bound in such neutron halo system. Fig. 5.17 shows energy levels of ^{6}He and $^{7}_{\Lambda}$He calculated by four body cluster model ($\alpha+n+n+\Lambda$) by E. Hiyama *et al.* [33]. The ground state (0^+) of ^{6}He is below the $\alpha+n+n$ breakup threshold by 1.03 MeV. On the other hand the excited state (0^+) is above the threshold by 0.83 MeV. Once a Λ is bound in nucleus, corresponding states become deeper bound from the lowest neutron emission threshold ($^{6}_{\Lambda}$H+n) by a few MeV. Particularly, the excited state (^{6}He; 2^+) become a bound state ($^{7}_{\Lambda}$He; $3/2^+$, $5/2^+$) due to the presence of Λ hyperon inside nucleus. This glue-like role of Λ particle can be observed by investigating low-lying level structures of $^{7}_{\Lambda}$He.

In the present study, the binding energy of the ground state was determined to be $-B_\Lambda = -5.55 \pm 0.10 \pm 0.11$ MeV. The binding energy is consistent with the theoretical calculations shown in Fig. 5.17, meaning that a Λ particle makes deeper bound state than the corresponding state of core nucleus (^{6}He) with respect to each lowest neutron emission threshold. The results

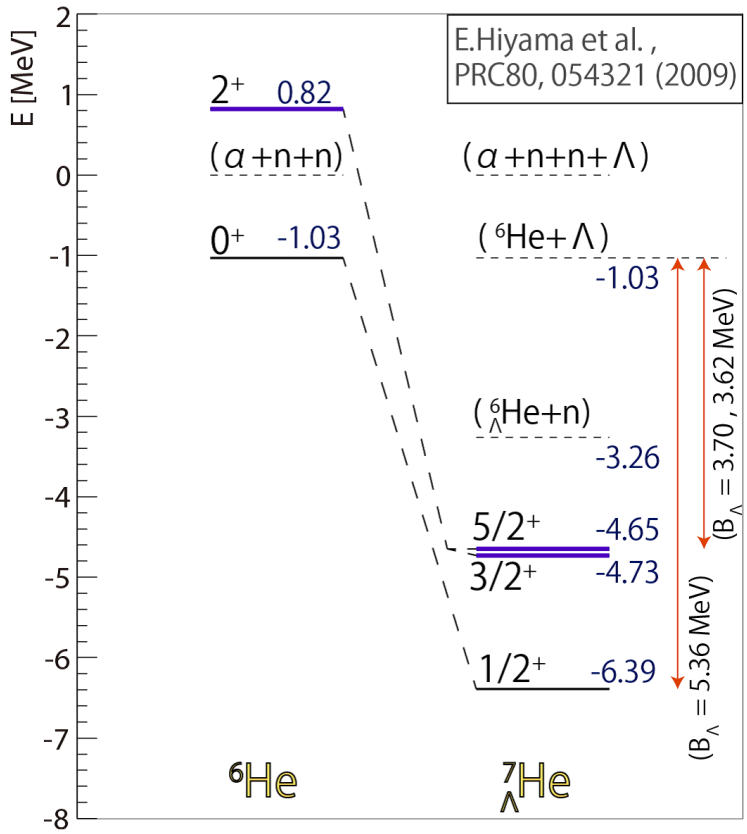

Figure 5.17: Energy levels of ^{6}He and $^{7}_{\Lambda}$He calculated by four body cluster model ($\alpha+n+n+\Lambda$) by E. Hiyama *et al.* [33]. The shown values for $^{7}_{\Lambda}$He was calculated without charge symmetry breaking effect in ΛN interaction.

of excited state was measured to be $E_\Lambda = 1.90 \pm 0.22 \pm 0.05$ MeV. The result is consistent with $3/2^+$ and $5/2^+$ states by the four-body cluster model calculation ($E_\Lambda \simeq$1.7 MeV) shown in Fig 5.17. In addition, a shell model calculation by M. Sotona and S. Frullani [97] shows a similar result for the first doublet of ${}^{7}_{\Lambda}$He to be $E_\Lambda \simeq 1.8$ MeV. Thus, it is considered to be bound states of $3/2^+$ and $5/2^+$ of which corresponding state is an unbound state in core nucleus.

Charge symmetry breaking effect

Charge symmetry breaking (CSB) effect in ΛN interaction is one of the interesting discussions. The argument was begun in A=4 Λ hypernuclear system, ${}^{4}_{\Lambda}$H ($p+n+n+\Lambda$) and ${}^{4}_{\Lambda}$He ($p+p+n+\Lambda$). The binding energy differences between ${}^{4}_{\Lambda}$H and ${}^{4}_{\Lambda}$He for the ground state (0^+) and the first excited state (1^+) were found to be 0.35 ± 0.06 MeV and 0.24 ± 0.06 MeV, respectively. However, the differences cannot be explained by only Coulomb effects [98][100][99]. Therefore, the binding energy differences after the Coulomb effect was subtracted were attributed to the CSB effect in ΛN interaction.

The ground state binding energy of ${}^{7}_{\Lambda}$He ($\alpha+n+n+\Lambda$) can be used for a test of the CSB effect in ΛN interaction by comparing with $T=1$ iso-triplet brothers, ${}^{7}_{\Lambda}$Li* ($\alpha+p+n+\Lambda$) and ${}^{7}_{\Lambda}$Be ($\alpha+p+p+\Lambda$) in the framework of four-body cluster model [33]. The superscript of " * " of ${}^{7}_{\Lambda}$Li* means that its core nucleus (^{6}Li) is the excited state with $T=1$. In the calculation, the CSB interaction were assumed by the following one-range Gaussian form:

$$V^{\rm CSB}_{\Lambda N}(r) = -\frac{\tau_z}{2}\Big[\frac{1+P_r}{2}\Big(v_0^{\rm even,CSB} + \sigma_{\mathbf{\Lambda}}\cdot\sigma_{\mathbf{N}} v^{\rm even,CSB}_{\sigma_\Lambda\cdot\sigma_N}\Big)e^{-\beta_{\rm even}r^2} + \frac{1-P_r}{2}\Big(v_0^{\rm odd,CSB} + \sigma_{\mathbf{\Lambda}}\cdot\sigma_{\mathbf{N}} v^{\rm odd,CSB}_{\sigma_\Lambda\cdot\sigma_N}\Big)e^{-\beta_{\rm odd}r^2}\Big] \tag{5.1}$$

which includes spin-independent and spin-dependent parts. In the case of calculations of ${}^{4}_{\Lambda}$H and ${}^{4}_{\Lambda}$He, contributions of odd-state interactions are negligible small. Therefore, $v_0^{\rm odd,CSB} = 0$ and $v^{\rm odd,CSB}_{\sigma_\Lambda\cdot\sigma_N} = 0$ were taken. $v_0^{\rm even,CSB}$ and $v^{\rm even,CSB}_{\sigma_\Lambda\cdot\sigma_N}$ were determined so as to reproduce the experimental binding energies of ${}^{4}_{\Lambda}$H and ${}^{4}_{\Lambda}$He. Fig. 5.18 show the predictions of binding energies for ${}^{7}_{\Lambda}$He, ${}^{7}_{\Lambda}$Li* and ${}^{7}_{\Lambda}$Be with (solid line) and without (dashed line) the ΛN CSB effects. Experimental data of ${}^{7}_{\Lambda}$He measured in JLab E05-115 (present data) and JLab E01-011 [31], ${}^{7}_{\Lambda}$Li* obtained by the combined information of the emulsion [34] and γ ray spectroscopic experiments [25], and ${}^{7}_{\Lambda}$Be measured in the emulsion experiment [34] are also plotted in the figure. The experimental data are preferable to the predictions without the CSB effects as shown in Fig.5.18. The theoretical model with even-state CSB effect in ΛN interaction which was phenomenologically introduced so as to reproduce A=4 iso-doublet systems cannot reproduce the A=7 iso-triplet systems.

Recently, odd-state interaction was taken into account so as to reproduce the experimental binding energies of ${}^{7}_{\Lambda}$Li*, ${}^{7}_{\Lambda}$Be and the theoretical prediction of ${}^{7}_{\Lambda}$He without the CSB interaction [101][102]. It is noted that the measured binding energy of JLab E01-011 was not used in the calculation. The contribution of the odd-state interaction to the binding energy is opposite sign of even-state interaction. Calculated binding energies of ${}^{7}_{\Lambda}$He, ${}^{7}_{\Lambda}$Li* and ${}^{7}_{\Lambda}$Be with even- and odd-state interactions are $B_\Lambda = 5.36$, 5.28 and 5.27 MeV, respectively. Further tests of the phenomenologically introduced both even- and odd-state CSB interactions were performed with A=10, $T=1/2$ iso-doublet hypernuclei, ${}^{10}_{\Lambda}$Be ($\alpha+\alpha+n+\Lambda$) and ${}^{10}_{\Lambda}$Be ($\alpha+\alpha+p+\Lambda$), which will be discussed in Sec. 5.4.

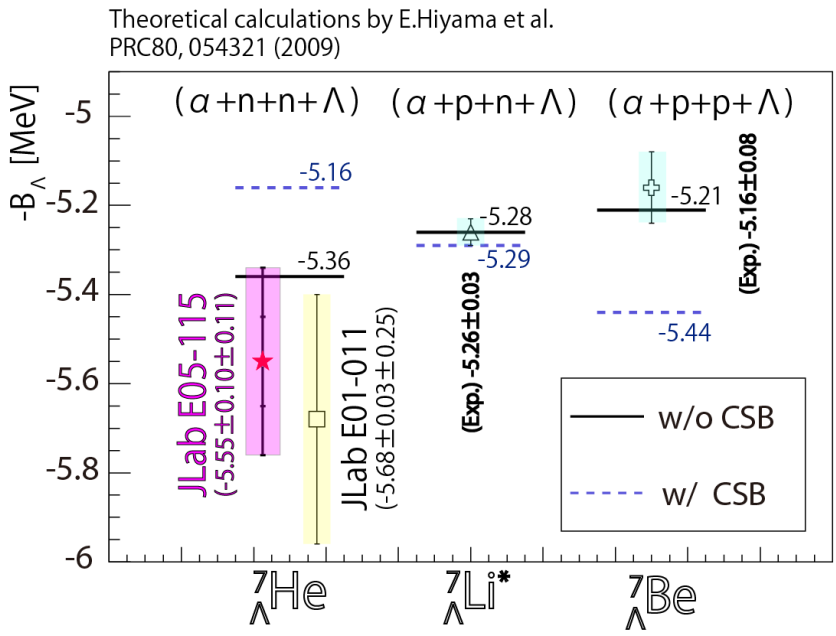

Figure 5.18: Binding energies for $^{7}_{\Lambda}$He, $^{7}_{\Lambda}$Li* and $^{7}_{\Lambda}$Be with and without the phenomenological even-state ΛN CSB interaction in the four-body cluster model calculation [33]. Experimental data of $^{7}_{\Lambda}$He measured in JLab E05-115 (present data) and JLab E01-011 [31], $^{7}_{\Lambda}$Li* obtained by the combined information of the emulsion [34] and γ ray spectroscopic experiments [25], and $^{7}_{\Lambda}$Be measured in the emulsion experiment [34] are also plotted.

5.4 ^{10}B(e,e′K^+)$^{10}_{\Lambda}$Be

Only three events of $^{10}_{\Lambda}$Be were identified so far by the emulsion experiment [34][35]. The present experiment (JLab E05-115) is the first attempt to spectroscopically investigate $^{10}_{\Lambda}$Be by a counter experiment. In this section, experimental results of $^{10}_{\Lambda}$Be structures with sub-MeV energy resolution will be shown and discussed.

5.4.1 Results

A Λ binding energy spectrum for the $^{10}_{\Lambda}$Be is shown in Fig. 5.19. A distribution of accidental coincidence events which is shown in the figure was obtained by the mixed event analysis (Sec. 4.9) to make contributions of its statistical errors negligible small when the accidental coincidence events are subtracted from the original histogram. The ordinate axis in the figure was converted to the differential cross section for the (γ^*,K^+) reaction which was defined in Eq. (4.31), and the result is shown in Fig. 5.20.

Peak fitting

Peak fitting was done as follows:

- **Significant peak search (Fig. 5.21)**
  The accidental coincidence background distributions which was obtained by the mixed event analysis (Sec. 4.9) and the quasi-free Λ distribution which was obtained by fitting to the unbound region ($-B_\Lambda > 0$) with a third order polynomial function, were subtracted from the original binding energy spectrum. Then, the ordinate axis was converted to the statistical significance (Fig. 5.21). The statistical significance is shown for binning of 0.3,

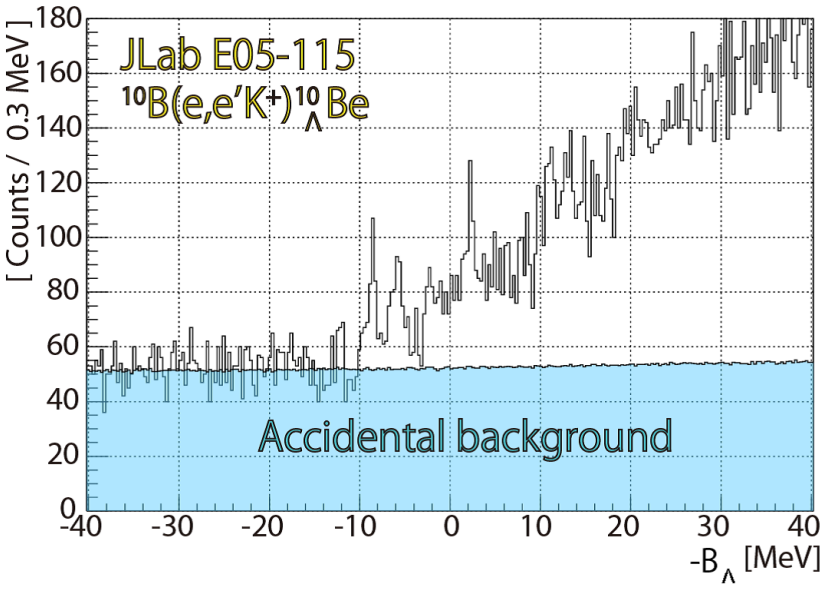

Figure 5.19: A Λ binding energy spectrum for the ^{10}B(e,e$'K^+$)$^{10}_{\Lambda}$Be.

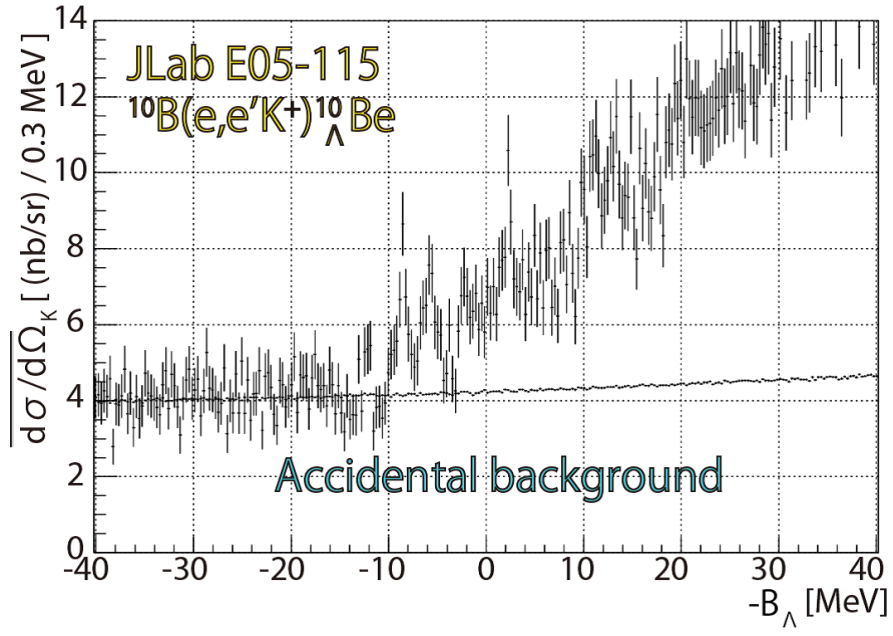

Figure 5.20: A Λ binding energy spectrum for the ^{10}B(e,e$'K^+$)$^{10}_{\Lambda}$Be. The ordinate axis is the differential cross section for the (γ^*,K^+) reaction which was defined in Eq. (4.31).

0.6 and 1.2 MeV/bin. Peaks which are above a threshold (e.g. $\geq 6\sigma$ for the binning of 1.2 MeV/bin) were chosen as peak candidates for the final fitting. The peak candidates are indicated by $P_{1,2,3,4}$ in Fig. 5.21.

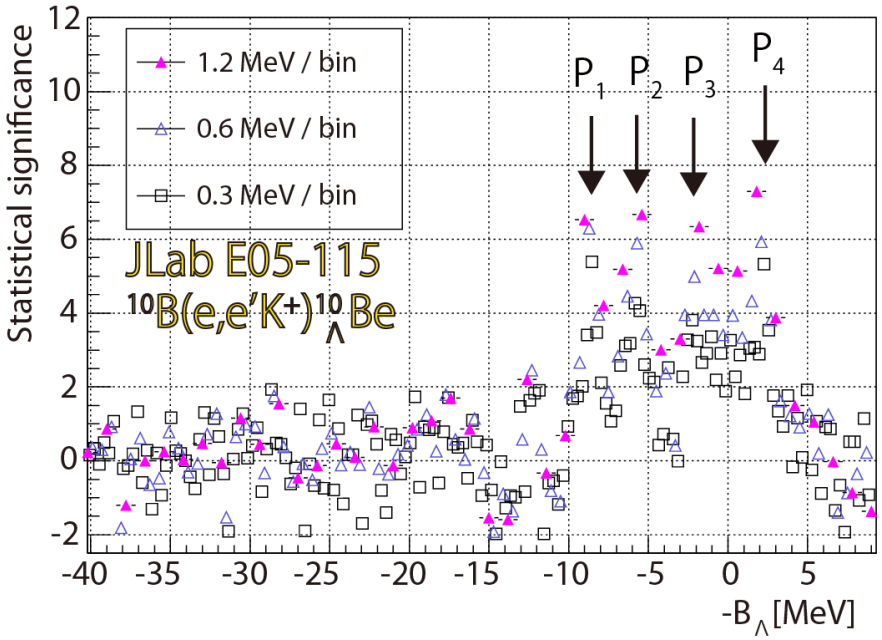

Figure 5.21: The statistical significance spectrum for $^{10}_{\Lambda}$Be after the quasi-free and the accidental background distribution was subtracted.

- **Fitting**

  At first a width which will be used for the further process was obtained by fitting to the P_1 with a Voigt function. Obtained width was 0.78 MeV (FWHM). There is a shoulder on the right hand side of P_2 (it can seen in top figure of Fig. 5.22. These are indicated by P_2^L and P_2^R.). It was found that the fitting χ^2 is better when P_2 was fitted by two Voigt functions with the same width of 0.78 MeV (FWHM). Thus, P_2 will be treated as two peaks. Top figure of Fig. 5.22 shows the fitting results with five Voigt functions for $P_{1,3,4}$ and $P_2^{L,R}$ and a third order polynomial function for the quasi-free Λ in the unbound region ($-B_\Lambda > 0$). Bottom figure of Fig. 5.22 shows the binding energy spectrum after the above fitting function was subtracted. Residual events after the subtraction of the fitting function were distributed widely. The bump of the residual events might contain some states which cannot be separated by the experimental energy resolution. In the present analysis, the residual events are treated as one broad state. The residual events were fitted with a Voigt function as shown in the bottom figure of Fig. 5.22. The obtained width of the fitting to the residual events was 2.87 MeV in FWHM.

  Finally, the binding energy spectrum was fitted by five Voigt functions with FWHM = 0.78 MeV for $P_{1,3,4}$ and $P_2^{L,R}$, a third order polynomial function for the quasi-free Λ, and a Voigt function with FWHM = 2.87 MeV for the residual events. Fitting results were shown in Fig. 5.23. Obtained binding energy, excitation energy and differential cross section for each peak which were derived by the fitting are summarized in Table. 5.10.

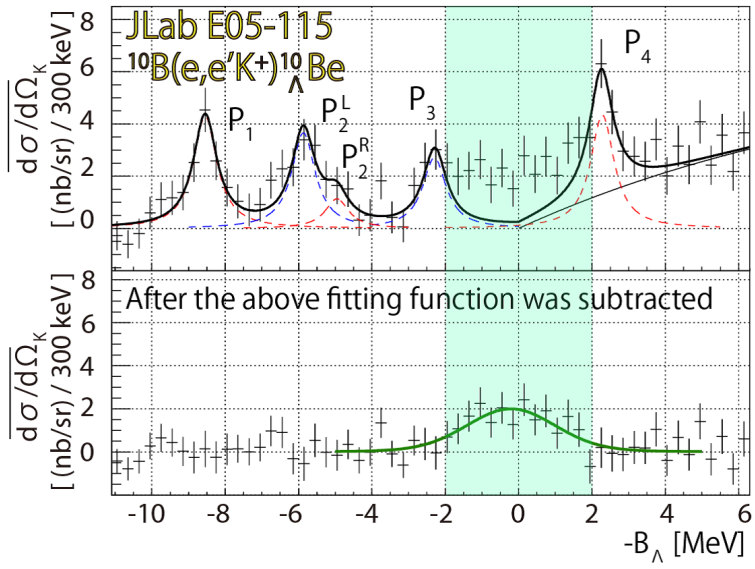

Figure 5.22: (Top) Fitting results with five Voigt functions for $P_{1,3,4}$ and $P_2^{L,R}$ and a third order polynomial function for the quasi-free Λ in the unbound region ($-B_\Lambda > 0$). (Bottom) Fitting results for residual events after the above fitting function was subtracted.

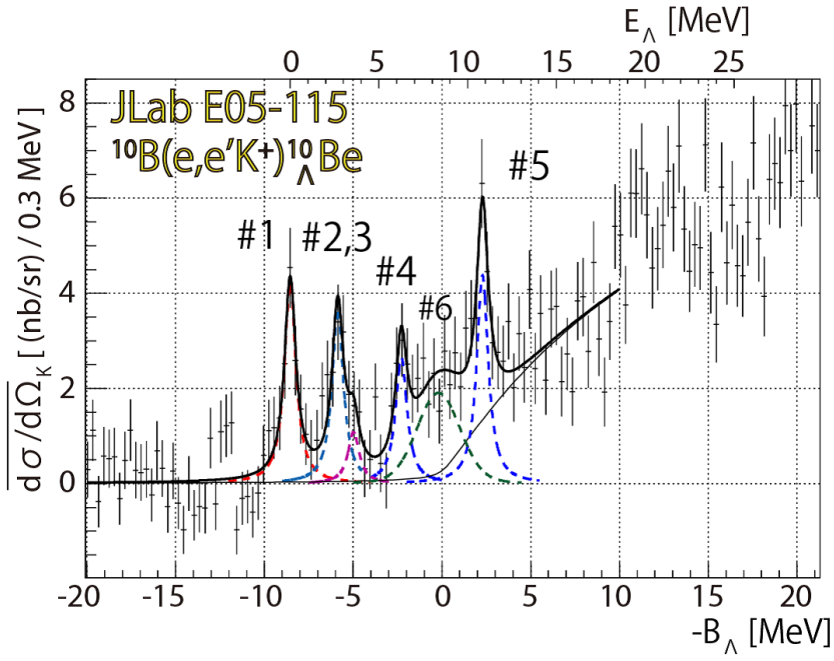

Figure 5.23: A binding energy and excitation energy spectrum for ^{10}B(e,e'K^+)$^{10}_{\Lambda}$Be with the fitting results. The ordinate axis is the differential cross section for the (γ^*, K^+) reaction which was defined in Eq. (4.31).

Table 5.10: Fitting results of the binding energy, excitation energy and differential cross section for (γ^*, K^+) reaction for ^{10}B(e,e$'K^+)^{10}_{\Lambda}$Be.

Peak number	State $^9\mathrm{B}[J_C; E_x] \otimes j^\Lambda$	Number of events	$-B_\Lambda$ [MeV] (E_Λ)	$\overline{\left(\frac{d\sigma}{d\Omega_K}\right)}\Big\vert_{1^\circ-13^\circ}$ [nb/sr]	FWHM [MeV]
1	1^-, 2^- $[3/2^-;\ \mathrm{g.s.}] \otimes s^\Lambda_{1/2}$	203±6	-8.55±0.07±0.11 (0.0)	17.1±0.5±1.5	0.78
2	2^-, 3^- $[5/2^-;\ 2.43] \otimes s^\Lambda_{1/2}$	172±5	-5.87±0.18±0.11 (2.68±0.19±0.05)	14.5±0.4±1.3	0.78
3	1^-, 0^- $[1/2^-;\ 2.78] \otimes s^\Lambda_{1/2}$	52±2	-4.98±0.53±0.11 (3.57±0.53±0.05)	4.4±0.1±0.4	0.78
4	3^-, 4^- $[7/2^-_1;\ 6.38] \otimes s^\Lambda_{1/2}$	127±4	-2.29±0.14±0.11 (6.26±0.15±0.05)	10.7±0.3±1.0	0.78
6		243±7	-0.19±0.38±0.11 (8.36±0.39±0.05)	20.5±0.6±1.8	2.87
5	3^-, 4^- $[7/2^-_2;\ 11.28] \otimes s^\Lambda_{1/2}$	210±6	2.29±0.07±0.11 (10.83±0.10±0.05)	17.7±0.5±1.6	0.78

5.4.2 Discussion

Comparison with $^{10}_{\Lambda}$B

$^{10}_{\Lambda}$Be can be compared with a mirror Λ hypernucleus, $^{10}_{\Lambda}$B which was measured by the (π^+,K^+) reaction. Fig. 5.24 shows binding energy spectra of $^{10}_{\Lambda}$B (top) taken from Ref. [22] and $^{10}_{\Lambda}$Be (bottom) measured in the present experiment. Global structures of these hypernuclei are similar. The energy resolution are 2.2 MeV and 0.78 MeV in FWHM for $^{10}_{\Lambda}$B and $^{10}_{\Lambda}$Be, respectively. A peak separation is much better in the present data thanks to the almost three times better energy resolution, thus, finer structures can be investigated in the binding energy spectrum.

The ground state binding energies of $^{10}_{\Lambda}$B and $^{10}_{\Lambda}$Be are good samples to be compared each other for a test of the CSB effect in ΛN interaction as will be discussed later in this section. However, only three events of $^{10}_{\Lambda}$Be (ground state) were observed in the emulsion experiments [34][35]. Therefore, measurement of ground state binding energy of $^{10}_{\Lambda}$Be by a counter experiment had been awaited to confirm the three events measured in the emulsion experiments. The present experiment is the first measurement of $^{10}_{\Lambda}$Be by a counter experiment.

Comparison with theoretical calculations

Fig.5.25 shows the excitation energies of present data (JLab E05-115) and some of theoretical predictions. Theoretical predictions shown in the figure are shell model calculations by T. Motoba *et al.* [48] and D. J. Millener [110], cluster model calculation by E. Hiyama and Y. Yamamoto [101], and hyperAMD calculation by M. Isaka *et al.* [111].

Possible state assignment for the observed peaks in the present data (Table. 5.10) were based on the sell-model calculation by D. J. Millener [110]. In the shell-model calculation, radial integrals of each term ($\overline{V}$, Δ, S_Λ,S_N and T) of the effective ΛN interaction shown in Eq. (1.3) were determined by using available experimental data of γ-ray spectroscopy of Λ hypernuclei up to $A \leq 16$ (22 γ-ray transitions).

Peak number 1 is interpreted to be 1^- (ground state) and 2^- doublet states ($^9\mathrm{B}[J_C; E_x] \otimes j^\Lambda = [3/2^-;\ \mathrm{g.s.}] \otimes s^\Lambda_{1/2}$). 1^- and 2^- spacing in a mirror hypernucleus, $^{10}_{\Lambda}$B was tried to be

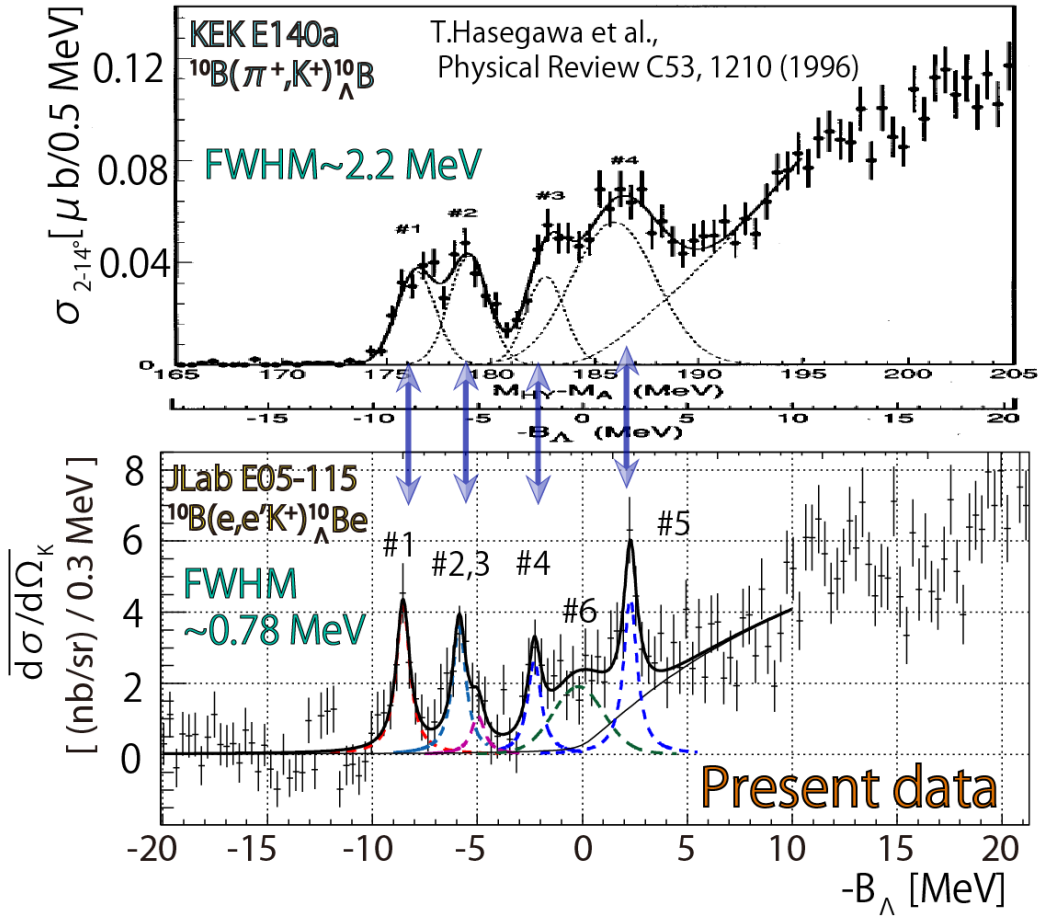

Figure 5.24: Binding energy spectra of $^{10}_{\Lambda}$B (top) taken from Ref. [22] and $^{10}_{\Lambda}$Be (bottom) measured in the present experiment. FWHMs in each hypernuclear spectrum are 2.2 MeV and 0.78 MeV, respectively.

measured in γ-ray spectroscopy at BNL [112]. However, a γ ray from these state was not observed. It suggests that the energy spacing between 1^- and 2^- is less than 100 keV which corresponds to the lowest energy for the γ-ray detection, or the order of these states are opposite (1^- is above 2^-). Assuming that the 1^- state is the ground state as predicted in the above theoretical calculations, it can be considered that the energy spacing between 1^- and 2^- states in $^{10}_{\Lambda}$Be is also less than 100 keV which cannot be separated by the our experimental energy resolution of 0.78 MeV in FWHM. Peak number 2, 3, 4 and 5 are interpreted to be states of

$$\begin{aligned} {}^9\mathrm{B}[J_C; E_x] \otimes j^\Lambda \;\; = \;\; & [5/2^-; 2.43] \otimes s^\Lambda_{1/2} \;\; , \\ & [1/2^-; 2.78] \otimes s^\Lambda_{1/2} \;\; , \\ & [7/2^-; 6.38] \otimes s^\Lambda_{1/2} \;\; \text{and} \\ & [7/2^-; 11.28] \otimes s^\Lambda_{1/2} \;\; , \end{aligned}$$

respectively. In the peak number 6, there may be some states which have positive parities. In addition, the $p^\Lambda_{3/2}$ sate ($[3/2^-$; g.s.$]\otimes p^\Lambda_{3/2}$) which is a resonant state is expected to be seen at $E_x \sim 9$ MeV with a natural width of 0.5 MeV according to the shell model calculation by D. J. Millener [113]. Therefore, the $p^\Lambda_{3/2}$ might also be contained in the peak number 6 ($E_\Lambda = 8.36 \pm 0.39 \pm 0.05$ with FWHM of 2.87 MeV).

Glue-like role of Λ

^{9}Be $(\alpha+\alpha+n)$[106][107][108] is a core nucleus of $^{10}_{\Lambda}$Be $(\alpha+\alpha+n+\Lambda)$. Some of energy levels of ^{9}Be taken from the Ref. [109] are listed in Table. 5.11.

Table 5.11: Energy levels of ^{9}Be taken from Ref. [109].

Excitation energy E_X (MeV±keV)	J^π;T	Γ [keV]	Decay
g.s.	$\frac{3}{2}^-;\frac{1}{2}$		stable
1.684±7	$\frac{1}{2}^+$	217 ± 10	γ, n
2.4294±1.3	$\frac{5}{2}^-$	0.78 ± 0.13	γ, n, α
2.78±120	$\frac{1}{2}^-$	1080 ± 110	n
6.38±60	$\frac{7}{2}^-$	1210 ± 230	γ, n
11.283±24	$\frac{7}{2}^-$	575 ± 50	n

Fig. 5.26 shows the theoretical predictions of energy levels of ^{9}B and $^{10}_{\Lambda}$Be in the four-body cluster model by E. Hiyama and Y. Yamamoto [101]. $3/2^-$ state is a ground state of ^{9}B which is below a three body breakup threshold to $\alpha+\alpha+n$. On the other hand, the low-lying excited states of $1/2^+$ and $5/2^-$ of ^{9}B which are resonant states are just above the breakup threshold. For the $^{10}_{\Lambda}$Be, 1^- and 2^- are the ground state doublet which correspond to $3/2^-$ state in ^{9}Be nucleus. The 1^-, 2^- states become much deeper bound by $\sim$4 MeV than the corresponding state ($3/2^-$) in ^{9}Be due to the presence of Λ hyperon. Similarly, excited doublet states of 3^-, 2^- and 0^+, 2^+ which respectively correspond to $5/2^-$ and $1/2^+$ resonant states become bound states. In addition, the order of these excited states of 3^-, 2^- and 0^+, 2^+ are reversed with respect to those of ^{9}Be ($1/2^+$, $5/2^-$). This phenomenon is also predicted by the HyperAMD model [111]. It is considered to be caused by the difference of deformations between $1/2^+$ and $5/2^-$ states. Spatial overlaps between Λ and $1/2^+$ of ^{9}Be, and Λ and $5/2^-$ of ^{9}Be are different due to the different deformations of ^{9}Be. In the prediction, $1/2^+$ state is more deformed than

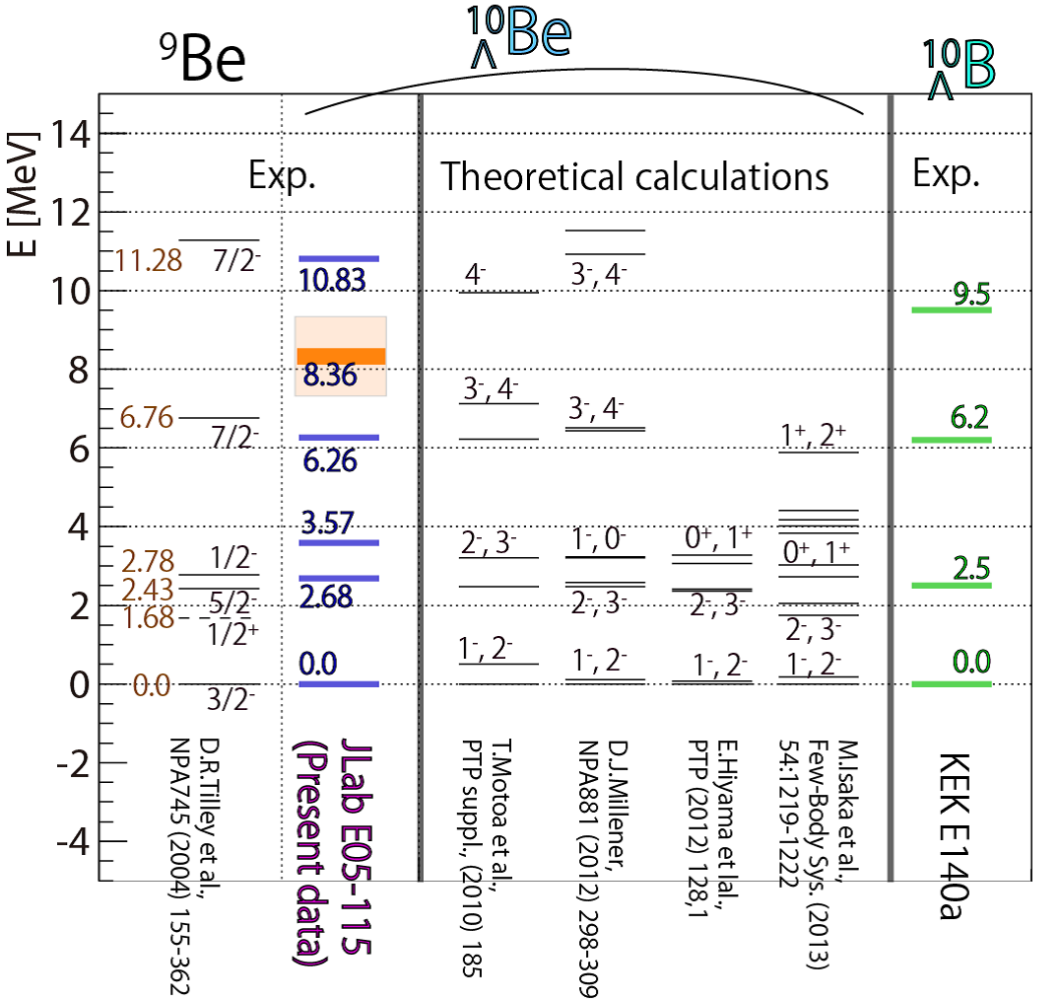

Figure 5.25: An excitation energies of present data and some of theoretical predictions for ${}^{10}_{\Lambda}$Be. In addition, the experimental result of ${}^{10}_{\Lambda}$B [22] is also shown for comparison.

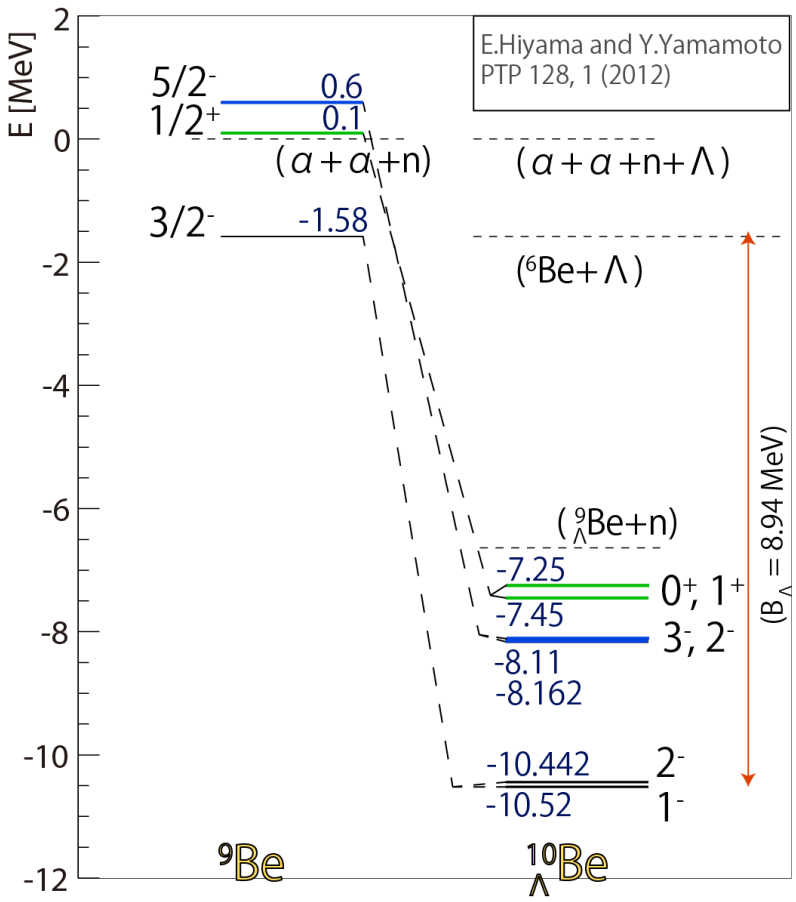

Figure 5.26: Energy levels of ^{9}Be and $^{10}_{\Lambda}$Be predicted by a four-body cluster model calculation by E. Hiyama and Y. Yamamoto [101].

$5/2^-$, meaning that $5/2^-$ state is more compact. Once a Λ is bound in the more compact state of ^{9}Be, the corresponding state of $^{10}_{\Lambda}$Be becomes deeper bound than that of ^{9}Be having larger size.

The results of the present study shows that the excitation energies of low-lying excited states are:

$$E_\Lambda(\text{peak number 2}) = 2.68 \pm 0.19 \pm 0.05 \text{ MeV},$$
$$E_\Lambda(\text{peak number 3}) = 3.57 \pm 0.53 \pm 0.05 \text{ MeV}.$$

In the four-body cluster model calculation [101], the excitation energies of 2^- (3^-) and 1^+ (0^+) are 2.41 (2.36) MeV and 3.27 (3.07) MeV. The peak number 2 and 3 might be interpreted to be 2^-, 3^- and 0^+, 1^+ states according to the cluster model calculation although the experimental excitation energies are slightly lower. However, the peak number 3 can be also interpreted as 0^-, 1^- states according to the shell model calculation [110] as shown in Fig. 5.25. Further theoretical studies particularly for the cross sections are needed to understand the experimental results.

Charge symmetry breaking effect

$A = 10$, $T = 1/2$ iso-doublet Λ hypernuclei, $^{10}_{\Lambda}$Be ($\alpha + \alpha + n + \Lambda$) and $^{10}_{\Lambda}$B ($\alpha + \alpha + p + \Lambda$) are good samples for a test of charge symmetry breaking effect (CSB) in ΛN interaction. Binding energies of these Λ hypernuclei were calculated by four-body cluster model [101] with and without the phenomenologically introduced ΛN CSB interaction as is the case of $A = 7$, $T = 1$ iso-triplet hypernuclei (Sec. 5.3.2).

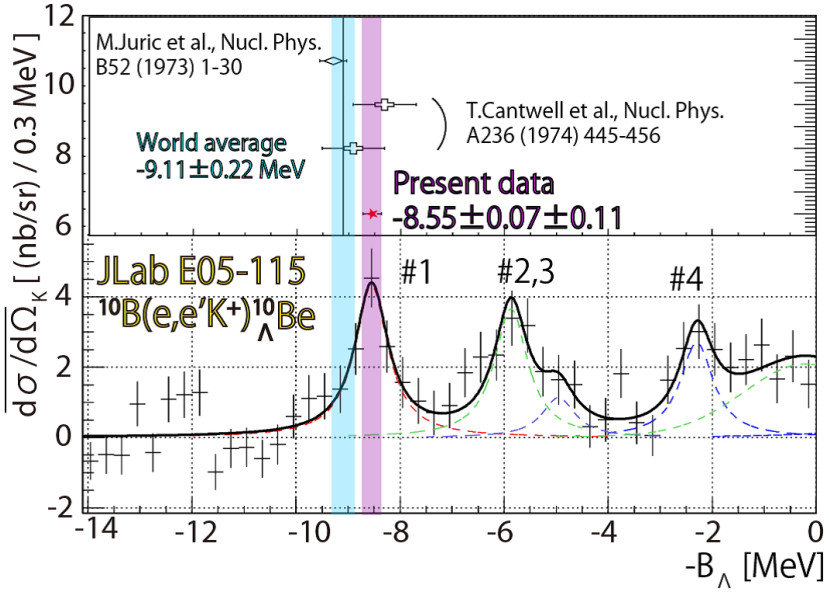

Figure 5.27: A comparison of the binding energies of the ground state of $^{10}_{\Lambda}$Be.

In the emulsion experiments, only three $^{10}_{\Lambda}$Be events were identified, and the ground state binding energy were determined [34][35]. Fig. 5.27 shows the present experimental results of ground state binding energy comparing with three data of emulsion experiments. An weighted average of these three emulsion data is $-B_\Lambda = -9.11 \pm 0.22$ MeV. The obtained binding energy of present data is $-B_\Lambda = -8.55 \pm 0.07 \pm 0.11$ MeV which is shallower than the emulsion results.

Fig. 5.28 shows the experimental data and the theoretical calculations with and without the ΛN CSB interactions by four-body cluster model [101], for $^{10}_{\Lambda}$Be and $^{10}_{\Lambda}$B. In the theoretical

calculation (See also Sec.5.3.2), even-state ΛN CSB interaction was determined so as to reproduce experimental binding energies of ${}^{4}_{\Lambda}$H and ${}^{4}_{\Lambda}$He. In addition, odd-state ΛN CSB interaction was determined so as to reproduce $A = 7$, $T = 1$ hypernuclei. The binding energy differences between ${}^{10}_{\Lambda}$Be (present data) , and ${}^{10}_{\Lambda}$B measured at KEK [22] ($-B_\Lambda = -8.10 \pm 0.10 \pm 0.50$ MeV) and that of emulsion experiments [118] ($-B_\Lambda = -8.89 \pm 0.12$ MeV) are:

$$\begin{aligned} & B_\Lambda({}^{10}_{\Lambda}\mathrm{Be}) - B_\Lambda({}^{10}_{\Lambda}\mathrm{B}) \\ = \; & 0.45 \pm 0.12(\mathrm{stat.}) \pm 0.61(\mathrm{sys.})\ \mathrm{MeV}\ \ (\mathrm{JLab} - \mathrm{KEK}), \\ & -0.34 \pm 0.14(\mathrm{stat.}) \pm 0.11(\mathrm{sys.})\ \mathrm{MeV}\ \ (\mathrm{JLab} - \mathrm{emulsion}), \end{aligned} \tag{5.2}$$

respectively. Apparently, the experimental errors particularly for the (π^+,K^+) experiment are too large to discuss about the CSB effect in the ΛN interaction for $A = 10$ systems. Further experimental efforts to reduce the errors are needed.

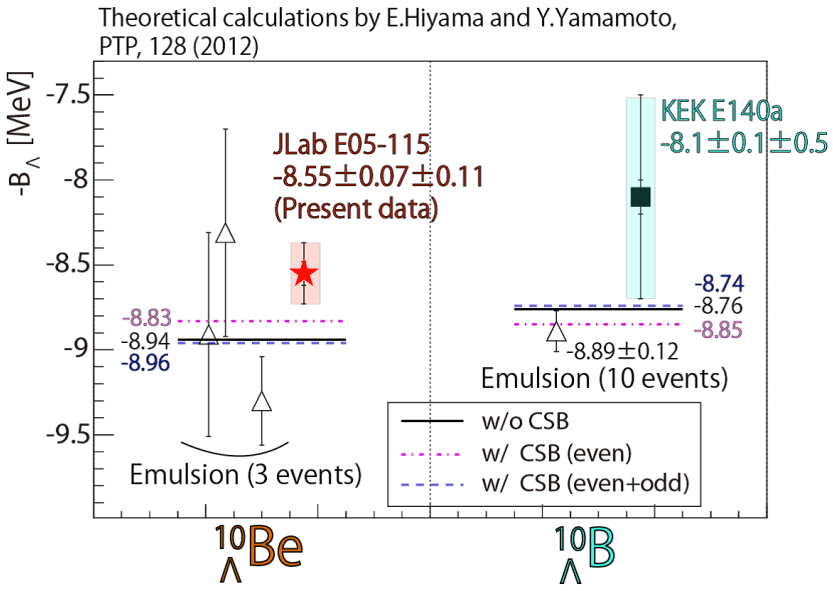

Figure 5.28: Theoretical calculations of the ground state binding energies of ${}^{10}_{\Lambda}$Be, ${}^{10}_{\Lambda}$B with and without the phenomenological ΛN CSB interaction [101]. The experimental results of ${}^{10}_{\Lambda}$Be (Emulsion: [34][35] and the present data) and ${}^{10}_{\Lambda}$B (Emulsion: [118], KEK [22]) are also plotted.

The even-state phenomenological ΛN CSB interaction was introduced so as to reproduced the experimental binding energies of ${}^{4}_{\Lambda}$He and ${}^{4}_{\Lambda}$H. Additionally, odd-state ΛN CSB interaction was taken into account to reproduce the binding energies of $A = 7$ iso-triplet hypernuclei as the calculations with only the even-state ΛN CSB interaction are not preferable to the experimental results for $A = 7$ iso-triplet hypernuclei. It is noted that an effect of the odd-state ΛN CSB interaction is negligible small for the s-shell hypernuclei, ${}^{4}_{\Lambda}$He and ${}^{4}_{\Lambda}$H. Thus, the calculation with both even- and odd-state ΛN interactions can reproduce the experimental binding energies of $A = 4$ and $A = 7$ hypernuclei simultaneously. However, still there is a room to discuss about the validity of the phenomenological ΛN CSB interaction.

Further studies are essential both experimentally and theoretically to understand the CSB effect in the ΛN interaction, of which discussion had been started from $A = 4$ systems. One attempt is measuring $A = 4$ hypernuclei by counter experiments to confirm the emulsion results. In fact, projects to measure ${}^{4}_{\Lambda}$H by the decay pion spectroscopy are in progress at MAMI and JLab. The decay pion spectroscopy is a new experimental technique which was originally proposed at JLab. The feasibility experiments have been carried out at MAMI in 2011 and

2012 [79][103], and the feasibility was confirmed by observing candidates of pionic decay events from ${}^{4}_{\Lambda}$H [104]. The data are still under analyses. Furthermore, at J-PARC, M1 transition from 1^+ to 0^+ in ${}^{4}_{\Lambda}$He is planned to be measured in E13 experiment [105] in the near future.

5.5 ^{52}Cr(e,e′K^+)$^{52}_{\Lambda}$V

In the present experiment (JLab E05-115), a pilot study for an investigation of the medium-heavy hypernucleus with the (e,e′K^+) reaction was done by measuring $^{52}_{\Lambda}$V. It is challenging for an experiment with the (e,e′K^+) reaction to measure Λ hypernuclei of medium or heavy mass region since background particles which originate from electromagnetic processes are roughly in proportional to Z^2 (Z: proton number of target). Results of $^{52}_{\Lambda}$V will be shown and discussed in this section.

5.5.1 Results

Fig. 5.29 shows a binding energy spectrum of ^{52}Cr(e,e′K^+)$^{52}_{\Lambda}$V. A distribution of the accidental coincidence events was obtained by the mixed event analysis (Sec. 4.9) to make contributions of its statistical errors negligible small when the accidental coincidence distribution was subtracted from the original histogram.

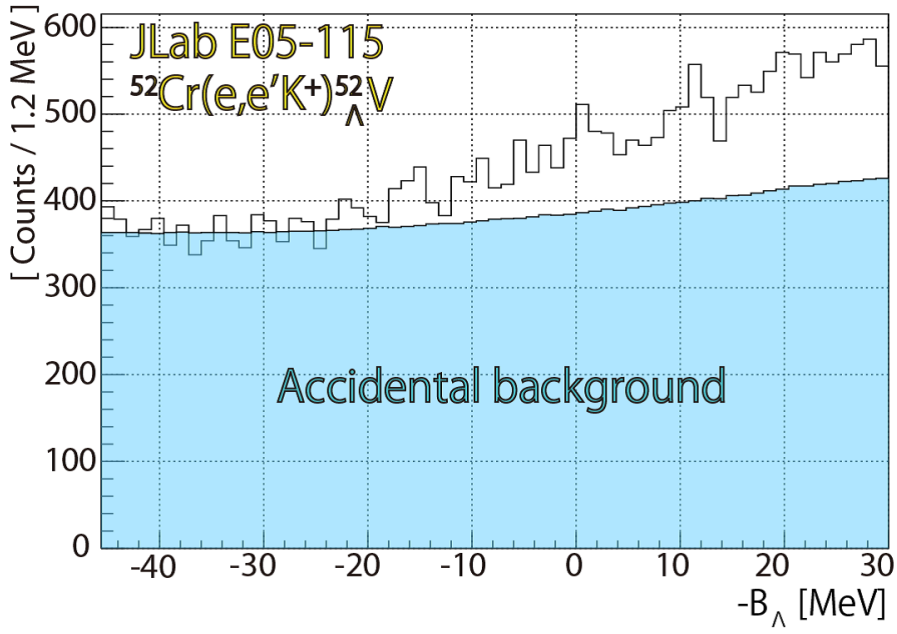

Figure 5.29: A binding energy spectrum of ^{52}Cr(e,e′K^+)$^{52}_{\Lambda}$V. A distribution of the accidental coincidence events was obtained by the mixed event analysis (Sec. 4.9)

Peak fitting

A peak fitting was performed as the following:

- **Significant peak search (Fig. 5.30)**
  An energy resolution for $^{52}_{\Lambda}$V is considered to be worse by at least $\sim$ 2 times ($\sim$ 2 MeV in FHWM) than that of the other Λ hypernucei (sub-MeV in FWHM) since the position resolution was worse by 2 times due to the high rate and high multiplicity in HKS (Sec. 4.4). Peaks which have withs of 2.0 to 2.5 MeV in FWHM were searched assuming the response function is a Gaussian [114][115][116], and a typical result is shown in Fig. 5.30. Bump structures which are indicated by orange markers were identified as peak candidates. A bump structure indicated by P_1 was identified as a peak when peaks were searched with

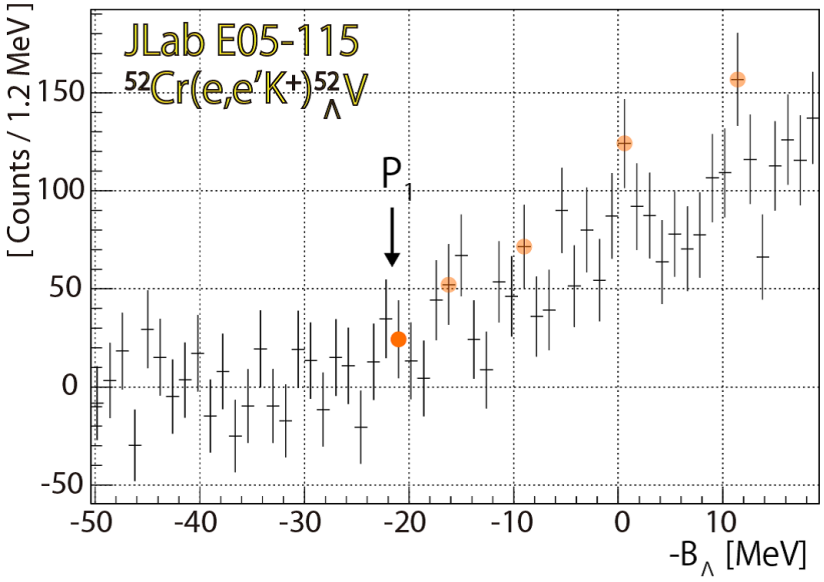

Figure 5.30: A typical result of the peak searching assuming the response function is a Gaussian with widths of 2.0 to 2.5 MeV in FWHM [114][115][116].

assumed Gaussian widths of 2.0 to 2.5 MeV in FWHM. In the present study, only the first bump structure (P_1) will be discussed as the energy resolution was not enough to distinguish other states unambiguously.

- **Fitting**
  Fitting to the spectrum was performed with a Voigt function for P_1, and the result is shown in Fig. 5.31. The peak is considered to be the ground state of $^{52}_{\Lambda}$V (3^-, 4^-). Obtained width was 2.2 MeV in FWHM. The energy resolution was worse than the other Λ hypernuclei since the particle tracking was not easily performed for $^{52}_{\Lambda}$V data due to the high multiplicity in the HKS tracking chambers as shown in Sec. 4.4. Obtained binding energy for the peak is summarized in Table. 5.12.

Table 5.12: Fitting results of ^{52}Cr(e,e'K^+)$^{52}_{\Lambda}$V spectrum.

Peak number	State ^{51}V$[J_C; E_x] \otimes j^{\Lambda}$	Number of events	$-B_{\Lambda}$ [MeV]
1	3^-, 4^- $[7/2^-;$ g.s.$] \otimes s^{\Lambda}_{1/2}$	73±37	-21.88±0.59±0.11

Binding energy accuracy for $^{52}_{\Lambda}$V

For the binding energy measurement of $^{52}_{\Lambda}$V, there are two major considerations as the following:

1. **Linearity of the inverse transfer matrix**
   The inverse transfer matrices of our spectrometer systems were optimized by Λ and Σ^0. However, the kinematic parameters for $^{52}_{\Lambda}$V are far from those of Λ and Σ^0 as shown in Fig. 2.28. It is not trivial whether the linearity of the inverse transfer matrices is kept such extrapolated kinematic region of $^{52}_{\Lambda}$V from those of Λ and Σ^0. Studies of the linearity were

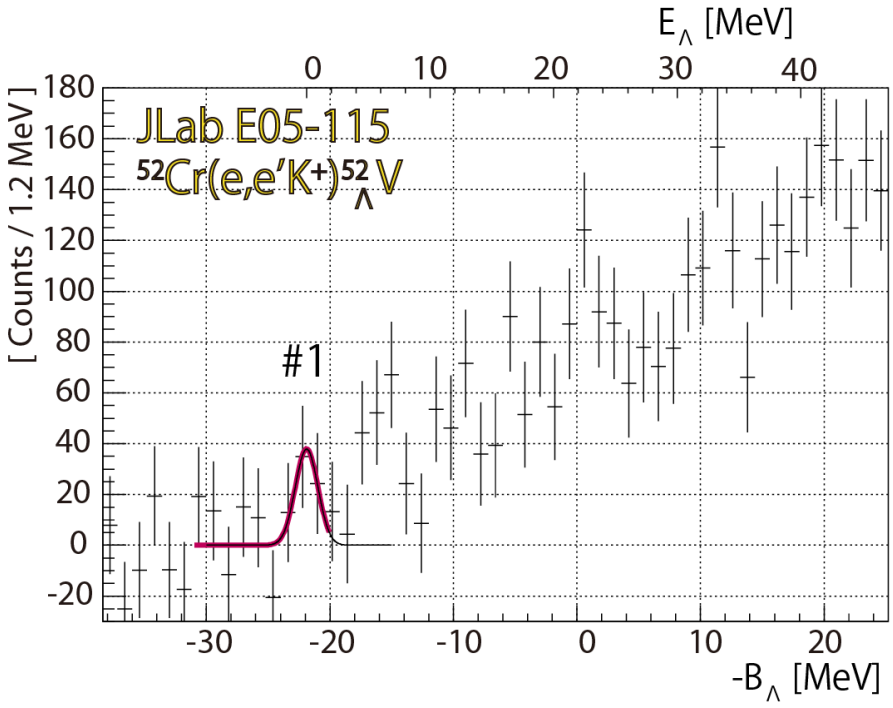

Figure 5.31: A binding energy spectrum of ^{52}Cr(e,e′K^+)$^{52}_{\Lambda}$V after the accidental background distribution which was obtained by the mixed event analysis (Sec. 4.9) was subtracted. The fitting result with a Voigt function is shown. The obtained width was 2.2 MeV in FWHM.

carefully performed by the full-modeled Monte Carlo simulation as shown in Sec. 4.11.1. It was found that the linearity is kept after the inverse transfer matrix optimization, and the systematic errors for $^{52}_{\Lambda}$V which originate from the linearity are similar level to the other hypernuclei (Table. 4.22).

2. **High rate and multiplicity environment**
   Conditions of rate and multiplicity in HKS were high for $^{52}_{\Lambda}$V data because of huge amount of e^-, e^+ background contamination as shown in Sec. 4.4. There might be a possibility that the binding energy is affected by the conditions of the high rate and multiplicity in the HKS detector systems. The rate and multiplicity conditions of $^{52}_{\Lambda}$V are similar to those of the H_2O target data (Table. 3.5). Missing masses of Λ and Σ^0 were reconstructed from the H_2O target (Appendix A), and these masses were compared with their PDG values [68]. Then, it was found that the reconstructed masses of Λ and Σ^0 from H_2O target were consistent with their PDG values within the errors. It suggests that a shift of a reconstructed mass due to the conditions of high rate and high multiplicity is not likely to be happened.

Regarding above items, the binding energy of $^{52}_{\Lambda}$V is able to be determined with similar systematic errors to those of the other Λ hypernuclei although the energy resolution is worse.

5.5.2 Discussion

Fig 5.32 shows a binding energy spectra of $^{51}_{\Lambda}$V which was measured by the (π^+,K^+) reaction at KEK [24] and $^{52}_{\Lambda}$V (present data). Widths of the spectra for $^{51}_{\Lambda}$V (KEK) and $^{52}_{\Lambda}$V (present data) are 2.0 and 2.2 MeV in FWHM, respectively. The binding energy of the ground states of

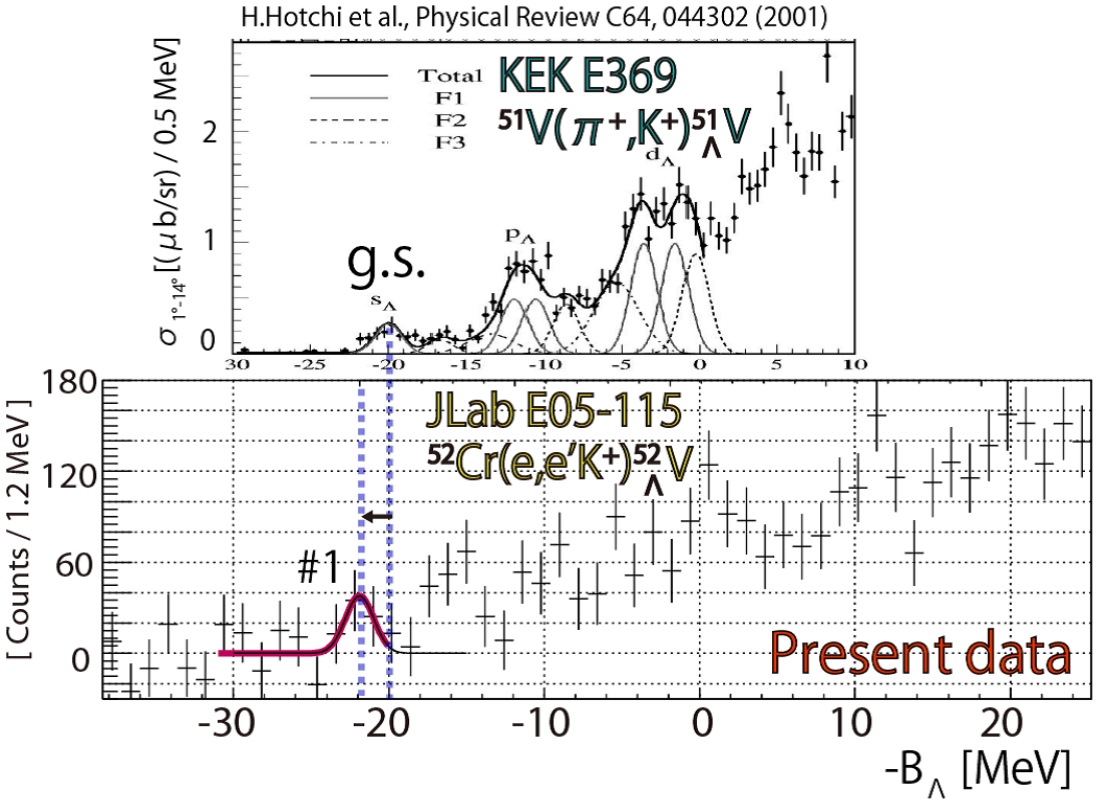

Figure 5.32: A comparison of the ground state binding energies between $^{51}_{\Lambda}$V measured at KEK [24] and $^{52}_{\Lambda}$V (present data).

$^{51}_{\Lambda}$V and $^{52}_{\Lambda}$V are:

$$\begin{aligned} -B_{\Lambda}(^{51}_{\Lambda}\mathrm{V}_{\mathrm{g.s}}) &= -19.97 \pm 0.13(\mathrm{stat.}) \pm 0.23(\mathrm{sys.}) + \Delta E(\mathrm{sys.})\ \mathrm{MeV}\ , \\ -B_{\Lambda}(^{52}_{\Lambda}\mathrm{V}_{\mathrm{g.s}}) &= -21.88 \pm 0.59(\mathrm{stat.}) \pm 0.11(\mathrm{sys.})\ \mathrm{MeV}\ , \end{aligned}$$

respectively. ΔE is a possible error of the measured value of $^{12}_{\Lambda}$C in the emulsion experiment [117][118], which has been used as a reference to obtain the binding energies of Λ hypernuclei in the (π^+,K^+) experiment. A difference of the ground state binding energies is:

$$\begin{aligned} \Delta B_{\Lambda}^{(52-51)} &= B_{\Lambda}(^{52}_{\Lambda}\mathrm{V}_{\mathrm{g.s}}) - B_{\Lambda}(^{51}_{\Lambda}\mathrm{V}_{\mathrm{g.s}}) \\ &= 1.91 \pm 0.60(\mathrm{stat.}) \pm 0.33(\mathrm{sys.}) - \Delta E(\mathrm{sys.})\ \mathrm{MeV}. \end{aligned} \tag{5.3}$$

The difference of the ground state binding energies, $\Delta B_{\Lambda}^{(52-51)}$ looks larger than what we expected. It might be explained by the following three factors:

1. **$A^{-2/3}$ dependence of the binding energy**
   Λ's binding energy has a dependence on $A^{-2/3}$ as shown in Fig. 1.14. Assuming the $A^{-2/3}$ dependence simply, the binding energy of $^{52}_{\Lambda}$V could be deeper by 0.10 MeV [113][119] than that of $^{51}_{\Lambda}$V.

2. **Excited state contamination in the ground state for $^{51}_{\Lambda}$V spectrum**
   Fig. 5.33 shows the normalized spectroscopic factors for for the ^{51}V(^{3}He,α)^{50}V [120] and ^{52}Cr(t,α)^{51}V [121] reactions. The abscissa axis is the excitation energy (E) for ^{50}V and ^{51}V, respectively. The ground state spectroscopic factor is normalized to be unity for each reaction. These spectroscopic factor directly affect the nuclear structures of $^{51}_{\Lambda}$V and $^{52}_{\Lambda}$V.

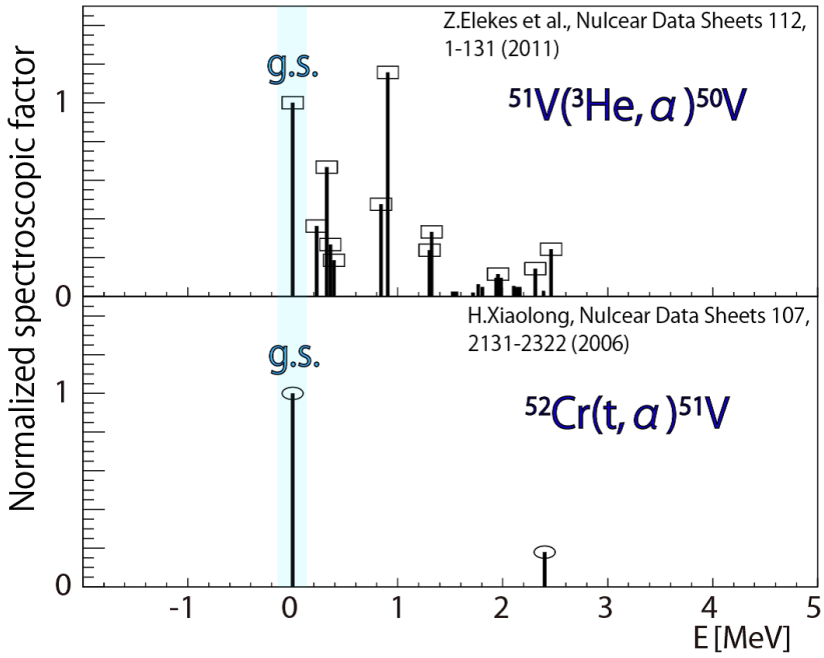

Figure 5.33: Normalized spectroscopic factors for ^{51}V(^{3}He,α)^{50}V [120] and ^{52}Cr(t,α)^{51}V [121] reactions. The abscissa axis is the excitation energy (E) for ^{50}V and ^{51}V, respectively. The ground state spectroscopic factor is normalized to be unity for each reaction.

A neutron pickup reaction, ^{51}V(^{3}He,α)^{50}V (top figure in Fig. 5.33) corresponds to the ^{51}V(π^+,K^+)$^{51}_{\Lambda}$V which was measured at KEK (top figure in Fig. 5.32). There are many neutron-hole states which are close to the ground state as seen in the figure. Particularly, there is a state with larger spectroscopic factor than the ground state at E $\sim$1 MeV. Excited states of $^{51}_{\Lambda}$V which corresponds to the excited states of ^{50}V are considered to be contaminated in the ground state for the experimental resolution of 1.95 MeV in FWHM. If these excited states were contained for the peak fitting of $^{51}_{\Lambda}$V ground state, the "real" ground state binding energy is considered to be deeper by $\sim$0.45 MeV than the shown value.

On the other hand, a proton pickup reaction, ^{52}Cr(t,α)^{51}V (bottom figure in Fig. 5.33) corresponds to the ^{52}Cr(e,e$'K^+$)$^{52}_{\Lambda}$V which was measured in the present experiment (bottom figure in Fig. 5.32). There are no prominent state in the region of E $\leq$2.5 MeV which means that no major contamination from the excited state is expected for the ground state measurement of $^{52}_{\Lambda}$V.

3. **Binding energy measurement in the (π^+,K^+) experiment**
In the (π^+,K^+) experiment, the binding energy of $^{12}_{\Lambda}$C which was determined in the emulsion experiment has been used as a reference to obtain the binding energies of Λ hypernuclei. Binding energies of Λ hypernuclei were measured by observing its week decay processes in the emulsion experiment. An identification of $^{12}_{\Lambda}$C was more difficult than the other hypernuclei since decay topologies of $^{12}_{\Lambda}$C were easily confused with other Λ hypernuclei as reported in Ref. [117]. In this situation, six events were identified as the ground sate of $^{12}_{\Lambda}$C, and a mean value of their binding energies had been reported [117][118]. The mean value of 10.76 $\pm$ 0.19 MeV has been used as the reference for the (π^+,K^+) experiment.

Table. 5.13 shows binding energy differences between available multiplet pairs which were

Table 5.13: Λ's binding energy differences between available multiplet pairs which were measured in emulsion experiments [118]. The present data of ${}^{10}_{\Lambda}$Be and ${}^{12}_{\Lambda}$B are also shown in replacement of those of emulsion experiments.

Multiplet pair	ΔB_Λ [MeV]	Remarks
${}^{4}_{\Lambda}$He − ${}^{4}_{\Lambda}$H	$+0.35 \pm 0.04$	${}^{4}_{\Lambda}$He: 279 events, ${}^{4}_{\Lambda}$H: 155 events
${}^{8}_{\Lambda}$Be − ${}^{8}_{\Lambda}$Li	$+0.04 \pm 0.06$	${}^{8}_{\Lambda}$Be: 68 events, ${}^{8}_{\Lambda}$Li: 787 events
${}^{9}_{\Lambda}$B − ${}^{9}_{\Lambda}$Li	-0.21 ± 0.22	${}^{9}_{\Lambda}$B: 4 events, ${}^{9}_{\Lambda}$Li: 8 events
${}^{10}_{\Lambda}$B − ${}^{10}_{\Lambda}$Be	-0.22 ± 0.25 $+0.34 \pm 0.14 \pm 0.11$	${}^{10}_{\Lambda}$B: 10 events, ${}^{10}_{\Lambda}$Be: 3 events present data for ${}^{10}_{\Lambda}$Be
${}^{12}_{\Lambda}$C − ${}^{12}_{\Lambda}$B	-0.57 ± 0.19 $-0.62 \pm 0.19 \pm 0.11$	${}^{12}_{\Lambda}$C: 6 events, ${}^{12}_{\Lambda}$B: 87 events present data for ${}^{12}_{\Lambda}$B

measured in emulsion experiments. The present data of ${}^{10}_{\Lambda}$Be and ${}^{12}_{\Lambda}$B are also shown in replacement of those of emulsion experiments. If charge symmetry in ΛN interaction is assumed, Λ's binding energies of the multiplet pair should be almost same (e.g. For ${}^{10}_{\Lambda}$B and ${}^{10}_{\Lambda}$Be, $\Delta B_\Lambda = -0.18$ MeV [101] as shown in Fig. 5.28). The binding energy difference between ${}^{12}_{\Lambda}$C and ${}^{12}_{\Lambda}$B is considerably large. Here, it is noted again that the discussion of the charge symmetry breaking (CSB) effect in ΛN interaction had begun from the binding energy difference between ${}^{4}_{\Lambda}$He and ${}^{4}_{\Lambda}$H [100]. Even when the CSB effect for $A = 4$ systems (${}^{4}_{\Lambda}$He and ${}^{4}_{\Lambda}$H) are taken into account by introducing Λ-Σ coupling effect, the CSB effect for $A = 12$ systems (${}^{12}_{\Lambda}$C and ${}^{12}_{\Lambda}$B) should be smaller by at least factor of four than that of $A = 4$ systems [113]. The difference of the binding energies of ${}^{12}_{\Lambda}$C and ${}^{12}_{\Lambda}$B is hard to be understand theoretically so far.

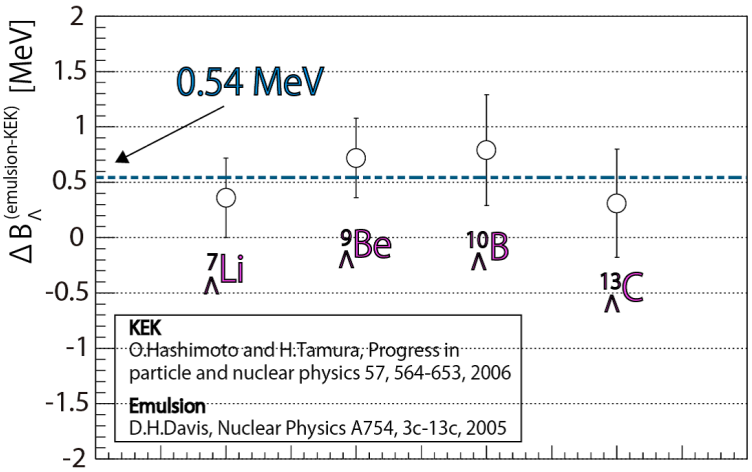

Figure 5.34: The binding energy difference between measured by (π^+,K^+) experiments [10] and emulsion experiments [118] ($\Delta B_\Lambda^{(\text{emulsion}-\text{KEK})}$) for ${}^{7}_{\Lambda}$Li, ${}^{9}_{\Lambda}$Be, ${}^{10}_{\Lambda}$B and ${}^{13}_{\Lambda}$C. The plots were fitted by a constant. The fitting result was $\Delta B_\Lambda^{(\text{emulsion}-\text{KEK})} = +0.54 \pm 0.21$ MeV, which means reported binding energies from the (π^+,K^+) experiments were systematically shallower than the emulsion experiments. It indicates the reported binding energy of ${}^{12}_{\Lambda}$C [117][118] which has been used for the binding energy measurements as the reference in the (π^+,K^+) experiments would be shallower by 0.54 ± 0.21 MeV.

Fig. 5.34 shows the binding energy difference between measured by (π^+,K^+) experi-

ments [10] and emulsion experiments [118] ($\Delta B_\Lambda^{(\mathrm{emulsion-KEK})}$) for ${}^{7}_{\Lambda}$Li, ${}^{9}_{\Lambda}$Be, ${}^{10}_{\Lambda}$B and ${}^{13}_{\Lambda}$C. These data were fitted by a constant, and it was found that the binding energies which were reported from the (π^+,K^+) experiments were systematically shallower by 0.54 ± 0.21 MeV than the emulsion experiments. It indicates that the reported binding energy of ${}^{12}_{\Lambda}$C [117][118] which has been used for the binding energy measurements as the reference in the (π^+,K^+) experiments would be shallower by 0.54 ± 0.21 MeV. It is noted that it can explain the binding energy difference between ${}^{12}_{\Lambda}$C and ${}^{12}_{\Lambda}$B (Table. 5.13) which is hard to be understood theoretically.

If the above three factors are simply considered, the ground state binding energy of ${}^{52}_{\Lambda}$V (present data) could be deeper by 1.1 ± 0.21 MeV than the reported value of the ground state of ${}^{51}_{\Lambda}$V. It means the obtained value of $\Delta B_\Lambda^{(52-51)}$ (Eq. (5.3)) is reasonable within the errors. In other wards, the present result of ${}^{52}_{\Lambda}$V indicates that the reported value of the ground state of ${}^{12}_{\Lambda}$C would be shallower by 0.54 ± 0.21 MeV than the "real" binding energy as also indicated by the measurements of the other Λ hypernuclei with the (π^+,K^+) and emulsion experiments (Fig. 5.34).

A remeasurement of the ground state binding energy of ${}^{12}_{\Lambda}$C is indispensable to confirm whether the reported ground state binding energy [117][118] which has been used as the reference for (π^+,K^+) experiments is correct or not.

Single particle energy of Λ

The binding energies of Λ hypernuclei were measured by the (K^-,π^-) and (π^+,K^+) experiments up to $A = 209$, and the single particle potential of Λ were studied with these data. It is possible that the binding energies of (π^+,K^+) experiments are systematically shallower by ~ 0.5 MeV since the reference data of ${}^{12}_{\Lambda}$C considered to be shifted by ~ 0.5 MeV when the above discussions are assumed.

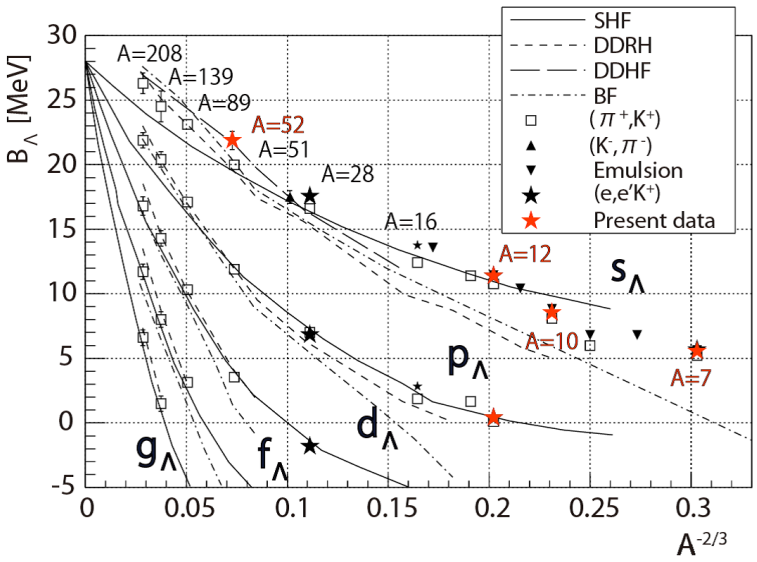

Figure 5.35: Λ's binding energies as a function of $A^{-2/3}$ for experimental data and theoretical predictions. The obtained binding energies in the present work are also plotted.

Fig. 5.35 shows the known single particle energies as a function of $A^{-2/3}$ with the present data of ${}^{7}_{\Lambda}$He, ${}^{10}_{\Lambda}$Be, ${}^{12}_{\Lambda}$B and ${}^{52}_{\Lambda}$V. The labels of the theoretical calculations in Fig. 5.35 are the same as Fig. 1.14. The present results of ${}^{52}_{\Lambda}$V is the first measurement of a ground state binding

energy of Λ hypernucleus without the emulsion reference in the medium-heavy mass region, which would be important information to understand the single particle potential of Λ. There are significance of the single particle energy measurements with the (e,e′K^+) reaction as follows:

- **Binding energy measurement with good calibration data**
  In the (e,e′K^+) experiment, the energy scale can be calibrated with well known masses of Λ and Σ^0 as a proton is converted to a Λ in the reaction. Therefore, the Λ's binding energies can be measured with less uncertainties. On the other hand, the emulsion data are necessary as the reference for (π^+,K^+) experiments to measure the binding energies.

- **High energy resolution**
  In the (π^+,K^+) experiments, global structures were successfully observed as shown in top figure of Fig. 5.32. However, excited states such as p_Λ and d_Λ in Fig. 5.32 had to be decomposed by fitting to obtain the single particle energy in each orbit. In this case, particle-hole states of core nucleus might contaminate to the peaks and affect the measured values of the single particle energies, depending on the fitting.

  The higher energy resolution (sub-MeV in FWHM) in the (e,e′K^+) experiment can minimize the contamination of the particle-hole states of the core nucleus to the major peaks. Thus, more precise single particle energies can be measured in the (e,e′K^+) experiment.

In the present study, the ground state binding energy of $^{52}_{\Lambda}$V has been determined overcoming the high multiplicity environment. The results of $^{52}_{\Lambda}$V which are independent from the emulsion reference in the medium-heavy mass region indicate that the single particle energies which were already measured by (π^+,K^+) experiments would be shifted by at least $\sim$ 0.5 MeV (Fig. 5.34).

The (e,e′K^+) experiment is a powerful tool to investigate single particle energies of Λ as explained above. Thus, the (e,e′K^+) experiment will serve to understand Λ's behaviors in a nucleus with less uncertainty.

Future plan to heavier Λ hypernuclei with (e,e′K^+) experiment

The energy resolution for the measurement of $^{52}_{\Lambda}$V was worse than those of other hypernuclei due to e^-, e^+ background particles in HKS, that increase in proportion to Z^2 (Z:target proton number) as shown in Sec. 4.4. The e^-, e^+ background particles caused not only the energy resolution deterioration, but also reduction of particle detection efficiencies both on-line and off-line. Overcoming these experimental difficulties, the ground state binding energy of $^{52}_{\Lambda}$V were measured in the present study.

It is essential to suppress the contamination of electromagnetic background particles in spectrometer systems in order to investigate heavier Λ hypernuclei in the future. A project to measure heavier Λ hypernuclei up to $A = 208$ by the (e,e′K^+) reaction at JLab has been started, and is now being prepared [122]. A Monte Carlo simulation (Geant4) has been performed to design new spectrometer systems to suppress the electromagnetic background contamination, and to quantitatively estimate yields and background rates [123]. According to Ref. [123], spectroscopy of the $A = 208$ hypernuclei would be feasible with the energy resolution of $\sim$0.7 MeV (FWHM) and the statistical significance of $\geq 5\ \sigma$ for its ground state (beam time of 60 days, beam current of 100 μA, target thickness of 100 mg/cm^2) at JLab. Prior to the experiment, many theoretical predictions of medium to heavy Λ hypernuclei by the (e,e′K^+) reaction have been intensively performed [124][125][126]. Finer structures which are hardly resolved with the existing meson beams are expected to be observed by the (e,e′K^+) experiment such as core-configuration mixing and ls splitting in the medium and heavy Λ hypernuclei. The spectroscopic results of medium to heavy Λ hypernuclei with sub-MeV (FHWM) energy resolution by the (e,e′K^+) reaction are being awaited.

Chapter 6

Summary

In 2009 (August-November), the E05-115 experiment have been performed at JLab to investigate Λ hypernuclei in the wide mass region up to $A = 52$ (^{7}Li, ^{9}Be, ^{10}B, ^{12}C and ^{52}Cr targets) with the (e,e$'K^+$) reaction. This is the first attempt to investigate the medium heavy Λ hypernucleus with the (e,e$'K^+$) reaction. In addition to HKS which was used in the previous (e,e$'K^+$) experiment (JLab E01-011) as a K^+ magnetic spectrometer, HES, SPL and pre-chicane beam line were newly constructed and introduced in JLab E05-115. In the (e,e$'K^+$) experiment, it is experimentally hard to measure heavier Λ hypernuclei since the rates of background particles originating from electromagnetic processes are roughly in proportional to Z^2 (Z: target proton number). In order to perform the JLab E05-115 experiment, many experimental techniques have been developed and introduced such as optimization of the electron spectrometer configuration (tilt method), clean kaon identification in HKS, particle tracking under high multiplicity environment, precise energy scale calibration and so on.

In the present thesis, experimental results of p(e,e$'K^+)\Lambda$, $^{7}_{\Lambda}$He, $^{10}_{\Lambda}$Be, $^{12}_{\Lambda}$B and $^{52}_{\Lambda}$V were shown with discussions as the following:

- p**(e,e$'K^+$)**Λ Elementary processes of the electroproduction of Λ and Σ^0, p(e,e$'K^+)\Lambda$, Σ^0 were used for the absolute energy scale calibration of our spectrometer systems.

  Understanding of the elementary process of Λ is essential for theoretical calculations of electroproduction of Λ hypernuclei. The differential cross section of the p(e,e$'K^+)\Lambda$ reaction at the small K^+ scattering angle ($\theta^{\rm CM}_{\gamma K} \simeq 15.5^\circ$), the small Q^2 ($\simeq 0.01$ [GeV/c]^2) and the total energy of $W = 1.92$ GeV where no experimental data exists was obtained to be $235 \pm 13^{+28}_{-24}$ nb/sr.

- $^{7}_{\Lambda}$**He** $^{7}_{\Lambda}$He was already measured in JLab E01-011 (2005). The Λ's binding energy of the ground state of this hypernucleus ($1/2^+$) is important to test the phenomenological ΛN CSB (Charge Symmetry Breaking) interaction for $A = 7$, $T = 1$ hypernuclear systems. In the present work, the ground state binding energy was obtained to be $B_\Lambda = 5.55 \pm 0.10$(stat.)$\pm$0.11(sys.) MeV which has smaller errors than that of JLab E01-011. The obtained ground state binding energy of $^{7}_{\Lambda}$He is consistent with that of JLab E01-011, and it is more preferable to the calculations without the ΛN CSB interaction.

  In addition, a peak which is interpreted as $3/2^+$ and $5/2^+$ states was obtained to be $B_\Lambda = 3.65 \pm 0.20 \pm 0.11$ MeV with sufficient statistic for the first time. A state of 2^+ in the core nucleus (^{6}He) which corresponds to the excited states ($3/2^+$, $5/2^+$) in $^{7}_{\Lambda}$He is an unbound state. The glue-like role of Λ was confirmed by observing the phenomenon that the unbound state becomes the bound states due to the presence of Λ in the nucleus.

- $^{10}_{\Lambda}$**Be** Only three events of the ground state of $^{10}_{\Lambda}$Be had been observed in the emulsion experiments. The present experiment is the first spectroscopic measurement of $^{10}_{\Lambda}$Be, and

its structure has been successfully measured for the first time. About three times better energy resolution was achieved in the present experiment (0.78 MeV in FWHM) than that of the mirror Λ hypernucleus, ${}^{10}_{\Lambda}$B (2.2 MeV in FWHM) which was measured in the (π^+,K^+) experiment at KEK.

The obtained Λ's ground state binding energy of ${}^{10}_{\Lambda}$Be was compared with ${}^{10}_{\Lambda}$B measured by the (π^+,K^+) and the emulsion experiments to test the ΛN CSB interaction. Large errors particularly for the ${}^{10}_{\Lambda}$B data, do not allow us to discuss about the small effects of the ΛN CSB interaction for $A = 10$ hypernuclear systems (effect of $\sim$ 100 keV). However, the results is consistent with little CSB effect. Further experimental and theoretical efforts are necessary.

- **${}^{12}_{\Lambda}$B** In the present study, ${}^{12}_{\Lambda}$B has been measured with the world's best energy resolution of 0.5 MeV (FWHM) as the reaction spectroscopy of Λ hypernuclei. Consistency of the binding energy and the differential cross section for each peak with the previous experiments was confirmed. It proved that the new magnetic spectrometer systems, SPL(new)+HES(new)+HKS which were dedicated to the Λ hypernuclear measurement were worked as well as what we designed.

  The obtained ground state binding energy of ${}^{12}_{\Lambda}$B ($B_\Lambda = 11.38 \pm 0.02 \pm 0.11$ MeV) is deeper by $0.62 \pm 0.19 \pm 0.11$ MeV than that of ${}^{12}_{\Lambda}$C which was measured by the emulsion experiments. The difference cannot be theoretically explained. The obtained binding energy in the present experiment was calibrated with Λ and Σ^0, and a careful Monte Carlo simulation shows that the systematic error of the binding energy is 0.11 MeV. If the effect of the CSB is negligibly small in $A = 12$ hypernuclear systems, the obtained binding energy of ${}^{12}_{\Lambda}$B indicates that the reported binding energy of ${}^{12}_{\Lambda}$C which has been used as the reference for (π^+,K^+) experiments is shallower by about a half MeV

- **${}^{52}_{\Lambda}$V** A pilot study for investigation in the medium-heavy mass region by the (e,e′K^+) experiment was performed with an isotopically enriched ${}^{52}_{\Lambda}$Cr target. Overcoming high multiplicity environment in the spectrometer systems, the ground state binding energy of ${}^{52}_{\Lambda}$V has been obtained to be $B_\Lambda = 21.88 \pm 0.59 \pm 0.11$ MeV. The present result is the first measurement of Λ's ground state binding energy without the emulsion reference in the medium-heavy mass region, which could be a substantial information particularly for an understanding of the single particle potential of Λ.

  Careful comparison of results from past emulsion experiments and (π^+,K^+) experiments with our ${}^{52}_{\Lambda}$V binding energy was done. It indicates that the reported value of ${}^{12}_{\Lambda}$C ground state binding energy is shallower by 0.54 ± 0.21 MeV, which is consistent with the binding energy difference between ${}^{12}_{\Lambda}$B (present data) and ${}^{12}_{\Lambda}$C ($\Delta B_\Lambda = 0.62 \pm 0.19 \pm 0.11$). Since the ${}^{12}_{\Lambda}$C ground state binding energy has been used as the reference for the binding energy measurements in the (π^+,K^+) experiments, this shift would give great impact.

The spectroscopy by the (e,e′K^+) experiment serves to investigate more precise and finer Λ hypernuclear structures which are hardly to be studied by the existing meson beam experiments, thanks to:

① the absolute energy scale calibration with Λ and Σ^0, and
② the high energy resolution (sub-MeV in FWHM).

In the present experiment, Λ hypernuclear measurement with a smaller systematic error ($\sim$ 0.1 MeV) by the (e,e′K^+) reaction has been established. Moreover, the present work opened a door to the heavier Λ hypernuclear measurement with the (e,e′K^+) reaction in the future.

Acknowledgment

I would like to thank my supervisor, Prof. S. N. Nakamura for his invaluable support and encouragement of my Ph.D. research and writing this thesis. This thesis would not have been possible without intense discussions with him day after day. Moreover, when I stayed at JLab for the present experiment, he supported and advised me both officially and privately. I am happy to have a mentor like him for my Ph.D. research. I would like to express heartfelt appreciation to Prof. O. Hashimoto who supervised and guided me to the present experiment. I am sorry that I could not finish this thesis before he passed away. He always motivated me for the Λ hypernuclear research with his fascinating personality. I am deeply grateful to Prof. H. Tamura for his constant advice, encouragement and help. His advice and suggestions always made me think about many valuable and important ideas. Furthermore, his seminars and talks motivated me to study nuclear physics all the time.

In addition to Prof. S. N. Nakamura and Prof. H. Tamura, I would like to thank the rest of my thesis committee, Prof. T. Kobayashi, Prof. K. Hagino and Prof. J. Shirai for their valuable advice, pithy suggestions and tough questions. When I visited them, they gave me opportunity to discuss about the present works, and they responded to me with great earnestness.

I would like to express my gratitude to Prof. L. Tang of Hampton University, Prof. J. Reinhold of Florida International University and Dr. S. A. Wood of JLab for their kind advise and support of the present research and the life in the United States. I have learned ways of thinking for research based on their experiences, which would be beneficial for me.

I owe thanks to Dr. Y. Fujii for allowing me to discuss with him about the data analyses with his experience of the previous (e,e$'K^+$) experiments. He also gave me advice of computer issues related to the analyses. I wish to acknowledge great support and advice of Dr. T. Maruta for the present research and the life in the same apartment in the United States. I could spend the research days with delight at JLab thanks to him. I would like to thank Dr. K. Tsukada for his invaluable advice and suggestions for the data analyses. He gave me a mass of ideas breaking through problems which arose during the work. I would like to express my thanks to Dr. D. Kawama for his lead of the experiment from the design to analysis phases. He always gave me precise advice, suggestions and encouragement for my Ph.D. research. From him, particularly, I have learned techniques of data analyses, Monte Carlo simulations and the other software such as TOSCA. I am deeply grateful for advice and suggestions of Ms. C. Chen. She was an only person who analyzed the data of JLab E05-115 in the final stage with me. Her words and suggestions during discussions about analyses were very encouraging for me. Moreover, she kindly supported and helped my life in the United States. I am indebted to Mr. N. Chiga who is a great technician for his technical assistance and warm encouragement. He made a good atmosphere surrounding us both in Tohoku University and in JLab with his unique character.

I thank my labmate who served for the JLab E05-115 experiment: Mr. T. Yamamoto, Mr. K. Yokota, Mr. N. Taniya, Ms. A. Maruta (Shichijo), Mr. S. Nagao, Mr. D. Doi, Mr. A. Chiba, Ms. M. Fujita, Mr. J. Bono, Mr. V. Maxwell, Dr. A. Asaturyan and Dr. A. Mkrtchyan for their requisite contributions to the preparation, operations and analyses of the experiment.

I would like to acknowledge my indebtedness to Prof. P. Bydžovský, Prof. D. J. Millener, Prof. T. Motoba, Prof. E. Hiyama and Dr. M. Isaka for their theoretical support, advice and calculations which are indispensable for this thesis.

I wish to express my sincere gratitude to Prof. J. Pochodzalla, Prof. P. Achenbach, Dr. C. Ayerbe Gayoso, Dr. A. Esser, Dr. L. Debenjak, Mr. F. Schulz, Ms. M. Gómez, Mr. S. Bleser, Mr. M. Steinen and Mr. J. Gerhard for their heartwarming support when I stayed in Mainz, Germany to take part in experiments for the elementary process of electroproduction of Λ (Σ^0) and the decay pion spectroscopy of Λ hypernuclei. I have learned many valuable things which were useful for the present research in the experiments and discussions with them.

I would like to express my great thanks to Prof. K. Maeda, Prof. K. Sekiguchi, Prof. T. Koike, Dr. M. Kaneta, Dr. K. Miwa, Dr. H. Kanda, Dr. M. Ukai, Dr. A. Matsumura, Dr. K. Futatsukawa, Dr. K. Shirotori, Dr. K. Hosomi and Dr. B. Beckford for their advice and support not only for the research, but also the life in Tohoku University. Especially, Dr. M. Ukai took care of me like a sister.

My thanks also goes to Mr. T. Yamamoto, Ms. M. Miwa (Sato), Mr. A. Okuyama, Mr. T. Fujii, Ms. C. Kimura and Mr. R. Honda for their warm support and encouragement. I could study hard with them, and keep my mental OK even when I struggled against big difficulties for the research thanks to them.

I also would like to thank secretaries: Ms. N. Kawamura, Ms. M. Shimaya, Ms. A. Yamanouchi, Ms. S. Fukataki and Ms. H. Arihara for their powerful support of paperwork, which was significant for me to focus on the research.

This thesis was done with a lot of support. I would like to express my great appreciation also to all collaboration members who were not written above.

Last, I thank my friends and family for their understanding and perpetual support.

Appendix A

Λ and Σ^0 from H_2O target

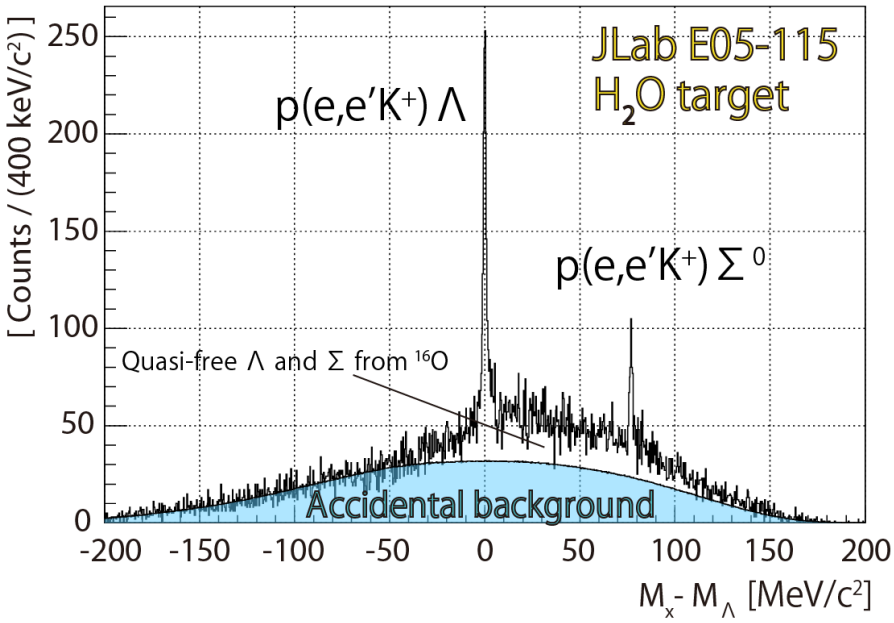

Figure A.1: A missing mass spectrum of Λ and Σ^0 from the H_2O target.

Fig. A.1 shows a missing mass spectrum with the H_2O target. Peaks of p(e,e$'K^+$)Λ and p(e,e$'K^+$)Σ^0 were clearly observed on background events. Origins of the background events are the following:

1. Quasi-free Λ and $\Sigma^{0,\pm}$ from a ^{16}O nucleus
2. $e'K^+$ accidental coincidence

The distribution of the accidental coincidence event was obtained by the mixed event analysis (Sec. 4.9). On the other hand, a distribution of the quasi-free Λ and $\Sigma^{0,\pm}$ from a ^{16}O nucleus cannot be obtained with data which was taken in the present experiment.

To obtain mean values, widths and number of events of Λ and Σ^0, the background distribution was estimated by using Statistics-sensitive Non-linear Iterative Peak-clipping (SNIP) algorithm [114][115][116] (Fig. A.2), and was subtracted from the original spectrum (Fig. A.3). The peaks of Λ and Σ^0 were fitted with Voigt functions to obtain the mean values and the widths. The number of events were evaluated by integrating the spectrum over the range of a mean value $\pm \sim 5$ MeV for each peak. The obtained width, FWHM and number of events for each peak are summarized in Table. A.1.

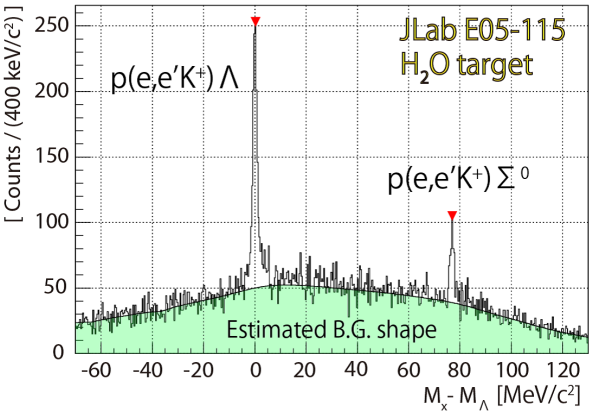

Figure A.2: A missing mass spectrum with the H_2O target. The background distribution was estimated by the SNIP algorithm [114][115][116].

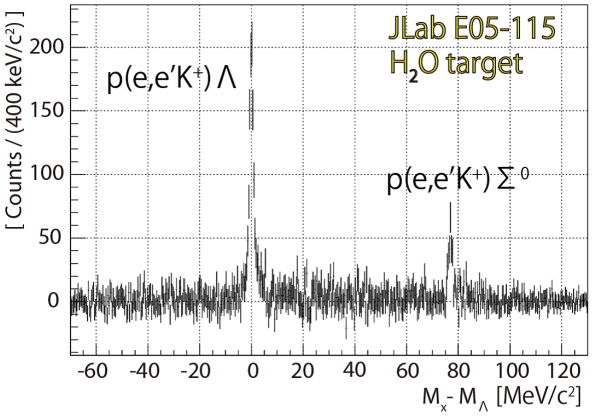

Figure A.3: A missing mass spectrum with the H_2O target after the background distribution which was estimated by the SNIP algorithm [114][115][116] (Fig. A.2) was subtracted.

Table A.1: The obtained widths, FWHMs and number of events for peaks of Λ and Σ^0 from the H_2O target.

		Λ	Σ^0
Fitting results (Voigt function)	Mean [keV]	76 ± 31	25 ± 78
	FWHM [MeV]	1.8	1.8
Number of events		1418 ± 93	383 ± 65

Appendix B

^{9}Be(e,e′K^{+})$^{9}_{\Lambda}$Li

$^{9}_{\Lambda}$Li has been measured in JLab E94-107 (Hall A), and reported in Ref. [127]. The present experiment is the second spectroscopic measurement of $^{9}_{\Lambda}$Li.

Fig. B.1 shows a binding energy spectrum for ^{9}Be(e,e′K^{+})$^{9}_{\Lambda}$Li. A distribution of $e'K^{+}$ accidental coincidence event was obtained by the mixed event analysis (Sec. 4.9) to make contributions of its statistical errors negligible small when the accidental coincidence distribution was subtracted from the original spectrum.

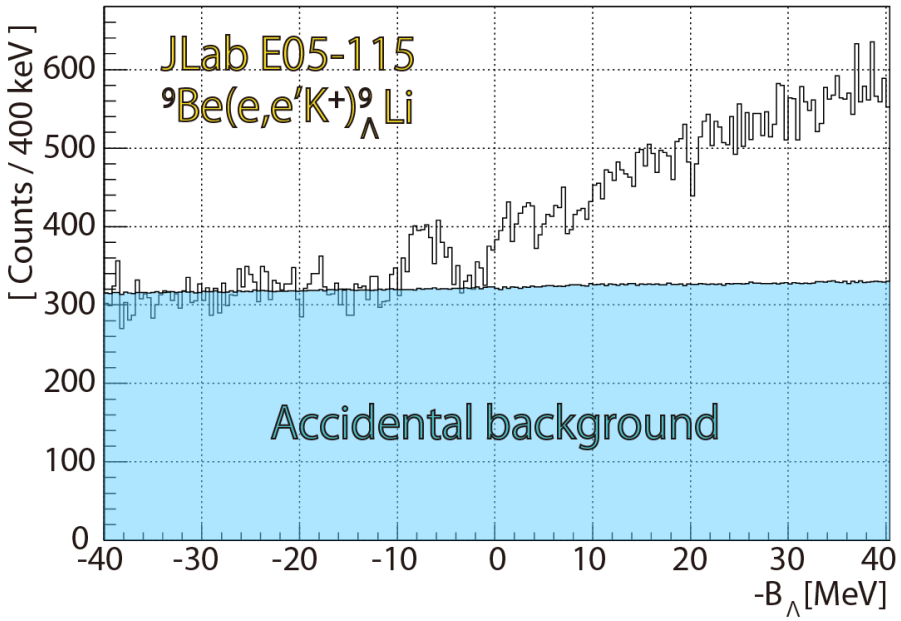

Figure B.1: A binding energy spectrum for ^{9}Be(e,e′K^{+})$^{9}_{\Lambda}$Li.

The ordinate axis was converted to the differential cross section for the (γ^{*}, K^{+}) reaction as defined in Eq. (4.31), and the spectrum is shown in Fig. B.1. Fig. B.3 shows a binding energy spectrum with the ordinate axis of the differential cross section after the distribution of the $e'K^{+}$ accidental coincidence event was subtracted.

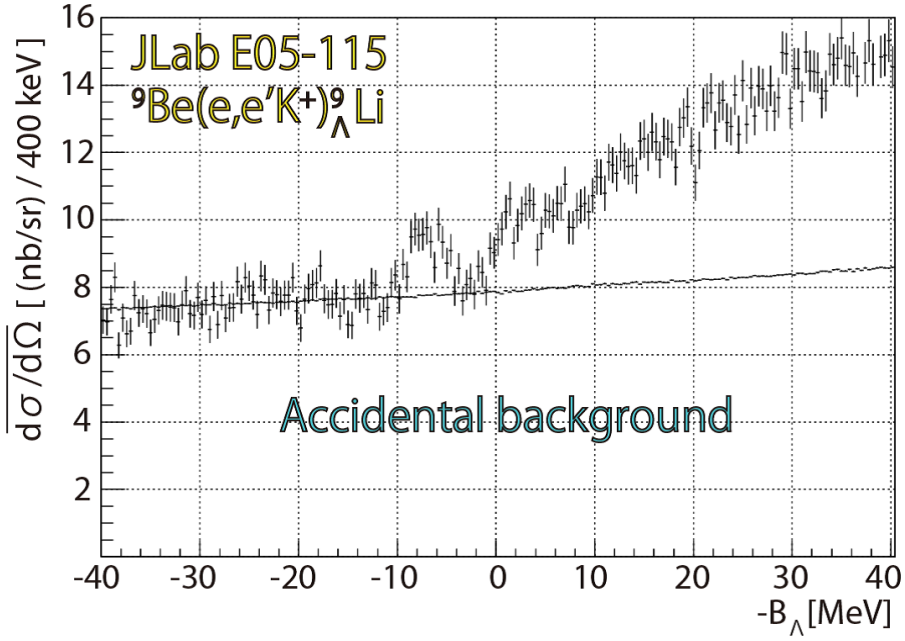

Figure B.2: A binding energy spectrum for ^{9}Be(e,e'K^{+})$^{9}_{\Lambda}$Li. The ordinate axis is the differential cross section for the (γ^{*}, K^{+}) reaction as defined in Eq. (4.31).

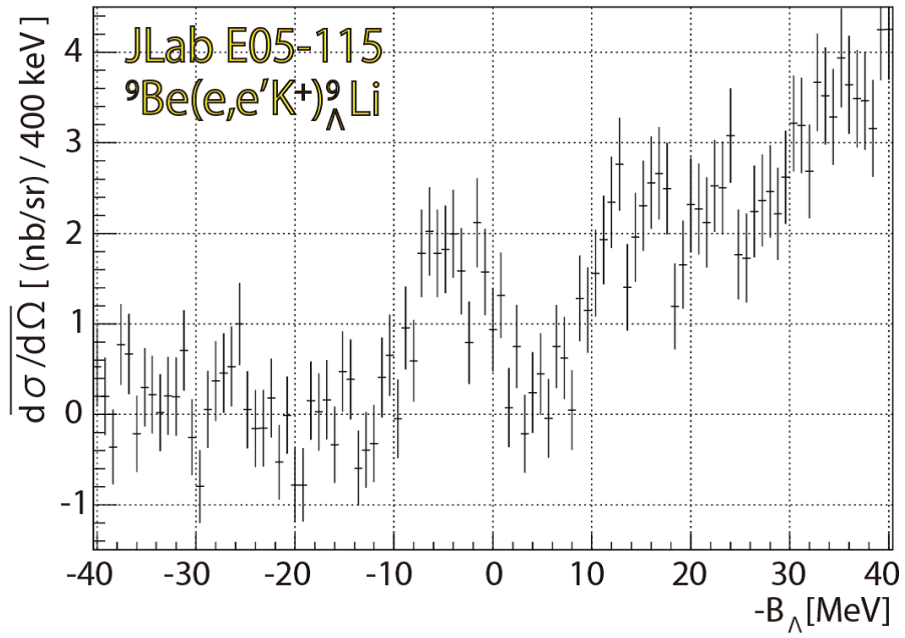

Figure B.3: A binding energy spectrum with the ordinate axis of the differential cross section after the distribution of the $e'K^{+}$ accidental coincidence event was subtracted.

Appendix C

Hit wire selection for particle tracking

A hit wire multiplicity in HKS was higher for heavier target data due to the e^-, e^+ background particles (Sec. 4.4). To reduce a risk of mistracking and a computation time for a particle tracking, a hit wire selection with TOF detectors was developed and introduced before a procedure of pattern recognition of hit wires (Fig. C.1).

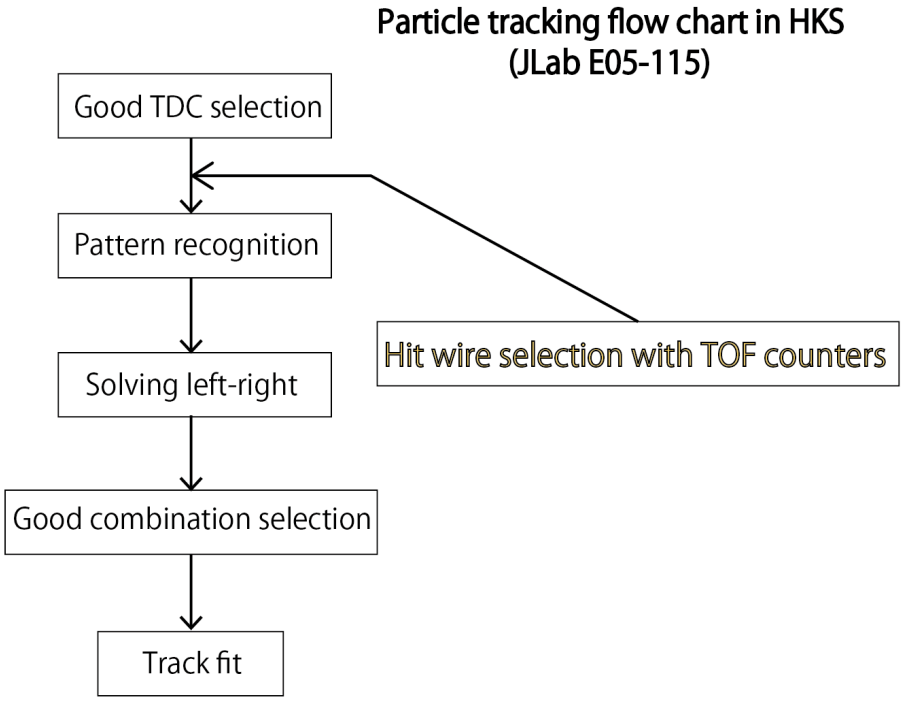

Figure C.1: A flow chart of the particle tracking in HKS.

C.1 x, x' layers

Fig. C.2 shows a concept of the hit wire selection with TOF detectors for the x and x' layers in HKS drift chambers (KDC1, KDC2). The hit wire selection was proceeded as follows:

① Making combinations of hit TOF segments between KTOF1 and KTOF2 taking into account the HKS optics (the grouping of HKS detectors as shown in Fig. 3.18).

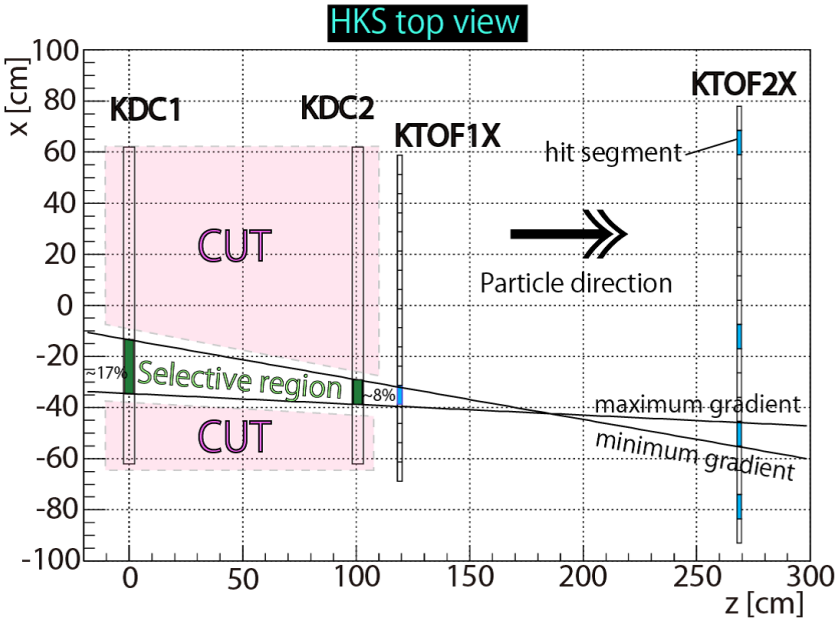

Figure C.2: A concept of the hit wire selection for the x ans x' layers in HKS.

② Regions in KDC1 and KDC2 which were used for the particle tracking were derived by using projected regions of the combinations of TOF detectors determined in ①.

③ Hit wires which were in the selective regions (②) were used for the further tracking process.

An allowance of the selective region was optimized with the following figure of merit (FOM):

$$FOM = \frac{S^2}{N} \tag{C.1}$$

where S and N are the number of events of K^+ candidates and the others. Fig. C.3 shows the normalized FOM $\left(NFOM = \frac{FOM_{(\text{w/ TOF-pre})}}{FOM_{(\text{w/o TOF-pre})}}\right)$ and the ratio of number of K^+ candidates $\left(R_K = \frac{N^K_{(\text{w/ TOF-pre})}}{N^K_{(\text{w/o TOF-pre})}}\right)$ as a function of the allowance (a shown in Fig. C.3). In the present analyses, $a = 2.5$ cm was chosen.

A sample of the hit wire selection with TOF detectors for the real data of ^{52}Cr target is shown in Fig. C.4. Red markers indicate wires which were selected and used for the particle tracking process.

C.2 u, u', v, v' layers

Hit wire selections with TOF detectors for the u, u′, v, v′ layers were also applied by projecting the selective region for x, x′ layers to u (u′) and v (v′) coordinates (Fig. C.5). The coordinates of the projected regions were calculated by the following:

$$x'_{min} = \frac{x_{min}}{\cos\theta} - \Big(x_{min}\tan\theta + h\Big)\sin\theta \tag{C.2}$$

$$x'_{max} = \frac{x_{max}}{\cos\theta} - \Big(x_{max}\tan\theta - h\Big)\sin\theta \tag{C.3}$$

where the variables are defined in Fig. C.5.

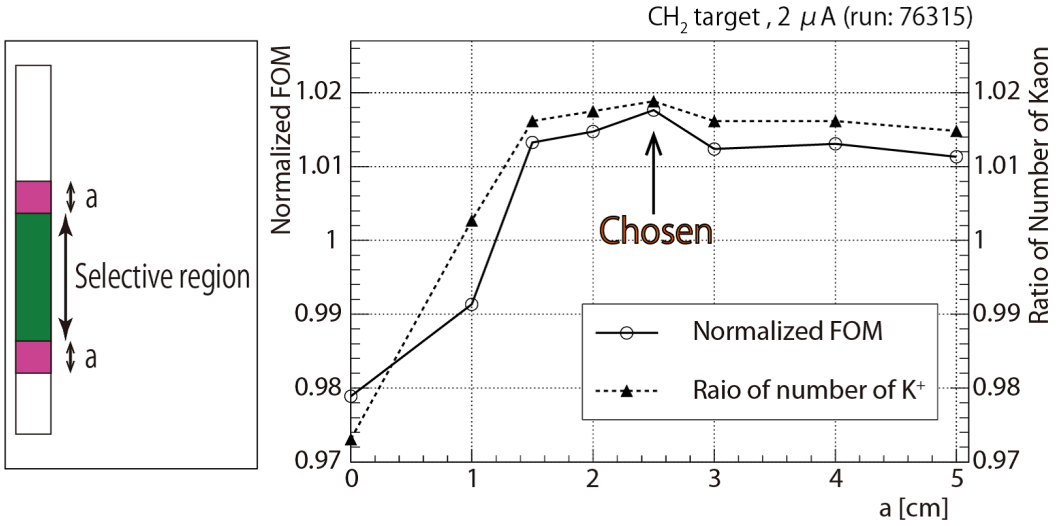

Figure C.3: $NFOM$ and R_K as a function of the allowance (a). In the present analyses, $a = 2.5$ cm was chosen.

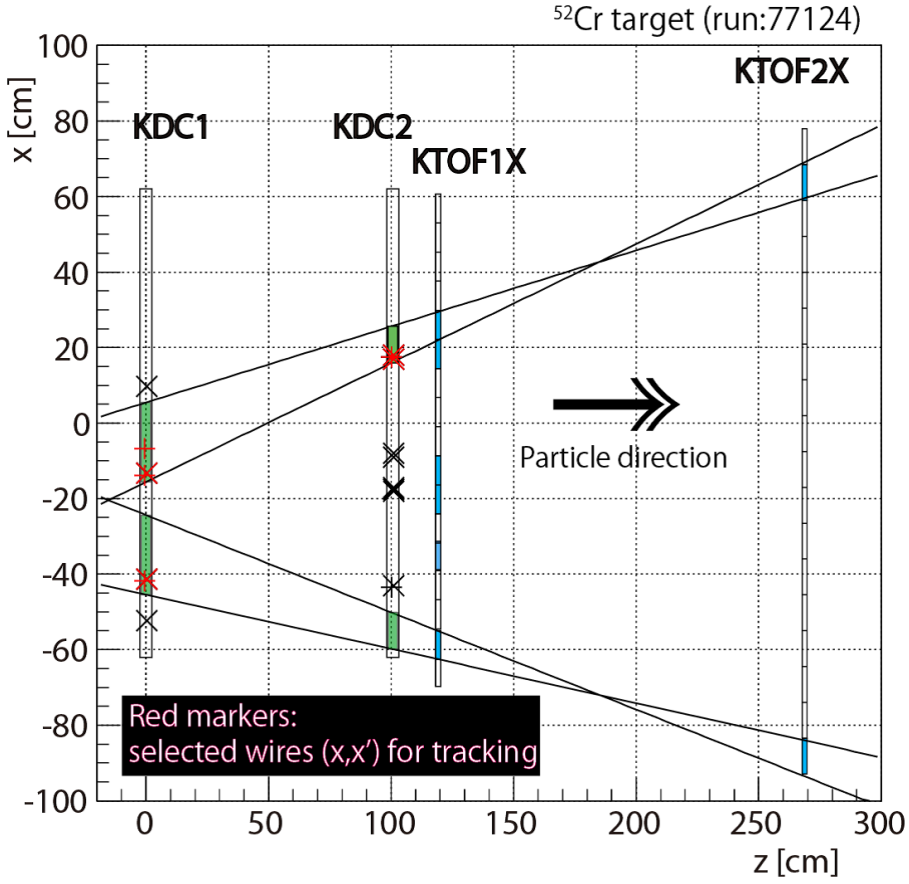

Figure C.4: A sample of the hit wire selection with TOF detectors for the real data of the ^{52}Cr target. Red markers indicate wires which were selected and used for the particle tracking process.

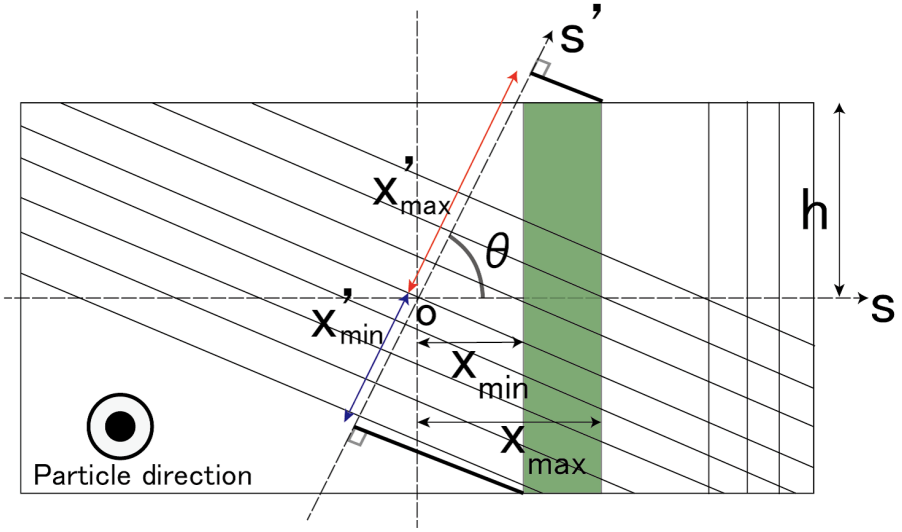

Figure C.5: The selective region for x and x' layers (green region in the figure) were projected to the u, u', v, v' coordinates.

Fig. C.6 shows a sample of the event display for KDC1 and KDC2. Green regions are the selective regions which were obtained with TOF detectors (KTOF1X and KTOF2X), and red markers and lines are hit wires which were chosen to be used for the tracking process.

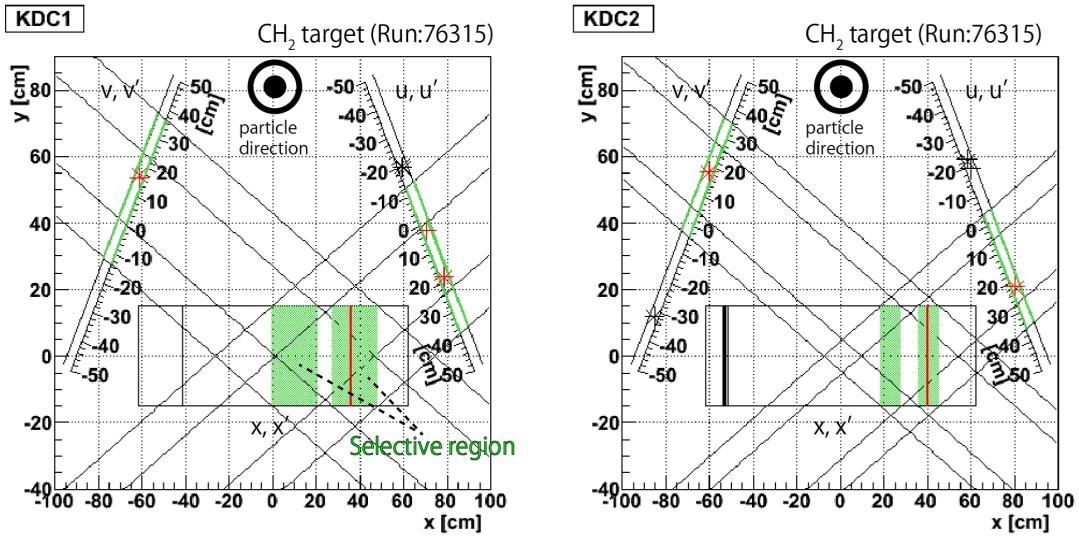

Figure C.6: A sample of the event display for KDC1 and KDC2. Green regions are the selective regions which were obtained with TOF detectors (KTOF1X and KTOF2X), and red markers and lines are hit wires which were chosen to be used for the tracking process.

C.3 Improvements

After the hit wire selection with TOF detectors was applied, wire multiplicity in KDC (x-layer) was reduced by 48% and 22% for the polyethylene target and the ^{52}Cr target, respectively. K^+ events which were hidden by background events were appeared with the hit wire selection, and

the number of the K^+ events was increased. The improvements of the analyses with the hit wire selection were summarized in Table. C.1.

Table C.1: The improvements of the analyses with the hit wire selection with TOF detectors (KTOF1X and KTOF2X).

CH_2 target (Run: 76315)			
	Hit wire selection with TOF detectors		variation [%]
	OFF	ON	
Analysis time (ENGINE REPLAY[*1])	17^m 22^s	15^m14^s	-14.2
ROOT file size [MB]	30.7	31.8	+3.6
Number of events	72602	75349	+3.8
Number of K^+ events	828	851	+2.8
Multiplicity (KDC1-u)	2.16	1.69	-21.8
Multiplicity (KDC1-x)	2.35	1.22	-48.1
^{52}Cr target (Run: 77124)			
	Hit wire selection with TOF detectors		variation [%]
	OFF	ON	
Analysis time (ENGINE REPLAY[*1])	5^h 16^m 46^s	$4^h33^m42^s$	-10.8
ROOT file size [MB]	13.3	17.9	+34.6
Number of events	33156	45285	+36.6
Number of K^+ events	56	70	+25.0
Multiplicity (KDC1-u)	4.63	4.38	-5.4
Multiplicity (KDC1-x)	4.97	3.87	-22.1

[*1] See Sec. 4.1.

Appendix D

Table of cross sections

Tables of the differential cross sections for ${}^{7}_{\Lambda}$He, ${}^{9}_{\Lambda}$Li, ${}^{10}_{\Lambda}$Be and ${}^{12}_{\Lambda}$B, and the counts for ${}^{52}_{\Lambda}$V will be shown in this section. A list of the tables is shown in Table. D.1.

Table D.1: A list of tables of the differential cross sections for ${}^{7}_{\Lambda}$He, ${}^{9}_{\Lambda}$Li, ${}^{10}_{\Lambda}$Be and ${}^{12}_{\Lambda}$B, and the counts for ${}^{52}_{\Lambda}$V.

Hypernucleus	(bin, $-B_\Lambda$ [MeV]: min, $-B_\Lambda$ [MeV]: max)	Table
${}^{7}_{\Lambda}$He	(320, −60, +60)	D.2, D.3, D.4, D.5
${}^{9}_{\Lambda}$Li	(300, −60, +60)	D.6, D.7, D.8
${}^{10}_{\Lambda}$Be	(400, −60, +60)	D.9, D.10, D.11, D.12
${}^{12}_{\Lambda}$B	(500, −60, +60)	D.13, D.14, D.15, D.16, D.17
${}^{52}_{\Lambda}$V	(100, −60, +60)	D.18

Table D.2: Table of the binding energy spectrum of ^{7}Li(e,e′K^{+})$^{7}_{\Lambda}$He. A range of the binding energy from −60 MeV to +60 MeV is divided by 320 bins. (1/4)

^{7}Li(e,e′K^{+})$^{7}_{\Lambda}$He (A range from −60 MeV to +60 MeV is divided by 320 bins)					
N_{bin}	$\left(\frac{d\sigma}{d\Omega_K}\right)\Big\|_{1^\circ-13^\circ}$ [nb/sr]		N_{bin}	$\left(\frac{d\sigma}{d\Omega_K}\right)\Big\|_{1^\circ-13^\circ}$ [nb/sr]	
	(Signal+Accidental)	(Accidental)		(Signal+Accidental)	(Accidental)
1	6.152 ± 0.368	6.065 ± 0.015	51	6.071 ± 0.367	6.227 ± 0.016
2	6.221 ± 0.369	6.061 ± 0.015	52	6.315 ± 0.394	6.169 ± 0.016
3	6.277 ± 0.371	6.084 ± 0.015	53	5.777 ± 0.359	6.205 ± 0.016
4	5.597 ± 0.350	6.060 ± 0.015	54	6.693 ± 0.387	6.204 ± 0.016
5	5.826 ± 0.357	6.087 ± 0.015	55	6.346 ± 0.377	6.188 ± 0.016
6	5.737 ± 0.355	6.085 ± 0.015	56	5.557 ± 0.351	6.185 ± 0.016
7	5.809 ± 0.357	6.102 ± 0.015	57	5.829 ± 0.361	6.195 ± 0.016
8	5.862 ± 0.359	6.104 ± 0.015	58	5.867 ± 0.362	6.188 ± 0.016
9	6.157 ± 0.367	6.093 ± 0.015	59	5.806 ± 0.360	6.173 ± 0.016
10	6.105 ± 0.366	6.092 ± 0.015	60	6.668 ± 0.386	6.200 ± 0.016
11	5.865 ± 0.360	6.109 ± 0.015	61	7.120 ± 0.399	6.186 ± 0.016
12	6.781 ± 0.386	6.075 ± 0.015	62	6.145 ± 0.371	6.193 ± 0.016
13	6.680 ± 0.384	6.108 ± 0.015	63	5.841 ± 0.362	6.195 ± 0.016
14	6.317 ± 0.374	6.113 ± 0.015	64	6.315 ± 0.377	6.170 ± 0.016
15	6.229 ± 0.370	6.131 ± 0.015	65	6.223 ± 0.373	6.215 ± 0.016
16	6.896 ± 0.390	6.119 ± 0.015	66	6.550 ± 0.385	6.199 ± 0.016
17	6.114 ± 0.368	6.126 ± 0.016	67	6.173 ± 0.373	6.182 ± 0.016
18	6.186 ± 0.369	6.135 ± 0.016	68	6.507 ± 0.382	6.202 ± 0.016
19	6.470 ± 0.377	6.116 ± 0.015	69	6.287 ± 0.376	6.190 ± 0.016
20	6.116 ± 0.367	6.148 ± 0.016	70	6.619 ± 0.385	6.182 ± 0.016
21	5.945 ± 0.362	6.141 ± 0.016	71	6.612 ± 0.386	6.227 ± 0.016
22	5.984 ± 0.363	6.140 ± 0.016	72	5.994 ± 0.367	6.207 ± 0.016
23	6.265 ± 0.373	6.133 ± 0.016	73	6.077 ± 0.372	6.246 ± 0.016
24	6.131 ± 0.368	6.155 ± 0.016	74	6.028 ± 0.368	6.190 ± 0.016
25	6.262 ± 0.372	6.152 ± 0.016	75	6.692 ± 0.390	6.213 ± 0.016
26	6.135 ± 0.367	6.122 ± 0.016	76	5.963 ± 0.366	6.225 ± 0.016
27	6.036 ± 0.365	6.153 ± 0.016	77	6.630 ± 0.386	6.230 ± 0.016
28	6.201 ± 0.370	6.165 ± 0.016	78	6.191 ± 0.373	6.259 ± 0.016
29	5.879 ± 0.360	6.170 ± 0.016	79	6.218 ± 0.375	6.234 ± 0.016
30	6.054 ± 0.367	6.169 ± 0.016	80	6.911 ± 0.394	6.233 ± 0.016
31	6.293 ± 0.373	6.182 ± 0.016	81	5.227 ± 0.343	6.237 ± 0.016
32	5.813 ± 0.363	6.164 ± 0.016	82	5.710 ± 0.358	6.243 ± 0.016
33	6.581 ± 0.386	6.172 ± 0.016	83	6.137 ± 0.372	6.245 ± 0.016
34	6.206 ± 0.370	6.156 ± 0.016	84	6.306 ± 0.378	6.300 ± 0.016
35	6.513 ± 0.379	6.140 ± 0.016	85	6.359 ± 0.379	6.278 ± 0.016
36	6.512 ± 0.381	6.169 ± 0.016	86	6.340 ± 0.378	6.278 ± 0.016
37	5.772 ± 0.358	6.193 ± 0.016	87	6.299 ± 0.377	6.255 ± 0.016
38	6.487 ± 0.382	6.153 ± 0.016	88	6.037 ± 0.372	6.256 ± 0.016
39	5.756 ± 0.358	6.125 ± 0.016	89	6.600 ± 0.386	6.273 ± 0.016
40	6.926 ± 0.391	6.166 ± 0.016	90	6.129 ± 0.372	6.288 ± 0.016
41	6.388 ± 0.377	6.177 ± 0.016	91	5.690 ± 0.358	6.266 ± 0.016
42	6.385 ± 0.377	6.181 ± 0.016	92	6.291 ± 0.377	6.270 ± 0.016
43	6.275 ± 0.373	6.175 ± 0.016	93	6.242 ± 0.376	6.297 ± 0.016
44	5.954 ± 0.364	6.170 ± 0.016	94	6.083 ± 0.372	6.307 ± 0.016
45	5.895 ± 0.363	6.165 ± 0.016	95	6.308 ± 0.378	6.279 ± 0.016
46	6.123 ± 0.371	6.159 ± 0.016	96	6.978 ± 0.397	6.267 ± 0.016
47	7.056 ± 0.396	6.187 ± 0.016	97	6.700 ± 0.390	6.297 ± 0.016
48	6.697 ± 0.385	6.154 ± 0.016	98	5.886 ± 0.366	6.288 ± 0.016
49	6.320 ± 0.375	6.177 ± 0.016	99	6.477 ± 0.384	6.316 ± 0.016
50	5.881 ± 0.368	6.177 ± 0.016	100	5.933 ± 0.367	6.307 ± 0.016

Table D.3: Table of the binding energy spectrum of ^{7}Li(e,e$'K^{+}$)$^{7}_{\Lambda}$He. A range of the binding energy from −60 MeV to +60 MeV is divided by 320 bins. (2/4)

^{7}Li(e,e$'K^{+}$)$^{7}_{\Lambda}$He (A range from −60 MeV to +60 MeV is divided by 320 bins)					
N_{bin}	$\overline{\left(\frac{d\sigma}{d\Omega_K}\right)}\Big\|_{1^\circ-13^\circ}$ [nb/sr]		N_{bin}	$\overline{\left(\frac{d\sigma}{d\Omega_K}\right)}\Big\|_{1^\circ-13^\circ}$ [nb/sr]	
	(Signal+Accidental)	(Accidental)		(Signal+Accidental)	(Accidental)
101	5.744 ± 0.361	6.293 ± 0.016	151	8.030 ± 0.432	6.521 ± 0.016
102	6.005 ± 0.369	6.314 ± 0.016	152	7.667 ± 0.423	6.522 ± 0.016
103	6.676 ± 0.390	6.327 ± 0.016	153	6.970 ± 0.403	6.504 ± 0.016
104	6.097 ± 0.372	6.310 ± 0.016	154	6.853 ± 0.398	6.514 ± 0.016
105	6.773 ± 0.401	6.322 ± 0.016	155	7.265 ± 0.411	6.537 ± 0.016
106	5.788 ± 0.363	6.348 ± 0.016	156	7.362 ± 0.414	6.553 ± 0.016
107	6.866 ± 0.394	6.293 ± 0.016	157	6.938 ± 0.402	6.540 ± 0.016
108	7.099 ± 0.403	6.304 ± 0.016	158	6.460 ± 0.387	6.537 ± 0.016
109	5.376 ± 0.349	6.305 ± 0.016	159	7.397 ± 0.415	6.548 ± 0.016
110	6.181 ± 0.374	6.331 ± 0.016	160	7.973 ± 0.429	6.577 ± 0.017
111	6.330 ± 0.379	6.333 ± 0.016	161	7.744 ± 0.425	6.504 ± 0.016
112	6.593 ± 0.388	6.326 ± 0.016	162	6.926 ± 0.401	6.553 ± 0.016
113	6.269 ± 0.378	6.338 ± 0.016	163	7.088 ± 0.407	6.551 ± 0.016
114	5.956 ± 0.369	6.375 ± 0.016	164	8.145 ± 0.437	6.546 ± 0.016
115	5.541 ± 0.355	6.363 ± 0.016	165	7.537 ± 0.420	6.574 ± 0.017
116	6.006 ± 0.370	6.367 ± 0.016	166	7.906 ± 0.430	6.604 ± 0.017
117	6.178 ± 0.375	6.344 ± 0.016	167	8.043 ± 0.434	6.604 ± 0.017
118	5.838 ± 0.366	6.351 ± 0.016	168	8.534 ± 0.447	6.579 ± 0.017
119	5.799 ± 0.364	6.333 ± 0.016	169	8.445 ± 0.446	6.557 ± 0.017
120	6.273 ± 0.379	6.379 ± 0.016	170	7.067 ± 0.410	6.583 ± 0.017
121	6.686 ± 0.391	6.389 ± 0.016	171	8.098 ± 0.436	6.608 ± 0.017
122	6.830 ± 0.396	6.372 ± 0.016	172	8.485 ± 0.447	6.606 ± 0.017
123	6.449 ± 0.385	6.379 ± 0.016	173	7.686 ± 0.425	6.605 ± 0.017
124	6.175 ± 0.375	6.416 ± 0.016	174	8.040 ± 0.438	6.608 ± 0.017
125	6.347 ± 0.380	6.387 ± 0.016	175	8.867 ± 0.456	6.644 ± 0.017
126	6.123 ± 0.374	6.383 ± 0.016	176	7.930 ± 0.433	6.588 ± 0.017
127	5.929 ± 0.370	6.385 ± 0.016	177	8.197 ± 0.439	6.640 ± 0.017
128	5.667 ± 0.360	6.395 ± 0.016	178	8.121 ± 0.439	6.660 ± 0.017
129	6.630 ± 0.390	6.390 ± 0.016	179	8.842 ± 0.456	6.632 ± 0.017
130	6.365 ± 0.382	6.370 ± 0.016	180	8.457 ± 0.446	6.599 ± 0.017
131	7.136 ± 0.418	6.425 ± 0.016	181	7.279 ± 0.414	6.621 ± 0.017
132	7.016 ± 0.402	6.403 ± 0.016	182	8.770 ± 0.454	6.650 ± 0.017
133	6.676 ± 0.391	6.441 ± 0.016	183	8.288 ± 0.442	6.663 ± 0.017
134	6.651 ± 0.397	6.423 ± 0.016	184	7.711 ± 0.428	6.664 ± 0.017
135	6.317 ± 0.382	6.445 ± 0.016	185	7.618 ± 0.424	6.684 ± 0.017
136	5.974 ± 0.371	6.470 ± 0.016	186	8.563 ± 0.449	6.657 ± 0.017
137	6.296 ± 0.382	6.460 ± 0.016	187	8.627 ± 0.451	6.701 ± 0.017
138	7.548 ± 0.418	6.442 ± 0.016	188	9.706 ± 0.479	6.679 ± 0.017
139	7.182 ± 0.408	6.459 ± 0.016	189	8.211 ± 0.441	6.728 ± 0.017
140	6.851 ± 0.398	6.459 ± 0.016	190	9.692 ± 0.479	6.691 ± 0.017
141	6.325 ± 0.384	6.506 ± 0.016	191	9.366 ± 0.472	6.734 ± 0.017
142	7.196 ± 0.409	6.470 ± 0.016	192	8.327 ± 0.444	6.697 ± 0.017
143	7.481 ± 0.418	6.492 ± 0.016	193	9.055 ± 0.463	6.748 ± 0.017
144	7.717 ± 0.423	6.477 ± 0.016	194	9.044 ± 0.463	6.729 ± 0.017
145	8.734 ± 0.450	6.519 ± 0.016	195	9.533 ± 0.483	6.726 ± 0.017
146	8.864 ± 0.453	6.480 ± 0.016	196	9.403 ± 0.473	6.758 ± 0.017
147	8.251 ± 0.437	6.495 ± 0.016	197	10.586± 0.518	6.750 ± 0.017
148	8.047 ± 0.431	6.520 ± 0.016	198	9.280 ± 0.470	6.728 ± 0.017
149	7.571 ± 0.419	6.525 ± 0.016	199	9.522 ± 0.476	6.742 ± 0.017
150	7.754 ± 0.424	6.496 ± 0.016	200	11.655± 0.528	6.789 ± 0.017

Table D.4: Table of the binding energy spectrum of ^{7}Li(e,e′K^{+})$^{7}_{\Lambda}$He. A range of the binding energy from −60 MeV to +60 MeV is divided by 320 bins. (3/4)

^{7}Li(e,e′K^{+})$^{7}_{\Lambda}$He (A range from −60 MeV to +60 MeV is divided by 320 bins)					
N_{bin}	$\left(\frac{d\sigma}{d\Omega_K}\right)\Big\|_{1^\circ-13^\circ}$ [nb/sr]		N_{bin}	$\left(\frac{d\sigma}{d\Omega_K}\right)\Big\|_{1^\circ-13^\circ}$ [nb/sr]	
	(Signal+Accidental)	(Accidental)		(Signal+Accidental)	(Accidental)
201	10.090 ± 0.490	6.812 ± 0.017	251	13.677 ± 0.582	7.071 ± 0.018
202	9.843 ± 0.486	6.793 ± 0.017	252	14.430 ± 0.598	7.045 ± 0.018
203	11.461 ± 0.529	6.801 ± 0.017	253	12.552 ± 0.557	7.086 ± 0.018
204	11.064 ± 0.514	6.799 ± 0.017	254	14.227 ± 0.593	7.033 ± 0.018
205	10.183 ± 0.494	6.832 ± 0.017	255	13.769 ± 0.586	7.059 ± 0.018
206	10.511 ± 0.503	6.846 ± 0.017	256	13.458 ± 0.576	7.070 ± 0.018
207	10.661 ± 0.505	6.845 ± 0.017	257	14.470 ± 0.600	7.075 ± 0.018
208	10.637 ± 0.505	6.838 ± 0.017	258	14.729 ± 0.605	7.083 ± 0.018
209	10.480 ± 0.502	6.840 ± 0.017	259	14.421 ± 0.598	7.142 ± 0.018
210	10.899 ± 0.510	6.865 ± 0.017	260	14.061 ± 0.589	7.141 ± 0.018
211	11.668 ± 0.530	6.827 ± 0.017	261	13.895 ± 0.589	7.105 ± 0.018
212	10.327 ± 0.497	6.830 ± 0.017	262	15.279 ± 0.617	7.138 ± 0.018
213	11.470 ± 0.525	6.858 ± 0.017	263	15.468 ± 0.621	7.132 ± 0.018
214	10.450 ± 0.501	6.844 ± 0.017	264	15.636 ± 0.627	7.140 ± 0.018
215	10.698 ± 0.507	6.860 ± 0.017	265	15.269 ± 0.621	7.117 ± 0.018
216	11.379 ± 0.526	6.866 ± 0.017	266	15.145 ± 0.617	7.147 ± 0.018
217	11.529 ± 0.526	6.863 ± 0.017	267	14.205 ± 0.592	7.128 ± 0.018
218	11.467 ± 0.526	6.862 ± 0.017	268	15.582 ± 0.625	7.187 ± 0.018
219	11.512 ± 0.529	6.871 ± 0.017	269	15.453 ± 0.623	7.159 ± 0.018
220	12.069 ± 0.540	6.882 ± 0.017	270	14.470 ± 0.608	7.158 ± 0.018
221	11.063 ± 0.518	6.886 ± 0.017	271	14.833 ± 0.612	7.184 ± 0.018
222	12.160 ± 0.542	6.879 ± 0.017	272	14.024 ± 0.594	7.221 ± 0.018
223	11.217 ± 0.525	6.910 ± 0.017	273	14.356 ± 0.600	7.186 ± 0.018
224	12.669 ± 0.554	6.897 ± 0.017	274	16.063 ± 0.636	7.207 ± 0.018
225	12.013 ± 0.541	6.916 ± 0.017	275	14.265 ± 0.598	7.165 ± 0.018
226	12.418 ± 0.552	6.921 ± 0.017	276	15.603 ± 0.628	7.214 ± 0.018
227	11.406 ± 0.526	6.926 ± 0.017	277	14.384 ± 0.603	7.208 ± 0.018
228	11.632 ± 0.533	6.935 ± 0.017	278	14.256 ± 0.599	7.208 ± 0.018
229	11.557 ± 0.530	6.934 ± 0.017	279	14.589 ± 0.608	7.210 ± 0.018
230	12.747 ± 0.557	6.905 ± 0.017	280	16.234 ± 0.648	7.247 ± 0.018
231	12.032 ± 0.543	6.931 ± 0.017	281	15.775 ± 0.633	7.251 ± 0.018
232	13.305 ± 0.574	6.932 ± 0.017	282	15.292 ± 0.625	7.260 ± 0.018
233	12.343 ± 0.549	6.957 ± 0.017	283	15.451 ± 0.624	7.273 ± 0.018
234	10.688 ± 0.511	6.933 ± 0.017	284	16.153 ± 0.643	7.278 ± 0.018
235	13.734 ± 0.586	6.931 ± 0.017	285	14.885 ± 0.622	7.275 ± 0.018
236	12.594 ± 0.555	6.943 ± 0.017	286	15.587 ± 0.629	7.331 ± 0.018
237	12.478 ± 0.552	6.980 ± 0.017	287	15.945 ± 0.636	7.324 ± 0.018
238	12.760 ± 0.559	7.001 ± 0.017	288	15.669 ± 0.631	7.266 ± 0.018
239	13.253 ± 0.569	6.987 ± 0.017	289	15.610 ± 0.634	7.288 ± 0.018
240	13.363 ± 0.571	6.963 ± 0.017	290	15.741 ± 0.631	7.306 ± 0.018
241	14.730 ± 0.603	6.984 ± 0.017	291	14.853 ± 0.613	7.279 ± 0.018
242	12.894 ± 0.563	7.014 ± 0.017	292	15.893 ± 0.637	7.326 ± 0.018
243	14.281 ± 0.592	6.992 ± 0.017	293	16.107 ± 0.645	7.333 ± 0.018
244	12.765 ± 0.562	6.997 ± 0.017	294	16.638 ± 0.654	7.332 ± 0.018
245	12.907 ± 0.563	7.004 ± 0.017	295	17.064 ± 0.661	7.367 ± 0.018
246	13.663 ± 0.585	7.025 ± 0.017	296	14.866 ± 0.620	7.352 ± 0.018
247	13.421 ± 0.575	7.016 ± 0.017	297	16.506 ± 0.648	7.360 ± 0.018
248	13.318 ± 0.572	7.033 ± 0.017	298	16.389 ± 0.651	7.342 ± 0.018
249	13.309 ± 0.574	7.063 ± 0.018	299	16.052 ± 0.648	7.398 ± 0.018
250	13.390 ± 0.572	7.045 ± 0.018	300	16.401 ± 0.646	7.362 ± 0.018

Table D.5: Table of the binding energy spectrum of ^{7}Li(e,e′K^{+})$^{7}_{\Lambda}$He. A range of the binding energy from −60 MeV to +60 MeV is divided by 320 bins. (4/4)

^{7}Li(e,e′K^{+})$^{7}_{\Lambda}$He (A range from −60 MeV to +60 MeV is divided by 320 bins)					
N_{bin}	$\overline{\left(\frac{d\sigma}{d\Omega_K}\right)}\Big\|_{1^\circ-13^\circ}$ [nb/sr]		N_{bin}	$\overline{\left(\frac{d\sigma}{d\Omega_K}\right)}\Big\|_{1^\circ-13^\circ}$ [nb/sr]	
	(Signal+Accidental)	(Accidental)		(Signal+Accidental)	(Accidental)
301	15.514 ± 0.633	7.351 ± 0.018	311	17.472 ± 0.675	7.390 ± 0.018
302	16.559 ± 0.654	7.367 ± 0.018	312	18.335 ± 0.699	7.423 ± 0.018
303	15.472 ± 0.638	7.336 ± 0.018	313	15.960 ± 0.646	7.401 ± 0.018
304	16.112 ± 0.644	7.405 ± 0.018	314	16.836 ± 0.670	7.425 ± 0.018
305	16.722 ± 0.655	7.389 ± 0.018	315	15.849 ± 0.646	7.457 ± 0.019
306	17.166 ± 0.675	7.421 ± 0.018	316	16.005 ± 0.645	7.467 ± 0.019
307	16.607 ± 0.657	7.384 ± 0.018	317	15.425 ± 0.636	7.417 ± 0.018
308	16.098 ± 0.641	7.414 ± 0.018	318	16.001 ± 0.649	7.482 ± 0.019
309	16.412 ± 0.651	7.413 ± 0.018	319	15.705 ± 0.647	7.445 ± 0.019
310	17.114 ± 0.668	7.403 ± 0.018	320	16.395 ± 0.655	7.436 ± 0.019

Table D.6: Table of the binding energy spectrum of ^{9}Be(e,e$'K^{+}$)$^{9}_{\Lambda}$Li. A range of the binding energy from −60 MeV to +60 MeV is divided by 300 bins. (1/3)

^{9}Be(e,e$'K^{+}$)$^{9}_{\Lambda}$Li (A range from −60 MeV to +60 MeV is divided by 300 bins)					
N_{bin}	$\left(\frac{d\sigma}{d\Omega_K}\right)\Big\|_{1^\circ-13^\circ}$ [nb/sr]		N_{bin}	$\left(\frac{d\sigma}{d\Omega_K}\right)\Big\|_{1^\circ-13^\circ}$ [nb/sr]	
	(Signal+Accidental)	(Accidental)		(Signal+Accidental)	(Accidental)
1	6.857 ± 0.396	7.258 ± 0.017	51	7.027 ± 0.404	7.364 ± 0.017
2	7.114 ± 0.403	7.212 ± 0.017	52	6.974 ± 0.403	7.363 ± 0.017
3	6.816 ± 0.395	7.233 ± 0.017	53	7.641 ± 0.425	7.388 ± 0.017
4	6.797 ± 0.395	7.263 ± 0.017	54	8.300 ± 0.440	7.390 ± 0.017
5	7.619 ± 0.430	7.227 ± 0.017	55	6.280 ± 0.382	7.334 ± 0.017
6	7.349 ± 0.410	7.247 ± 0.017	56	7.094 ± 0.408	7.405 ± 0.018
7	6.645 ± 0.391	7.247 ± 0.017	57	6.624 ± 0.395	7.387 ± 0.017
8	7.603 ± 0.418	7.231 ± 0.017	58	6.697 ± 0.395	7.361 ± 0.017
9	8.182 ± 0.454	7.281 ± 0.017	59	7.756 ± 0.426	7.403 ± 0.018
10	7.588 ± 0.418	7.247 ± 0.017	60	7.243 ± 0.413	7.407 ± 0.018
11	7.964 ± 0.428	7.332 ± 0.017	61	7.358 ± 0.415	7.404 ± 0.018
12	6.985 ± 0.401	7.274 ± 0.017	62	7.221 ± 0.411	7.407 ± 0.018
13	7.598 ± 0.418	7.285 ± 0.017	63	6.647 ± 0.395	7.416 ± 0.018
14	7.878 ± 0.426	7.324 ± 0.017	64	7.056 ± 0.407	7.434 ± 0.018
15	7.793 ± 0.424	7.298 ± 0.017	65	7.313 ± 0.413	7.412 ± 0.018
16	7.224 ± 0.408	7.324 ± 0.017	66	7.462 ± 0.418	7.431 ± 0.018
17	7.358 ± 0.411	7.324 ± 0.017	67	7.436 ± 0.418	7.443 ± 0.018
18	7.839 ± 0.425	7.296 ± 0.017	68	7.410 ± 0.424	7.449 ± 0.018
19	6.639 ± 0.391	7.328 ± 0.017	69	7.396 ± 0.417	7.429 ± 0.018
20	7.048 ± 0.404	7.305 ± 0.017	70	6.980 ± 0.406	7.440 ± 0.018
21	7.661 ± 0.419	7.318 ± 0.017	71	7.473 ± 0.419	7.482 ± 0.018
22	7.651 ± 0.420	7.285 ± 0.017	72	7.900 ± 0.432	7.454 ± 0.018
23	7.930 ± 0.428	7.328 ± 0.017	73	7.214 ± 0.414	7.467 ± 0.018
24	6.930 ± 0.400	7.330 ± 0.017	74	7.164 ± 0.410	7.438 ± 0.018
25	7.546 ± 0.419	7.353 ± 0.017	75	7.699 ± 0.426	7.459 ± 0.018
26	7.392 ± 0.413	7.321 ± 0.017	76	7.195 ± 0.411	7.491 ± 0.018
27	6.812 ± 0.396	7.287 ± 0.017	77	7.606 ± 0.424	7.478 ± 0.018
28	7.177 ± 0.408	7.313 ± 0.017	78	6.752 ± 0.399	7.481 ± 0.018
29	6.919 ± 0.401	7.308 ± 0.017	79	7.724 ± 0.431	7.516 ± 0.018
30	7.007 ± 0.402	7.323 ± 0.017	80	6.890 ± 0.405	7.480 ± 0.018
31	7.264 ± 0.411	7.355 ± 0.017	81	7.753 ± 0.428	7.470 ± 0.018
32	7.945 ± 0.429	7.332 ± 0.017	82	7.089 ± 0.410	7.479 ± 0.018
33	7.861 ± 0.427	7.362 ± 0.017	83	7.391 ± 0.418	7.535 ± 0.018
34	7.016 ± 0.403	7.333 ± 0.017	84	7.404 ± 0.419	7.501 ± 0.018
35	7.003 ± 0.402	7.375 ± 0.017	85	8.167 ± 0.439	7.525 ± 0.018
36	7.235 ± 0.410	7.318 ± 0.017	86	7.651 ± 0.426	7.507 ± 0.018
37	7.153 ± 0.407	7.341 ± 0.017	87	8.288 ± 0.444	7.518 ± 0.018
38	8.091 ± 0.432	7.362 ± 0.017	88	8.039 ± 0.437	7.516 ± 0.018
39	7.313 ± 0.412	7.358 ± 0.017	89	7.767 ± 0.428	7.567 ± 0.018
40	7.434 ± 0.415	7.351 ± 0.017	90	7.188 ± 0.412	7.549 ± 0.018
41	8.084 ± 0.436	7.358 ± 0.017	91	8.333 ± 0.446	7.563 ± 0.018
42	7.084 ± 0.415	7.374 ± 0.017	92	8.219 ± 0.444	7.552 ± 0.018
43	7.226 ± 0.410	7.348 ± 0.017	93	7.326 ± 0.418	7.543 ± 0.018
44	7.105 ± 0.407	7.341 ± 0.017	94	7.832 ± 0.430	7.534 ± 0.018
45	6.963 ± 0.403	7.372 ± 0.017	95	7.775 ± 0.429	7.557 ± 0.018
46	7.890 ± 0.429	7.330 ± 0.017	96	7.581 ± 0.424	7.561 ± 0.018
47	7.161 ± 0.407	7.378 ± 0.017	97	7.764 ± 0.429	7.560 ± 0.018
48	7.102 ± 0.407	7.325 ± 0.017	98	7.768 ± 0.430	7.573 ± 0.018
49	7.121 ± 0.408	7.351 ± 0.017	99	8.284 ± 0.444	7.579 ± 0.018
50	6.937 ± 0.401	7.368 ± 0.017	100	7.303± 0.417	7.558 ± 0.018

Table D.7: Table of the binding energy spectrum of ^{9}Be(e,e$'K^{+}$)$^{9}_{\Lambda}$Li. A range of the binding energy from −60 MeV to +60 MeV is divided by 300 bins. (2/3)

^{9}Be(e,e$'K^{+}$)$^{9}_{\Lambda}$Li (A range from −60 MeV to +60 MeV is divided by 300 bins)					
N_{bin}	$\overline{\left(\frac{d\sigma}{d\Omega_K}\right)}\Big\|_{1^\circ-13^\circ}$ [nb/sr]		N_{bin}	$\overline{\left(\frac{d\sigma}{d\Omega_K}\right)}\Big\|_{1^\circ-13^\circ}$ [nb/sr]	
	(Signal+Accidental)	(Accidental)		(Signal+Accidental)	(Accidental)
101	6.788 ± 0.402	7.587 ± 0.018	151	9.412 ± 0.481	7.851 ± 0.018
102	7.648 ± 0.427	7.594 ± 0.018	152	9.733 ± 0.490	7.806 ± 0.018
103	7.960 ± 0.440	7.592 ± 0.018	153	10.236 ± 0.505	7.894 ± 0.018
104	8.076 ± 0.438	7.619 ± 0.018	154	10.627 ± 0.512	7.863 ± 0.018
105	8.128 ± 0.441	7.602 ± 0.018	155	9.311 ± 0.477	7.908 ± 0.018
106	8.643 ± 0.454	7.645 ± 0.018	156	9.840 ± 0.490	7.882 ± 0.018
107	7.661 ± 0.426	7.610 ± 0.018	157	10.191 ± 0.499	7.885 ± 0.018
108	7.485 ± 0.423	7.644 ± 0.018	158	10.476 ± 0.508	7.915 ± 0.019
109	7.497 ± 0.423	7.652 ± 0.018	159	10.579 ± 0.510	7.916 ± 0.019
110	7.822 ± 0.432	7.644 ± 0.018	160	10.453 ± 0.506	7.960 ± 0.019
111	7.146 ± 0.413	7.676 ± 0.018	161	9.117 ± 0.473	7.926 ± 0.019
112	7.636 ± 0.427	7.647 ± 0.018	162	9.603 ± 0.487	7.949 ± 0.019
113	6.898 ± 0.407	7.681 ± 0.018	163	10.283 ± 0.512	7.964 ± 0.019
114	6.869 ± 0.405	7.651 ± 0.018	164	10.253 ± 0.503	7.983 ± 0.019
115	7.800 ± 0.431	7.649 ± 0.018	165	10.120 ± 0.498	7.999 ± 0.019
116	7.677 ± 0.428	7.652 ± 0.018	166	10.499 ± 0.508	7.973 ± 0.019
117	7.820 ± 0.434	7.659 ± 0.018	167	10.487 ± 0.509	7.983 ± 0.019
118	7.344 ± 0.419	7.682 ± 0.018	168	11.059 ± 0.521	7.981 ± 0.019
119	8.128 ± 0.443	7.660 ± 0.018	169	9.778 ± 0.494	8.012 ± 0.019
120	8.064 ± 0.440	7.677 ± 0.018	170	9.768 ± 0.491	8.041 ± 0.019
121	7.125 ± 0.413	7.719 ± 0.018	171	10.289 ± 0.505	8.047 ± 0.019
122	7.289 ± 0.418	7.684 ± 0.018	172	10.406 ± 0.507	8.040 ± 0.019
123	7.397 ± 0.424	7.719 ± 0.018	173	10.481 ± 0.510	8.019 ± 0.019
124	8.138 ± 0.442	7.731 ± 0.018	174	10.242 ± 0.506	8.026 ± 0.019
125	8.362 ± 0.449	7.712 ± 0.018	175	10.723 ± 0.516	8.103 ± 0.019
126	7.657 ± 0.433	7.709 ± 0.018	176	11.283 ± 0.530	8.068 ± 0.019
127	8.673 ± 0.457	7.717 ± 0.018	177	11.270 ± 0.528	8.078 ± 0.019
128	8.310 ± 0.449	7.720 ± 0.018	178	10.793 ± 0.517	8.109 ± 0.019
129	9.499 ± 0.481	7.720 ± 0.018	179	11.719 ± 0.539	8.051 ± 0.019
130	9.730 ± 0.486	7.707 ± 0.018	180	11.629 ± 0.537	8.111 ± 0.019
131	9.551 ± 0.481	7.772 ± 0.018	181	11.380 ± 0.531	8.092 ± 0.019
132	9.576 ± 0.481	7.754 ± 0.018	182	12.020 ± 0.547	8.082 ± 0.019
133	9.764 ± 0.487	7.769 ± 0.018	183	11.757 ± 0.541	8.115 ± 0.019
134	9.349 ± 0.476	7.767 ± 0.018	184	11.592 ± 0.536	8.104 ± 0.019
135	8.591 ± 0.457	7.799 ± 0.018	185	11.613 ± 0.540	8.149 ± 0.019
136	9.872 ± 0.489	7.754 ± 0.018	186	11.320 ± 0.533	8.160 ± 0.019
137	9.344 ± 0.479	7.771 ± 0.018	187	12.346 ± 0.555	8.093 ± 0.019
138	8.715 ± 0.459	7.779 ± 0.018	188	12.409 ± 0.556	8.153 ± 0.019
139	9.099 ± 0.471	7.784 ± 0.018	189	12.004 ± 0.550	8.146 ± 0.019
140	7.888 ± 0.437	7.816 ± 0.018	190	12.609 ± 0.561	8.163 ± 0.019
141	8.559 ± 0.457	7.811 ± 0.018	191	12.323 ± 0.555	8.148 ± 0.019
142	7.601 ± 0.428	7.817 ± 0.018	192	11.785 ± 0.544	8.166 ± 0.019
143	8.073 ± 0.444	7.833 ± 0.018	193	12.480 ± 0.560	8.149 ± 0.019
144	8.260 ± 0.449	7.815 ± 0.018	194	12.405 ± 0.558	8.146 ± 0.019
145	7.787 ± 0.435	7.834 ± 0.018	195	12.312 ± 0.556	8.215 ± 0.019
146	8.629 ± 0.458	7.878 ± 0.018	196	11.566 ± 0.539	8.178 ± 0.019
147	8.442 ± 0.453	7.821 ± 0.018	197	12.752 ± 0.566	8.186 ± 0.019
148	7.904 ± 0.438	7.859 ± 0.018	198	13.028 ± 0.576	8.194 ± 0.019
149	9.156 ± 0.473	7.876 ± 0.018	199	13.354 ± 0.580	8.147 ± 0.019
150	9.028 ± 0.469	7.878 ± 0.018	200	12.192 ± 0.555	8.222 ± 0.019

Table D.8: Table of the binding energy spectrum of ^{9}Be(e,e′K^{+})$^{9}_{\Lambda}$Li. A range of the binding energy from −60 MeV to +60 MeV is divided by 300 bins. (3/3)

^{9}Be(e,e′K^{+})$^{9}_{\Lambda}$Li (A range from −60 MeV to +60 MeV is divided by 300 bins)					
N_{bin}	$\left(\frac{d\sigma}{d\Omega_K}\right)\Big\|_{1^\circ-13^\circ}$ [nb/sr]		N_{bin}	$\left(\frac{d\sigma}{d\Omega_K}\right)\Big\|_{1^\circ-13^\circ}$ [nb/sr]	
	(Signal+Accidental)	(Accidental)		(Signal+Accidental)	(Accidental)
201	11.107 ± 0.530	8.197 ± 0.019	251	14.537 ± 0.619	8.596 ± 0.020
202	12.063 ± 0.551	8.214 ± 0.019	252	14.349 ± 0.614	8.630 ± 0.020
203	13.334 ± 0.588	8.248 ± 0.019	253	15.951 ± 0.658	8.592 ± 0.020
204	13.470 ± 0.583	8.235 ± 0.019	254	14.019 ± 0.607	8.631 ± 0.020
205	13.771 ± 0.591	8.224 ± 0.019	255	15.973 ± 0.652	8.610 ± 0.020
206	12.664 ± 0.565	8.241 ± 0.019	256	15.502 ± 0.638	8.649 ± 0.020
207	13.479 ± 0.583	8.239 ± 0.019	257	16.231 ± 0.654	8.634 ± 0.020
208	13.549 ± 0.590	8.264 ± 0.019	258	15.223 ± 0.632	8.641 ± 0.020
209	12.887 ± 0.572	8.223 ± 0.019	259	16.792 ± 0.666	8.634 ± 0.020
210	12.780 ± 0.569	8.296 ± 0.019	260	15.405 ± 0.641	8.677 ± 0.020
211	13.711 ± 0.590	8.267 ± 0.019	261	15.162 ± 0.636	8.691 ± 0.020
212	12.534 ± 0.565	8.290 ± 0.019	262	16.072 ± 0.652	8.713 ± 0.020
213	14.133 ± 0.599	8.297 ± 0.019	263	15.170 ± 0.631	8.661 ± 0.020
214	12.837 ± 0.573	8.288 ± 0.019	264	15.626 ± 0.648	8.689 ± 0.020
215	13.917 ± 0.596	8.307 ± 0.019	265	15.535 ± 0.643	8.727 ± 0.020
216	13.087 ± 0.579	8.352 ± 0.019	266	16.228 ± 0.653	8.736 ± 0.020
217	13.965 ± 0.599	8.329 ± 0.019	267	16.097 ± 0.657	8.739 ± 0.020
218	13.891 ± 0.596	8.334 ± 0.019	268	17.319 ± 0.686	8.780 ± 0.020
219	13.224 ± 0.582	8.327 ± 0.019	269	15.987 ± 0.653	8.748 ± 0.020
220	13.981 ± 0.598	8.332 ± 0.019	270	16.587 ± 0.672	8.747 ± 0.020
221	13.231 ± 0.584	8.348 ± 0.019	271	16.191 ± 0.666	8.817 ± 0.020
222	13.628 ± 0.592	8.364 ± 0.019	272	16.549 ± 0.664	8.715 ± 0.020
223	14.973 ± 0.621	8.362 ± 0.019	273	15.201 ± 0.640	8.759 ± 0.020
224	14.930 ± 0.620	8.379 ± 0.019	274	15.756 ± 0.653	8.784 ± 0.020
225	13.301 ± 0.589	8.393 ± 0.019	275	15.766 ± 0.655	8.738 ± 0.020
226	14.490 ± 0.610	8.361 ± 0.019	276	14.644 ± 0.624	8.779 ± 0.020
227	14.493 ± 0.611	8.413 ± 0.020	277	15.865 ± 0.666	8.767 ± 0.020
228	13.521 ± 0.599	8.411 ± 0.020	278	15.648 ± 0.645	8.791 ± 0.020
229	14.987 ± 0.623	8.388 ± 0.019	279	16.659 ± 0.686	8.810 ± 0.020
230	14.429 ± 0.610	8.409 ± 0.020	280	16.134 ± 0.669	8.824 ± 0.020
231	14.408 ± 0.615	8.408 ± 0.020	281	15.252 ± 0.641	8.808 ± 0.020
232	14.369 ± 0.607	8.438 ± 0.020	282	16.490 ± 0.673	8.787 ± 0.020
233	13.612 ± 0.596	8.481 ± 0.020	283	15.756 ± 0.650	8.829 ± 0.020
234	13.833 ± 0.600	8.479 ± 0.020	284	16.408 ± 0.676	8.874 ± 0.021
235	14.922 ± 0.621	8.462 ± 0.020	285	16.304 ± 0.662	8.846 ± 0.021
236	14.611 ± 0.616	8.516 ± 0.020	286	16.143 ± 0.659	8.849 ± 0.021
237	14.804 ± 0.622	8.534 ± 0.020	287	15.548 ± 0.652	8.843 ± 0.021
238	15.404 ± 0.633	8.487 ± 0.020	288	17.439 ± 0.694	8.883 ± 0.021
239	14.592 ± 0.614	8.483 ± 0.020	289	16.703 ± 0.675	8.895 ± 0.021
240	14.552 ± 0.614	8.531 ± 0.020	290	15.777 ± 0.658	8.887 ± 0.021
241	14.955 ± 0.626	8.470 ± 0.020	291	14.756 ± 0.633	8.859 ± 0.021
242	14.264 ± 0.612	8.549 ± 0.020	292	17.175 ± 0.689	8.882 ± 0.021
243	16.374 ± 0.651	8.503 ± 0.020	293	16.428 ± 0.676	8.917 ± 0.021
244	14.663 ± 0.620	8.577 ± 0.020	294	14.994 ± 0.640	8.890 ± 0.021
245	15.317 ± 0.637	8.522 ± 0.020	295	17.145 ± 0.688	8.899 ± 0.021
246	14.626 ± 0.618	8.553 ± 0.020	296	16.097 ± 0.659	8.885 ± 0.021
247	16.994 ± 0.674	8.574 ± 0.020	297	16.458 ± 0.676	8.908 ± 0.021
248	14.836 ± 0.624	8.593 ± 0.020	298	16.835 ± 0.688	8.925 ± 0.021
249	14.898 ± 0.630	8.577 ± 0.020	299	16.817 ± 0.686	8.941 ± 0.021
250	15.319 ± 0.631	8.571 ± 0.020	300	15.692 ± 0.662	8.951 ± 0.021

Table D.9: Table of the binding energy spectrum of ^{10}B(e,e′K^+)$^{10}_{\Lambda}$Be. A range of the binding energy from −60 MeV to +60 MeV is divided by 400 bins. (1/4)

^{10}B(e,e′K^+)$^{10}_{\Lambda}$Be (A range from −60 MeV to +60 MeV is divided by 400 bins)					
N_{bin}	$\left(\frac{d\sigma}{d\Omega_K}\right)\Big\|_{1^\circ-13^\circ}$ [nb/sr]		N_{bin}	$\left(\frac{d\sigma}{d\Omega_K}\right)\Big\|_{1^\circ-13^\circ}$ [nb/sr]	
	(Signal+Accidental)	(Accidental)		(Signal+Accidental)	(Accidental)
1	3.390 ± 0.511	3.819 ± 0.022	51	4.214 ± 0.573	3.999 ± 0.023
2	3.738 ± 0.534	3.821 ± 0.022	52	3.722 ± 0.537	4.007 ± 0.023
3	4.262 ± 0.570	3.777 ± 0.022	53	4.668 ± 0.603	3.971 ± 0.023
4	5.243 ± 0.631	3.885 ± 0.023	54	4.447 ± 0.589	3.945 ± 0.023
5	5.053 ± 0.622	3.830 ± 0.022	55	4.377 ± 0.580	4.003 ± 0.023
6	4.470 ± 0.587	3.828 ± 0.022	56	2.549 ± 0.444	3.967 ± 0.023
7	3.967 ± 0.555	3.833 ± 0.022	57	4.021 ± 0.558	3.951 ± 0.023
8	4.550 ± 0.592	3.853 ± 0.022	58	4.383 ± 0.586	3.958 ± 0.023
9	4.043 ± 0.555	3.858 ± 0.022	59	3.808 ± 0.544	3.994 ± 0.023
10	4.078 ± 0.560	3.866 ± 0.023	60	4.248 ± 0.573	4.008 ± 0.023
11	4.041 ± 0.555	3.905 ± 0.023	61	3.505 ± 0.522	3.989 ± 0.023
12	3.299 ± 0.503	3.924 ± 0.023	62	3.705 ± 0.535	3.996 ± 0.023
13	4.505 ± 0.587	3.866 ± 0.023	63	3.249 ± 0.501	4.001 ± 0.023
14	3.928 ± 0.550	3.914 ± 0.023	64	4.296 ± 0.579	3.969 ± 0.023
15	4.360 ± 0.577	3.859 ± 0.022	65	3.503 ± 0.522	3.976 ± 0.023
16	4.148 ± 0.564	3.883 ± 0.023	66	4.417 ± 0.585	3.971 ± 0.023
17	3.566 ± 0.526	3.899 ± 0.023	67	4.087 ± 0.561	3.999 ± 0.023
18	4.138 ± 0.563	3.911 ± 0.023	68	4.155 ± 0.571	3.963 ± 0.023
19	3.730 ± 0.533	3.881 ± 0.023	69	3.927 ± 0.555	3.979 ± 0.023
20	3.927 ± 0.550	3.942 ± 0.023	70	4.264 ± 0.575	3.978 ± 0.023
21	2.896 ± 0.470	3.909 ± 0.023	71	4.115 ± 0.565	3.995 ± 0.023
22	4.548 ± 0.592	3.929 ± 0.023	72	4.580 ± 0.596	3.942 ± 0.023
23	3.239 ± 0.500	3.919 ± 0.023	73	2.793 ± 0.466	3.994 ± 0.023
24	3.679 ± 0.531	3.926 ± 0.023	74	3.918 ± 0.554	4.033 ± 0.023
25	3.533 ± 0.521	3.953 ± 0.023	75	3.885 ± 0.549	3.959 ± 0.023
26	4.329 ± 0.578	3.920 ± 0.023	76	4.123 ± 0.566	4.014 ± 0.023
27	3.672 ± 0.530	3.868 ± 0.023	77	4.826 ± 0.613	4.007 ± 0.023
28	3.954 ± 0.554	3.986 ± 0.023	78	3.659 ± 0.534	3.976 ± 0.023
29	4.109 ± 0.559	3.969 ± 0.023	79	4.202 ± 0.572	4.038 ± 0.023
30	4.001 ± 0.555	3.965 ± 0.023	80	3.296 ± 0.509	3.959 ± 0.023
31	4.254 ± 0.574	3.986 ± 0.023	81	4.113 ± 0.570	3.988 ± 0.023
32	5.022 ± 0.623	3.956 ± 0.023	82	3.535 ± 0.527	4.024 ± 0.023
33	3.343 ± 0.504	3.948 ± 0.023	83	3.865 ± 0.547	3.936 ± 0.023
34	4.238 ± 0.572	3.902 ± 0.023	84	4.719 ± 0.609	4.009 ± 0.023
35	3.992 ± 0.554	3.949 ± 0.023	85	4.204 ± 0.583	4.045 ± 0.023
36	2.785 ± 0.464	3.951 ± 0.023	86	4.123 ± 0.566	4.008 ± 0.023
37	3.084 ± 0.488	3.946 ± 0.023	87	4.034 ± 0.559	4.032 ± 0.023
38	3.758 ± 0.537	3.925 ± 0.023	88	3.822 ± 0.546	4.061 ± 0.023
39	3.079 ± 0.487	3.974 ± 0.023	89	3.634 ± 0.530	4.031 ± 0.023
40	3.397 ± 0.512	3.927 ± 0.023	90	4.414 ± 0.590	4.075 ± 0.023
41	3.758 ± 0.537	3.952 ± 0.023	91	4.790 ± 0.613	3.988 ± 0.023
42	3.530 ± 0.520	3.951 ± 0.023	92	3.788 ± 0.547	3.994 ± 0.023
43	3.960 ± 0.554	3.921 ± 0.023	93	4.693 ± 0.606	4.000 ± 0.023
44	3.861 ± 0.546	3.973 ± 0.023	94	4.401 ± 0.588	4.014 ± 0.023
45	4.301 ± 0.580	3.952 ± 0.023	95	3.832 ± 0.547	4.027 ± 0.023
46	4.104 ± 0.564	3.996 ± 0.023	96	3.095 ± 0.489	4.028 ± 0.023
47	3.511 ± 0.523	3.985 ± 0.023	97	4.065 ± 0.564	4.039 ± 0.023
48	3.381 ± 0.510	3.950 ± 0.023	98	4.547 ± 0.597	4.042 ± 0.023
49	4.386 ± 0.581	4.001 ± 0.023	99	4.823 ± 0.612	4.039 ± 0.023
50	4.193 ± 0.571	3.977 ± 0.023	100	4.060 ± 0.563	4.023 ± 0.023

Table D.10: Table of the binding energy spectrum of ^{10}B(e,e$'K^+$)$^{10}_{\Lambda}$Be. A range of the binding energy from −60 MeV to +60 MeV is divided by 400 bins. (2/4)

^{10}B(e,e$'K^+$)$^{10}_{\Lambda}$Be (A range from −60 MeV to +60 MeV is divided by 400 bins)					
N_{bin}	$\left(\frac{d\sigma}{d\Omega_K}\right)\Big\|_{1^\circ-13^\circ}$ [nb/sr]		N_{bin}	$\left(\frac{d\sigma}{d\Omega_K}\right)\Big\|_{1^\circ-13^\circ}$ [nb/sr]	
	(Signal+Accidental)	(Accidental)		(Signal+Accidental)	(Accidental)
101	4.280 ± 0.577	4.043 ± 0.023	151	3.681 ± 0.543	4.091 ± 0.024
102	4.565 ± 0.599	4.028 ± 0.023	152	3.173 ± 0.502	4.145 ± 0.024
103	3.603 ± 0.531	4.049 ± 0.023	153	4.128 ± 0.572	4.122 ± 0.024
104	4.255 ± 0.579	4.071 ± 0.023	154	3.507 ± 0.529	4.170 ± 0.024
105	5.274 ± 0.644	4.029 ± 0.023	155	3.636 ± 0.536	4.122 ± 0.024
106	4.326 ± 0.583	4.041 ± 0.023	156	3.626 ± 0.535	4.138 ± 0.024
107	4.279 ± 0.582	4.020 ± 0.023	157	5.092 ± 0.636	4.135 ± 0.024
108	4.088 ± 0.567	4.039 ± 0.023	158	3.727 ± 0.544	4.157 ± 0.024
109	3.705 ± 0.540	4.043 ± 0.023	159	5.284 ± 0.650	4.194 ± 0.024
110	3.926 ± 0.555	4.030 ± 0.023	160	5.356 ± 0.654	4.141 ± 0.024
111	4.864 ± 0.618	3.996 ± 0.023	161	5.451 ± 0.656	4.173 ± 0.024
112	3.130 ± 0.495	4.066 ± 0.023	162	3.194 ± 0.505	4.169 ± 0.024
113	3.993 ± 0.559	4.040 ± 0.023	163	3.825 ± 0.552	4.131 ± 0.024
114	3.681 ± 0.537	4.039 ± 0.023	164	3.844 ± 0.555	4.120 ± 0.024
115	4.699 ± 0.607	4.028 ± 0.023	165	3.539 ± 0.533	4.139 ± 0.024
116	3.675 ± 0.542	4.080 ± 0.023	166	3.937 ± 0.562	4.135 ± 0.024
117	5.040 ± 0.630	4.003 ± 0.023	167	4.741 ± 0.617	4.142 ± 0.024
118	3.669 ± 0.535	4.093 ± 0.024	168	5.215 ± 0.647	4.097 ± 0.024
119	4.546 ± 0.597	4.024 ± 0.023	169	5.330 ± 0.651	4.157 ± 0.024
120	3.479 ± 0.524	4.091 ± 0.024	170	5.565 ± 0.670	4.188 ± 0.024
121	4.179 ± 0.574	4.083 ± 0.023	171	6.662 ± 0.731	4.143 ± 0.024
122	4.186 ± 0.575	4.089 ± 0.024	172	8.653 ± 0.837	4.117 ± 0.024
123	4.790 ± 0.618	4.020 ± 0.023	173	6.730 ± 0.734	4.141 ± 0.024
124	3.225 ± 0.504	4.079 ± 0.023	174	5.753 ± 0.725	4.185 ± 0.024
125	4.643 ± 0.604	4.054 ± 0.023	175	5.212 ± 0.647	4.173 ± 0.024
126	4.738 ± 0.612	4.077 ± 0.024	176	4.884 ± 0.625	4.174 ± 0.024
127	4.354 ± 0.587	4.092 ± 0.024	177	5.047 ± 0.641	4.136 ± 0.024
128	3.639 ± 0.537	4.067 ± 0.023	178	6.050 ± 0.699	4.204 ± 0.024
129	3.353 ± 0.517	4.078 ± 0.023	179	6.443 ± 0.720	4.156 ± 0.024
130	4.534 ± 0.600	4.101 ± 0.024	180	6.509 ± 0.723	4.164 ± 0.024
131	4.415 ± 0.590	4.082 ± 0.024	181	7.566 ± 0.785	4.173 ± 0.024
132	3.838 ± 0.548	4.030 ± 0.023	182	7.359 ± 0.771	4.174 ± 0.024
133	4.120 ± 0.571	4.061 ± 0.023	183	6.065 ± 0.700	4.191 ± 0.024
134	4.416 ± 0.590	4.117 ± 0.024	184	5.804 ± 0.709	4.162 ± 0.024
135	5.159 ± 0.640	4.039 ± 0.023	185	5.730 ± 0.680	4.224 ± 0.024
136	3.685 ± 0.543	4.063 ± 0.023	186	4.533 ± 0.600	4.218 ± 0.024
137	4.682 ± 0.610	4.104 ± 0.024	187	4.711 ± 0.619	4.204 ± 0.024
138	4.613 ± 0.606	4.090 ± 0.024	188	5.988 ± 0.696	4.169 ± 0.024
139	4.651 ± 0.611	4.090 ± 0.024	189	4.573 ± 0.606	4.150 ± 0.024
140	3.785 ± 0.546	4.100 ± 0.024	190	4.258 ± 0.585	4.196 ± 0.024
141	4.600 ± 0.604	4.112 ± 0.024	191	5.826 ± 0.687	4.187 ± 0.024
142	5.210 ± 0.646	4.087 ± 0.024	192	6.765 ± 0.747	4.235 ± 0.024
143	4.396 ± 0.593	4.112 ± 0.024	193	7.253 ± 0.769	4.236 ± 0.024
144	4.296 ± 0.590	4.065 ± 0.023	194	6.750 ± 0.745	4.239 ± 0.024
145	4.395 ± 0.587	4.094 ± 0.024	195	6.194 ± 0.710	4.199 ± 0.024
146	3.865 ± 0.552	4.106 ± 0.024	196	6.354 ± 0.719	4.139 ± 0.024
147	4.799 ± 0.620	4.106 ± 0.024	197	6.833 ± 0.746	4.196 ± 0.024
148	4.423 ± 0.591	4.102 ± 0.024	198	5.874 ± 0.692	4.207 ± 0.024
149	3.650 ± 0.538	4.140 ± 0.024	199	6.564 ± 0.734	4.248 ± 0.024
150	4.396 ± 0.593	4.128 ± 0.024	200	5.806 ± 0.684	4.281 ± 0.024

Table D.11: Table of the binding energy spectrum of ^{10}B(e,e′K^+)$^{10}_{\Lambda}$Be. A range of the binding energy from −60 MeV to +60 MeV is divided by 400 bins. (3/4)

^{10}B(e,e′K^+)$^{10}_{\Lambda}$Be (A range from −60 MeV to +60 MeV is divided by 400 bins)					
N_{bin}	$\overline{\left(\frac{d\sigma}{d\Omega_K}\right)}\Big\|_{1^\circ-13^\circ}$ [nb/sr]		N_{bin}	$\overline{\left(\frac{d\sigma}{d\Omega_K}\right)}\Big\|_{1^\circ-13^\circ}$ [nb/sr]	
	(Signal+Accidental)	(Accidental)		(Signal+Accidental)	(Accidental)
201	6.995 ± 0.754	4.208 ± 0.024	251	8.812 ± 0.856	4.377 ± 0.025
202	6.312 ± 0.719	4.233 ± 0.024	252	7.726 ± 0.801	4.382 ± 0.025
203	6.997 ± 0.754	4.246 ± 0.024	253	10.642 ± 0.941	4.412 ± 0.025
204	6.278 ± 0.715	4.247 ± 0.024	254	9.064 ± 0.872	4.427 ± 0.025
205	7.518 ± 0.784	4.251 ± 0.024	255	10.247 ± 0.924	4.393 ± 0.025
206	7.695 ± 0.794	4.217 ± 0.024	256	8.972 ± 0.863	4.390 ± 0.025
207	7.775 ± 0.798	4.290 ± 0.024	257	8.796 ± 0.854	4.432 ± 0.025
208	10.587± 0.936	4.280 ± 0.024	258	9.894 ± 0.911	4.403 ± 0.025
209	8.703 ± 0.845	4.250 ± 0.024	259	11.535 ± 0.982	4.373 ± 0.025
210	7.200 ± 0.768	4.240 ± 0.024	260	9.546 ± 0.894	4.402 ± 0.025
211	6.995 ± 0.759	4.237 ± 0.024	261	8.342 ± 0.834	4.405 ± 0.025
212	6.867 ± 0.749	4.295 ± 0.024	262	10.803 ± 0.947	4.406 ± 0.025
213	7.705 ± 0.795	4.295 ± 0.024	263	11.121 ± 0.964	4.397 ± 0.025
214	6.277 ± 0.715	4.262 ± 0.024	264	10.754 ± 0.951	4.427 ± 0.025
215	7.388 ± 0.779	4.234 ± 0.024	265	12.354 ± 1.019	4.410 ± 0.025
216	6.730 ± 0.743	4.286 ± 0.024	266	11.429 ± 0.973	4.430 ± 0.025
217	8.351 ± 0.827	4.271 ± 0.024	267	12.434 ± 1.022	4.455 ± 0.025
218	6.685 ± 0.743	4.265 ± 0.024	268	10.804 ± 0.948	4.452 ± 0.025
219	7.883 ± 0.805	4.310 ± 0.025	269	12.994 ± 1.044	4.403 ± 0.025
220	6.447 ± 0.725	4.272 ± 0.024	270	11.955 ± 1.000	4.439 ± 0.025
221	7.959 ± 0.808	4.293 ± 0.024	271	11.464 ± 0.979	4.463 ± 0.025
222	8.021 ± 0.810	4.301 ± 0.024	272	11.976 ± 1.002	4.450 ± 0.025
223	6.451 ± 0.730	4.304 ± 0.025	273	11.963 ± 1.004	4.479 ± 0.025
224	7.007 ± 0.756	4.281 ± 0.024	274	11.183 ± 0.970	4.439 ± 0.025
225	6.231 ± 0.715	4.295 ± 0.024	275	11.094 ± 0.969	4.482 ± 0.025
226	8.161 ± 0.820	4.323 ± 0.025	276	11.259 ± 0.973	4.479 ± 0.025
227	8.227 ± 0.823	4.305 ± 0.025	277	11.301 ± 0.976	4.506 ± 0.025
228	7.063 ± 0.762	4.289 ± 0.024	278	11.432 ± 0.980	4.427 ± 0.025
229	8.946 ± 0.857	4.293 ± 0.025	279	11.974 ± 1.001	4.461 ± 0.025
230	7.353 ± 0.775	4.311 ± 0.025	280	11.648 ± 0.988	4.482 ± 0.025
231	6.215 ± 0.723	4.288 ± 0.025	281	12.732 ± 1.040	4.454 ± 0.025
232	7.752 ± 0.800	4.346 ± 0.025	282	11.754 ± 0.993	4.528 ± 0.025
233	9.741 ± 0.893	4.336 ± 0.025	283	12.002 ± 1.011	4.511 ± 0.025
234	9.557 ± 0.891	4.332 ± 0.025	284	13.152 ± 1.056	4.474 ± 0.025
235	8.043 ± 0.817	4.291 ± 0.025	285	11.815 ± 0.999	4.496 ± 0.025
236	10.429± 0.929	4.321 ± 0.025	286	13.155 ± 1.053	4.512 ± 0.025
237	10.472± 0.929	4.373 ± 0.025	287	12.197 ± 1.020	4.524 ± 0.025
238	10.966± 0.951	4.350 ± 0.025	288	12.154 ± 1.016	4.526 ± 0.025
239	9.977 ± 0.907	4.335 ± 0.025	289	11.362 ± 0.982	4.531 ± 0.025
240	8.865 ± 0.857	4.333 ± 0.025	290	14.957 ± 1.131	4.527 ± 0.025
241	9.273 ± 0.876	4.338 ± 0.025	291	12.823 ± 1.047	4.520 ± 0.025
242	9.794 ± 0.905	4.358 ± 0.025	292	11.841 ± 1.001	4.508 ± 0.025
243	10.931± 0.955	4.363 ± 0.025	293	11.744 ± 0.996	4.530 ± 0.025
244	10.166± 0.920	4.362 ± 0.025	294	13.103 ± 1.056	4.494 ± 0.025
245	11.485± 0.974	4.394 ± 0.025	295	13.829 ± 1.083	4.566 ± 0.026
246	9.693 ± 0.896	4.342 ± 0.025	296	13.381 ± 1.068	4.528 ± 0.025
247	8.815 ± 0.852	4.355 ± 0.025	297	13.674 ± 1.081	4.528 ± 0.025
248	9.403 ± 0.888	4.376 ± 0.025	298	11.384 ± 0.980	4.517 ± 0.025
249	9.351 ± 0.880	4.397 ± 0.025	299	12.778 ± 1.043	4.532 ± 0.026
250	11.469± 0.980	4.347 ± 0.025	300	14.618 ± 1.121	4.557 ± 0.026

Table D.12: Table of the binding energy spectrum of ^{10}B(e,e$'K^+$)$^{10}_{\Lambda}$Be. A range of the binding energy from −60 MeV to +60 MeV is divided by 400 bins. (4/4)

^{10}B(e,e$'K^+$)$^{10}_{\Lambda}$Be (A range from −60 MeV to +60 MeV is divided by 400 bins)					
N_{bin}	$\left(\frac{d\sigma}{d\Omega_K}\right)\Big\|_{1^\circ-13^\circ}$ [nb/sr]		N_{bin}	$\left(\frac{d\sigma}{d\Omega_K}\right)\Big\|_{1^\circ-13^\circ}$ [nb/sr]	
	(Signal+Accidental)	(Accidental)		(Signal+Accidental)	(Accidental)
301	13.527 ± 1.073	4.569 ± 0.026	351	15.063 ± 1.152	4.703 ± 0.026
302	15.497 ± 1.149	4.551 ± 0.026	352	16.415 ± 1.191	4.701 ± 0.026
303	11.573 ± 0.992	4.541 ± 0.026	353	17.917 ± 1.254	4.708 ± 0.026
304	15.405 ± 1.151	4.500 ± 0.025	354	19.087 ± 1.293	4.737 ± 0.026
305	12.427 ± 1.032	4.583 ± 0.026	355	17.153 ± 1.235	4.666 ± 0.026
306	14.290 ± 1.109	4.569 ± 0.026	356	15.518 ± 1.160	4.740 ± 0.026
307	14.033 ± 1.092	4.586 ± 0.026	357	16.192 ± 1.184	4.728 ± 0.026
308	14.121 ± 1.096	4.559 ± 0.026	358	17.457 ± 1.244	4.749 ± 0.027
309	15.425 ± 1.153	4.552 ± 0.026	359	16.604 ± 1.211	4.715 ± 0.026
310	12.438 ± 1.033	4.552 ± 0.026	360	17.310 ± 1.243	4.811 ± 0.027
311	12.623 ± 1.041	4.523 ± 0.026	361	15.998 ± 1.179	4.731 ± 0.026
312	14.686 ± 1.126	4.620 ± 0.026	362	17.521 ± 1.252	4.778 ± 0.027
313	13.312 ± 1.066	4.543 ± 0.026	363	16.175 ± 1.209	4.704 ± 0.026
314	16.149 ± 1.175	4.619 ± 0.026	364	18.148 ± 1.267	4.678 ± 0.026
315	13.189 ± 1.066	4.623 ± 0.026	365	18.950 ± 1.301	4.744 ± 0.027
316	14.465 ± 1.106	4.582 ± 0.026	366	17.851 ± 1.269	4.830 ± 0.027
317	14.210 ± 1.110	4.625 ± 0.026	367	16.975 ± 1.228	4.720 ± 0.026
318	15.955 ± 1.173	4.632 ± 0.026	368	16.291 ± 1.204	4.802 ± 0.027
319	14.926 ± 1.135	4.621 ± 0.026	369	17.360 ± 1.240	4.789 ± 0.027
320	13.362 ± 1.080	4.617 ± 0.026	370	16.792 ± 1.225	4.778 ± 0.027
321	14.967 ± 1.135	4.557 ± 0.026	371	16.080 ± 1.202	4.797 ± 0.027
322	11.976 ± 1.016	4.580 ± 0.026	372	19.180 ± 1.299	4.813 ± 0.027
323	16.122 ± 1.182	4.632 ± 0.026	373	16.086 ± 1.186	4.833 ± 0.027
324	14.736 ± 1.124	4.585 ± 0.026	374	17.164 ± 1.242	4.763 ± 0.027
325	16.021 ± 1.175	4.640 ± 0.026	375	17.716 ± 1.256	4.767 ± 0.027
326	15.570 ± 1.157	4.652 ± 0.026	376	16.911 ± 1.247	4.843 ± 0.027
327	14.207 ± 1.109	4.615 ± 0.026	377	15.317 ± 1.178	4.840 ± 0.027
328	13.834 ± 1.101	4.693 ± 0.026	378	17.631 ± 1.241	4.823 ± 0.027
329	15.021 ± 1.139	4.633 ± 0.026	379	19.329 ± 1.328	4.817 ± 0.027
330	16.428 ± 1.201	4.645 ± 0.026	380	16.056 ± 1.200	4.821 ± 0.027
331	15.447 ± 1.158	4.672 ± 0.026	381	18.040 ± 1.289	4.869 ± 0.027
332	16.262 ± 1.196	4.682 ± 0.026	382	17.607 ± 1.288	4.820 ± 0.027
333	13.386 ± 1.075	4.641 ± 0.026	383	18.390 ± 1.278	4.795 ± 0.027
334	15.331 ± 1.156	4.641 ± 0.026	384	19.482 ± 1.313	4.821 ± 0.027
335	16.438 ± 1.199	4.672 ± 0.026	385	18.211 ± 1.278	4.856 ± 0.027
336	15.011 ± 1.141	4.635 ± 0.026	386	17.479 ± 1.249	4.855 ± 0.027
337	16.186 ± 1.184	4.644 ± 0.026	387	19.267 ± 1.320	4.786 ± 0.027
338	14.935 ± 1.142	4.655 ± 0.026	388	19.636 ± 1.318	4.804 ± 0.027
339	16.114 ± 1.188	4.642 ± 0.026	389	18.054 ± 1.270	4.862 ± 0.027
340	15.744 ± 1.173	4.664 ± 0.026	390	17.857 ± 1.263	4.890 ± 0.027
341	17.085 ± 1.227	4.718 ± 0.026	391	17.142 ± 1.250	4.813 ± 0.027
342	15.238 ± 1.152	4.681 ± 0.026	392	20.448 ± 1.357	4.860 ± 0.027
343	16.178 ± 1.189	4.655 ± 0.026	393	17.361 ± 1.240	4.855 ± 0.027
344	14.340 ± 1.116	4.635 ± 0.026	394	16.765 ± 1.239	4.838 ± 0.027
345	15.942 ± 1.175	4.628 ± 0.026	395	21.179 ± 1.396	4.890 ± 0.027
346	15.540 ± 1.165	4.731 ± 0.026	396	18.416 ± 1.289	4.860 ± 0.027
347	17.525 ± 1.255	4.682 ± 0.026	397	15.994 ± 1.195	4.859 ± 0.027
348	15.911 ± 1.170	4.715 ± 0.026	398	16.383 ± 1.221	4.855 ± 0.027
349	16.011 ± 1.177	4.730 ± 0.026	399	19.336 ± 1.334	4.921 ± 0.027
350	15.294 ± 1.153	4.690 ± 0.026	400	16.161 ± 1.215	4.907 ± 0.027

Table D.13: Table of the binding energy spectrum of ^{12}C(e,e′K^+)$^{12}_{\Lambda}$B. A range of the binding energy from −60 MeV to +60 MeV is divided by 500 bins. (1/5)

^{12}C(e,e′K^+)$^{12}_{\Lambda}$B (A range from −60 MeV to +60 MeV is divided by 500 bins)					
N_{bin}	$\left(\frac{d\sigma}{d\Omega_K}\right)\Big\|_{1^\circ-13^\circ}$ [nb/sr]		N_{bin}	$\left(\frac{d\sigma}{d\Omega_K}\right)\Big\|_{1^\circ-13^\circ}$ [nb/sr]	
	(Signal+Accidental)	(Accidental)		(Signal+Accidental)	(Accidental)
1	10.584 ± 1.122	10.850 ± 0.047	51	11.789± 1.185	11.127 ± 0.048
2	10.401 ± 1.109	10.848 ± 0.047	52	9.627 ± 1.076	11.163 ± 0.048
3	12.173 ± 1.199	10.832 ± 0.047	53	10.824± 1.135	11.070 ± 0.048
4	13.460 ± 1.261	10.900 ± 0.048	54	12.072± 1.201	11.154 ± 0.048
5	10.542 ± 1.117	10.925 ± 0.048	55	9.561 ± 1.069	11.151 ± 0.048
6	11.277 ± 1.151	10.864 ± 0.048	56	12.418± 1.218	11.129 ± 0.048
7	10.289 ± 1.103	10.804 ± 0.047	57	11.385± 1.168	11.204 ± 0.049
8	12.051 ± 1.193	10.783 ± 0.047	58	9.132 ± 1.047	11.117 ± 0.048
9	10.401 ± 1.115	10.923 ± 0.048	59	11.940± 1.194	11.129 ± 0.048
10	9.233 ± 1.045	11.021 ± 0.048	60	13.910± 1.292	11.086 ± 0.048
11	10.167± 1.096	10.904 ± 0.048	61	10.058± 1.097	11.212 ± 0.049
12	9.957 ± 1.086	10.853 ± 0.048	62	10.620± 1.126	11.265 ± 0.049
13	10.345± 1.103	10.952 ± 0.048	63	10.419± 1.117	11.120 ± 0.048
14	9.199 ± 1.042	10.913 ± 0.048	64	11.200± 1.155	11.149 ± 0.048
15	11.455± 1.163	10.949 ± 0.048	65	10.110± 1.103	11.219 ± 0.049
16	9.934 ± 1.084	10.934 ± 0.048	66	11.553± 1.173	11.222 ± 0.049
17	11.824± 1.182	10.977 ± 0.048	67	15.283± 1.351	11.271 ± 0.049
18	9.896 ± 1.080	10.887 ± 0.048	68	11.356± 1.165	11.209 ± 0.049
19	9.603 ± 1.067	10.944 ± 0.048	69	11.307± 1.160	11.203 ± 0.049
20	12.154± 1.203	11.050 ± 0.048	70	11.595± 1.177	11.206 ± 0.049
21	10.972± 1.144	10.980 ± 0.048	71	13.179± 1.262	11.229 ± 0.049
22	10.305± 1.105	10.950 ± 0.048	72	11.779± 1.190	11.243 ± 0.049
23	10.831± 1.129	11.000 ± 0.048	73	12.758± 1.239	11.248 ± 0.049
24	10.058± 1.091	10.983 ± 0.048	74	10.921± 1.145	11.241 ± 0.049
25	10.555± 1.119	10.910 ± 0.048	75	11.346± 1.164	11.247 ± 0.049
26	10.270± 1.107	10.949 ± 0.048	76	11.061± 1.153	11.299 ± 0.049
27	14.038± 1.292	10.946 ± 0.048	77	11.446± 1.174	11.277 ± 0.049
28	11.040± 1.145	10.938 ± 0.048	78	12.828± 1.240	11.328 ± 0.049
29	10.883± 1.135	11.001 ± 0.048	79	10.554± 1.125	11.173 ± 0.049
30	11.023± 1.149	11.035 ± 0.048	80	12.584± 1.228	11.265 ± 0.049
31	10.445± 1.113	11.012 ± 0.048	81	11.076± 1.155	11.226 ± 0.049
32	9.729 ± 1.081	11.011 ± 0.048	82	11.047± 1.152	11.303 ± 0.049
33	12.267± 1.209	10.947 ± 0.048	83	10.749± 1.139	11.167 ± 0.049
34	10.531± 1.116	11.080 ± 0.048	84	11.034± 1.150	11.232 ± 0.049
35	11.025± 1.143	11.015 ± 0.048	85	12.321± 1.214	11.318 ± 0.049
36	10.270± 1.107	10.966 ± 0.048	86	9.660 ± 1.080	11.199 ± 0.049
37	10.571± 1.121	11.045 ± 0.048	87	9.743 ± 1.076	11.308 ± 0.049
38	9.681 ± 1.076	11.065 ± 0.048	88	11.560± 1.186	11.196 ± 0.049
39	12.814± 1.239	11.166 ± 0.048	89	10.619± 1.138	11.238 ± 0.049
40	11.623± 1.180	11.095 ± 0.048	90	10.157± 1.108	11.217 ± 0.049
41	10.697± 1.134	11.092 ± 0.048	91	11.135± 1.155	11.203 ± 0.049
42	10.619± 1.126	11.113 ± 0.048	92	11.645± 1.195	11.286 ± 0.049
43	12.476± 1.218	11.223 ± 0.048	93	11.109± 1.158	11.227 ± 0.049
44	12.226± 1.205	11.092 ± 0.048	94	9.329 ± 1.056	11.343 ± 0.049
45	11.974± 1.191	11.148 ± 0.048	95	11.061± 1.153	11.225 ± 0.049
46	9.775 ± 1.079	11.194 ± 0.048	96	11.204± 1.162	11.258 ± 0.049
47	10.880± 1.141	11.086 ± 0.048	97	10.742± 1.132	11.368 ± 0.049
48	12.579± 1.228	11.135 ± 0.048	98	13.266± 1.265	11.291 ± 0.049
49	10.674± 1.125	11.097 ± 0.048	99	10.871± 1.146	11.219 ± 0.049
50	9.946 ± 1.092	11.123 ± 0.048	100	13.572± 1.288	11.265 ± 0.049

Table D.14: Table of the binding energy spectrum of ^{12}C(e,e′K^+)$^{12}_{\Lambda}$B. A range of the binding energy from −60 MeV to +60 MeV is divided by 500 bins. (2/5)

^{12}C(e,e′K^+)$^{12}_{\Lambda}$B (A range from −60 MeV to +60 MeV is divided by 500 bins)					
N_{bin}	$\overline{\left(\frac{d\sigma}{d\Omega_K}\right)}\Big\|_{1°-13°}$ [nb/sr]		N_{bin}	$\overline{\left(\frac{d\sigma}{d\Omega_K}\right)}\Big\|_{1°-13°}$ [nb/sr]	
	(Signal+Accidental)	(Accidental)		(Signal+Accidental)	(Accidental)
101	12.012 ± 1.207	11.245 ± 0.049	151	13.606 ± 1.286	11.468 ± 0.050
102	10.769 ± 1.135	11.238 ± 0.049	152	11.510 ± 1.194	11.473 ± 0.050
103	10.138 ± 1.113	11.244 ± 0.049	153	11.201 ± 1.168	11.513 ± 0.050
104	10.117 ± 1.104	11.271 ± 0.049	154	11.903 ± 1.209	11.355 ± 0.049
105	14.017 ± 1.301	11.293 ± 0.049	155	11.309 ± 1.173	11.423 ± 0.050
106	12.081 ± 1.208	11.294 ± 0.049	156	11.040 ± 1.170	11.484 ± 0.050
107	10.896 ± 1.149	11.332 ± 0.049	157	13.035 ± 1.260	11.527 ± 0.050
108	11.156 ± 1.157	11.311 ± 0.049	158	11.193 ± 1.167	11.549 ± 0.050
109	12.584 ± 1.234	11.259 ± 0.049	159	11.938 ± 1.206	11.520 ± 0.050
110	11.243 ± 1.166	11.272 ± 0.049	160	11.167 ± 1.171	11.525 ± 0.050
111	12.290 ± 1.223	11.311 ± 0.049	161	11.056 ± 1.165	11.463 ± 0.050
112	11.631 ± 1.187	11.377 ± 0.049	162	11.916 ± 1.204	11.531 ± 0.050
113	12.669 ± 1.236	11.379 ± 0.049	163	10.426 ± 1.131	11.421 ± 0.050
114	9.168 ± 1.059	11.288 ± 0.049	164	12.113 ± 1.217	11.502 ± 0.050
115	9.502 ± 1.069	11.257 ± 0.049	165	10.069 ± 1.105	11.547 ± 0.050
116	10.563 ± 1.132	11.343 ± 0.049	166	10.334 ± 1.128	11.545 ± 0.050
117	10.992 ± 1.152	11.272 ± 0.049	167	10.406 ± 1.129	11.527 ± 0.050
118	11.351 ± 1.171	11.251 ± 0.049	168	10.244 ± 1.131	11.491 ± 0.050
119	10.593 ± 1.129	11.308 ± 0.049	169	10.034 ± 1.108	11.572 ± 0.050
120	10.415 ± 1.123	11.252 ± 0.049	170	10.488 ± 1.131	11.537 ± 0.050
121	9.695 ± 1.084	11.327 ± 0.049	171	10.574 ± 1.140	11.530 ± 0.050
122	10.180 ± 1.117	11.402 ± 0.049	172	11.600 ± 1.196	11.588 ± 0.050
123	12.256 ± 1.220	11.285 ± 0.049	173	13.244 ± 1.274	11.477 ± 0.050
124	12.508 ± 1.263	11.281 ± 0.049	174	11.188 ± 1.166	11.624 ± 0.050
125	11.196 ± 1.167	11.393 ± 0.049	175	11.956 ± 1.208	11.552 ± 0.050
126	9.839 ± 1.093	11.267 ± 0.049	176	10.667 ± 1.137	11.657 ± 0.050
127	9.875 ± 1.097	11.250 ± 0.049	177	10.739 ± 1.151	11.558 ± 0.050
128	11.524 ± 1.182	11.338 ± 0.049	178	11.253 ± 1.180	11.556 ± 0.050
129	12.840 ± 1.247	11.299 ± 0.049	179	13.258 ± 1.282	11.659 ± 0.050
130	12.006 ± 1.207	11.327 ± 0.049	180	11.768 ± 1.201	11.570 ± 0.050
131	10.896 ± 1.155	11.239 ± 0.049	181	11.397 ± 1.182	11.742 ± 0.050
132	11.258 ± 1.174	11.413 ± 0.049	182	10.835 ± 1.155	11.593 ± 0.050
133	12.442 ± 1.232	11.360 ± 0.049	183	12.704 ± 1.252	11.643 ± 0.050
134	13.363 ± 1.274	11.303 ± 0.049	184	10.722 ± 1.149	11.586 ± 0.050
135	10.080 ± 1.113	11.310 ± 0.049	185	10.986 ± 1.165	11.593 ± 0.050
136	10.675 ± 1.144	11.416 ± 0.049	186	12.473 ± 1.241	11.703 ± 0.050
137	12.631 ± 1.239	11.342 ± 0.049	187	13.008 ± 1.263	11.681 ± 0.050
138	10.724 ± 1.143	11.432 ± 0.049	188	12.650 ± 1.259	11.755 ± 0.050
139	9.287 ± 1.072	11.408 ± 0.049	189	10.223 ± 1.122	11.623 ± 0.050
140	10.742 ± 1.152	11.434 ± 0.050	190	12.342 ± 1.234	11.659 ± 0.050
141	11.194 ± 1.167	11.393 ± 0.049	191	11.471 ± 1.202	11.718 ± 0.050
142	10.484 ± 1.131	11.378 ± 0.049	192	11.807 ± 1.211	11.745 ± 0.051
143	13.235 ± 1.274	11.470 ± 0.050	193	12.426 ± 1.236	11.700 ± 0.050
144	10.484 ± 1.131	11.422 ± 0.049	194	13.331 ± 1.289	11.678 ± 0.050
145	11.087 ± 1.162	11.468 ± 0.050	195	11.116 ± 1.172	11.695 ± 0.050
146	12.541 ± 1.242	11.419 ± 0.050	196	13.576 ± 1.300	11.684 ± 0.050
147	12.015 ± 1.214	11.446 ± 0.050	197	12.744 ± 1.256	11.761 ± 0.051
148	12.137 ± 1.214	11.416 ± 0.050	198	13.863 ± 1.322	11.791 ± 0.051
149	12.417 ± 1.229	11.464 ± 0.050	199	13.406 ± 1.290	11.703 ± 0.050
150	11.252 ± 1.173	11.494 ± 0.050	200	14.854 ± 1.356	11.740 ± 0.051

Table D.15: Table of the binding energy spectrum of ^{12}C(e,e′K^+)$^{12}_{\Lambda}$B. A range of the binding energy from −60 MeV to +60 MeV is divided by 500 bins. (3/5)

^{12}C(e,e′K^+)$^{12}_{\Lambda}$B (A range from −60 MeV to +60 MeV is divided by 500 bins)					
N_{bin}	$\left(\frac{d\sigma}{d\Omega_K}\right)\Big\|_{1^\circ-13^\circ}$ [nb/sr]		N_{bin}	$\left(\frac{d\sigma}{d\Omega_K}\right)\Big\|_{1^\circ-13^\circ}$ [nb/sr]	
	(Signal+Accidental)	(Accidental)		(Signal+Accidental)	(Accidental)
201	17.673 ± 1.478	11.762 ± 0.051	251	19.461 ± 1.573	12.009 ± 0.052
202	25.887 ± 1.795	11.727 ± 0.051	252	21.395 ± 1.636	11.982 ± 0.051
203	42.343 ± 2.313	11.720 ± 0.051	253	19.067 ± 1.547	12.190 ± 0.052
204	28.443 ± 1.888	11.746 ± 0.051	254	20.560 ± 1.610	12.028 ± 0.052
205	17.015 ± 1.454	11.708 ± 0.051	255	20.017 ± 1.592	12.119 ± 0.052
206	16.121 ± 1.419	11.798 ± 0.051	256	19.420 ± 1.560	12.090 ± 0.052
207	15.265 ± 1.405	11.848 ± 0.051	257	18.734 ± 1.540	12.166 ± 0.052
208	16.328 ± 1.427	11.730 ± 0.051	258	21.376 ± 1.669	12.095 ± 0.052
209	14.523 ± 1.343	11.772 ± 0.051	259	19.164 ± 1.565	12.173 ± 0.052
210	13.618 ± 1.298	11.851 ± 0.051	260	20.409 ± 1.645	12.059 ± 0.052
211	12.789 ± 1.260	11.799 ± 0.051	261	20.158 ± 1.604	12.141 ± 0.052
212	15.039 ± 1.379	11.711 ± 0.051	262	14.421 ± 1.357	12.083 ± 0.052
213	12.104 ± 1.223	11.886 ± 0.051	263	18.123 ± 1.516	12.189 ± 0.052
214	12.851 ± 1.266	11.909 ± 0.051	264	18.251 ± 1.526	12.087 ± 0.052
215	17.440 ± 1.479	11.863 ± 0.051	265	16.465 ± 1.450	12.087 ± 0.052
216	16.155 ± 1.417	11.759 ± 0.051	266	17.185 ± 1.468	12.110 ± 0.052
217	14.776 ± 1.360	11.790 ± 0.051	267	20.118 ± 1.595	12.229 ± 0.052
218	14.973 ± 1.367	11.877 ± 0.051	268	19.901 ± 1.583	12.196 ± 0.052
219	10.834 ± 1.162	11.881 ± 0.051	269	17.950 ± 1.506	12.250 ± 0.052
220	11.720 ± 1.209	11.801 ± 0.051	270	19.683 ± 1.597	12.115 ± 0.052
221	13.614 ± 1.310	11.810 ± 0.051	271	20.933 ± 1.635	12.213 ± 0.052
222	13.466 ± 1.302	11.819 ± 0.051	272	20.140 ± 1.607	12.270 ± 0.052
223	11.997 ± 1.224	11.837 ± 0.051	273	20.838 ± 1.617	12.279 ± 0.052
224	12.085 ± 1.233	11.884 ± 0.051	274	17.460 ± 1.492	12.251 ± 0.052
225	16.218 ± 1.422	11.855 ± 0.051	275	19.593 ± 1.594	12.337 ± 0.052
226	15.267 ± 1.394	11.873 ± 0.051	276	17.142 ± 1.481	12.284 ± 0.052
227	13.706 ± 1.313	11.889 ± 0.051	277	21.193 ± 1.645	12.305 ± 0.052
228	14.682 ± 1.357	11.926 ± 0.051	278	20.584 ± 1.627	12.282 ± 0.052
229	16.433 ± 1.436	11.828 ± 0.051	279	22.611 ± 1.695	12.280 ± 0.052
230	13.952 ± 1.324	11.962 ± 0.051	280	22.730 ± 1.704	12.111 ± 0.052
231	15.847 ± 1.412	11.875 ± 0.051	281	18.291 ± 1.524	12.336 ± 0.052
232	12.624 ± 1.256	11.948 ± 0.051	282	20.620 ± 1.620	12.181 ± 0.052
233	12.308 ± 1.243	11.838 ± 0.051	283	20.531 ± 1.628	12.308 ± 0.052
234	14.432 ± 1.346	11.953 ± 0.051	284	21.512 ± 1.665	12.360 ± 0.052
235	15.784 ± 1.406	11.882 ± 0.051	285	19.843 ± 1.594	12.353 ± 0.052
236	12.921 ± 1.273	11.955 ± 0.051	286	19.256 ± 1.567	12.315 ± 0.052
237	10.667 ± 1.157	12.048 ± 0.051	287	22.490 ± 1.700	12.348 ± 0.053
238	12.858 ± 1.267	12.084 ± 0.052	288	22.853 ± 1.708	12.452 ± 0.053
239	12.386 ± 1.245	11.957 ± 0.051	289	22.013 ± 1.674	12.498 ± 0.053
240	12.855 ± 1.273	11.973 ± 0.051	290	20.328 ± 1.612	12.386 ± 0.053
241	14.751 ± 1.364	11.940 ± 0.051	291	22.454 ± 1.697	12.368 ± 0.053
242	14.449 ± 1.347	11.981 ± 0.051	292	21.904 ± 1.680	12.402 ± 0.053
243	15.711 ± 1.405	12.019 ± 0.051	293	20.390 ± 1.617	12.434 ± 0.053
244	15.184 ± 1.380	12.020 ± 0.051	294	22.802 ± 1.704	12.399 ± 0.053
245	15.996 ± 1.419	11.980 ± 0.051	295	21.443 ± 1.664	12.546 ± 0.053
246	18.776 ± 1.549	11.946 ± 0.051	296	18.784 ± 1.549	12.496 ± 0.053
247	22.075 ± 1.664	12.021 ± 0.051	297	18.924 ± 1.556	12.452 ± 0.053
248	29.275 ± 1.922	12.143 ± 0.052	298	18.003 ± 1.527	12.516 ± 0.053
249	33.152 ± 2.056	12.084 ± 0.052	299	22.068 ± 1.678	12.498 ± 0.053
250	28.923 ± 1.915	12.153 ± 0.052	300	20.384 ± 1.622	12.438 ± 0.053

Table D.16: Table of the binding energy spectrum of ^{12}C(e,e′K^+)$^{12}_{\Lambda}$B. A range of the binding energy from −60 MeV to +60 MeV is divided by 500 bins. (4/5)

^{12}C(e,e′K^+)$^{12}_{\Lambda}$B (A range from −60 MeV to +60 MeV is divided by 500 bins)					
N_{bin}	$\overline{\left(\frac{d\sigma}{d\Omega_K}\right)}\Big\|_{1°-13°}$ [nb/sr]		N_{bin}	$\overline{\left(\frac{d\sigma}{d\Omega_K}\right)}\Big\|_{1°-13°}$ [nb/sr]	
	(Signal+Accidental)	(Accidental)		(Signal+Accidental)	(Accidental)
301	20.420 ± 1.619	12.587 ± 0.053	351	24.805 ± 1.809	12.736 ± 0.054
302	23.081 ± 1.720	12.511 ± 0.053	352	22.598 ± 1.713	12.771 ± 0.054
303	23.958 ± 1.757	12.461 ± 0.053	353	25.079 ± 1.810	12.737 ± 0.054
304	19.325 ± 1.583	12.546 ± 0.053	354	27.921 ± 1.918	12.882 ± 0.054
305	20.698 ± 1.626	12.521 ± 0.053	355	22.131 ± 1.707	12.717 ± 0.054
306	24.253 ± 1.774	12.603 ± 0.053	356	25.472 ± 1.824	12.802 ± 0.054
307	19.737 ± 1.601	12.469 ± 0.053	357	26.548 ± 1.868	12.842 ± 0.054
308	20.506 ± 1.621	12.494 ± 0.053	358	21.698 ± 1.689	12.816 ± 0.054
309	22.034 ± 1.680	12.600 ± 0.053	359	27.441 ± 1.955	12.805 ± 0.054
310	24.204 ± 1.770	12.535 ± 0.053	360	26.329 ± 1.857	12.817 ± 0.054
311	20.649 ± 1.638	12.486 ± 0.053	361	28.333 ± 1.937	12.847 ± 0.054
312	20.385 ± 1.627	12.561 ± 0.053	362	23.061 ± 1.743	12.726 ± 0.054
313	22.265 ± 1.698	12.558 ± 0.053	363	26.715 ± 1.875	12.867 ± 0.054
314	21.027 ± 1.647	12.552 ± 0.053	364	26.356 ± 1.873	12.860 ± 0.054
315	21.806 ± 1.677	12.603 ± 0.053	365	24.072 ± 1.789	12.913 ± 0.054
316	24.514 ± 1.778	12.608 ± 0.053	366	21.928 ± 1.702	12.936 ± 0.055
317	22.471 ± 1.699	12.565 ± 0.053	367	24.612 ± 1.795	13.004 ± 0.055
318	21.465 ± 1.681	12.671 ± 0.053	368	25.680 ± 1.844	12.791 ± 0.054
319	24.121 ± 1.764	12.596 ± 0.053	369	27.533 ± 1.909	12.940 ± 0.055
320	24.050 ± 1.768	12.574 ± 0.053	370	28.418 ± 1.938	13.045 ± 0.055
321	27.166 ± 1.879	12.650 ± 0.053	371	26.186 ± 1.861	12.862 ± 0.054
322	22.243 ± 1.691	12.615 ± 0.053	372	26.167 ± 1.855	12.926 ± 0.055
323	24.067 ± 1.769	12.703 ± 0.054	373	25.396 ± 1.828	12.920 ± 0.055
324	24.122 ± 1.764	12.702 ± 0.054	374	26.219 ± 1.863	12.908 ± 0.055
325	22.370 ± 1.701	12.500 ± 0.053	375	25.096 ± 1.821	12.839 ± 0.054
326	25.637 ± 1.831	12.708 ± 0.054	376	25.156 ± 1.840	12.961 ± 0.055
327	23.901 ± 1.772	12.637 ± 0.053	377	28.494 ± 1.943	12.962 ± 0.055
328	22.697 ± 1.711	12.750 ± 0.054	378	25.158 ± 1.820	12.913 ± 0.055
329	24.019 ± 1.766	12.646 ± 0.054	379	27.670 ± 1.919	12.929 ± 0.055
330	20.682 ± 1.645	12.663 ± 0.054	380	25.283 ± 1.825	13.025 ± 0.055
331	24.109 ± 1.763	12.725 ± 0.054	381	30.607 ± 2.014	12.984 ± 0.055
332	26.135 ± 1.857	12.677 ± 0.054	382	25.718 ± 1.856	13.034 ± 0.055
333	28.446 ± 1.922	12.611 ± 0.053	383	25.173 ± 1.821	13.106 ± 0.055
334	23.584 ± 1.753	12.613 ± 0.053	384	28.923 ± 1.977	13.006 ± 0.055
335	25.454 ± 1.818	12.691 ± 0.054	385	27.849 ± 1.917	12.969 ± 0.055
336	22.872 ± 1.744	12.625 ± 0.054	386	30.249 ± 2.012	13.176 ± 0.055
337	25.209 ± 1.819	12.705 ± 0.054	387	26.932 ± 1.900	13.156 ± 0.055
338	25.336 ± 1.824	12.743 ± 0.054	388	29.675 ± 2.014	13.134 ± 0.055
339	26.957 ± 1.878	12.709 ± 0.054	389	26.584 ± 1.870	13.012 ± 0.055
340	27.918 ± 1.908	12.733 ± 0.054	390	25.423 ± 1.840	13.022 ± 0.055
341	25.753 ± 1.826	12.780 ± 0.054	391	26.934 ± 1.886	13.068 ± 0.055
342	27.128 ± 1.877	12.738 ± 0.054	392	30.155 ± 2.015	13.012 ± 0.055
343	26.391 ± 1.852	12.688 ± 0.054	393	28.106 ± 1.944	13.151 ± 0.055
344	25.394 ± 1.828	12.765 ± 0.054	394	29.211 ± 1.969	13.165 ± 0.055
345	22.604 ± 1.719	12.787 ± 0.054	395	27.317 ± 1.936	13.081 ± 0.055
346	27.178 ± 1.880	12.766 ± 0.054	396	30.655 ± 2.017	13.135 ± 0.055
347	23.944 ± 1.760	12.832 ± 0.054	397	32.988 ± 2.095	13.115 ± 0.055
348	24.281 ± 1.776	12.826 ± 0.054	398	29.699 ± 1.989	13.143 ± 0.055
349	19.423 ± 1.607	12.727 ± 0.054	399	30.336 ± 2.045	13.256 ± 0.056
350	22.744 ± 1.710	12.748 ± 0.054	400	30.021 ± 2.019	13.148 ± 0.055

Table D.17: Table of the binding energy spectrum of ^{12}C(e,e′K^+)$^{12}_{\Lambda}$B. A range of the binding energy from −60 MeV to +60 MeV is divided by 500 bins. (5/5)

^{12}C(e,e′K^+)$^{12}_{\Lambda}$B (A range from −60 MeV to +60 MeV is divided by 500 bins)					
N_{bin}	$\left(\frac{d\sigma}{d\Omega_K}\right)\Big\|_{1^\circ-13^\circ}$ [nb/sr]		N_{bin}	$\left(\frac{d\sigma}{d\Omega_K}\right)\Big\|_{1^\circ-13^\circ}$ [nb/sr]	
	(Signal+Accidental)	(Accidental)		(Signal+Accidental)	(Accidental)
401	25.074 ± 1.843	13.178 ± 0.055	451	30.886 ± 2.064	13.490 ± 0.057
402	30.801 ± 2.035	13.163 ± 0.055	452	27.178 ± 1.961	13.534 ± 0.057
403	26.647 ± 1.903	13.224 ± 0.056	453	29.508 ± 2.008	13.498 ± 0.057
404	31.971 ± 2.094	13.192 ± 0.055	454	30.192 ± 2.031	13.491 ± 0.057
405	27.549 ± 1.929	13.184 ± 0.055	455	32.450 ± 2.121	13.438 ± 0.057
406	31.659 ± 2.056	13.250 ± 0.056	456	30.481 ± 2.050	13.644 ± 0.057
407	30.227 ± 2.024	13.187 ± 0.055	457	33.981 ± 2.162	13.615 ± 0.057
408	30.789 ± 2.048	13.187 ± 0.055	458	32.431 ± 2.111	13.549 ± 0.057
409	26.846 ± 1.903	13.314 ± 0.056	459	27.633 ± 1.949	13.589 ± 0.057
410	28.596 ± 1.959	13.193 ± 0.056	460	31.097 ± 2.082	13.546 ± 0.057
411	28.584 ± 2.058	13.306 ± 0.056	461	30.200 ± 2.045	13.606 ± 0.057
412	28.543 ± 1.965	13.295 ± 0.056	462	31.919 ± 2.091	13.612 ± 0.057
413	29.149 ± 1.974	13.247 ± 0.056	463	34.865 ± 2.218	13.544 ± 0.057
414	29.260 ± 1.982	13.284 ± 0.056	464	30.362 ± 2.056	13.523 ± 0.057
415	30.935 ± 2.072	13.215 ± 0.056	465	27.023 ± 1.940	13.648 ± 0.057
416	28.955 ± 1.975	13.273 ± 0.056	466	29.682 ± 2.020	13.659 ± 0.057
417	29.286 ± 1.988	13.243 ± 0.056	467	28.390 ± 1.978	13.584 ± 0.057
418	31.526 ± 2.061	13.391 ± 0.056	468	30.023 ± 2.038	13.656 ± 0.057
419	30.841 ± 2.038	13.349 ± 0.056	469	30.126 ± 2.031	13.677 ± 0.057
420	26.781 ± 1.903	13.335 ± 0.056	470	26.519 ± 1.914	13.624 ± 0.057
421	25.935 ± 1.872	13.220 ± 0.056	471	30.983 ± 2.084	13.658 ± 0.057
422	28.073 ± 1.942	13.425 ± 0.056	472	27.361 ± 1.949	13.584 ± 0.057
423	26.328 ± 1.885	13.177 ± 0.056	473	29.901 ± 2.030	13.599 ± 0.057
424	27.353 ± 1.959	13.334 ± 0.056	474	32.501 ± 2.125	13.625 ± 0.057
425	30.678 ± 2.041	13.409 ± 0.056	475	31.464 ± 2.112	13.839 ± 0.058
426	31.099 ± 2.069	13.326 ± 0.056	476	33.249 ± 2.174	13.602 ± 0.057
427	31.562 ± 2.063	13.345 ± 0.056	477	27.448 ± 1.971	13.662 ± 0.058
428	30.085 ± 2.019	13.330 ± 0.056	478	32.584 ± 2.144	13.547 ± 0.057
429	32.051 ± 2.095	13.423 ± 0.056	479	27.935 ± 1.966	13.591 ± 0.057
430	29.285 ± 2.011	13.346 ± 0.056	480	32.513 ± 2.144	13.763 ± 0.058
431	29.316 ± 1.990	13.321 ± 0.056	481	29.145 ± 2.041	13.807 ± 0.058
432	31.102 ± 2.060	13.463 ± 0.056	482	28.657 ± 2.011	13.753 ± 0.058
433	28.525 ± 2.012	13.516 ± 0.057	483	30.780 ± 2.061	13.710 ± 0.058
434	28.474 ± 1.989	13.359 ± 0.056	484	31.793 ± 2.115	13.644 ± 0.058
435	33.187 ± 2.147	13.329 ± 0.056	485	30.789 ± 2.071	13.763 ± 0.058
436	25.302 ± 1.850	13.376 ± 0.056	486	29.936 ± 2.061	13.737 ± 0.058
437	30.821 ± 2.050	13.471 ± 0.056	487	29.124 ± 2.019	13.756 ± 0.058
438	26.294 ± 1.888	13.362 ± 0.056	488	33.148 ± 2.162	13.730 ± 0.058
439	31.484 ± 2.063	13.440 ± 0.056	489	26.996 ± 1.928	13.697 ± 0.058
440	29.270 ± 2.025	13.501 ± 0.057	490	30.832 ± 2.088	13.847 ± 0.058
441	30.134 ± 2.041	13.481 ± 0.057	491	30.178 ± 2.044	13.892 ± 0.058
442	32.049 ± 2.113	13.506 ± 0.057	492	31.529 ± 2.111	13.745 ± 0.058
443	31.012 ± 2.077	13.461 ± 0.057	493	30.278 ± 2.041	13.756 ± 0.058
444	27.771 ± 1.964	13.518 ± 0.057	494	32.030 ± 2.126	13.865 ± 0.058
445	29.140 ± 2.006	13.402 ± 0.056	495	32.354 ± 2.162	13.744 ± 0.058
446	31.605 ± 2.116	13.472 ± 0.057	496	31.696 ± 2.147	13.779 ± 0.058
447	32.394 ± 2.127	13.588 ± 0.057	497	31.463 ± 2.102	13.814 ± 0.058
448	28.681 ± 1.979	13.457 ± 0.057	498	29.116 ± 2.014	13.793 ± 0.058
449	31.123 ± 2.066	13.526 ± 0.057	499	32.059 ± 2.123	13.771 ± 0.058
450	29.691 ± 2.006	13.574 ± 0.057	500	31.477 ± 2.177	13.841 ± 0.058

Table D.18: Table of the binding energy spectrum of ^{52}Cr(e,e′K^+)$^{52}_{\Lambda}$V. A range of the binding energy from −60 MeV to +60 MeV is divided by 100 bins.

^{52}Cr(e,e′K^+)$^{52}_{\Lambda}$V (A range from −60 MeV to +60 MeV is divided by 100 bins)					
N_{bin}	Counts		N_{bin}	Counts	
	(Signal+Accidental)	(Accidental)		(Signal+Accidental)	(Accidental)
1	342.00 ± 18.49	356.26 ± 0.10	51	511.00 ± 22.61	386.90 ± 0.11
2	392.00 ± 19.80	356.59 ± 0.10	52	480.00 ± 21.91	388.07 ± 0.11
3	375.00 ± 19.36	360.93 ± 0.11	53	478.00 ± 21.86	390.60 ± 0.11
4	377.00 ± 19.42	359.65 ± 0.11	54	453.00 ± 21.28	389.31 ± 0.11
5	367.00 ± 19.16	360.48 ± 0.11	55	470.00 ± 21.68	392.11 ± 0.11
6	350.00 ± 18.71	360.62 ± 0.11	56	464.00 ± 21.54	393.56 ± 0.11
7	358.00 ± 18.92	359.70 ± 0.11	57	473.00 ± 21.75	395.49 ± 0.11
8	353.00 ± 18.79	361.00 ± 0.11	58	504.00 ± 22.45	397.55 ± 0.11
9	354.00 ± 18.81	362.24 ± 0.11	59	508.00 ± 22.54	398.87 ± 0.11
10	366.00 ± 19.13	362.76 ± 0.11	60	557.00 ± 23.60	400.29 ± 0.11
11	381.00 ± 19.52	362.68 ± 0.11	61	519.00 ± 22.78	402.99 ± 0.11
12	334.00 ± 18.28	363.73 ± 0.11	62	469.00 ± 21.66	402.83 ± 0.11
13	393.00 ± 19.82	363.66 ± 0.11	63	519.00 ± 22.78	406.30 ± 0.11
14	379.00 ± 19.47	363.82 ± 0.11	64	533.00 ± 23.09	406.93 ± 0.11
15	359.00 ± 18.95	363.82 ± 0.11	65	525.00 ± 22.91	409.39 ± 0.11
16	367.00 ± 19.16	363.42 ± 0.11	66	549.00 ± 23.43	411.95 ± 0.11
17	380.00 ± 19.49	362.88 ± 0.11	67	571.00 ± 23.90	413.59 ± 0.11
18	349.00 ± 18.68	363.78 ± 0.11	68	569.00 ± 23.85	417.31 ± 0.11
19	372.00 ± 19.29	364.08 ± 0.11	69	542.00 ± 23.28	417.21 ± 0.11
20	338.00 ± 18.38	363.05 ± 0.11	70	571.00 ± 23.90	419.44 ± 0.11
21	354.00 ± 18.81	363.75 ± 0.11	71	560.00 ± 23.66	420.40 ± 0.11
22	383.00 ± 19.57	363.59 ± 0.11	72	569.00 ± 23.85	422.52 ± 0.11
23	354.00 ± 18.81	363.72 ± 0.11	73	580.00 ± 24.08	423.04 ± 0.11
24	346.00 ± 18.60	363.27 ± 0.11	74	586.00 ± 24.21	425.24 ± 0.11
25	384.00 ± 19.60	364.87 ± 0.11	75	555.00 ± 23.56	426.29 ± 0.11
26	377.00 ± 19.42	363.48 ± 0.11	76	616.00 ± 24.82	426.19 ± 0.11
27	353.00 ± 18.79	364.52 ± 0.11	77	583.00 ± 24.15	428.81 ± 0.12
28	380.00 ± 19.49	364.96 ± 0.11	78	655.00 ± 25.59	430.11 ± 0.12
29	376.00 ± 19.39	365.15 ± 0.11	79	596.00 ± 24.41	430.75 ± 0.12
30	345.00 ± 18.57	365.54 ± 0.11	80	612.00 ± 24.74	432.49 ± 0.12
31	379.00 ± 19.47	366.10 ± 0.11	81	609.00 ± 24.68	433.99 ± 0.12
32	402.00 ± 20.05	367.18 ± 0.11	82	607.00 ± 24.64	435.16 ± 0.12
33	392.00 ± 19.80	367.74 ± 0.11	83	600.00 ± 24.49	436.39 ± 0.12
34	382.00 ± 19.54	368.72 ± 0.11	84	634.00 ± 25.18	439.77 ± 0.12
35	375.00 ± 19.36	370.62 ± 0.11	85	648.00 ± 25.46	439.96 ± 0.12
36	414.00 ± 20.35	369.70 ± 0.11	86	650.00 ± 25.50	441.78 ± 0.12
37	423.00 ± 20.57	370.84 ± 0.11	87	637.00 ± 25.24	443.82 ± 0.12
38	439.00 ± 20.95	371.93 ± 0.11	88	610.00 ± 24.70	444.23 ± 0.12
39	398.00 ± 19.95	373.73 ± 0.11	89	664.00 ± 25.77	446.88 ± 0.12
40	383.00 ± 19.57	374.35 ± 0.11	90	651.00 ± 25.51	447.70 ± 0.12
41	428.00 ± 20.69	374.41 ± 0.11	91	652.00 ± 25.53	448.26 ± 0.12
42	422.00 ± 20.54	375.81 ± 0.11	92	638.00 ± 25.26	450.47 ± 0.12
43	449.00 ± 21.19	377.36 ± 0.11	93	696.00 ± 26.38	452.62 ± 0.12
44	415.00 ± 20.37	379.08 ± 0.11	94	626.00 ± 25.02	453.30 ± 0.12
45	419.00 ± 20.47	379.72 ± 0.11	95	637.00 ± 25.24	455.37 ± 0.12
46	470.00 ± 21.68	380.04 ± 0.11	96	691.00 ± 26.29	455.68 ± 0.12
47	433.00 ± 20.81	381.58 ± 0.11	97	687.00 ± 26.21	457.35 ± 0.12
48	464.00 ± 21.54	383.95 ± 0.11	98	700.00 ± 26.46	457.90 ± 0.12
49	438.00 ± 20.93	383.53 ± 0.11	99	633.00 ± 25.16	458.55 ± 0.12
50	472.00 ± 21.73	384.81 ± 0.11	100	643.00 ± 25.36	460.95 ± 0.12

Bibliography

[1] B. Povh, *Progress in Particle and Nuclear Physics* **18**, 183 (1987)

[2] P. M. Maessen, T. A. Rijken, J. J. de Swart, *Physical Review* **C 40**, 2226 (1989)

[3] T. A. Rijken *et al.*, *Physical Review* **C 59**, 21 (1999)

[4] B. Holzenkamp *et al.*, *Nuclear Physics* **A 500**, 485 (1989)

[5] T. A. Rijken *et al.*, *Nuclear Physics* **A 547**, 245 (1992)

[6] Y. Yamamoto *et al.*, *Progress of Theoretical Physics Supplement* **118**, 361 (1994)

[7] D. J. Millener *et al.*, *Physical Review* **C 31**, 2, 499 (1984)

[8] K. Maeda, H. Tamura, S. N. Nakamura, O. Hashimoto, *Proc. Int. Symp. on Electrophotoproduction of strangeness on nucleons and nuclei, SENDAI03* p.221 (2003)

[9] P. Bydžovský *et al.*, *Nuclear Physics* **A 881**, 199-217 (2012)

[10] O. Hashimoto, H. Tamura, *Progress in Particle and Nuclear Physics* **57**, 564653 (2006)

[11] W. Brückner *et al.*, *Physical Review Letters* **B 55**, 107 (1975)

[12] W. Brückner *et al.*, *Physical Review Letters* **B 62**, 481 (1976)

[13] W. Brückner *et al.*, *Physical Review Letters* **B 79**, 157 (1978)

[14] R. Bertini *et al.*, *Physical Review Letters* **A 368**, 365 (1981)

[15] R. E. Chrien *et al.*, *Physical Review Letters* **B 89**, 31 (1979)

[16] M. May *et al.*, *Physical Review Letters* **47**, 1106 (1981)

[17] M. A. Faessler *et al.*, *Physical Review Letters* **B 46**, 468 (1973)

[18] C. Milner *et al.*, *Physical Review Letters* **54**, 1237 (1985)

[19] P. H. Pile *et al.*, *Physical Review Letters* **66**, 2585 (1991)

[20] M. Akei *et al.*, *Nuclear Physics* **A 534**, 478 (1991)

[21] T. Hasegawa *et al.*, *Physical Review Letters* **74**, 224 (1995)

[22] T. Hasegawa *et al.*, *Physical Review* **C 53**, 1210 (1996)

[23] O. Hashimoto *et al.*, *Nuclear Physics* **A 639**, 93c (1998)

[24] H. Hotchi *et al.*, *Physical Review* **C 64**, 044302 (2001)

[25] H. Tamura *et al.*, *Physical Review Letter* **84**, 5963 (2000)

[26] S. Cohen and D. Kurath, *Nuclear Physics* **73**, 1 (1965)

[27] M. Danysz and J. Pniewski, *Phil. Mag.* **44**, 348 (1953)

[28] T. Miyoshi *et al.*, *Physical Review Letters* **90**, 23 (2003)

[29] L. Yuan *et al.*, *Physical Review* **C 73**, 044607 (2006)

[30] J. E. Spencer and H. A. Enge, *Nuclear Instruments and Methods* **49**, 181-193 (1967)

[31] S. N. Nakamura, *Physical Review Letters* **110**, 012502 (2013)

[32] A. Matsumura, *Doctoral thesis* (2009)

[33] E. Hiyama *et al.*, *Physical Review* **C 80**, 054321 (2009)

[34] M. Jurič *et al.*, *Nuclear Physics* **B 52**, 1-30 (1973)

[35] T.Cantwell *et al.*, *Nuclear Physics* **A 236**, 445-456 (1974)

[36] H. Tamura *et al.*, *Physical Review Letters* **84**, 5963-5966 (2000)

[37] T. Motoba *et al.*, *Sendai2008, Strangeness in nuclear and hadronic system*, p.178

[38] J. J. LeRose *et al.*, *Nuclear Physics* **A804**, 116-124 (2008)

[39] M. Iodice *et al.*, *Physical Revie Letters* **99**, 052501 (2007)

[40] F. Cusanno *et al.*, *Physical Review Letters* **103**, 202501 (2009)

[41] R. Bradford *et al.*, *Physical Review* **C 73**, 035202 (2006)

[42] K. -H. Glander *et al.*, *Europian Physical Journal* **A 19**, 251 (2004)

[43] M. Q. Tran *et al.*, *Physical Letters* **B 445**, 20 (1998)

[44] A. Bleckmann *et al.*, *Z. Physik* **239**, 1 (1970)

[45] R. A. Adelseck and B. Saghai, *Physical Review* **C 42**, 108 (1990)

[46] P. Bydžovský and T. Mart, *Physical Review* **C 76**, 065202 (2007)

[47] T. Motoba, M. Sotona and K. Itonaga, *Theoretical Physics Supplement*, **117** (1994)

[48] T. Motoba, P. Bydžovský, M. Sotona and K. Itonaga, *Progress of Theoretical Physics Supplement*, **185** (2010)

[49] Th. A. Rijken *et al.*, *Physical Review* **C 59**, 21 (1999)

[50] Y. Akaishi *et al.*, *Physical Review Letters* **84** (2000)

[51] A. Nogga *et al.*, *Physical Review Letters* **88** (2002)

[52] C. B. Dover, *in Proceedings of the International Symmposium on Medium Energy Physics*, Beijing, p.257 (1987)

[53] R. Bertini *et al.*, *Physics Letters* **83 B**, 3, 4 (1979)

[54] D. J. Millener and C. B. Dover, *Physical Review* **C 38**, 2700 (1988)

[55] C. M. Keil *et al.*, *Physical Review* **C 61**, 064309 (2000)

[56] Y. Yamamoto and H. Bando, *Progress of Theoretical Physics* **83**, 2 (1990)

[57] D. Halderson, *Physical Review* **C61**, 034001 (2000)

[58] M. Sotona and S. Frullani, *Progress of Theoretical Physics Supplement* **177** (1994).

[59] Ed V. Hunberford, *Progress of Theoretical Physics Supplement* **117** (1994).

[60] R. H. Rode for the JLab 12 GeV Project Team, *AIP Conference Proceedings* **1218**, 26 (2010)

[61] Y. -C. Chao *et al.*, *CP732, Beam Instrumentation Workshop 2004: Eleventh Workshop* (2004)

[62] P. Chevtsov *et al.*, *Nuclear Instruments and Methods in Physics Research* **A 557**, 324-327 (2006)

[63] A. Shichijo, *Master's thesis* (2009).

[64] *Chronological scientific tables* (2009).

[65] M. Sotona, *private communication.*

[66] Y. Tsai, *Reviews of Modern Physics* **46**, 4 (1974).

[67] C. Itzykson, J. Zuber, *Quantum Field Theory* (Dover, 1980).

[68] K. Nakamura *et al., Journal of Physics* **G 37**, 075021 (2010).

[69] A. Chiba, *Master's thesis* (2010).

[70] T. Gogami *et al., Nuclear Instruments and Methods in Physics Research* **A 729**, 816-824 (2013).

[71] N. Taniya, *Master's thesis* (2009).

[72] W. A. Watson III *et. al., IEEE transactions on nuclear science* **41**, 1 (1994).

[73] D. J. Abbott *et. al.*, "CODA performance in the real world".

[74] B. Moffit, IEEE (2012).

[75] E. Jastrzembski *et. al., Proceeding of the real time* **99** conference (1999).

[76] K. Yokota, *Master's thesis* (2008).

[77] D. Kawama, *Doctoral thesis* (2011).

[78] P. Achenbach, C. Ayerbe Gayoso, R. Bohm *et al.*, *EPJ Web of Conference* **37**, 06004 (2004).

[79] P. Achenbach, A. Esser, C. Ayerbe Gayoso *et al.*, *Nuclear Physics* **A 881**, 187-198 (2012).

[80] P. Achenbach, C. Ayerbe Gayoso, J. C. Bernauer *et al.*, *European Physical Journal* **A 48**, 14 (2012).

[81] J. C. David *et al., Physical Review* **C 52**, 2613 (1996).

[82] T. Mart and C. Bennhold, *Physical Review* **C 61**, 012201 (R) (1999).

[83] F. Dohrmann, A. Ahmidouch *et al.*, *arXiv:0707.3059v2* (2007).

[84] P. Markoviz *et al.*, *Proceedings of SENDAI08* (2009).

[85] M. A. Mariscotti, *Nuclear Instruments and Methods* **50**, 309-320 (1967).

[86] T. Motoba, *private communication* (2014).

[87] D. H. Davis, *Nuclear Physics* **A 547**, 369c (1992).

[88] O. Richter, M. Sotona and J. Žofka, *Physical Review* **C 43**, 6 (1991).

[89] J. Pniewski and M. Danysz, *Physical Letters* **1**, 143 (1962).

[90] R. H. Dalitz and A. Gal, *Nuclear Physics* **B 1**, 1 (1967).

[91] J. Pniewski *et al.*, *Nuclear Physics* **B 2**, 317 (1967).

[92] K. W. Allen *et al.*, *"Energy levels of* ^{6}*Li and* ^{6}*Li from a study of the* ^{7}*Li(*^{3}*He,*α*)*^{6}*Li and* ^{7}*Li(t,*α*)*^{6}*He"* (1960)

[93] S. Aoyama *et al.*, *Progress of Theoretical Physics* **93**, 1 (1995)

[94] T. Nakamura, *The European Physical Journal* **A 13**, 33-37 (2002)

[95] S. K. Dutta *et al.*, *Journal of Physics G: Nuclear and Particle Physics* **29**, 2411-2421 (2003)

[96] F. Ajzenberg-Selove, *Nuclear Physics* **A 413**, 1-214 (1984).

[97] M. Sotona and M. Frullani, *Progress of Theoretical Physics Supplement* **117** (1994).

[98] R. H. Dalitz *et al.*, *Physical Letters* **10**, 153 (1964).

[99] J. L. Friar *et al.*, *Physical Review* **C 18**, 908 (1978).

[100] A. R. Bodmer and Q. N. Usmani, *Physical Review* **C 31**, 1400 (1985).

[101] E. Hiyama and Y. Yamamoto, *Progress of Theoretical Physics* **128**, 1 (2012).

[102] E. Hiyama, *Nuclear Physics* **A 914**, 130-139 (2013).

[103] K. Tsukada *et al.*, *Few-Body Systems* **54**:375-379 (2013).

[104] S. Nagao *et al.*, *Proceedings of XV international conference on hadron spectroscopy (Hadron2013)* **185** (2013).

[105] *J-PARC proposals.* http://j-parc.jp/NuclPart/Proposal_e.html (2006).

[106] R. J. Peterson, *Nuclear Physics* **A 377**, 41-52 (1982)

[107] J. P. Glickman *et al.*, *Physical Review* **C 43**, 4, 1740 (1991)

[108] S. Dixit *et al.*, *Physical Review* **C 43**, 4, 1758 (1991)

[109] D. R. Tilley *et al.*, *Nuclear Physics* **A 745**, 155-362 (2004).

[110] D. J. Millener, *Nuclear Physics* **A 881**, 298-309 (2012).

[111] M. Isaka *et al.*, *Few Body Systems* **54**:1219-1222 (2013).

[112] H. Tamura *et al.*, *Nuclear Physics* **A 754**, 58c-69c (2005).

[113] D. J. Millener, *private communication* (2014).

[114] M. Morháč *et al.*, *Nulcear Instruments and Methods in Physics Research* **A 401**, 113-132 (1997).

[115] C. G. Ryan *et al.*, *Nulcear Instruments and Methods in Physics Research* **B 34**, 396-402 (1988).

[116] http: //root.cern.ch/root/htmldoc/TSpectrum.html

[117] P. Dluzewski *et al.*, *Nulcear Physics* **A 484**, 520-524 (1988).

[118] D. H. Davis, *Nuclear Physics* **A 754**, 3c-13c (2005).

[119] Y. Yamamoto, *private communication* (2014).

[120] Z. Elekes and J. Timar, *Nuclear Data Sheets* **112**, 1-131 (2011).

[121] H. Xiaolong, *Nuclear Data Sheets* **107**, 2131-2322 (2006).

[122] P. Bydžovský, F. Garibaldi, J. J. LeRose, P. Markowitz, D. J. Millener, S. N. Nakamura, J. Reinhold, L. Tang *et al.*, *Proposal to JLab PAC 40 for "A Study with High Precision on the Electro-production of the* Λ *and* Λ*-Hypernuclei in the Full Mass Range"* (2013).

[123] J.Kusaka, *Master's thesis* (2013).

[124] P. Bydžovský, M. Sotona, T. Motoba, K. Itonaga, K. Ogawa, O. Hashimoto, *Nuclear Physics* **A 881**, 199-217 (2012).

[125] T. Motoba, *Nuclear Physics* **A 914**, 23-33 (2013).

[126] P. Bydžovský *et al.*, *arXiv:0706.3836v1 [nucl-th]* 26June2007.

[127] F. Cusanno *et al.*, *Nuclear Physics* **A 835**, 129-135 (2010).